PERFORMANCE OF CRACKED REINFORCED CONCRETE PIPES SUBJECTED TO DIFFERENT ENVIRONMENTAL CONDITIONS

By

Bassam Hatem Karim Al-lami

DISSERTATION

Submitted in partial fulfillment of the requirements

for the degree of Doctor of Philosophy at

The University of Texas at

Arlington August 2020

ARLINGTON, TEXAS

Supervising Committee:

Dr. Himan Hojat Jalali, Supervising Professor

Dr. Ali Abolmaali

Dr. Melanie Sattler

Dr. Ardashir Anjomani

ABSTRACT

PERFORMANCE OF CRACKED REINFORCED CONCRETE PIPES SUBJECTED TO DIFFERENT ENVIRONMENTAL CONDITIONS

Bassam Hatem Karim Al-lami, Ph.D.

The University of Texas at Arlington, 2020

Advisors: Dr. Himan Hojat Jalali and Professor Ali Abolmaali

Performance of reinforced concrete pipes, as a major part of the water and waste-water infrastructure, plays an important role in the resilience and sustainability of today's modern cities. Cracks may appear in these pipes due to handling and placement and might affect their long-term performance due to corrosion concerns. Current practice for quality control after installation of these pipes is quite strict and any pipe with a crack width of more than 0.01″ is not approved. The goal of this research project is to evaluate the performance of cracked reinforced concrete pipes subjected to saline environments with three different concentration of sodium chloride. The reinforced concrete pipes in this study are cracked to keep the cracks open to 0.05″. The evaluation is based on strength degradation for the pipes and tension coupons, weight loss in steel specimens and elemental analysis of steel and concrete. To this end, 102 reinforced concrete pipes (RCP), each 2 ft long with an inside diameter of 24″ and 3″ wall thickness, are tested to find their respective D-load; among the 102 RCPs, twelve were tested as control specimens, while the

remaining 81 were considered for the main tests with 9 additional ones as spare specimens. The research project consists of two phases: pre-immersion and post-immersion. In the pre-immersion phase, 90 RCPs were cracked, and spacers were inserted in the crack to keep the cracks open to 0.05″. For post-immersion phase, the cracked RCPs were immersed in sodium chloride solutions with concentrations of 200, 2000 and 30000 part per million (ppm). The RCPs in the 200 and 2000 ppm solutions are tested on a bi-monthly basis while the pipes in the 30000 ppm solutions are tested monthly. For each solution, three specimens are tested. In addition to the RCPs, steel specimens were used to monitor the weight loss over time as well as strength reduction in tension test. Scanning Electron Microscope and Energy-dispersive X-ray (SEM/EDX) was also used to study the elemental analysis on the surfaces of the corroded steel and degraded concrete specimens, as well as to take more precise readings for the diameter change of the steel specimens.

ACKNOWLEDGEMENT

I would like to express my sincere appreciation and gratitude to my advisors, Dr. Himan Hojat Jalali and Professor Dr. Ali Abolmaali, without whom this research would not have been completed. They were always there when I needed help and guidance during my course work and research at the Structural Engineering Research/Simulation and Pipeline Inspection.

I would like to thank my committee members, Dr. Melanie Sattler and Dr. Ardashir Anjomani for their valuable time and suggestions related to my research work.

I would also like to thank the American Concrete Pipe Association and Forterra Pipe Plant and specially the plant manager Brian Gregory for providing the required material and transportation to the civil engineering laboratory building.

Special thanks to my friends at the Structural Engineering Research/Simulation and Pipeline Inspection, Maziar Mahdavi for his time, help and support throughout the experimental work related to my research project, Yong Hoon , Amit Pokharel and Mitesh Shah for their help during the experimental work.

Finally, I would like to thank Dr. Andrew Makeev and Brian Shonkwiler from the Mechanical Engineering Department for their help to allow me to use their MTS machine despite of their tight schedule.

August 2020

DEDICATION

I would like to thank my wife, Sarah, for her continuous support, encouragement and help during my study and the hard times I was going through. I would also like to thank my parents, sisters, my kids, and friends for being so supportive to me during my Ph.D. coursework and research. Their emotional support, wishes and prayers were so inspiring to me.

TABLE OF CONTENTS

LIST OF FIGURES

LIST OF TABLES

CHAPTER 1. INTRODUCTION

1.1 Overview

The use of the storm water drainage systems dates back to 4000 - 2500 BC in Eshnunna/Babylonia - Mesopotamian Empire (Iraq). Originally, they were built from sun baked brick or from cut stones. It has been well acknowledged that the earliest known pipe was manufactured in Babylonia by molding clay using a potter's wheel (sewerhistory.org, 2004). Angle and tee joints were also produced from clay and then baked to manufacture drainage pipes. Figure 1 shows knee and T-joints that were found in the excavations at Nippur, Babylonia as per sewerhistory.org (2004). The British Museum is currently in possession of a piece of clay pipe (shown in Figure 2) that was discovered in 1927 in Mesopotamia and it is believed to be backdated to (2100 – 2000 BC). In Egypt and Palestine (2000 – 500 BC), copper pipes had been used. After around 200 years, pipes of lead and bronze were used in Greece. Romans were using lead pipes made out of lead sheets, bent around wooden mandrel and jointed by solder (sewerhistory.org, 2004).

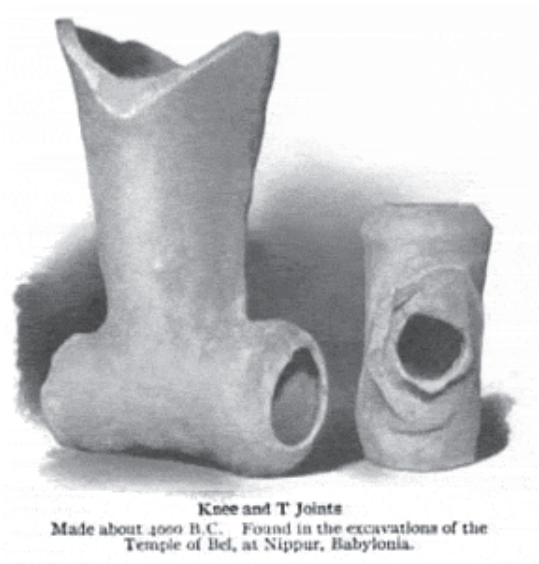

Figure 1: Knee and T-Joints at Nippur, Babylonia (sewerhistory.org, 2004).

Figure 2: Pottery drainpipe found in Ur-Iraq (British Museum, 2000).

Romans were the first to use cement-like materials by mixing slaked lime with pozzolanic volcanic ash. The product is hydraulic cement that hardens under water and does not change its hardened properties when exposed to moisture.

Hogan (2008) reported that the first recorded sanitary sewer reinforced concrete pipe was in Mohawk, New York in 1842. Several installed concrete pipes since late 1800's are still in service today. This is a great evidence that for some applications a service life of 100 years can be reached by using RCPs.

1.2 Corrosion

Corrosion is an electrochemical reaction between the metal and the surrounding environment, which will deteriorate the metal and its mechanical properties. Rust refers to corrosion of steel rebars embedded in concrete. Rust usually results in 2-4 times increase in the volume of the steel, that in turn results in compressing the surrounding concrete and eventually spalling if the cover is not enough. In addition, corrosion produces pits or holes at steel surface which will negatively

impact the section capacity due to loss of cross-sectional area. In some applications, such as in tensioning strands of prestressed concrete members, corrosion effects are detrimental.

Steel has a protective passive non-corrosive layer. Once chloride ions (mostly coming from sea water or deicing salts) permeate into concrete, they will cause the steel to corrode and the protective layer is disrupted. Pitting will also occur when steel corrodes. This type of corrosion is called “chloride-induced” corrosion which is considered as a localized corrosion as it occurs at some spots of the steel bars. “Carbonation” corrosion is another type of corrosion which appears as a generalized corrosion of the steel bars. Third type of corrosion is called “stress corrosion cracking” which occurs mostly in the prestressed wires. Figure 3 shows the three types of steel corrosion in concrete. In our research, we will focus on chloride-induced corrosion only.

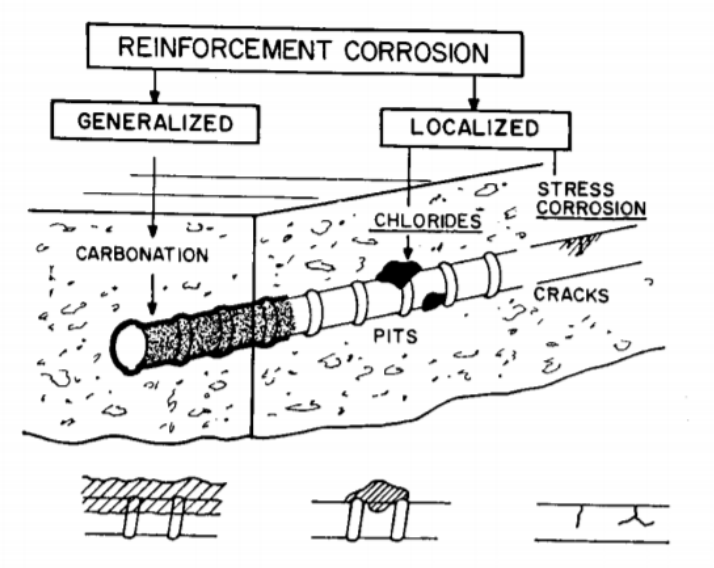

Figure 3: Types and formation of the corrosion in concrete: generalized (carbonation), localized (chlorides) and stress corrosion cracking (in prestressed wires) (Vavpetic 2008).

As mentioned earlier, corrosion is an electrochemical process that involves electrons exchange. Iron dissolves at the anode (the negatively charged part) and reacts to form rust, which is the solid product of corrosion. Since steel bars are surrounded by concrete, the formation of rust on

the surface will force the formed oxide and compress the concrete causing it to spall.

Differences in the electrical potential on the surface of the steel bars will lead to the formation of anodic (negatively charged area) and cathodic (positively charged area) spots. This in addition the presence of moist environments, will lead to corrosion where the metal will oxidize at the anodic areas according to equation 1:

$$\text{Fe (metal)} \rightarrow \text{Fe}^{2+} + 2\text{e}^{-} \quad (1)$$

At the same time, the typical cathodic processes are shown in equation (2) and (3):

$$^{1}/_{2}\,\text{O}_2 + \text{H}_2\text{O} + 2\text{e}^{-}\,(\text{metal}) \rightarrow 2\text{OH}^{-} \quad (2)$$

$$2\text{H}^{+} + 2\text{e}^{-}\,(\text{metal}) \rightarrow \text{H}_2\,(\text{gas}) \quad (3)$$

The electron products of the process are conducted through the metal while the ions are transported through the moisture or the pore water that acts as the electrolyte. Figure (4) illustrates this process.

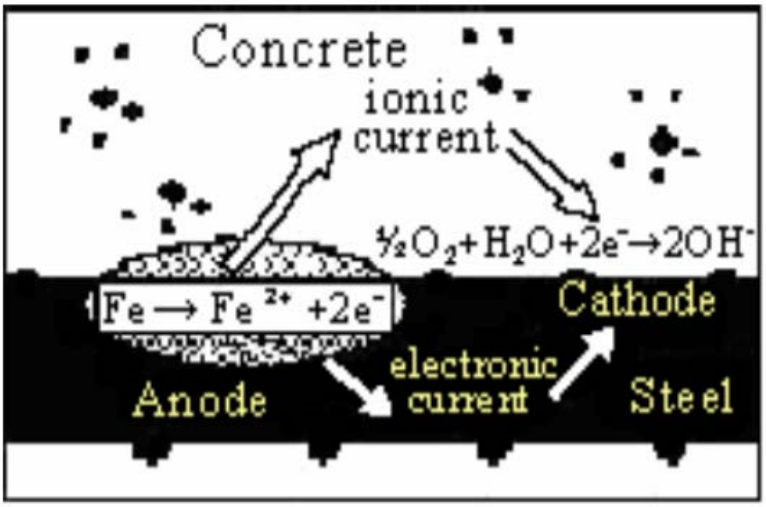

Figure 4: Typical electrochemical process of corrosion in steel (Vavpetic 2008).

Those reactions can be represented by equation (4):

$$Fe + 3O_2 + 2H_2O \rightarrow 2Fe_2O_3H_2O \quad (4)$$

where $Fe_2O_3H_2O$ is the Hydrated ferric Oxide which occurs after further hydration of Fe_2O_3 (ferric or iron oxide which is known as "Rust") (Daziel, 2018).

1.3 Thesis Outline

The research is presented in six chapters: introduction, literature review, reinforced concrete pipes, experimental program, results and summary, conclusions and recommendations for future work in the last chapter.

Chapter one, "Introduction", discusses the history of pipes, corrosion process and the research objectives. Chapter two, Literature review, discusses the previous works related to the corrosion studies, the autogenous healing of cracked concrete and the SEM/EDX analysis done in previous studies. Chapter three, reinforced concrete pipes, explains the theory of stresses and forces in pipes, design of reinforced concrete pipes, testing protocol, preparation of concrete pipe sections and preparation of steel specimens. In chapter four, experimental work, the details of D-load test, tension test and weight loss measurements will be discussed. The results of all the tests will be presented in chapter five. Chapter six will discuss the obtained results in this research, conclusions and provide some recommendations for the future work. In addition to the six chapters, Appendices – A, B and C will include the pre-immersion D-load – Displacement curves, D-load – Displacement curves for the post-immersion tests and finally pictures for the diameter measurements using the SEM, respectively.

1.4 Research Objectives

The goal of this research project is to evaluate the performance of cracked RCP subjected to corrosive environments based on the research methodology outlined in the following testing

protocol. The evaluation is based on strength loss in the RCPs, strength loss in tensile test coupons, weight loss in steel cages and rebar specimens and elemental analysis of the concrete and steel specimens. Since RCPs are used in many infrastructures, they are required to have a service life of 50 and 100 for storm water and sewer drainage systems, respectively as per the requirements of Florida Department of Transportation drainage manual (2020). The testing protocol includes cracking the pipes to 0.05" crack width, immersing them in 200, 2000 and 30000 ppm (part per million) sodium chloride solutions and testing them periodically to find the ultimate loads for post-immersion phase. Test is based on ASTM C497 (2020) for D-load test of the pipes. The tensile test is based on ASTM A370 (2019) for tension coupons taken from the same steel used for pipe reinforcement cages. The main reinforcement for the RCP is the helical reinforcement which comes in loops to the plant and then welded to the longitudinal rebars to make the cages. Therefore, tension coupons were made out of those helical bars by straightening them and sending them to the machine shop to make the reduced sections.

This is the first large scale test that measures the ultimate strength reduction of reinforced concrete pipes after being immersed in sodium chloride solutions and the reinforcing steel is being intentionally subjected to corrosion with this large number of specimens.

CHAPTER 2. LITERATURE REVIEW

2.1 Overview

The literature review will discuss the parts related to the research topic, i.e. the corrosion studies, the autogenous healing of concrete, pipe D-load and Scanning Electron Microscopy.

2.2 Corrosion

Baweja et. al (1998) tested 50 specimens of small reinforced concrete slabs that were half immersed in 3% (30,000 PPM) NaCl solution, representing marine conditions, with 4 different types of cement for their mixes. The study showed that for water/binder (cement) ratio greater than 0.55, the blended cement concretes had more corroded areas in the steel reinforcement than Portland cement concretes at equal measurements of electrochemical corrosion activity A_{cr}. The research by Baweja et. al (1998) and Baweja et. al (1999) suggested that an optimized performance for concrete is obtained in terms of corrosion of steel subjected to high-chloride environment when using low w/b ratios. The data obtained by Baweja et. al (1998) provided information to help engineers decide how to maintain the existing infrastructures and help them design the marine structures such that their life span increased, while the maintenance cost decreased.

Baweja et. al (1999) found out that concrete made with blended cement and low w/b ratios had better performance than concrete made with Ordinary Portland Cement (OPC). Concretes made with blended cement showed lower weight loss of steel, as well as lower corrosion rates and higher resistivity characteristics when compared to concrete made with OPC.

Busba and Sagüés (2013) stated that corrosion occurs when chloride from seawaters and deicing salts finds its way to the steel rebars inside any reinforced concrete member. The chloride content at corrosion initiation stage is called the Chloride Threshold Level (CLT). Any chloride content

that is equal to or exceeds the CLT will cause corrosion. It was found that the key factor for CLT is the actual content of entrapped air voids at the steel-concrete interface as per Busba and Sagüés (2013) and Rossi et al. (2020). Compared to other factors such as chloride binding, cement or binder matrix buffering capacity, air void content was the most dominant factor. Using corrosion inhibitors results in raising the CLT, which physically means that the steel will be more resistant to corrosion and will need higher chloride content for corrosion initiation.

Busba and Sagüés (2013) found that the mass loss in localized corrosion was less for RC pipes without consolidation voids around rebars as compared to those with voids. They also observed that the localized corrosion extended twice the diameter of the rebar for rebars without consolidation voids while there was an extension of corrosion for up to 30 times the diameter when voids were present around rebars. The study of Rossi et al. (2020) showed that deep pits of corrosion were found at the steel-concrete interface (SCI) where there were voids. After 20 years, their specimens made with OPC had shown more corrosion in terms of volume loss than specimens made with blended cement. Direction of casting of concrete relative to rebars orientation is another factor they took into account. For specimens with casting direction perpendicular to the steel rebars, more bleeding water was formed under the bars. This in turn will lead to a defect in the SCI, resulting in the formation of voids. Therefore, the underside of the rebar in this case shows more corrosion than other parts. One of their findings was that rebars were corroded at the side exposed to crack more than other parts of the rebar. It was also noticed that there is a transition from pitting to general corrosion while moving away from crack opening. Angst et al. (2010) mentioned that due to the microscopic defects which form on the lower side of rebars, corrosion is more likely to initiate at these areas. Other visual or macroscopic defects like voids that are in touch with the steel surface may not always be the reason to start corrosion where they are present.

The voids that are not filled with water will not cause corrosion because of the restricted electrochemical reaction at those spots.

Brandt et al. (2017) stated that in most rivers and lakes, the chloride ion concentration is 50 mg/l (50 ppm) or less. Therefore, any increase in the concentration of chloride ions is an indication of pollution due to sewage. If this increase was seasonal, it might be due to the run-off water coming from the use of deicing salts in roads. Seawater has a typical chloride ion concentration of 20,000 mg/l (20,000 ppm). While in some studies (Baweja et. al 1998 and Baweja et. al 1999), 30000 ppm was used to represent seawater conditions.

Shao and Li (2014) found an analytical solution for the chloride diffusion equation in cracked reinforced concrete pipe piles. They also found a mathematical expression for the relationship between crack width and equivalent diffusion coefficient which led to finding a method to predict the service life of cracked reinforced concrete pipe pile considering crack effects on the chloride diffusion. Their results demonstrated the importance taking the effect of cracks into account for accurate prediction of service life of reinforced concrete pipe piles subjected to marine environments. An empirical model for the prediction of chloride-induced rate of corrosion for cracked reinforced concrete structures was proposed by Otieno et al. (2016). Previous models failed to predict the actual corrosion rate because they were based on un-cracked concrete. Otieno at al. (2016) tackled this problem by including the effects of crack width on corrosion rate for the crack propagation phase. With their model, designers can determine the most suitable combination of concrete strength, cover depth and crack width that meet a certain durability and exposure performance in the marine environments.

The effect of sodium chloride on concrete itself was studied by some researchers to determine its effect on the service life of concrete mostly because of using the deicing salts. Cody et. al (1996), Lee et. al (2000) and Mussato et. al (2004 studied the effects of deicing salts on concrete deterioration and found that the effect of magnesium chloride was more severe on concrete than sodium chloride. Sodium chloride has a small effect in terms of concrete deterioration when it is accompanied by freezing and thawing. This is not the case in the reinforced concrete pipes and it mainly occurs in concrete pavements in snowy areas.

2.3 Autogenous Healing in Concrete

Hearn (1998) defines the autogenous healing as the capability of cement to heal cracks in the fractured zones. This process is very common in culverts, pipes, and water-retaining structures. The first time it was detected was in 1863 by the French Academy of Science. It was found that cracks are filled by crystalline precipitate as a result of either the reaction of calcium hydrogen carbonate $Ca(HCO_3)_2$ in water with calcium hydroxide $Ca(OH)_2$ or carbonation of calcium hydroxide when exposed to atmosphere. Loving N. W. in 1968 was the first to propose the carbonation explanation of this phenomenon because he found calcium carbonate deposits inside the cracks. Healing rate depends on the crack width where the narrower cracks showed faster healing. The process of autogenous healing is considered as flow dependent because the debris carried by the flow causes mechanical blockage. Carbonation reaction is considered as a considerable contribution to the autogenous healing process.

Maes et al. (2016) found that autogenous healing is faster by precipitation of calcium carbonates than in continuously immersed specimens. They also found out that crack width less than 105 μm will heal completely but for those larger than 105 μm will a complete healing was not observed.

In their study, they considered the 10 μm as the critical crack width above which chloride can penetrate. Marine structures with crack widths less than 105 μm will be able to seal those cracks as well as stabilize the penetration of chloride ions.

Palin et al. (2015) studied OPC and blast furnace slag (BFS) cement specimens in both fresh and seawater environments. Results demonstrated that OPC specimen in seawater had shown the highest rate of autogenous healing as compared to OPC and BFS specimen in fresh water, while BFS specimen in seawater had shown the slowest healing rate. On the other hand, OPC specimen in seawater show unacceptable loss in compressive strength compared to other specimens. The reason behind the differences in the rate of healing is due to the presence of calcium hydroxide in the cement and other ions in seawater.

2.4 Pipes D-load

Wilson (2012) performed more than 150 D-load tests for synthetic fiber and steel fiber reinforced concrete pipes according to the ASTM C497 (2020). According to the study by Wilson (2012), Wilson and Abolmaali (2014) and Wilson et. al (2017), the ASTM standard C1818 (2019) was established to consider the requirements of the synthetic fiber reinforced concrete pipes which are new in the concrete pipes industry.

Darabnoush Tehrani (2016), Kouchesfehani et. al (2019) and Darabnoush Tehrani (2020) performed several D-load tests for ordinary reinforced concrete pipes. Their studies also included finite element analysis and modeling of the tested pipes to obtain solid models that can replicate the actual behavior of reinforced concrete pipes with different diameters and wall thicknesses.

2.5 Scanning Electron Microscopy

The scanning electron microscopy is a state-of-art technique used to determine the microstructural details in terms of the chemical elements on the surface of the specimens being scanned according to Stutzman and Clifton (1999).

Ragab et. al (2016) in a study for the effect of seawater on concrete deterioration found out that there is a combination of reactions between concrete and chlorides, sulfates, and magnesium. Those reactions lead to the formation of different products that might change concrete properties. Figure 5 shows the SEM results for scanned field concrete specimens taken from wave repellent blocks subjected to seawater. Using the same technique, Ragab el. al (2016) were also able to find the chloride ion concentration at different depths of the different concrete specimens as shown in Figure 6.

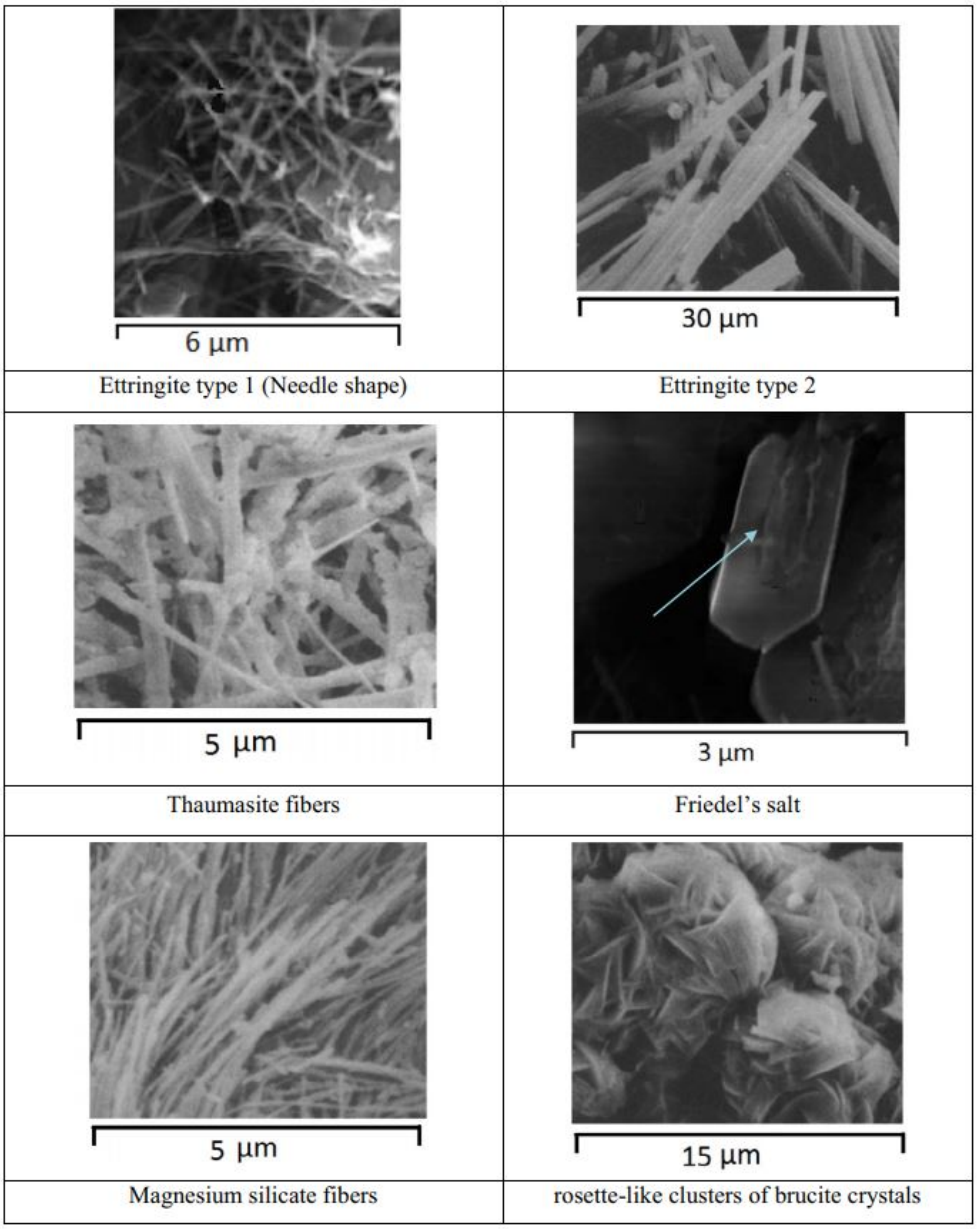

Figure 5: SEM snapshot of the main compounds in concrete specimens (Ragab et. al. 2016)

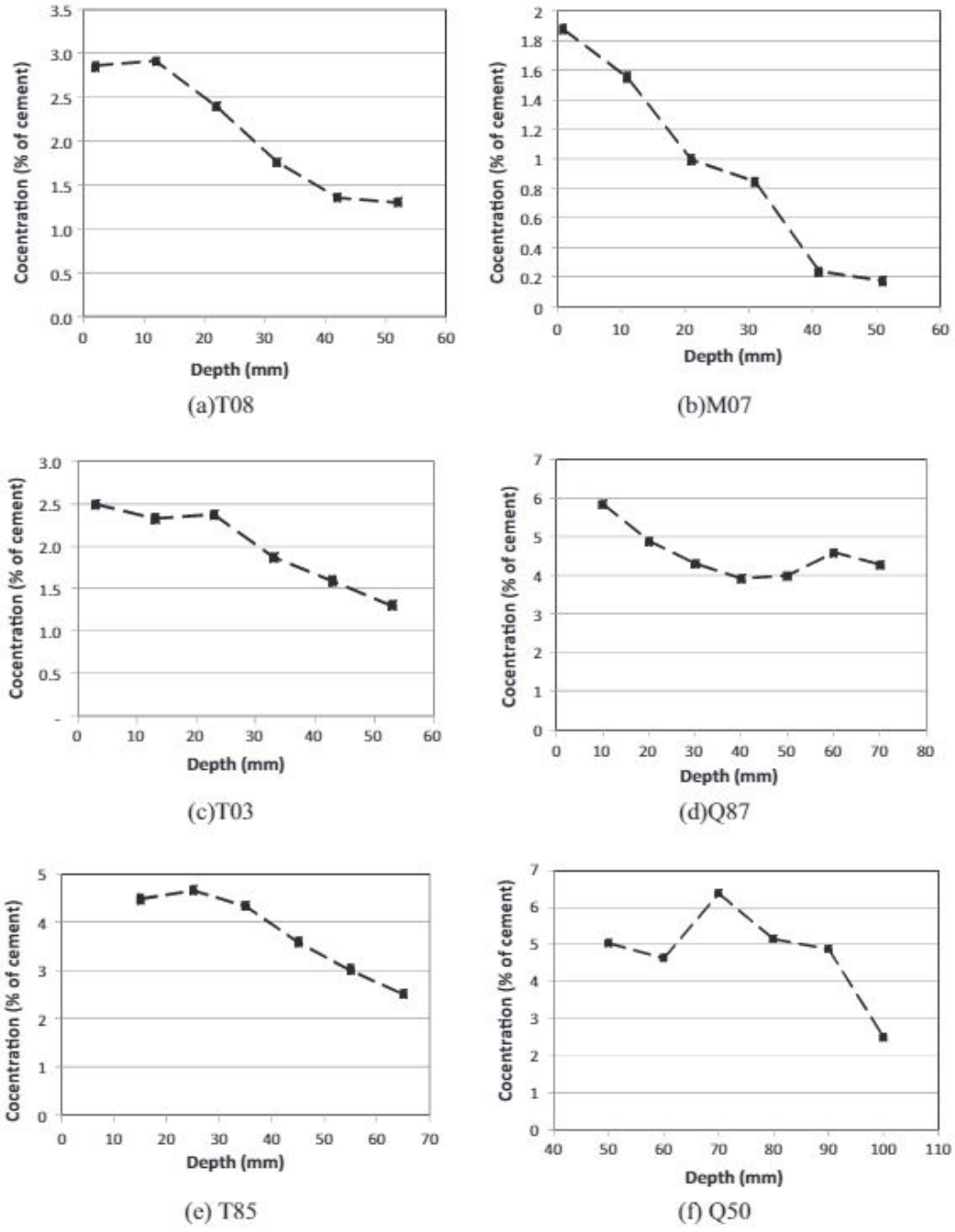

Figure 6: Chloride ion concentration at different depths in concrete specimens (Ragab et al. 2016)

Figure 7 shows the SEM snapshot for a concrete specimen. In this figure, the different compounds on the scanned surface are shown on the figure in addition to the micro-crack.

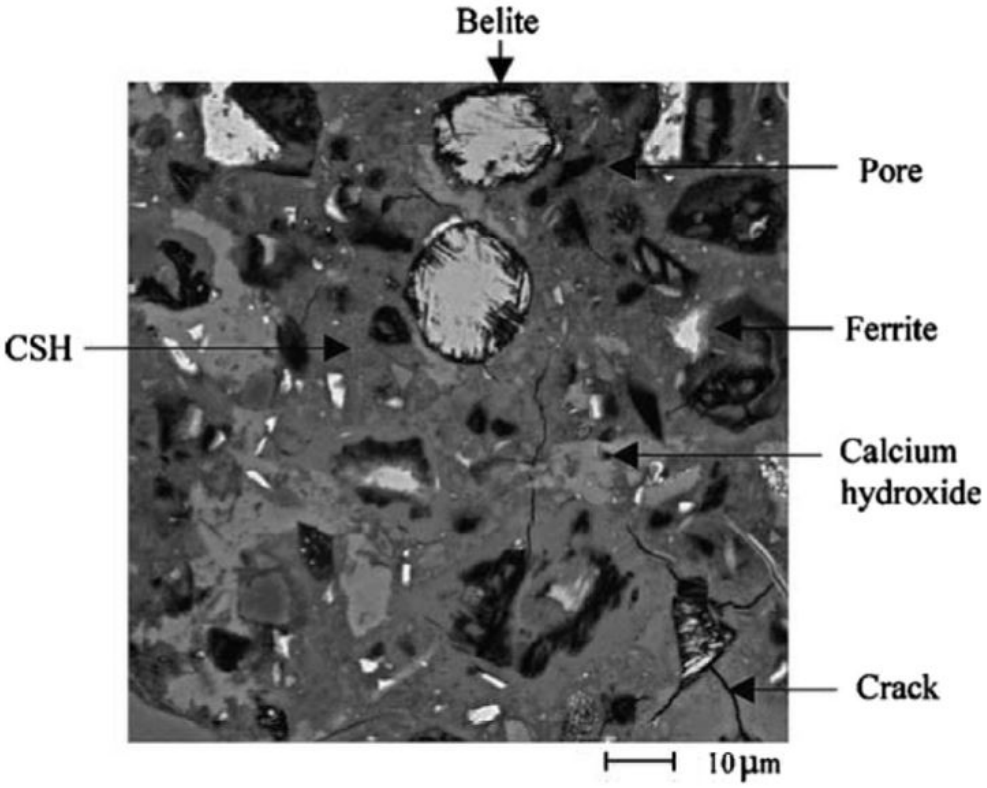

Figure 7: Concrete Compounds in SEM image, (Ragab et al. 2016).

The results of the SEM/DEX technique for Ragab et. al (2016) and Mahdavi (2019) show that the siliceous particles, “the aggregate”, show no traces of chloride or sulfates as the aggregates are inert materials. The visual inspection and the SEM snapshots show that the surface deterioration is caused by the erosion in the mortar around the coarse aggregates. Mahdavi (2019), in his dissertation to determine the service life of synthetic fiber reinforced concrete pipes, showed that the more the concrete is subjected to sulfuric acid, the more deterioration will occur as shown in the figures below, where Figure 8 is the SEM snapshot for the control specimens and Figures 9 through 13 are for specimens subjected to pH 2 and temperature (T=50) for 2, 5, 8 and 12 months

and pH 4 and T=25 for 2, 5, 8 and 12 months, respectively. The pictures are shown with different magnifications (upper left–100x, upper right–1000x, lower left–3000x and lower right–5000x).

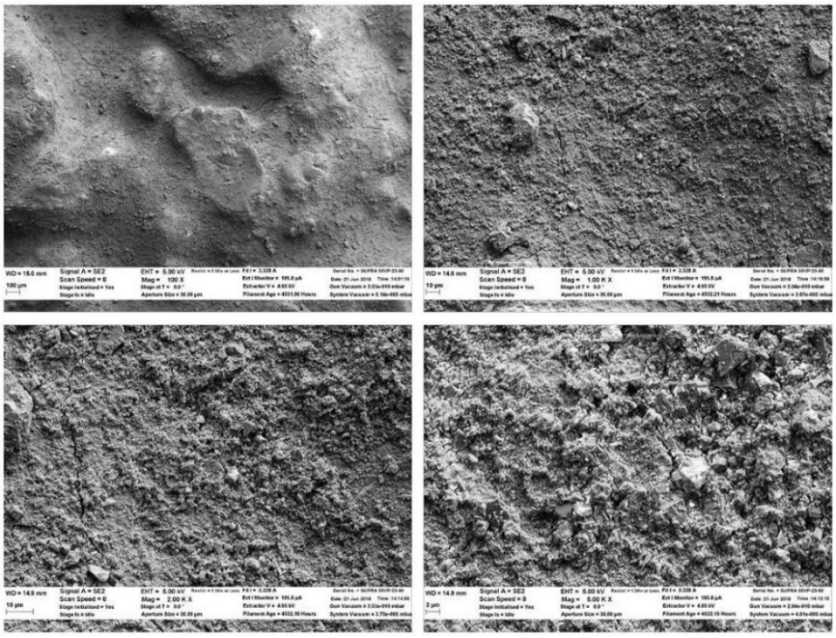

Figure 8: SEM snapshot for control specimens (Mahdavi 2019).

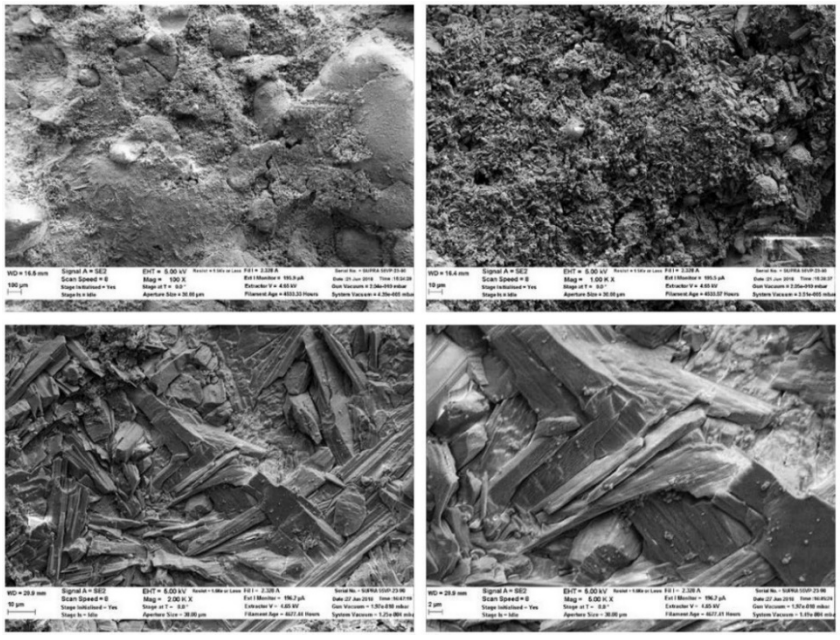

Figure 9: SEM snapshot for pH2-T50 specimen – 2 Months (Mahdavi 2019).

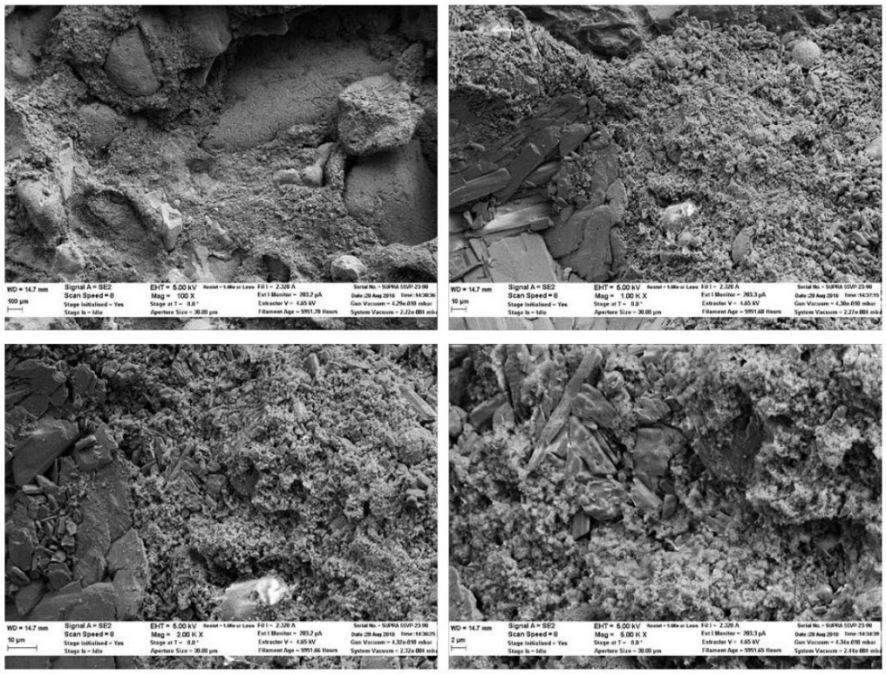

Figure 10: SEM snapshot for pH2-T50 specimen – 5 Months (Mahdavi 2019).

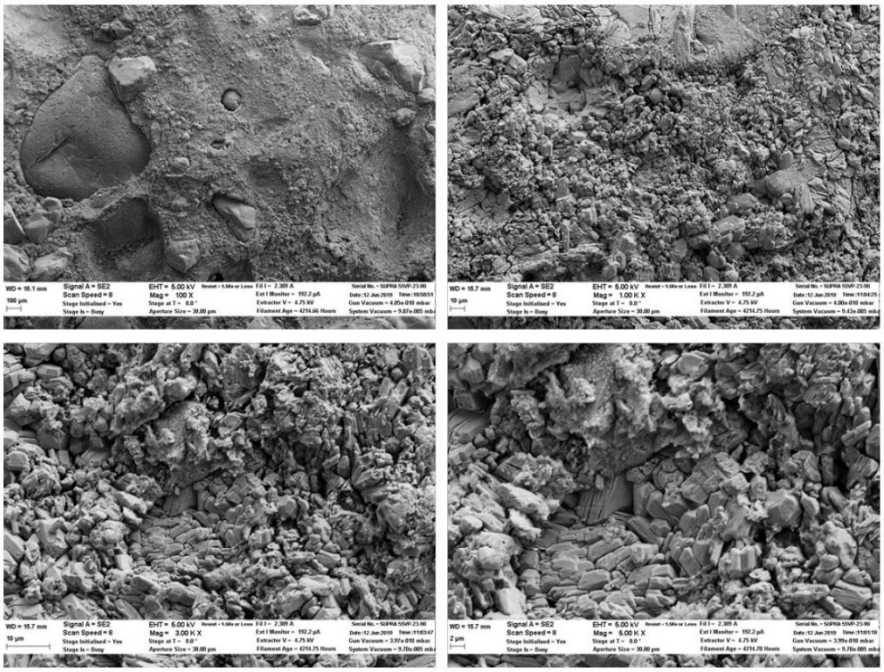

Figure 11: SEM snapshot for pH2-T50 specimen – 8 Months (Mahdavi 2019).

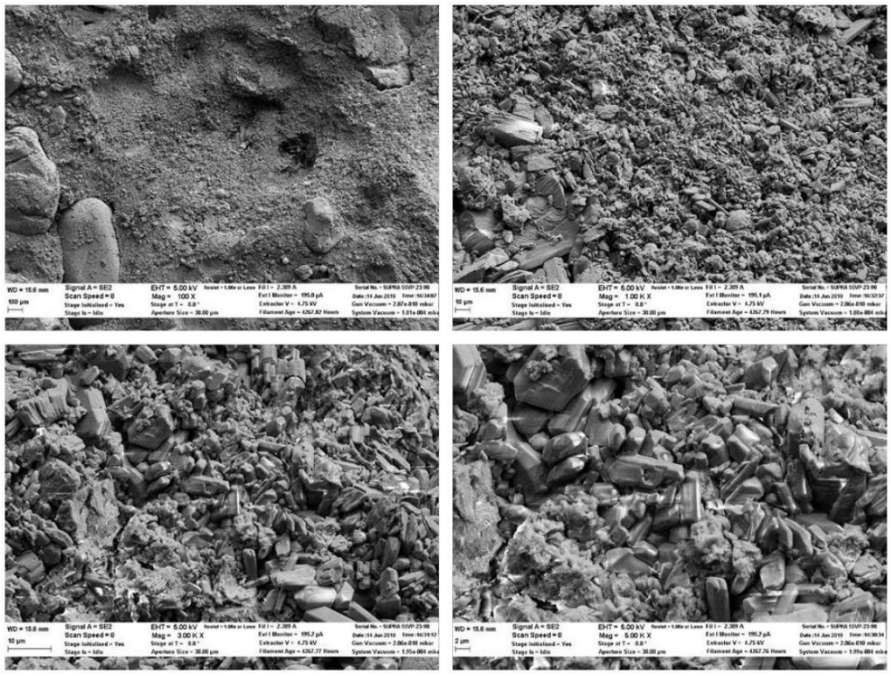

Figure 12: SEM snapshot for pH2-T50 specimen – 12 Months (Mahdavi 2019).

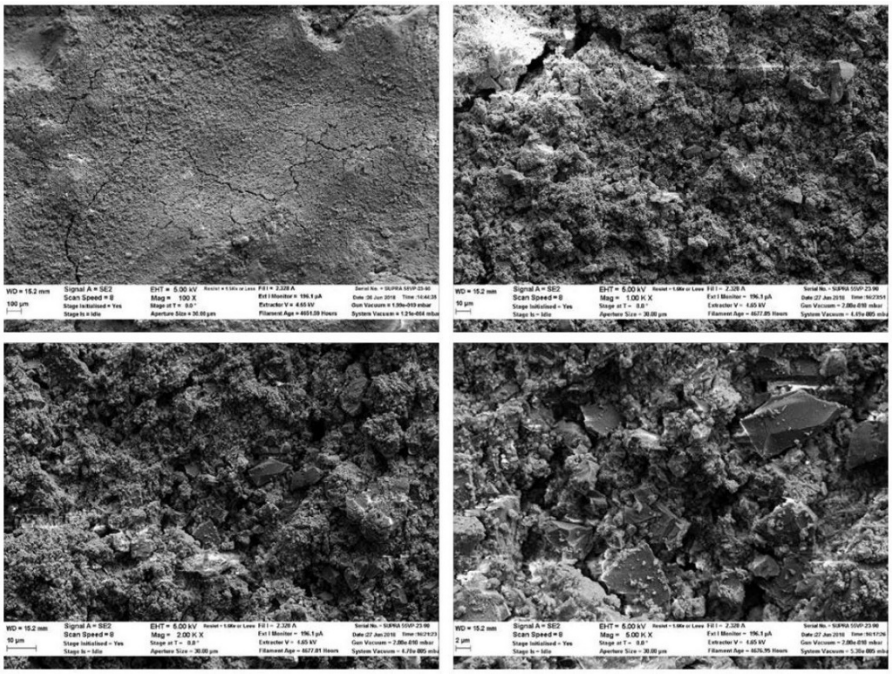

Figure 13: SEM snapshot for pH4-T25 specimen – 2 Months (Mahdavi 2019).

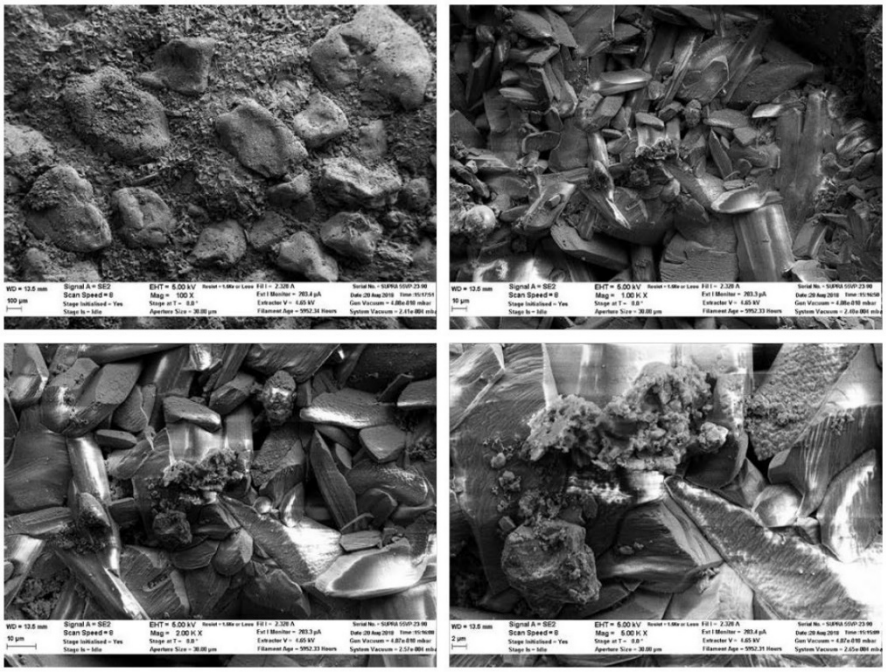

Figure 14: SEM snapshot for pH4-T25 specimen – 5 Months (Mahdavi 2019).

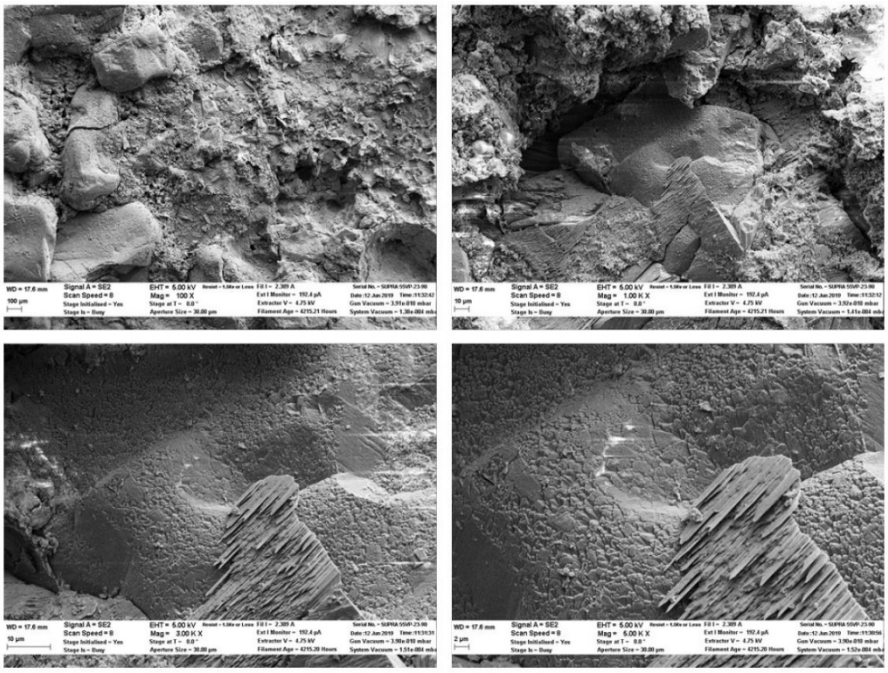

Figure 15: SEM snapshot for pH4-T25 specimen – 8 Months (Mahdavi 2019).

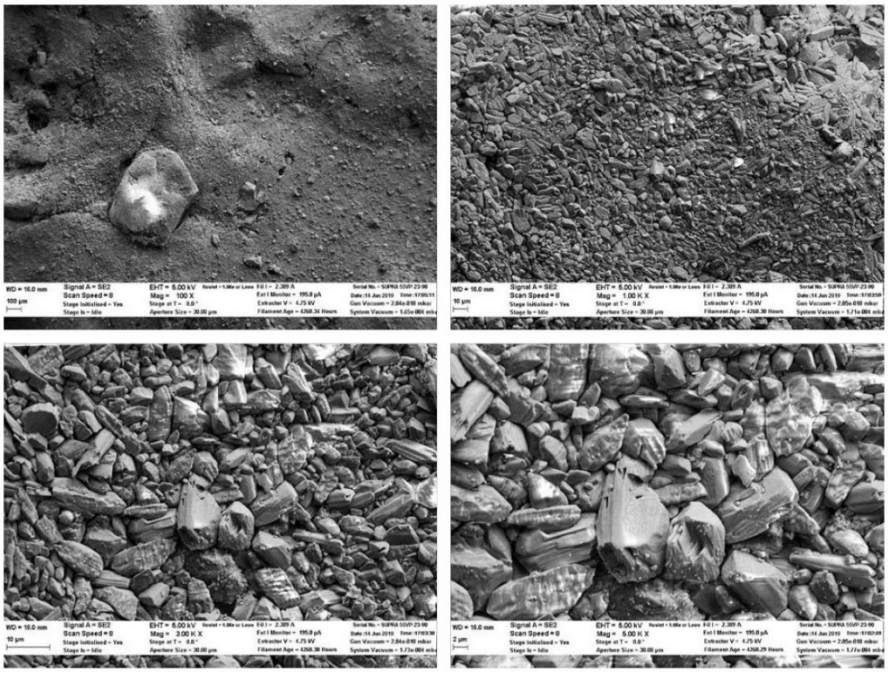

Figure 16: SEM snapshot for pH4-T25 specimen – 12 Months (Mahdavi 2019).

CHAPTER 3. REINFORCED CONCRETE PIPES

3.1 Overview

The reinforced concrete pipes were manufactured in Forterra pipe and precast plant located in Grand Prairie, Tx. The RCPs are manufactured with 8 ft long, 24″ inside diameter and 3″ thick walls. The RCP's came with a 3 – 4 inches lifting holes as per customer requirements. According to ASTM C-76 (2019), for a 24″ inside diameter, the 3″ thick wall is called "Wall B" as part of the requirements of class III pipes. Class III pipes are required to have a minimum of 1350 and 2000 lbs/ft/ft D-load for the service and ultimate loads, respectively. The D-load is defined as the applied load divided by the length (in ft.) along which it is applied and the pipe diameter (in ft.). The service load is the load at which a 0.01″ crack width is produced, while the ultimate load is the highest load the pipe can support before it fails. The pipe must have a minimum of 4000 psi concrete compressive strength and 0.07 in^2 of steel reinforcement in a single cage per linear foot of pipe length as illustrated in Table 1.

Table 1: Requirement of Class III RCP's (ASTM C-76-19)

NOTE 1—See Section 5 for basis of acceptance specified by the owner. The strength test requirements in pounds-force per linear foot of pipe under the three-edge-bearing method shall be either the D-load (test load expressed in pounds-force per linear foot per foot of diameter) to produce a 0.01-in. crack, or the D-loads to produce the 0.01-in. crack and the ultimate load as specified below, multiplied by the internal diameter of the pipe in feet.

D-load to produce a 0.01-in. crack	1350
D-load to produce the ultimate load	2000

Internal Designated Diameter, in.	Reinforcement, in.²/linear ft of pipe wall											
	Wall A				Wall B				Wall C			
	Concrete Strength, 4000 psi				Concrete Strength, 4000 psi				Concrete Strength, 4000 psi			
	Wall Thicknesses, in.	Circular Reinforcement[B] Inner Cage	Circular Reinforcement[B] Outer Cage	Elliptical Reinforcement[C]	Wall Thicknesses, in.	Circular Reinforcement[B] Inner Cage	Circular Reinforcement[B] Outer Cage	Elliptical Reinforcement[C]	Wall Thicknesses, in.	Circular Reinforcement[B] Inner Cage	Circular Reinforcement[B] Outer Cage	Elliptical Reinforcement[C]
12	1¾	0.07[D]	...	...	2	0.07[D]	...	...	2¾	0.07[D]	...	...
15	1⅞	0.07[D]	...	...	2¼	0.07[D]	...	...	3	0.07[D]	...	...
18	2	0.07[D]	...	0.07[D]	2½	0.07[D]	...	0.07[D]	3¼	0.07[D]	...	0.07[D]
21	2¼	0.14	...	0.11	2¾	0.07[D]	...	0.07[D]	3½	0.07[D]	...	0.07[D]
24	2½	0.17	...	0.14	3	0.07[D]	...	0.07[D]	3¾	0.07	...	0.07[D]
27	2⅝	0.18	...	0.16	3¼	0.16	...	0.14	4	0.08	...	0.07[D]
30	2¾	0.19	...	0.18	3½	0.18	...	0.15	4¼	0.10	...	0.08
33	2⅞	0.21	...	0.20	3¾	0.20	...	0.17	4½	0.12	...	0.10
36	3	0.21	0.12	0.23	4[E]	0.17	0.10	0.19	4¾[E]	0.08	0.07	0.09
42	3½	0.24	0.15	0.27	4½	0.21	0.12	0.23	5¼	0.12	0.07	0.12
48	4	0.32	0.19	0.35	5	0.24	0.14	0.27	5¾	0.16	0.10	0.18
54	4½	0.38	0.23	0.42	5½	0.29	0.17	0.32	6¼	0.21	0.12	0.23
60	5	0.44	0.26	0.49	6	0.34	0.20	0.38	6¾	0.24	0.15	0.27
66	5½	0.50	0.30	0.55	6½	0.41	0.24	0.45	7¼	0.31	0.19	0.34
72	6	0.57	0.34	0.63	7	0.49	0.29	0.54	7¾	0.36	0.21	0.40

3.2 Stress Analysis

According to Olander (1950), analysis of stresses in concrete pipes is partly based on the assumed earth pressure distribution. The most common assumption is that the vertical earth load is uniformly distributed along the horizontal width of the pipe; while the horizontal earth load has a trapezoidal distribution, on both sides of the pipe and is extending along the full pipe height. In addition to the above assumptions, the reaction is assumed to be uniformly distributed over the surface contacting the lower side of the pipe. Those assumptions are arbitrary, and more studies needed to be conducted to get a more precise idea about what the actual soil pressure distribution around the pipe is.

Watkins and Anderson (2000) mentioned that the analysis of pipes subjected to earth, live and fluid loads is a plane strain problem because of the possibility of neglecting the strain in the longitudinal axis of the pipe. The late Dr. Marston, in 1930 (Marston, 1930), studied the earth pressure and soil reaction around buried pipes and found that the earth pressure exerted on the pipe

and the reaction of soil under the pipe would have bulb-like shapes. This finding was confirmed by experimental investigation that was carried out and reported by Watkins and Spangler (1958). The soil pressure distribution is shown in Figure (17). The study of Dr. Marston in 1930 was based on the least work method by summation but a mathematical solution was developed by Olander (1950).

In normal conditions, pipes in service are subjected to earth pressure, dead load (self-weight), and interior hydrostatic pressure. The hydrostatic pressure includes two parts: (a) one part produces an uniform internal pressure equal to 62.4 Hr_0 where H is in ft and r_0 is the interior radius, where the head (H) is measured from the hydraulic gradient to the top part of the pipe inside. (b) The pressure produced by the head measured from the top to the bottom of the inside of the pipe and this pressure is called the water load. All the symbols are illustrated in Figure (18).

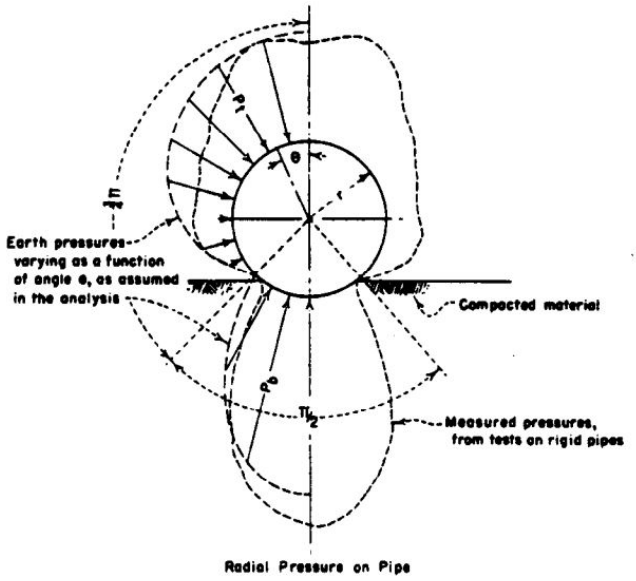

Figure 17: Earth pressure around rigid pipes installed on a compacted backfill (Olander 1950).

Based on the results obtained by Dr. Marston in 1930, the earth pressure and soil reaction distribution are similar to those shown in Figure (17). The distribution of earth pressure and soil reactions varies as a function of the angle (θ) shown in Figure (18). Olander (1950) mentioned that generally a central angle of 90^0 is used but the analysis of stresses has also been solved for central angles of 45^0, 90^0, 120^0 and 180^0.

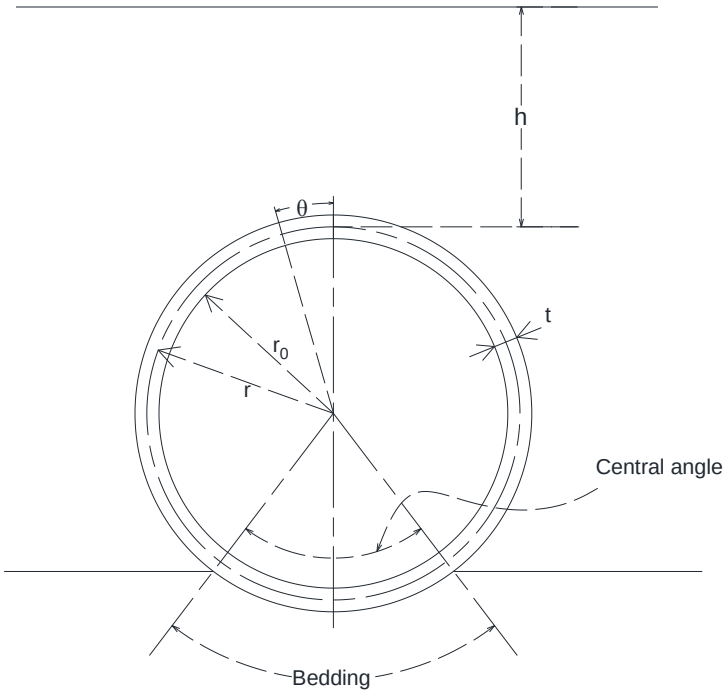

Figure 18: Symbols used for analysis of stresses in rigid pipes, Olander (1950).

The analysis of stresses in the pipe presented by Marston (1930) is based on the least work method. The deflected shape of the pipe ring, due to the symmetrical applied loading on the pipe, will be symmetrical about the vertical axis. Therefore, both top and bottom points will not show any lateral deflection or rotation. Hence, the pipe can be represented by a half-circle with a free end at the top

and a fixed support at the bottom. With the pipe represented as a half pipe cut, the forces on the free body diagram must be considered in order to solve the equilibrium equation. Figure (19) shows the free body diagram at (a) the top point and (b) at a section at an angle (θ) from the top point where M_0 and M'_θ are the bending moments at the top and at an angle (θ), V'_θ is the shear force acting at a section at an angle θ, H_0 is the horizontal thrust acting perpendicular to the section at the top of the pipe and P'_θ is the axial force acting perpendicular to a section at an angle (θ).

As mentioned earlier, the central angle was taken as 45^0, 90^0, 120^0 and 180^0, and the analysis was made based on the angle considered. The equations for bending moment, axial force and shear force were derived for each load (earth pressure, self-weight, and water load) as a function of the angle (θ).

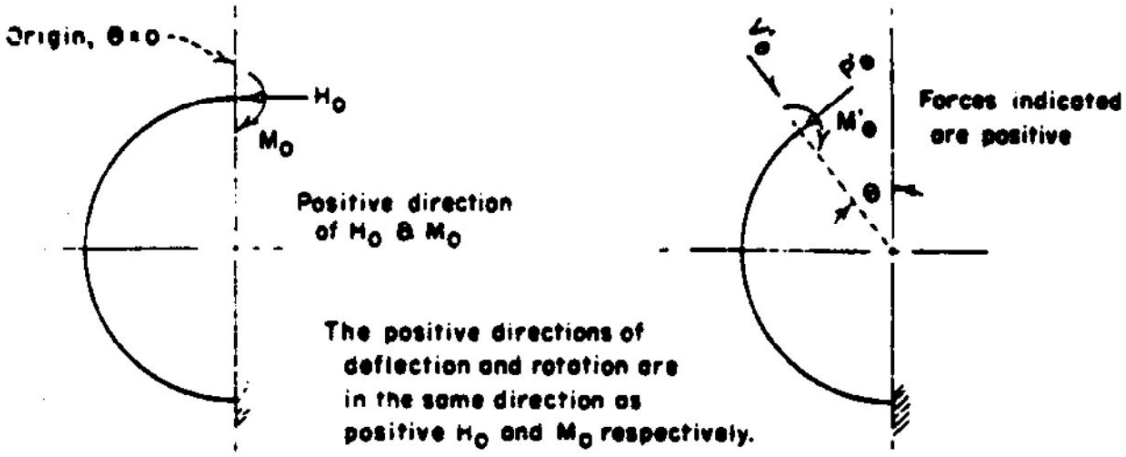

Figure 19: Moment, shear and thrust acting on the free body diagram of the pipe (a) at the vertical centerline and (b) at an angle θ to the vertical centerline, (Olander 1950).

Based on the pressure load distribution shown in Figure 20, the final equations for the bending moment, axial and shear forces are shown in equations 5 through 7.

For $0 \leq \theta \leq \frac{3}{4}\pi$

$$\mathrm{M}_\theta = \mathrm{Ar}\left(1.061\cos\frac{2}{3}\theta - 0.678\cos\theta - 0.450\right) \quad (5)$$

$$P_\theta = A\left(1.061\,cos\frac{2}{3}\theta - 0.678\,cos\,\theta\right) \quad (6)$$

$$V_\theta = A\left(0.678\,sin\,\theta - 0.707\,sin\frac{2}{3}\theta\right) \quad (7)$$

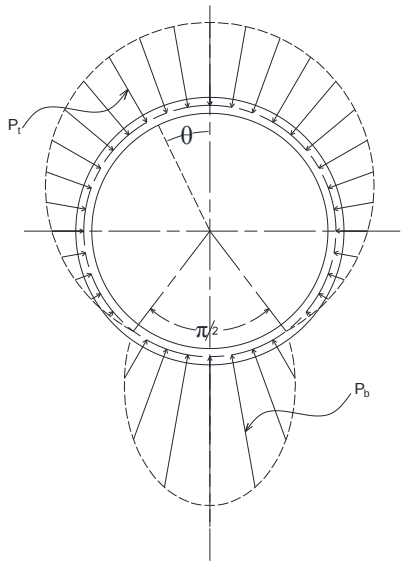

Figure 20: Bulb-like shape of Earth pressure and the associated reaction for a central angle of 90^0, (Olander 1950).

For $\frac{3}{4}\pi \leq \theta \leq \pi$

$$M_\theta = Ar(-0.354\,cos\,2\theta - 0.678\,cos\,\theta - 0.450) \quad (8)$$

$$P_\theta = A(-0.354\,cos\,2\theta - 0.678\,cos\,\theta) \quad (9)$$

$$V_\theta = A(0.707\, sin\, 2\theta + 0.678\, sin\, \theta) \quad (10)$$

Where (A) is the total earth load on the pipe, (r) is the radius of the pipe wall centerline and θ is the angle measured from top as shown in Figure 20.

For the forces caused by water pressure shown in Figure 21, the equations are as below:

For $0 \leq \theta \leq \frac{3}{4}\pi$

$$M_\theta = Wr(0.099\, cos\, \theta + 0.159\, \theta\, sin\, \theta - 0.169) \quad (11)$$

$$P_\theta = W(0.099\, cos\, \theta + 0.159\, \theta\, sin\, \theta - 0.319) \quad (12)$$

$$V_\theta = W(0.061\, sin\, \theta + 0.159\, \theta\, cos\, \theta) \quad (13)$$

For $\frac{3}{4}\pi \leq \theta \leq \pi$

$$M_\theta = Wr(0.159\, \theta\, sin\, \theta - 0.500\, sin\, \theta - 0.401\, cos\, \theta - 0.354\, cos\, 2\theta - 0.169) \quad (14)$$

$$P_\theta = W(0.159\, \theta\, sin\, \theta - 0.500\, sin\, \theta - 0.401\, cos\, \theta - 0.354\, cos\, 2\theta - 0.319) \quad (15)$$

$$V_\theta = W(0.561\, sin\, \theta + 0.159\, \theta\, cos\, \theta - 0.500\, cos\, \theta + 0.707\, sin\, 2\theta) \quad (16)$$

Where (W) is the total water weight inside the pipe per foot of pipe length.

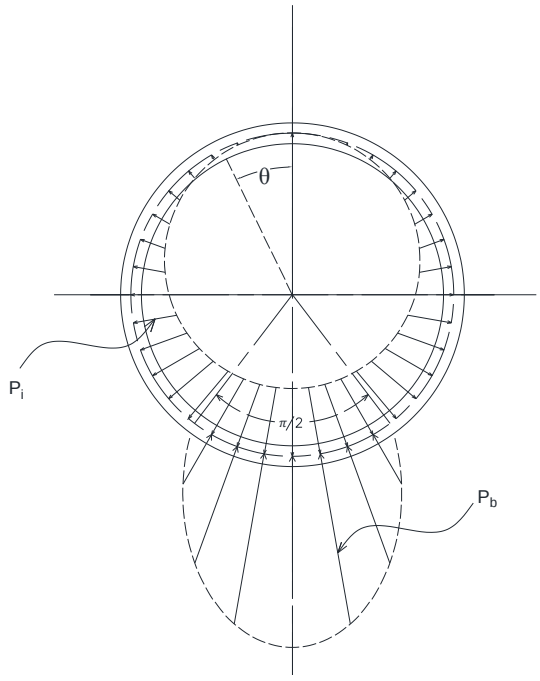

Figure 21: Water pressure inside the pipe, (Olander 1950).

Finally, the self-weight of the concrete pipe load (shown in Figure 22) is considered and the equations for the bending moment, axial and shear forces are as shown below:

For $0 \leq \theta \leq \frac{3}{4}\pi$

$$M_\theta = Dr(0.159\,\theta\,sin\,\theta + 0.099\,cos\,\theta - 0.169) \quad (17)$$

$$P_\theta = D(0.159\,\theta\,sin\,\theta - 0.061\,cos\,\theta) \quad (18)$$

$$V_\theta = D(0.159\,\theta\,cos\,\theta + 0.061\,sin\,\theta) \quad (19)$$

For $\frac{3}{4}\pi \leq \theta \leq \pi$

$$M_\theta = Dr(0.159\,\theta\,sin\,\theta - 0.500\,sin\,\theta - 0.401\,cos\,\theta - 0.354\,cos\,2\theta - 0.169) \quad (20)$$

$$P_\theta = D(0.159\,\theta\,sin\,\theta - 0.561\,cos\,\theta - 0.500\,sin\,\theta - 0.354\,cos\,2\theta) \quad (21)$$

$$V_\theta = D(0.159\,\theta\,cos\,\theta - 0.500\,cos\,\theta + 0.561\,sin\,\theta + 0.707\,sin\,2\theta) \quad (22)$$

Where (D) is the total water weight inside the pipe per foot of pipe length.

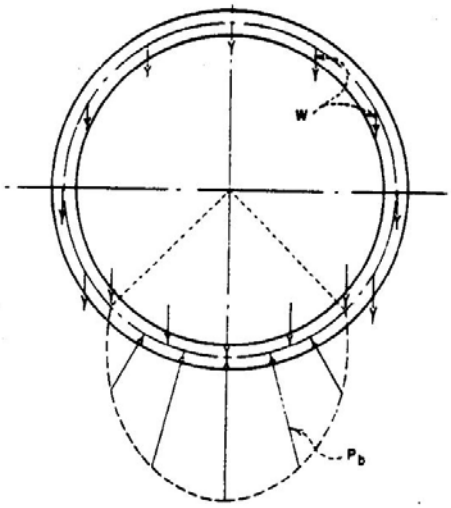

Figure 22: Self-weight of the pipe (Olander 1950).

Similarly, the bending moments, axial and shear forces were also derived for other central angles of 45^0, 120^0 and 180^0. A better representation of the complicated equations was also prepared by Olander (1950) by using charts as shown in Figure 23, as it is easier to find the X, Y and Z factors for bending moment, axial and shear forces, respectively, at any angle θ.

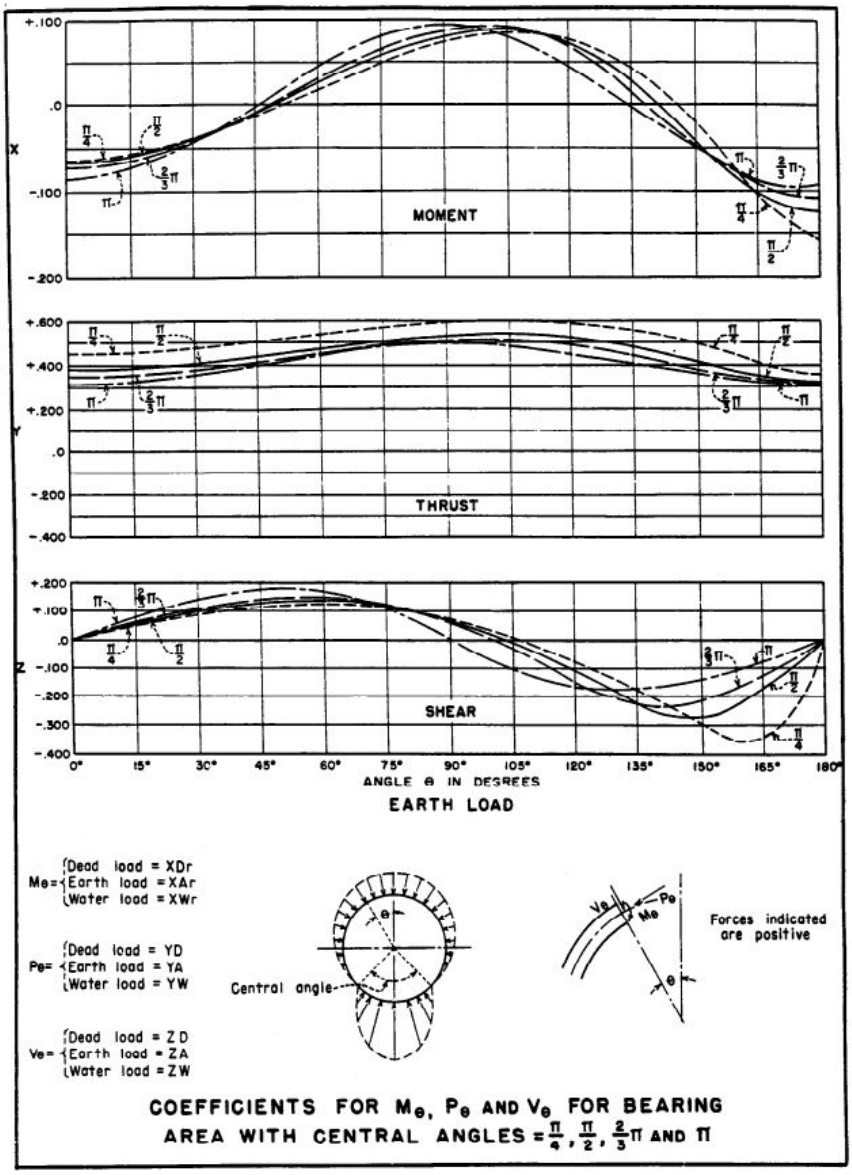

Figure 23: Coefficients charts for bending moments, axial and shear forces, (Olander 1950).

3.3 Design of Reinforced Concrete Pipes

Two main type of reinforced concrete pipes that are discussed in the Concrete pipe design manual (2011), prepared by American Concrete Pipe Association (ACPA), are the sanitary sewer and storm sewer. The sanitary sewers are designed for domestic, industrial, and commercial sewage with the possibility of infiltration of ground water while the storm sewer pipes are designed to

carry runoff, surface water and in some cases, ground water. Based on the hydraulics of the sewer, the size of the pipe is determined at this point. In general, the average flow in gallons per day is obtained from records and then multiplied by a factor in order to obtain the peak flow, which is essential to find the required conduit size. The minimum flow is studied as well to decide if the flow velocity is enough to prevent solids deposition.

With the size of the pipe known, it is important to identify the loads and design the pipe to support the applied loads. Generally, the procedure of selecting the pipe strength requires finding the following:

1- The maximum expected earth load
2- Live load from traffic
3- Selection of the proper bedding and determining the bedding factor
4- Factor of safety
5- Pipe strength.

When the pipe strength is determined, ASTM C76 (2019) is used to determine the wall thickness and the required steel area per linear foot of the pipe length.

The type of installation of the reinforced concrete pipe is also important in the design process because a lot of factors will be determined accordingly. In fact, the earth load will depend on the type of installation method used. The four types of installations are: Trench, Positive Projecting Embankment, Negative Projecting Embankment and Jacking or Tunneling. In the trench type of installation, the pipe is installed in a relatively narrow trench, laid on undisturbed soil and backfilled all the way to the natural ground surface. When the pipe is installed on the original ground and covered by an embankment or earth fill, this type of installation is known as Positive

Projecting Embankment, while when the pipe is installed at a level below the natural ground level and then covered with soil to the natural ground level, this is called Negative Projecting Embankment. The fourth type of installation “jacking or tunneling” is used when it is difficult to use the above mentioned three types. A jacking pit is excavated, the required machinery is used inside this pit and the pipes are driven horizontally. Figure 24 shows the four types of installations of reinforced concrete pipes.

ACPA came up with a finite element comprehensive computer program for the analysis and design of buried pipes taking into account the soil-pipe interaction, also known as SPIDA (Soil-Pipe Interaction Design and Analysis). This design method is known as the direct design method and it was adopted for the design of buried reinforced concrete pipes.

With the use of SPIDA in some research studies, the following concepts were proven after they were proposed by past experiences:

1- A significant reduction in stresses in pipe is noticed when the bedding under the invert is loose and un-compacted.
2- The soil from the foundation to the springline of the pipe helps reduce stresses in the pipe since it provides a significant support to the pipe.
3- The level of compaction for the soil from the springline to the top of the pipe does not help in stresses reduction in pipes. Compaction is not necessary in this area unless it is required for pavement structures.

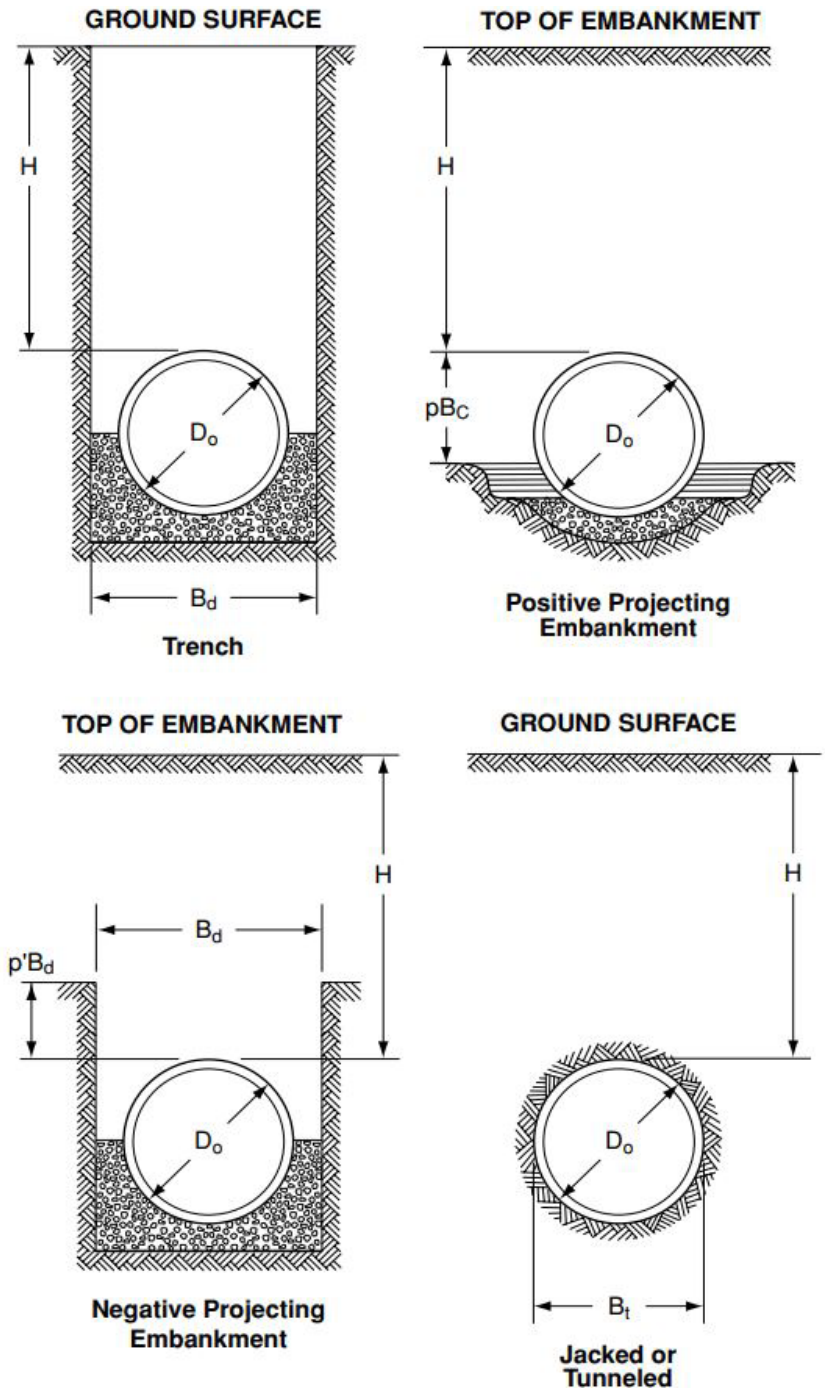

Figure 24: Types of pipe installations, (ACPA 2011).

4- The level of compaction and the selection of the backfill materials below the springline have a significant effect on the pipe structural behavior.

The terminology used in the design and installation is all shown in Figure 25.

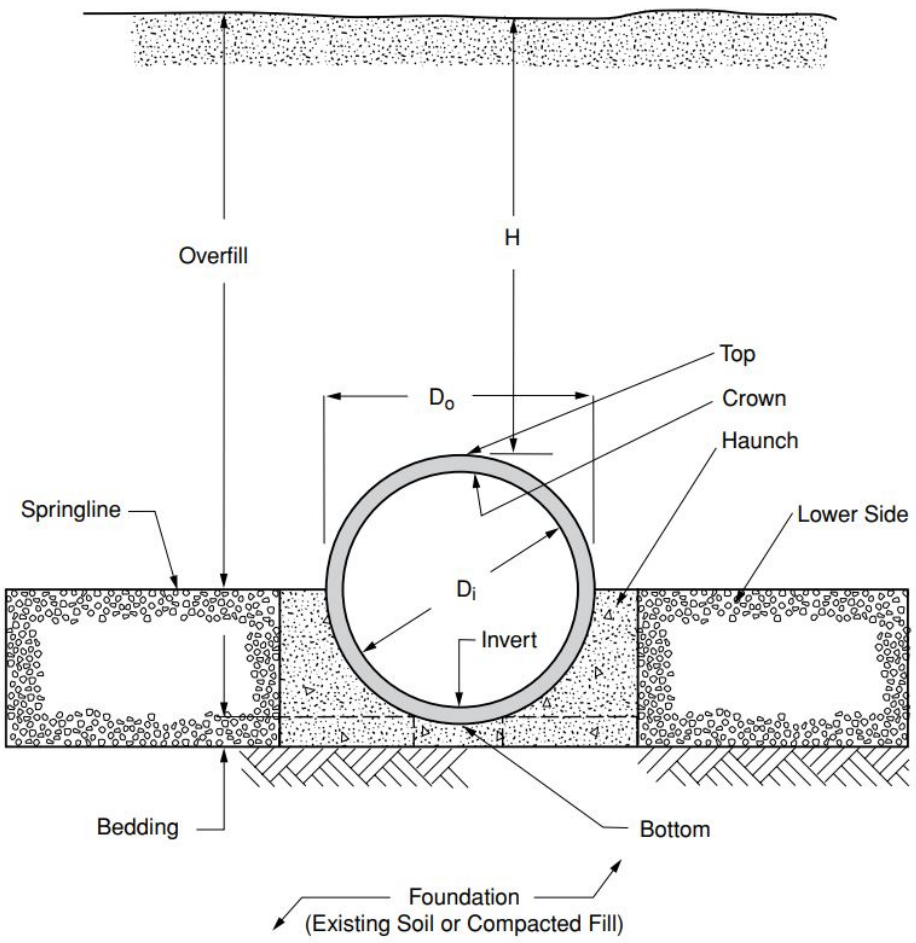

Figure 25: Pipe Installation and Design Terminology, (ACPA 2011).

In order to find the earth load for different types of installation, the prism load (PL) is found first with the use of equation 23 for the earth load of the positive projecting embankment.

$$PL = \gamma_s \left[H + \frac{D_0(4-\pi)}{8}\right] D_0 \qquad (23)$$

Where:

γ_s= unit weight of soil in lb/ft^3.

H= fill height in ft.

D_0= outer diameter of pipe in ft.

Four new standard installations were introduced based on the soil category and the required compaction as shown in table 2.

Table 2: Standard Installations Soil and Minimum Compaction Requirements, (ACPA 2011).

Installation Type	Bedding Thickness	Haunch and Outer Bedding	Lower Side
Type 1	Do/24 minimum, not less than 75 mm (3"). If rock foundation, use Do/12 minimum, not less than 150 mm (6").	95% Category I	90% Category I, 95% Category II, or 100% Category III
Type 2	Do/24 minimum, not less than 75 mm (3"). If rock foundation, use Do/12 minimum, not less than 150 mm (6").	90% Category I or 95% Category II	85% Category I, 90% Category II, or 95% Category III
Type 3	Do/24 minimum, not less than 75 mm (3"). If rock foundation, use Do/12 minimum, not less than 150 mm (6") .	85% Category I, 90% Category II, or 95% Category III	85% Category I, 90% Category II, or 95% Category III
Type 4	No bedding required, except if rock foundation, use Do/12 minimum, not less than 150 mm (6").	No compaction required, except if Category III, use 85% Category III	No compaction required, except if Category III, use 85% Category III

The categories of soil are based on Unified Soil Classification System (USCS) and American State Highway and Transportation Officials (AASHTO). Soil classification and the equivalent type of soils in the four standard installations are shown in Table 3.

Table 3: USCS and AASHTO Soil Classification, (ACPA 2011).

	Representative Soil Types		Percent Compaction	
SIDD Soil	**USCS,**	**Standard AASHTO**	**Standard Proctor**	**Modified Proctor**
Gravelly Sand (Category 1)	SW, SP, GW, GP	A1,A3	100 95 90 85 80 61	95 90 85 80 75 59
Sandy Silt (Category II)	GM, SM, ML, Also GC, SC with less than 20% passing #200 sieve	A2, A4	100 95 90 85 80 49	95 90 85 80 75 46
Silty Clay (Category III)	CL, MH, GC, SC	A5, A6	100 95 90 85 80 45	90 85 80 75 70 40

Table 4 represents the coefficients used to find the earth distribution in different zones around the pipe as shown in Figure 26.

Table 4: Earth pressure coefficients for different types of installations, (ACPA 2011).

Installation Type	VAF	HAF	A1	A2	A3	A4	A5	A6	a	b	c	e	f	u	v
1	1.35	0.45	0.62	0.73	1.35	0.19	0.08	0.18	1.40	0.40	0.18	0.08	0.05	0.80	0.80
2	1.40	0.40	0.85	0.55	1.40	0.15	0.08	0.17	1.45	0.40	0.19	0.10	0.05	0.82	0.70
3	1.40	0.37	1.05	0.35	1.40	0.10	0.10	0.17	1.45	0.36	0.20	0.12	0.05	0.85	0.60
4	1.45	0.30	1.45	0.00	1.45	0.00	0.11	0.19	1.45	0.30	0.25	0.00	-	0.90	-

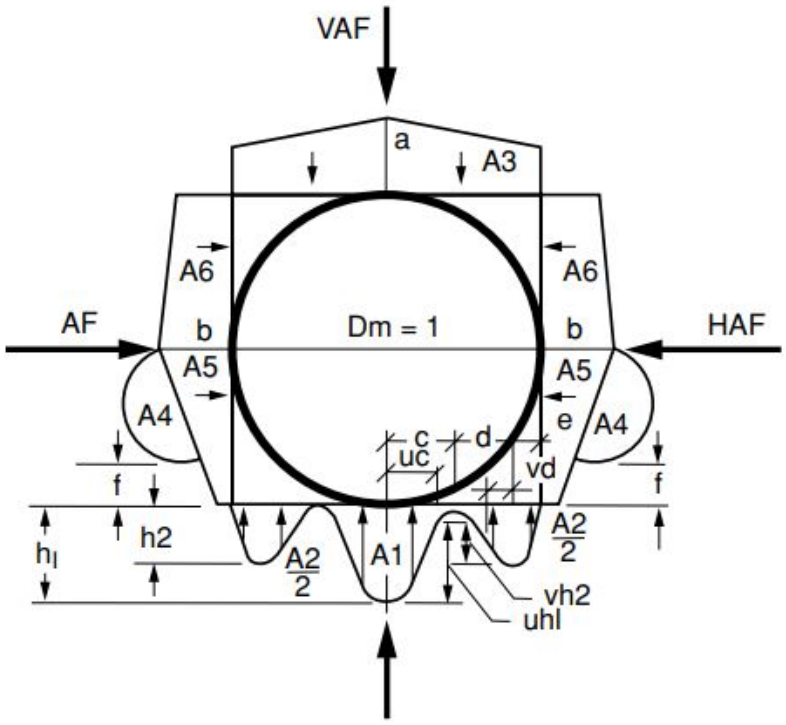

Figure 26: Arching coefficients and earth pressure distribution, (ACPA 2011).

The trench soil load (W_d) in pounds per linear foot, can be determined according to equation 24:

$$W_d = C_d \gamma_s B_d^2 + \frac{D_0^2(4-\pi)}{8}\gamma_s \quad (24)$$

Where $C_d = \frac{1-e^{-2K\mu'\frac{H}{B_d}}}{2K\mu'}$

B_d= trench width in ft.

K= ratio of active lateral unit pressure to vertical unit pressure

$\mu' = tan\emptyset'$, coefficient of friction between fill material and trench sides.

There is a certain limit when the width of the trench increases, the load will be similar to the case of the positive projecting embankment. At this width the friction between the soil and the walls of

the trench will not contribute to the structural behavior of the pipe anymore and the soil will settle on the sides of the pipe as in the case of the embankment. This width is known as the transition width. So, any pipe installed in a trench whose width is equal or greater than the transition width will be designed for the case of embankment.

Now for the case of the negative projecting embankment, the fill load on the installed pipe can be calculated according to Equation 25, where the settlement is taken into account in this case of loading:

$$W_n = C_n W B_d^2 \tag{25}$$

Where:

$$C_n = \frac{1 - e^{-2K\mu' \frac{H}{B_d}}}{2K\mu'} \qquad when\ H < H_e$$

$$C_n = \frac{1 - e^{-2K\mu' \frac{H}{B_d}}}{2K\mu'} + \left(\frac{H}{B_d} + \frac{H_e}{B_d}\right) e^{-2K\mu' \frac{H_e}{B_d}} \qquad when\ H > H_e$$

Where:

H_e=the height of the plane that has equal settlement above the top of the pipe in feet as shown in Figure 27.

P'= the projection ratio which is the distance from the top of the pipe to the natural ground surface divided by the trench width.

For the last type of installation, the jacked or tunneled installation, the soil load can be obtained from Equation 26:

$$W_t = C_t w B_t^2 - 2cC_t B_t \quad (26)$$

Where:

$$C_t = \frac{1 - e^{-2K\mu' \frac{H}{B_t}}}{2K\mu'}$$

B_t=width of tunnel bore in feet.

c=cohesion of undisturbed soil in pounds per square foot. Some conservative values of (c) are given in table 5.

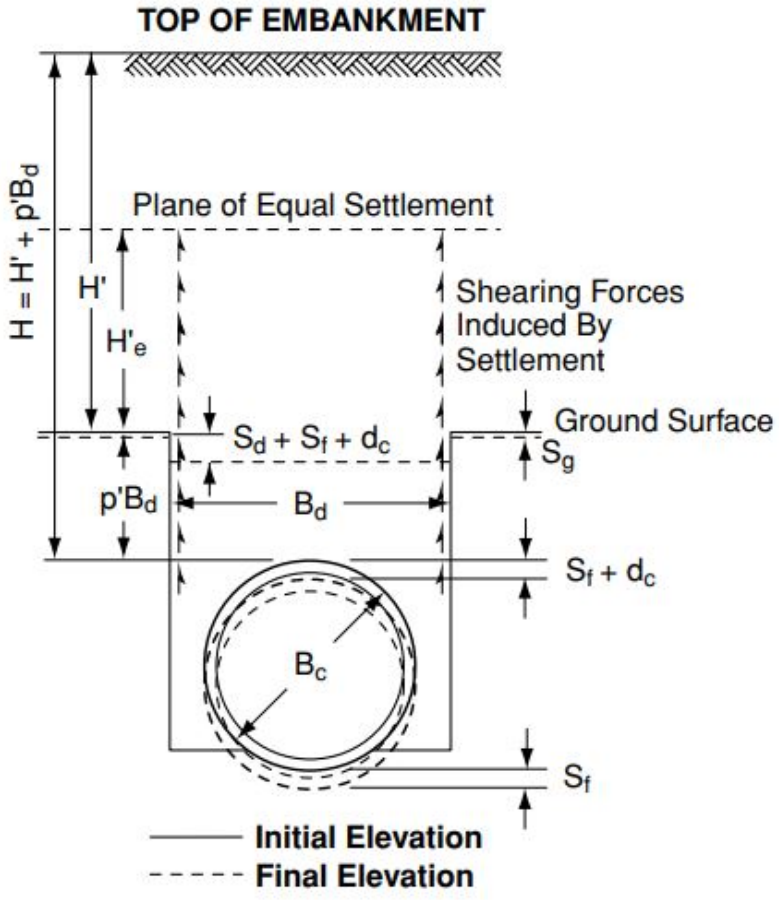

Figure 27: Settlement in the negative embankment installation, (ACPA 2011).

Fluid load is mostly considered in the design of large diameter pipes and it has been neglected in the past since there was no documented failure because of neglecting the fluid weight. However, AASHTO nowadays requires that the load of fluid to be considered in the design calculations. In general, it is based on the fluid unit weight, γ_w, of 62.4 pounds per cubic feet.

Table 5: Design Values of Coefficient of Cohesion c (ACPA 2011).

Type of Soil	Values of c
Clay	
Soft	40
Medium	250
Hard	1000
Sand	
Loose Dry	0
Silty	100
Dense	300
Top Soil	
Saturated	100

After finding the earth load which is considered as a deal load applied on the pipe, it is necessary to evaluate the live load coming from traffic over the pipe. So, if the pipe was installed under asphalt, flexible pavement, or shallow earth fill, it is essential to take the live load effects into account plus the dead and surcharge loads. If the pavement was rigid and the pipe is buried with relatively large depths of fill between the pipe and the pavement, the effect is usually negligible as the live loads' effects fade away with increasing depth.

AASHTO LRFD (Load Resisting Factor Design) usually designates HL93 as Live Load. It contains the larger of HS 20 that has 32,000 lbs per axle in the normal truck configuration or a 25,000 lbs axle load in the alternate load configuration. 640 lbs per linear foot lane load is also

considered and is applied over a 10 ft. lane width for depths of the pipe less than 8 ft. Figure 28 shows the details of the HS20 with 32,000 pounds and 25,000 pounds arrangement, as well as the contact area which is considered as rectangular. The live load pressure caused by the wheels on the pipe is calculated using Equation 27, while the lane load pressure is calculated by using Equation 28.

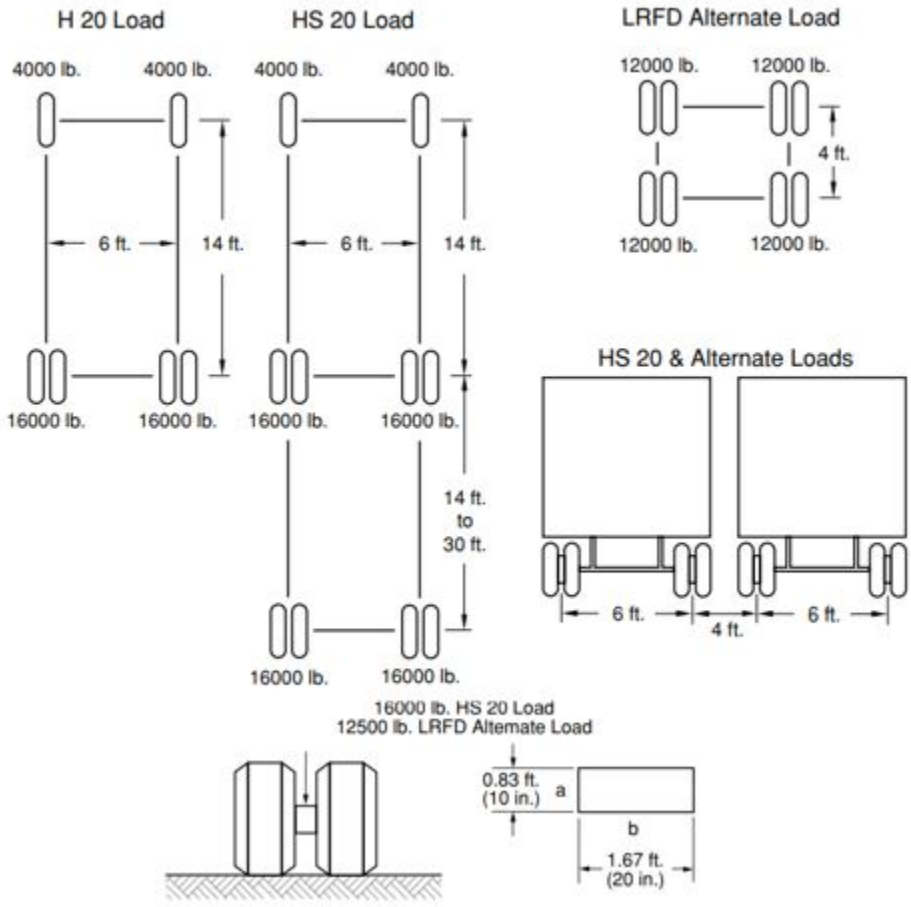

Figure 28: AASHTO wheel loads, spacings and contact area, (ACPA 2011).

$$w = \frac{P(1+IM)}{A} \tag{27}$$

Where:

w=the average pressure intensity caused by wheel loads, in pounds per square foot.

P=total live load applied at the surface in pounds.

A=spread wheel load area on the top of the pipe in square feet.

IM=dynamic load allowance = $\frac{33(1.0-0.125H)}{100}$

$$W_T = (w + L_L)\, L\, S_L \tag{28}$$

Where:

W_T=total live load in pounds

w=wheel load average pressure (from Equation 27)

L_L=lane load in pounds per square foot = 64 for 0≤H≤8 ft. and equals (0) for H≥8 ft.

L= dimension of load area parallel to the pipe longitudinal axis in feet

S_L=the smallest of dimension D_0 in Figure 13 or the dimension of the load area transverse to the pipe longitudinal axis.

Table 6 provide an easy method to obtain the values of (spread a) and (spread b) after considering the travel direction with respect to the orientation of the pipe. The area (A) in Equation 27 is visually represented in Figure 29 to better understand how it is calculated for being used in this equation for different combinations of wheels, (a) single dual wheel, (b) two single dual wheels in passing mode and (c) two single dual wheels of two alternate loads in passing mode. Also, for the calculation of the area A, it is important to consider the travel direction in regard to the longitudinal axis of the pipe.

For the design of reinforced concrete pipes installed within the runway in an airport, the aircraft wheel distribution depends on the aircraft loads, the configuration of its landing gear, pavement type and subgrade conditions.

Table 6: Spread dimensions at the top of the pipe and LRFD critical wheel loads, (ACPA 2011).

Vehicle Traveling Perpendicular to Pipe				
	H, ft	**P, lbs**	**Spread a, ft**	**Spread b, ft**
Live Load Distribution of 1.15 x H for Select Granular Fill	$H + 1.15D_o < 2.05$	16,000	a + 1.15H	b + 1.15H
	$2.05 - 1.15D_o < H < 5.5$	32,000	a + 4 + 1.15H	b + 1.15H
	$5.5 < H$	50,000	a + 4 + 1.15H	b + 4 + 1.15H
Live Load Distribution of 1.0 x H for Other Soils	$H + 1.30D_o < 2.30$	16,000	a + 1.00H	b + 1.00H
	$2.30 - 1.30\ D_o < H < 6.3$	32,000	a + 4 + 1.00H	b + 1.00H
	$6.3 < H$	50,000	a + 4 + 1.00H	b + 4 + 1.00H
Vehicle Traveling Parallel to Pipe				
Live Load Distribution of 1.15 x H for Select Granular Fill	$H < 2.03$	16,000	a + 1.15H	b + 1.15H
	$2.03 < H < 5.5$	32,000	a + 4 + 1.15H	b + 1.15H
	$5.5 < H$	50,000	a + 4 + 1.15H	b + 4 + 1.15H
Live Load Distribution of 1.0 x H for Other Soils	$H < 2.33$	16,000	a + 1.00H	b + 1.00H
	$2.33 < H < 6.3$	32,000	a + 4 + 1.00H	b + 1.00H
	$6.3 < H$	50,000	a + 4 + 1.00H	b + 4 + 1.00H

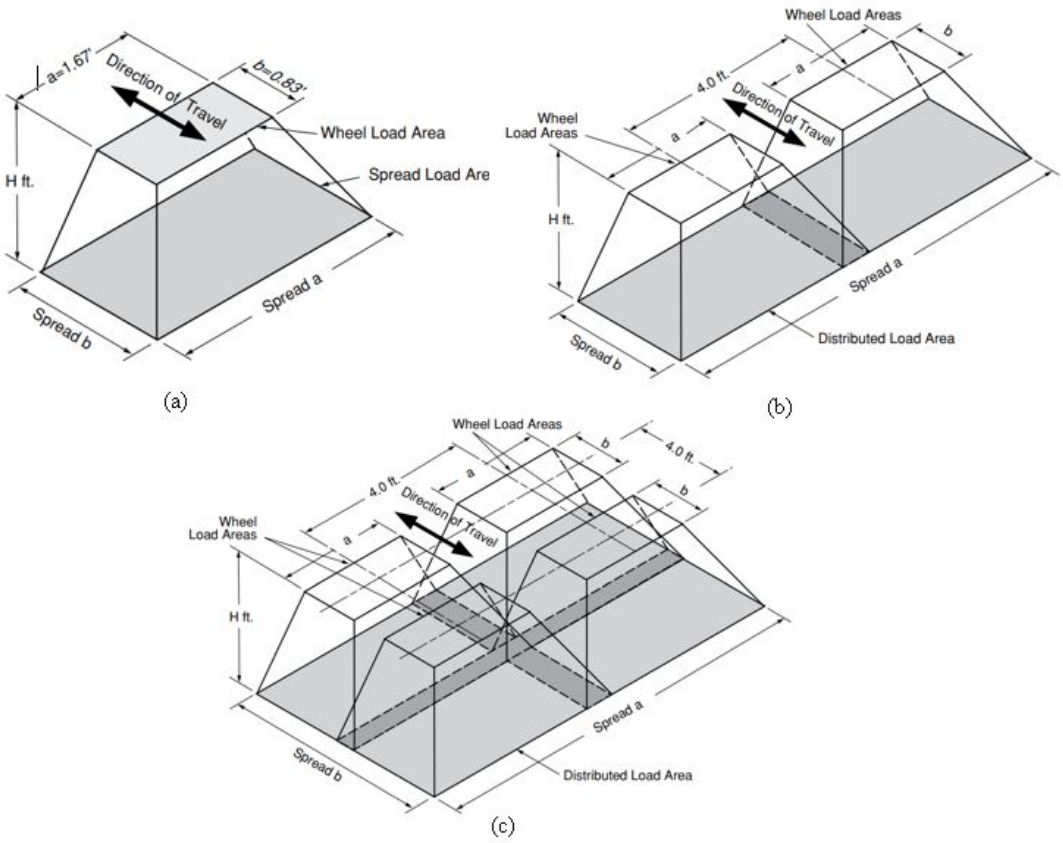

Figure 29: Spread Load Area for (a) single dual wheel, (b) two single dual wheels in passing mode and (c) two single dual wheels of two alternate loads in passing mode, ACPA (2011).

When rigid pavement is used, and at a certain elevation under the pavement level, the aircraft wheel load will be distributed over a larger area when compared with flexible pavement. Also, for the same types of pavement and soil, the pressure intensity decreases as we move away from the pavement as shown in Figure 30. The dynamic impact is not considered in the design but instead the takeoff weight of the aircraft is considered instead of the landing weight which is around 75% of the takeoff weight.

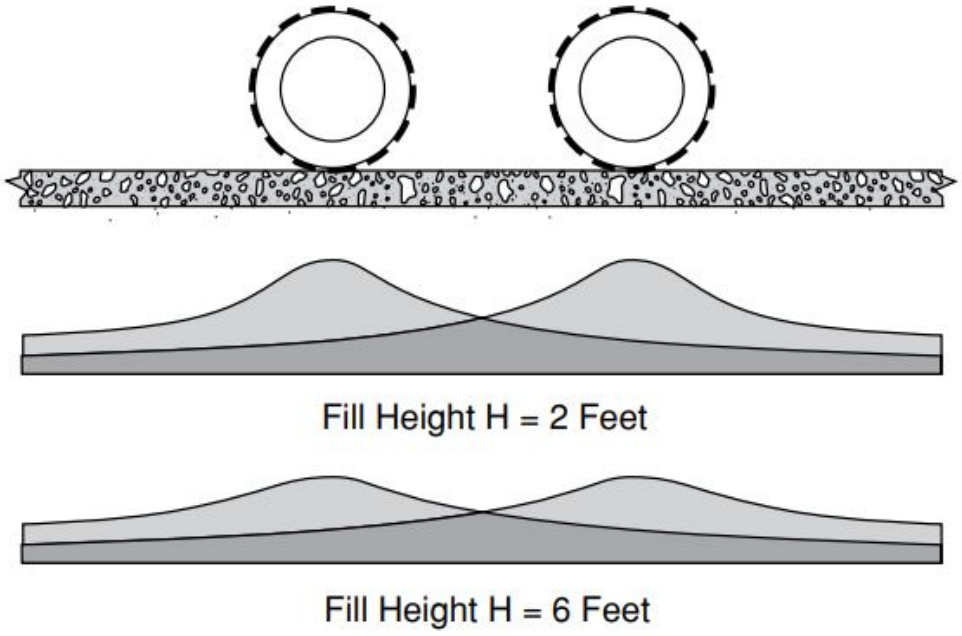

Figure 30: Aircraft pressure distribution, ACPA 2011.

In the design of RC pipes passing under railroad tracks, the American Railway Engineering and Maintenance of Way Association (AREMA) recommends the use of Cooper E80 live load where the loads for each axle and the spaces are illustrated in Figure 31. The weight of the locomotive driver axle is considered as axle loads while the track structure is considered uniformly distributed load area occupied by the drivers and multiplied by the ties length.

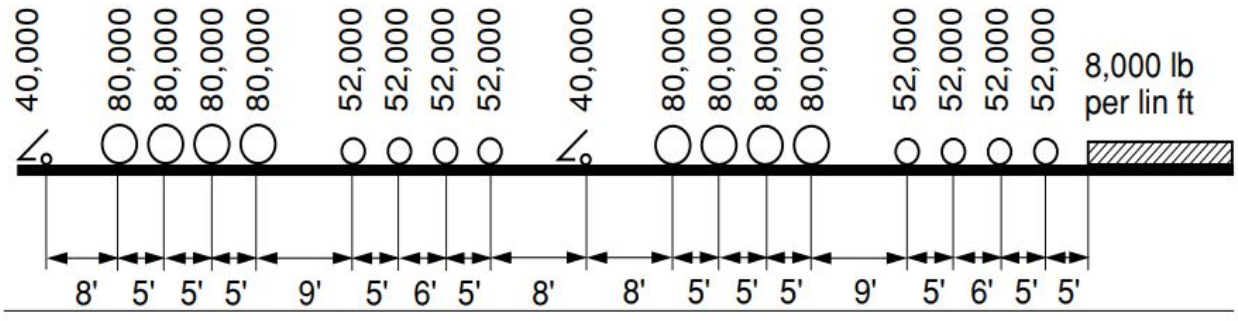

Figure 31: Cooper E 80 Wheel loads and axle Spacing, (ACPA 2011)

Final load to be considered is the construction loads. It is necessary in some cases that a heavy construction equipment to be operated over a pipe. This may cause load concentration that might not have been taken into account during the design which might also exceed the design load. It is very important to fill the pipe with at least 3 feet of soil above the pipe in order to allow for a heavy equipment to pass. This fill should be wide enough to prevent any possible lateral displacement in the installed pipe.

At this point, the bedding selection is the next to consider and accordingly the bedding factors. The bedding layer will distribute the vertical reaction along the lower surface of the pipe which leads to reduce stresses in the pipe walls. The supported load depends on the width of the bedding contact area and the quality of the bedding material. An ideal load distribution will be obtained by using clean coarse sand, pea-gravel that is well rounded or well-graded crushed rock. Those materials will shift to provide positive contact when the pipe settles.

The bedding factor is defined as the ratio of the maximum moment in the three-edge bearing test (TEB) to the maximum moment in the buried pipe under buried condition with the vertical loads being the same in both cases.

A general equation (Equation 29) for finding the variable trench bedding factor is used and two tables (Tables 7 and 8) to find the embankment bedding factor, B_{fe} and the minimum bedding factor B_{f0}:

$$B_{fv} = \frac{[B_{fe} - B_{fo}][B_d - B_c]}{[B_{dt} - B_c]} + B_{f0} \quad (29)$$

Where:

B_c= outside horizontal span of the pipe in ft.

B_d= trench width at the top of the pipe in ft.

B_{dt}= transition width in ft.

B_{fe}= embankment bedding factor

B_{f0}= trench minimum bedding factor

B_{fv}= trench variable bedding factor

Table 7: Embankment Bedding Factor, B_{fe}, (ACPA 2011).

Pipe Diameter	Standard Installation			
	Type 1	Type 2	Type 3	Type 4
12 in.	4.4	3.2	2.5	1.7
24 in.	4.2	3.0	2.4	1.7
36 in.	4.0	2.9	2.3	1.7
72 in.	3.8	2.8	2.2	1.7
144 in.	3.6	2.8	2.2	1.7

For pipe diameters other than the ones listed in Table 7, linear interpolation is permitted.

Table 8: Embankment Bedding Factor, B_{f0}, (ACPA 2011).

Standard Installation	Minimum Bedding Factor, B_{f_0}
Type 1	2.3
Type 2	1.9
Type 3	1.7
Type 4	1.5

Finally, for live load, the bedding factor B_{fLL} for HS20 can be found from Table 9.

Table 9: Bedding factor, B_{fLL} for HS20 Live loads, (ACPA 2011).

Fill Height, Ft.	Pipe Diameter, Inches										
	12	24	36	48	60	72	84	96	108	120	144
0.5	2.2	1.7	1.4	1.3	1.3	1.1	1.1	1.1	1.1	1.1	1.1
1.0	2.2	2.2	1.7	1.5	1.4	1.3	1.3	1.3	1.1	1.1	1.1
1.5	2.2	2.2	2.1	1.8	1.5	1.4	1.4	1.3	1.3	1.3	1.1
2.0	2.2	2.2	2.2	2.0	1.8	1.5	1.5	1.4	1.4	1.3	1.3
2.5	2.2	2.2	2.2	2.2	2.0	1.8	1.7	1.5	1.4	1.4	1.3
3.0	2.2	2.2	2.2	2.2	2.2	2.2	1.8	1.7	1.5	1.5	1.4
3.5	2.2	2.2	2.2	2.2	2.2	2.2	1.9	1.8	1.7	1.5	1.4
4.0	2.2	2.2	2.2	2.2	2.2	2.2	2.1	1.9	1.8	1.7	1.5
4.5	2.2	2.2	2.2	2.2	2.2	2.2	2.2	2.0	1.9	1.8	1.7
5.0	2.2	2.2	2.2	2.2	2.2	2.2	2.2	2.2	2.0	1.9	1.8

Factor of safety is also used as part of the design parameters that needs to be considered in order to determine the required pipe strength. If the 0.01-inch crack strength is used as the required design criteria instead of the ultimate strength, a factor of safety of 1.0 is used. If the ultimate strength was the design criteria, a factor of safety of 1.5 is used for ultimate load of 2,000 and less, 1.25 for ultimate load of 3,000 or more and linear interpolation for ultimate load between 2,000 and 3,000.

Final step is the pipe strength. In this step, different specifications are used depending on the conduit type. ASTM C14 (2020), ASTM C76 (2019), ASTM C506 (2019), ASTM C507 (2019), ASTM C655 (2019), and ASTM C985 (2019) are used for non-reinforced concrete pipes, reinforced concrete pipes and culverts, reinforced concrete arch culverts, reinforced concrete elliptical culverts and pipes, reinforced concrete elliptical culverts and pipes and non-reinforced concrete specified strength culverts and pipes, respectively. For the reinforced concrete pipe in this study, ASTM C76 (2019) is the one that was used in the design of those pipes. The required D-load for the pipe strength can be calculated from Equation 30:

$$D - load = \left[\left(\frac{W_E + W_F}{B_f}\right) + \frac{W_L}{B_{fLL}}\right] \times \frac{F.S.}{D} \quad (30)$$

When HS20 live load is used, B_{fLL} must be incorporated in Equation 30 and it must be equal or less than B_f.

Referring to ASTM C76 (2019), after finding the required D-load, for each class of reinforced concrete pipe, the minimum concrete compressive strength and the minimum reinforcement area per foot length of the pipe are specified there in addition to the wall thickness.

Cracks in reinforced concrete pipes, as well as any other reinforced concrete structure, occurs when the tensile stresses in concrete exceeds its tensile strength. The tensile strength of concrete is generally neglected in design.

Previously, the first visible crack in a TEB test was considered as the acceptance criterion for crack width in terms of pipe performance. This method is qualitative and not accurate since the first observed crack is difficult to notice and depends mainly on sight strength of the observer. Therefore, the feeler gauge was used to measure the 0.01-inch crack width. This approach became the acceptance criterion for crack width.

Since reinforced concrete pipes, as other types of pipes, carry harsh liquids that might lead to deterioration of the pipe material, crack width is an important factor to be considered in the design process. Generally, cracks are wider at the surface and narrows down until they reach the reinforcing steel. At the level of the reinforcing steel bars, it is essential to know whether this crack width is enough to allow oxygen and moisture to trigger corrosion on the surface of the reinforcing steel bars or not. As per ACPA (2011), if the crack width is not wide enough to permit circulation of moisture and sufficient supply of oxygen, corrosion is not likely to occur. Another factor that

contributes to the unlikelihood of corrosion to occur, is the alkalinity of the cement in which the reinforcing steel bars are embedded. Previous inspection of pipes where cracks wider than 0.01 inch were observed, did not show any evidence of corrosion. Therefore, the 0.01 was taken as the maximum acceptable and conservative crack width.

Cracking of a reinforced concrete pipe indicates that the tensile stresses are carried by the reinforcing steel bars. In the meantime, the occurrence of the 0.01-inch crack width is not harmful and does not indicate any structural failure. ACPA (2011) recommends that cracks that are much wider than 0.01 inch to be sealed in order to provide protection to the steel bars. In case of concrete covers greater than 1 inch, it is allowed to increase the limit of the 0.01-inch crack width acceptance criterion and the increase in the limit will be proportional to the additional cover.

3.4 Reinforced Concrete Pipes Testing Protocol

In this research, 102 pipes sections were used (2 ft each), 51 of them were top section and 51 were bottom section. 12 control specimens were tested, 3 top sections from the first day of production, 3 top sections from the second day of production, 3 bottom sections from the first day of production and 3 bottom sections from the second day of production. The top and bottom sections are named according to the way the pipes are being manufactured at the plant where the top section is the socket joint of the pipe and the bottom section is the spigot joint of the pipe. The pipes were produced on two different production dates as mentioned above, 11/8 and 11/9 of 2018.

The D-load test was used to test these reinforced concrete pipes. The D-load is defined as the applied load to the pipe top divided by the pipe length and the inside diameter in feet. Therefore, the D-load is a measure of pipe strength regardless of its diameter.

For the first phase of this research, the pre-immersion phase, 90 pipes were tested for D-load until a crack of 0.05 inch (5 times the currently allowable limit) was obtained and stainless steel spacers were

inserted inside the cracks to keep them open for the whole period they are immersed in the sodium chloride solution. For the second phase, the post-immersion phase, the 90 (81 are for the main test for the post-immersion phase and 9 spare specimens) pipes were immersed in sodium chloride solutions with three different sodium chloride contents, i.e. 200, 2000 and 30000 parts per million (ppm). Then 3 pipes for each concentration were tested for D-load after being immersed for one whole month. After the first month of full immersion in sodium chloride solutions, the pipes are subjected to 2 weeks dry – 2 weeks wet cycles to the end of the testing period as shown in the test protocol in Figure 32. This is to provide the optimum environment for corrosion to start and increase its rate where moisture and oxygen are intentionally introduced to the steel reinforcing bars through the open cracks.

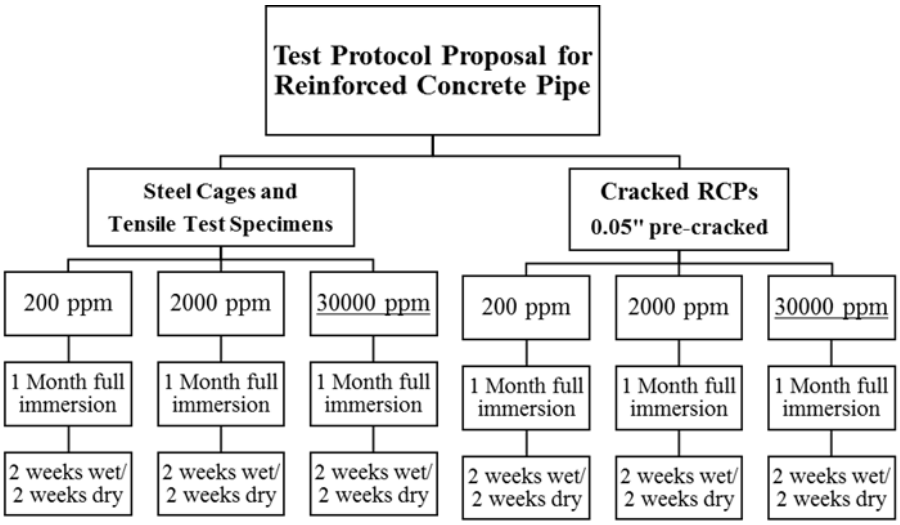

Figure 32: Test protocol.

For the 30,000 ppm, three pipes are being tested monthly, while for the 200 and 2000 ppm, three pipes are tested on a bi-monthly basis. The total testing period is 1 year. In addition to the reinforced concrete pipes, steel specimens as shown in Figure 33 (a) (cages, helical bars and tension coupons) were tested as well for weight loss monitoring and tensile test. Steel half cages and around 8 inches long helical reinforcing steel bars were used for weight loss measurements. The tension coupons were used for the tensile test to monitor strength loss in steel reinforcing bars over time due to diameter reduction caused

by corrosion. Since the original main reinforcement of the steel cages is the helical reinforcement where they are delivered to the plant in hoops, it was important to get those helical bars straightened at the plant and take 10 inches parts from them to make the tension coupons. The tension coupons were sent to the machine shop to introduce the reduced section at the mid-length of those straightened bars in order to make sure that the failure occurs within this length. The reduced section is shown in Figure 33 (b). All the steel specimens were immersed in the same solutions with the pipes.

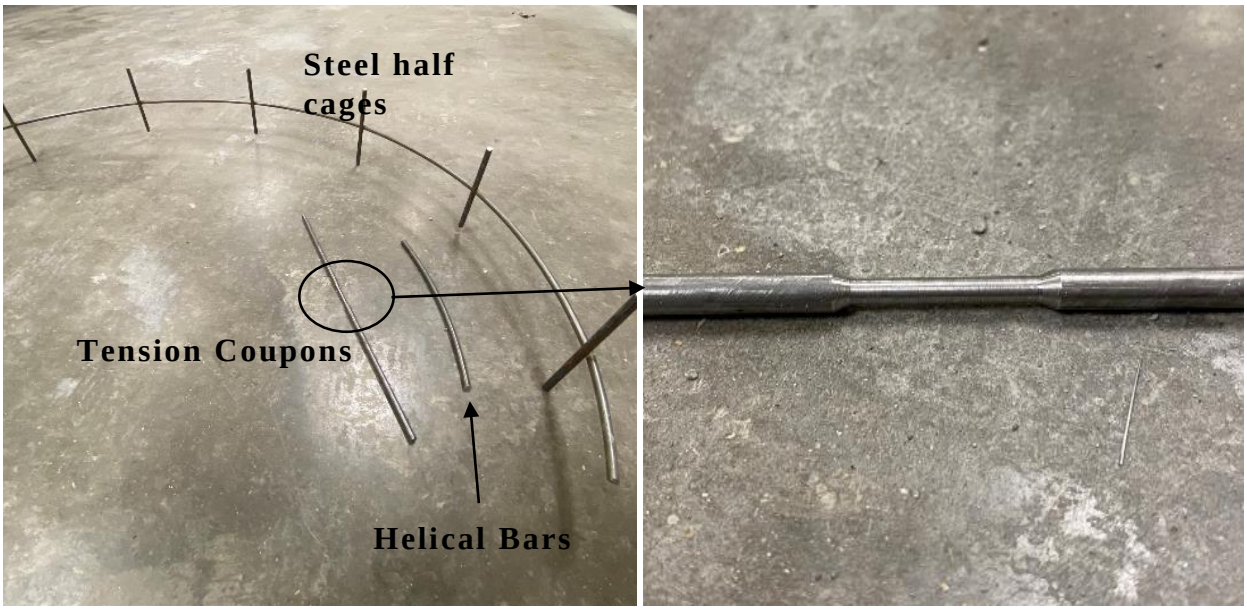

(a) (b)

Figure 33: Steel specimens, (a) steel half cage, helical bar and tension coupon and (b) reduced section in the tension coupon specimen.

Based on this test plan, the total number of pipes is 93 pipe sections as illustrated in Table 10.

Table 10: Test plan.

Control		Total
Initial tests		
12 (three from the top - day 1, three from the top - day 2, three from the bottom – day 2, and three from the bottom – day 1)		12
200 ppm		
1 Month immersion	*Two-weeks-wet/ two-weeks dry (Every two months)*	
3	3 specimens× 6 tests = 18	21
2,000 ppm		
1 Month immersion	*Two-weeks-wet/ two-weeks dry (Every two months)*	
3	3 specimens× 6 tests = 18	21
30,000 ppm		
1 Month immersion	*Two-weeks-wet/ two-weeks dry (Every month)*	
3	3 specimens× 12 tests = 36	39
Total		**93**

The total number of tests is 192 D-load test, 12 for control specimens, 90 pipes are tested for pre-immersion phase and the same 90 pipes are tested for post-immersion phase (this includes the 81 pipe sections in the table above plus 9 spare sections).

Before sending the manufactured pipes at Forterra pipe plant, one pipe was tested to represent the 51 pipes that were sent to Civil Engineering Laboratory Building (CELB). The test results are shown in Figure 22 and the test report shows that the pipe passes the requirement of ASTM C76 (2019) for both service and ultimate strength requirements for class III pipes, wall B where the required service and ultimate strengths are 1350 and 2000 lbs/ft/ft, respectively. As shown in Figure 34, the actual service and ultimate strengths were 1625 and 2608 lbs/ft/ft, respectively, which are higher than the minimum required strengths in ASTM C76 (2019).

FORTERRA

Three Edge Bearing Test Report

Plant:	Grand Prairie, Tx	Production Date:	11-9-18	Test Date:	10-18-19
Size:	24"	Class:	III	Age in Days:	343
Wall:	B - 3"	Tested Length:	8'	Specification:	C497

Reinforcing	Style	Required Area	Actual Area
Inner Cage	Hellical	.07	.08
Outer Cage			
Elliptical Cage			
Extra (Stirrups, etc):			

Test Result □ **No Crack** □ **0.01" Crack** □ **115% +**

Test 1	Design Load	Actual Load	Actual D-Load
0.01" Crack	21,600	26,006	1,625
Ultimate	32,000	41,735	2,608
Highest Load (If not Ultimate)			

Figure 34: D-load test report by Forterra.

3.5 Preparation of Reinforced Concrete Pipe Sections

The pipes were manufactured at Forterra Pipe Plant in Grand Prairie, Tx. The original pipe is 8 ft long as shown in Figure 35. The pipes have 24 inches inner diameter and 3 inches wall thickness (wall B – according to ASTM C76 (2019)). During the manufacturing of the pipes, the pipe formwork is placed vertically on the floor. The packer-head comes all the way down inside the formwork and starts rotating and vibrating to push the concrete against the wall of the formwork as the dry concrete mix is poured from the top through a conveyor belt. While the concrete mix is poured into the formwork, the packer-head moves up until the 8 ft long pipe is shaped to the required dimensions inside the formwork which is called “the jacket”. Then by using a forklift, the pipe and the jacket are transported to the steam curing yard and the jacket is taken of while the pipe remains standing to be cured for 24 hours. The end A in Figure 35 is the end that is touching

the floor when the pipe is standing vertically, and the end B is the top of the pipe. Therefore, the end A is the bottom section while the end B is the top section.

Figure 35: Full length 24 inches reinforced concrete pipe manufactured by Forterra Pipe Plant.

When the pipes were delivered to CELB, the pipes were cut to 2 feet top and bottom sections. Therefore, all the pipe sections having a spigot joint A are named bottom section and all the sections having a socket joint B are named top sections.

Since this research is a part of a bigger project, the pipes were labeled as P-1B-XX(B or T), where P-1B stands for (Phase 1-B) of the project, XX refers to the pipe number (from 01-51) and B or T refer to bottom or top section, respectively. Figure 36 shows a sample of the 102 pipes and how it was labeled. The pipe shown in Figure 36 represents a bottom section from the pipe numbered 47 for phase 1-B of the project. The pipe number as mentioned above was ranging from 01 to 51. For the first production date, 26 full length pipes were delivered to CELB, while for the second production date 25 full length pipes were delivered. All the pipes had a lifting hole of 3-4 inches

in diameter and because of the presence of those lifting holes it was not possible to get exactly 2 feel sections from the middle sections of the pipes.

Before cutting the pipes to 2 ft top and bottom sections, a line on top of the pipe was drawn on each pipe (the line shown in figure 35) to ensure that both top and bottom sections are loaded during the D-load test along this line and not being loaded in a random direction. This line is set at a point where a small piece of the cage is bent out at the bottom section. It is very important to adopt the same line of loading because the number of reinforcing steel loops involved in resisting the applied will be different if the loading line is random since the cage is helical in shape.

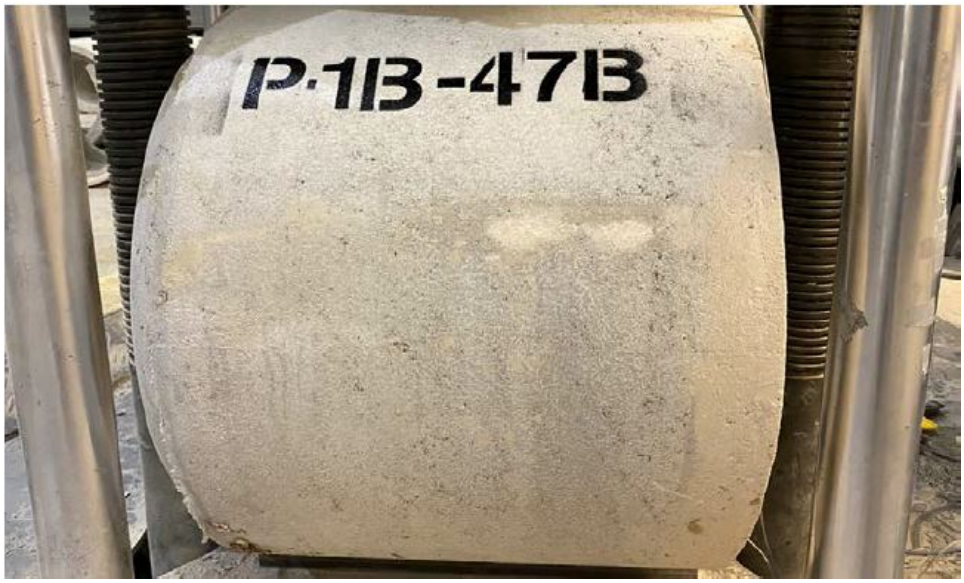

Figure 36: Sample of pipe labeling.

The cutting process was done by the use of a gas operated portable concrete saw similar to the one shown in Figure 37. The pipe is laid horizontally on the ground and the cutting process starts along the existing line of the 2 ft measurement and the rolled to cut the sides and the bottom until it is all cut.

Figure 37: Portable concrete saw, (https://www.stihlusa.com/products/cut-off-machines/professional-cut-off-machines//ts800/?rev=BVSpotlights, 2020)

After the 102 pipe sections were all cut, they had to be prepared for both phases of the research project, the pre-immersion and post-immersion phases. The pipe sections were labeled according to the label sample shown in Figure 36.

In order to ensure that the moisture going to the reinforcing steel bars come only from the inner surface of the pipe, the cut sections were sealed using rubber sealant. This rubber sealant comes in either paint cans or paint spray bottles and it has a fast setting time. Therefore, timewise it was decided to use the spray bottles. At the cut sections, there are some holes for the longitudinal bars. At those holes and round them, a thicker layer of the rubber sealant was applied to minimize or eliminate any saline water to go through those holes. Figure 38 shows the pipes with their cut sides sealed with the rubber sealant. All the pipes were laid here waiting for the next step of the test.

Figure 38: Cut sections of the pipes sealed with rubber sealant.

Since all the pipe sections are to be immersed in saline solutions, laminated tags including the pipe label were prepared for each pipe. They were attached to the bent-out bars of the cages at the bottom sections and a bracket was glued to the top sections where there is nothing to be attached to. All the tags were attached to the bars and the brackets using cable ties as shown in Figure 39.

Figure 39: Labeled pipe sections.

Prior to receiving the pipes at CELB, 275 and 330 gallons were bought and delivered to CELB. The dimensions of the 275- and 330-gallons totes are 45 x 40 x 46 in and 48 x 40 x 53 in. (L x W x H), respectively. Figure 40 shows the totes that were used in this study.

Figure 40: 275- and 330-Gallons Totes.

In order to immerse the pipes in the saline solutions, we had to cut the top part of the totes. After cutting the tops of the totes, the inside of the totes had to be cleaned using power washer to get rid of any chemical residues that might have been there.

Figure 41 shows the final layout of the totes placed outside CELB with all the tops cut and ready to receive the sodium chloride, water, pipes, and the other steel specimens.

Figure 41: Layout of totes outside CELB.

The Environmental, Health and safety department at UTA requested that the totes must be labeled to indicate their contents as a general recommendation by the safety regulations related to the storage of any chemicals as shown in Figure 42.

Figure 42: Labels for the contents of the totes and the tags on the totes to indicate the concentration of sodium chloride

The sodium chloride was also supplied from Fisher Chemical Company in packages of 50 kg as shown in Figure 43.

Figure 43: Sodium chloride manufactured by Fisher Chemical Company.

With the totes' tops open, the insides of the totes being clean and sodium chloride being available, the next step was to add water inside the totes to a level where it ends up around 3 inches above the top of the pipes when they are immersed inside the totes. Based on an initial trial, an average of 850 liters (225 gallons) of water were added to the totes to make sure there is around 3 inches of water above the pipe when it is placed inside the tote.

In order to get the required saline solution concentrations, 0.17, 1.70 and 25.5 kg of sodium chloride were added to get 200, 2000 and 30000 ppm solutions, respectively. Then by the use of paddle mixer and a cordless drill, the sodium chloride and water were mixed. At this moment, the totes were ready to receive the pipes to be immersed inside them.

To finalize the preparation of the concrete pipe sections, the pipes must be tested for D-load as per ASTM C497 (2020) and measure the crack width until it reaches 0.05 inch. Stainless steel spacers (shown in Figure 44) of 0.063-inch-thick and 0.25 x 1 inch (L x W) were used to be inserted inside

the cracks to keep them open to as close as possible to 0.05 inch. The reason for using 0.063 inch is to allow for rebound where the crack width is monitored till the spacers can be inserted inside the crack. When all the spacers are inserted in the crack, the pipe will be unloaded causing the concrete to rebound and the crack to reach a crack width less than 0.063 inch, since some concrete will be crushed around the spacers. The details of the D-load test and its procedures (step-by-step) are discussed in chapter 4.

Figure 44: Stainless steel spacer with a thickness of 0.063 inch.

3.6 Preparation of Steel Specimens

Three types of steel specimens were used in this study. The first one was the half cage. Several full-length steel cages were manufactured in Forterra pipe plant and delivered to CELB as shown in Figure 45. The steel bars in those full-length steel cages were clean and rust-free at the time they were delivered to CELB. They came with a thin layer of oil to provide protection from corrosion to a certain level. By using a bolt cutter, half steel cages were cut from the full-length steel cages. The diameter of the longitudinal and the helical bars is identical to the ones used in the pipe sections used in our study. The purpose of these specimen was to monitor the weight loss after

each immersion and wet-dry cycle and following the test protocol and plan. Three half cages were considered for each testing period for each concentration.

Figure 45: Steel cages delivered to CELB.

The second type of steel specimen is the helical bars. Each specimen was around 8 inches long and they were cut from the full-length steel cages. Those specimens were used as an additional weight loss monitoring specimen with the half steel cages. Three specimens were also prepared for each testing period and for each concentration of sodium chloride.

The third type is the tension coupons which were used to determine the strength loss in the main reinforcement due to the loss of the cross-sectional area of the bars caused by corrosion. As mentioned earlier, those bars were made out of the helical reinforcement after straightening them in Forterra pipe plant (shown in Figure 46) and sending them to the machine shop to make the

reduced section to ensure that failure occurs within this zone. Four tension coupons were prepared for each testing period.

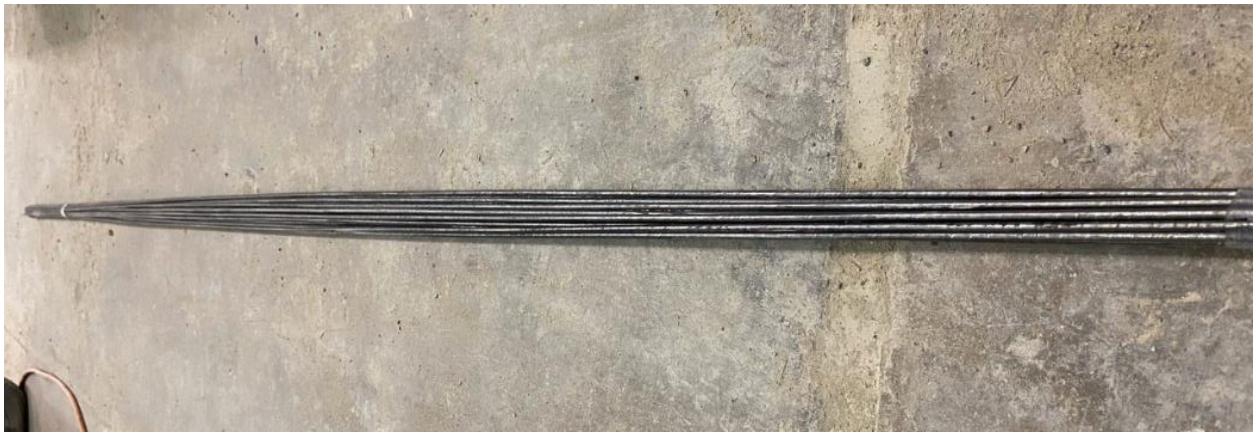

Figure 46: Straightened bars to make tension coupons.

For the weight loss monitoring specimens, the initial weight at a rust-free state was recorded for each specimen and tagged to each specimen in a laminated tag attached to the steel specimen using a cable tie. The specimens were weighed using a digital scale with a capacity of 300 grams and a precision of 0.001 grams.

For tension coupons, the original diameter of the reduced section for each specimen was recorded and tagged to each specimen using a laminated tag as well. The diameter measurement was taken using a digital Vernier caliper with a precision of 0.01 mm.

CHAPTER 4. EXPERIMENTAL WORK

4.1 Overview

In this chapter, the details of the performed tests are discussed. As previously mentioned, this research consists of two phases, pre-immersion and post-immersion phases. In the pre-immersion phase, all the specimens were prepared and then immersed in sodium chloride solutions and then tested periodically to evaluate the effect of corrosion on the weight loss and strength degradation in both steel specimens and the concrete pipes.

4.2 D-load test

The D-load test is used for both phases of this research since it is the method used to find the service load in the pre-immersion phase and the ultimate load in the post-immersion phase. Since the pipes are cracked, immersed in saline solutions and then tested again for their ultimate strength, the control specimens must be tested in a way to mimic these loading, unloading and reloading stages. A typical D-load test is done in one step where the pipe is loaded until is the pipe cracks, the load drops at this point and then starts to increase until the ultimate pipe strength is reached. After the ultimate load is reached, the pipe cannot withstand any additional load and the crack width will increase significantly until the pipe fails. For control specimens of this research, this is not the case since they must represent the case of both phases of the test. Therefore, and in order for the pipes to be considered as control specimens, the load is applied to the pipe until it cracks, the crack is monitored using a feeler gauge to investigate a crack width of 0.063 inch. As soon as the 0.063-inch crack width is obtained, the pipe will be unloaded until there is no more load to mimic the case of pre-immersion phase. The pipe is reloaded again to failure to represent the case of the post-immersion phase.

The test setup for the D-load is following the requirements in ASTM C497 (2020). A steel platform is placed on the base of the testing machine, two rubber strips are placed on the steel base and the reinforced concrete pipe is placed on them. On top of the reinforced concrete pipe, a rubber flat strip and a wooden rigid beam are placed. The purpose of using the rubber strips is to ensure full contact between the reinforced concrete pipe and the wooden beam from top and the steel base from the bottom side. Figure 47 shows the setup parts used for the D-load test.

During the test, the pipe is lifted with the overhead bridge crane using chains and lifting straps around the pipe in order not to cause any damage to the edges of the pipe. The top block of the testing machine is moved upward until the space between the lower base and the top block is enough to accommodate the pipe and the setup parts above and below it in addition to the load cell. The pipe is placed near the base of the MTS 400 Kips machine and then rolled on the base and finally on the steel base shown in Figure 47 (d) in such a way that the marked line on the pipe is located on top where the load is applied to the pipe and the imaginary line between the pipe invert and crown is set to be vertical and perpendicular to both the lower base and the top block of the machine. The flat rubber strip and the rigid wooden beam are placed on top of the pipe and the load cell is placed on the rigid wooden beam at the mid-length point of the beam, as shown in Figure 48. A close view of the load cell and its calibration values is shown Figure 49. A Cable-Extension Displacement Sensor (CDS-05) with a max reading of 5 inches was used to read the relative displacement between the crown and the invert during the D-load test. The CDS-05 is shown in Figure 48 inside the pipe and in Figure 50. A fish line is connected to the upper end of the CDS-05 and a hook is connected to the other end of the fish line. The hook is then attached to an L-shaped bracket glued to the inner surface of the pipe at the crown. In this way, any relative displacement between the invert and the crown of the pipe will be recorded by the CDS-05.

The software used to control the load application is known as (Horizon). It has several options to control the load application as force or displacement control with the ability to add several control segments. This software has also the ability to record the applied load and the relative displacement between the lower base and the top block.

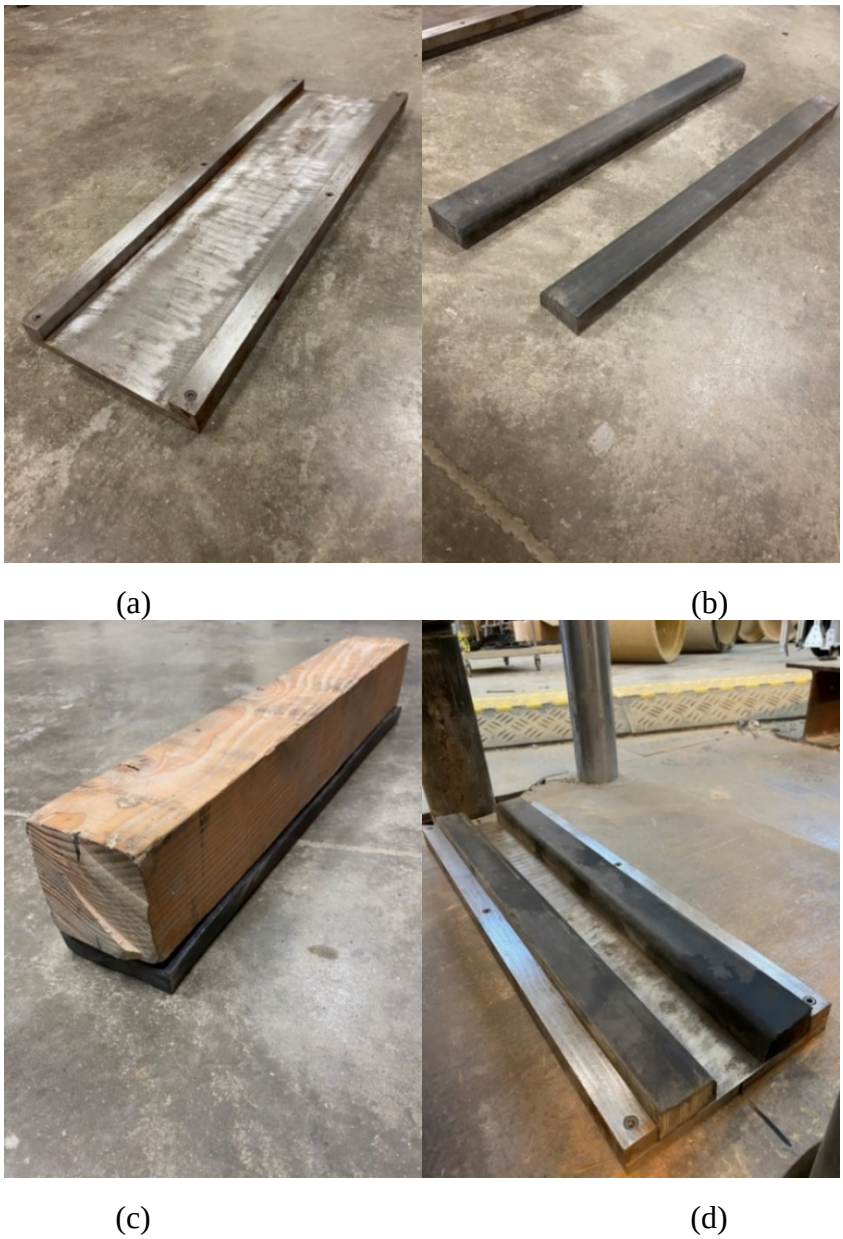

(a) (b)

(c) (d)

Figure 47: D-load test setup parts: (a) steel base (b) rubber strips (c) wooden rigid beam and a flat rubber strip and (d) steel base with rubber strips placed on the base of the test machine.

Figure 48: D-load setup.

Figure 49: Load cell and the calibration values shown on the sticker.

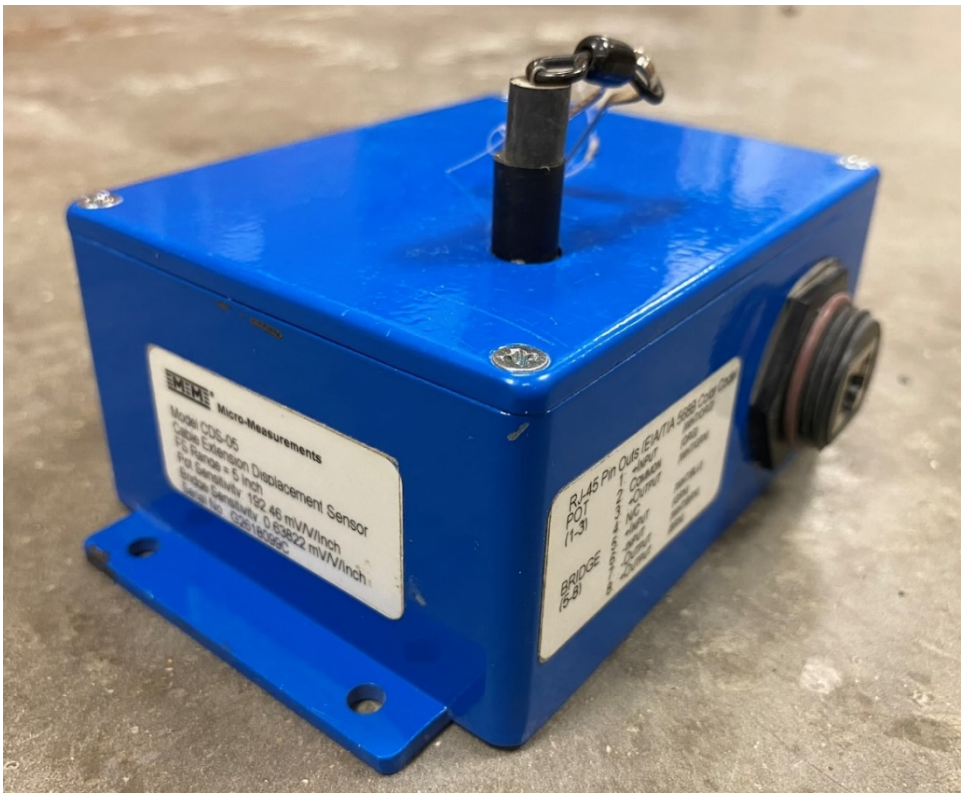

Figure 50: Cable-Extension Displacement Sensor (CDS-05).

Figure 51 shows the 400 kips MTS testing machine where all the D-load test was performed.

Figure 51: 400 Kips MTS testing machine.

A simple way to check load cell accuracy is to compare its readings with the software readings.

A data acquisition system manufactured by MicroMeasurements was used to record all the data for the D-load test. The system is called system 8000 as shown in Figure 52.

Figure 52: Data Acquisition System, System 8000, (a) front panel and (b) back panel.

4.3 Tensile Test

The tension test for the steel rebars is based on ASTM A370 (2019) and ASTM E8/E8M (2013) which specify the requirements for the tension test for metallic specimens. They also describe the dimensions and method of preparing the specimens. As mentioned earlier, the tension coupons were made out of straightened bars because the bars are supplied as hoops to the plant. Specimens were 10-inch-long each with a diameter of 4.5mm (0.178 inch). A reduced section of 3mm (0.118 inch) diameter and 22.5 mm (0.885 inch) length was made for each specimen at the mid-length of the specimen.

The machine used to perform the test is known as the MTS machine. It has two heads: upper and lower heads; in each head two grips are placed. The hydraulic pump pushes both heads apart to

apply load to the grips in order to hold the specimens and this is controlled manually so that one can grip one end of the specimen and then grip the other end of the specimen. Figure 53 shows the MTS machine and its details.

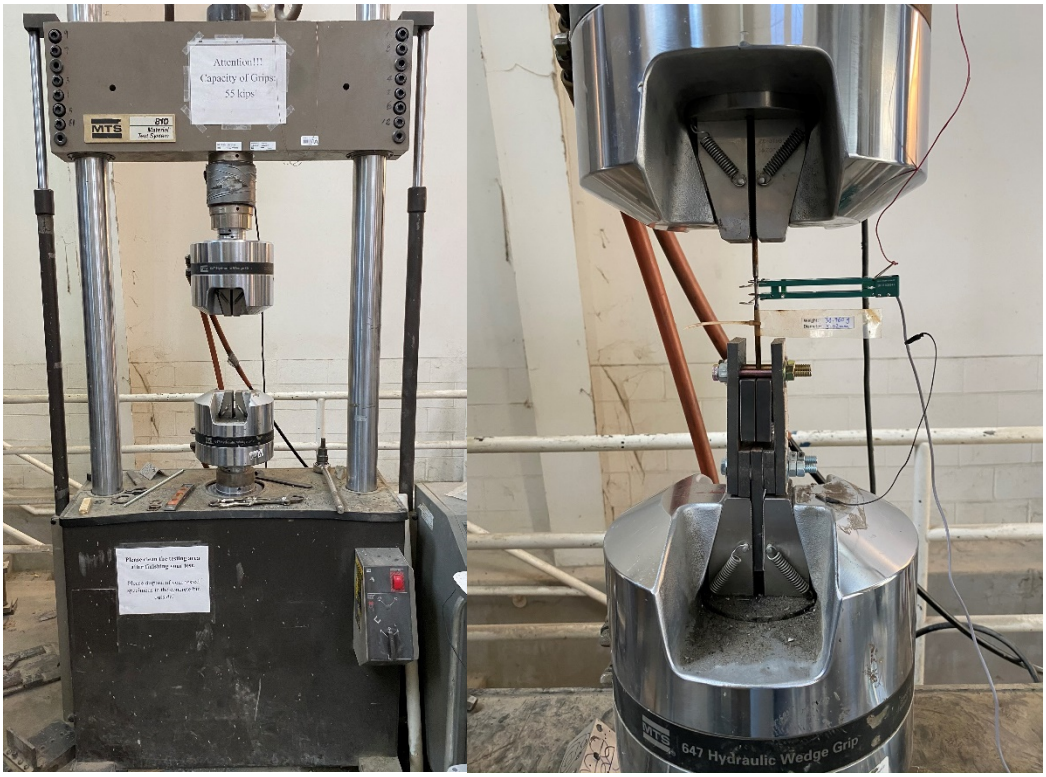

Figure 53: MTS Machine and heads details.

The MTS machine applies a compressive force to the specimen while gripping because of the gripping mechanism. This is usually not an important point to consider during the test of specimens with a relatively large cross-section. But for the case of the specimens of this research, this problem caused failure by buckling of few specimens. Therefore, an attachment was used to help eliminate the applied compressive force to the small tension coupons. The idea was to design an attachment that can be held by the lower grips, while the upper grips are attached to the upper end of the tension coupon. Then with this attachment, the lower end of the tension coupon is gripped by

applying horizontal forces to make the additional grips come close to each other. Figure 54 shows the attachment and the additional grips.

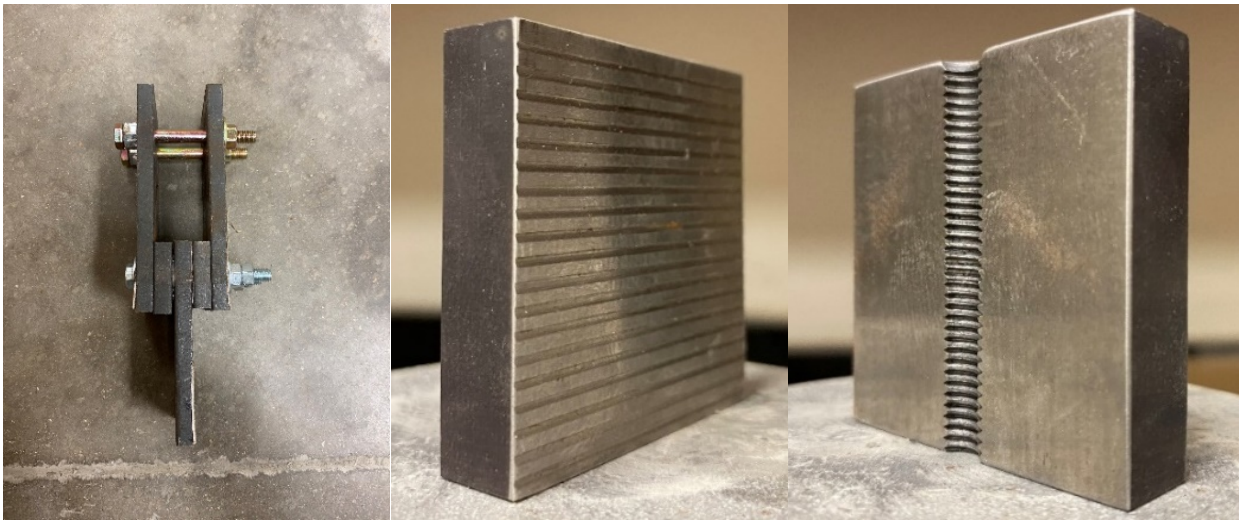

(a) (b) (c)

Figure 54: (a) attachment, (b) back of the additional grip and (c) front of the additional grip.

The upper two bolts are loosened to allow the two additional grips to be inserted in between the upper two steel strips with the lower end of the specimen is in between the additional grips. Then by tightening the upper two bolts, the steel strips will push the additional grips closer and grip the lower end of the tension coupon tightly so that the specimens do not slide while being subjected to tension force. The upper bolts provide two benefits: the first one is to apply compression force to the additional grips to hold the tension coupons and the second one is to as a bearing member to the additional grips during the test.

After gripping the tension coupon from both ends, the extensometer is placed on the reduced section. The extensometer is made by Epsilon and has a gauge length of 10 mm as shown in Figure

55. The calibration values for this extensometer were provided by the manufacturer to be input to the data acquisition system in order to read accurate displacement values.

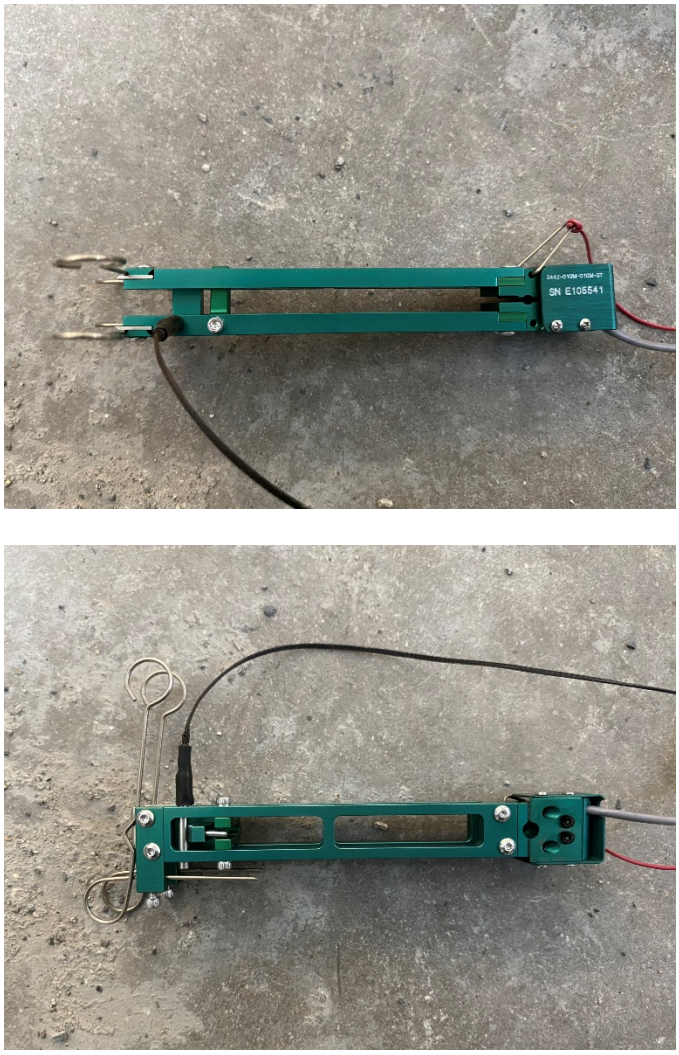

Figure 55: Epsilon Extensometer used in Tension test.

The application of the tension force or displacement is controlled by the Station Manager software through which all the test segments and parameters can be entered according to the required test. A strain rate of 0.02 in/in/min [mm/mm/min] was used according to ASTM E8/E8M (2013) as this specification sets a range of strain rate of 0.015 in/in/min ± 0.006 in/in/min [mm/mm/min]. The

data acquisition system receives three signals from three sensors for this test: the extensometer, the MTS load and the MTS displacement. The extensometer measures the displacement in the tension coupon within the 10 mm gauge length. Therefore, the strain will simply be the reading of the extensometer divided by 10. The MTS load is also recorded on one of the channels of the DAQ system and the third channel records the displacement between the two heads of the MTS machine which is not the same as the extensometer. This is used as a backup plan in case the readings of the extensometer are not good or are disconnected for any reason.

4.4 SEM/EDX Analysis

The purpose of the SEM/EDX test is to determine the chemical composition of the surfaces of the specimens being scanned. The SEM/EDX also has the ability to measure dimensions of the bar to a high precision because of the higher magnification power it has. Concrete samples of around 1x1x0.5 in (LxWxH) were prepared after breaking each concrete pipe section to failure by cutting a concrete chunk with concrete saw (shown in Figure 56) to the dimensions mentioned above. A bolt cutter was used to cut two steel samples from steel cage of the pipes after failure at the pipe invert at the cracked zone. One specimen is cleaned to measure the actual diameter after being immersed in sodium chloride solution and the other specimen is kept as it is to find the chemical composition of the surface. Figure 57 shows a sample picture of the SEM/EDX specimens. In Figure 58 (a), the SEM machine is shown and (b) the specimens set on the stage.

Figure 56: Concrete Saw used to cut SEM/EDX specimens

Figure 57: SEM/EDX concrete and steel specimens.

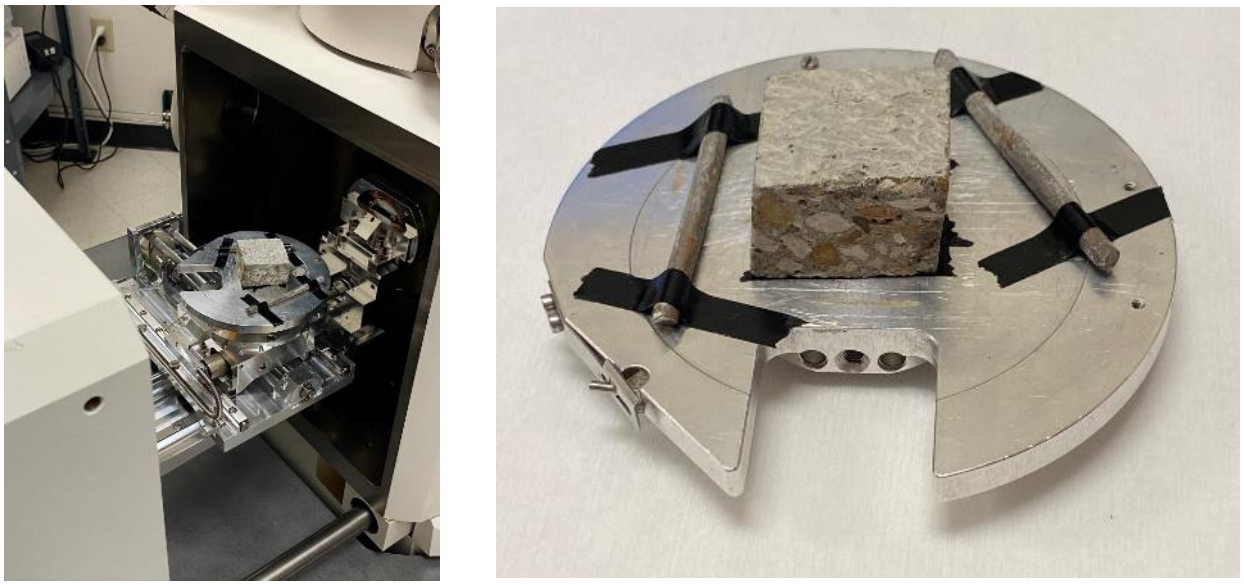

(a) (b)

Figure 58: (a) SEM machine and (b) specimens placed on the stage

4.5 Weight Loss Measurement

The corrosion is basically a portion of the steel that, when reacting with the surrounding environment chemicals, will be consumed to converted to different compounds. Therefore, the corrosion process is accompanied by weight loss of the steel. A digital electronic scale with a 300 grams capacity and a precision of 0.001 gram was used to measure the weight of the steel cages and the helical bars before and after immersion in the three different solutions of sodium chloride. The scale is shown in Figure 59.

Figure 59: Digital Electronic Scale for weight loss measurements.

Following the requirements of the ASTM G1-09 (2011), the rusted steel was power brushed to reach the clean shiny metal surface. For the control specimens from both the half steel cages and the helical bars, the preparation of the specimens was easy because the cages and the helical bars were clean and rust-free. But starting from the fourth month of immersion, the cleaning process became harder and more time consuming than before since deeper and tougher layers of corrosion were noticed.

4.6 Instrumentation

This data acquisition system (DAQ system) is used to collect the data obtained from different sensors (such as extensometer, cable-extension displacement sensor, load cell, etc.) and transfer the readings to the computer to which the data acquisition system is connected. The collected data can then be converted to either text files, excel files, etc.

The system 8000 is controlled using the “StrainSmart” software through which one can assign sensors and channels (the Ethernet ports on the back of the system 8000), calibrate all the sensors, zero the readings, record data, end the recording, export data to different file forms like Excel. Figure 60 shows the StrainSmart version 5.3 software startup page.

Figure 60: StrainSmart startup page.

A very important point to consider while using the StrainSmart and the system 8000 is that the computer must not be connected to the internet and windows firewall must be turned off otherwise the connection between the computer and the system will be interrupted.

First of all, to power the DAQ system, the power cord is plugged into the left port in the back panel of the DAQ system as shown in Figure 52 (b). Then it can be turned on by the on/off button on the right of Figure 52 (a). On the front panel of system 8000 (Figure 52 (a)), the Ethernet port is used to connect a computer to the system 8000 using a crossover Ethernet cable. A single system 8000 has a capacity to connect 8 different sensors at once through the Ethernet ports on the back (Figure

52 (b)). If the test requires the use of more than 8 sensors, two or more data acquisition systems can be connected through a network switch where the computer is connected to the switch and all the DAQ systems are connected the network switch. All the Ethernet cables in the case of multiple DAQ systems are straight through cables.

The StrainSmart software shows 7 tabs on its screen, in our tests, 4 of those tabs were used. The tabs are: Sensors, materials, Channels, Assignments, Data, Audit Trail and Notes as shown in Figure 61. The commonly four used tabs are: Sensors, Channels, Assignments and Data.

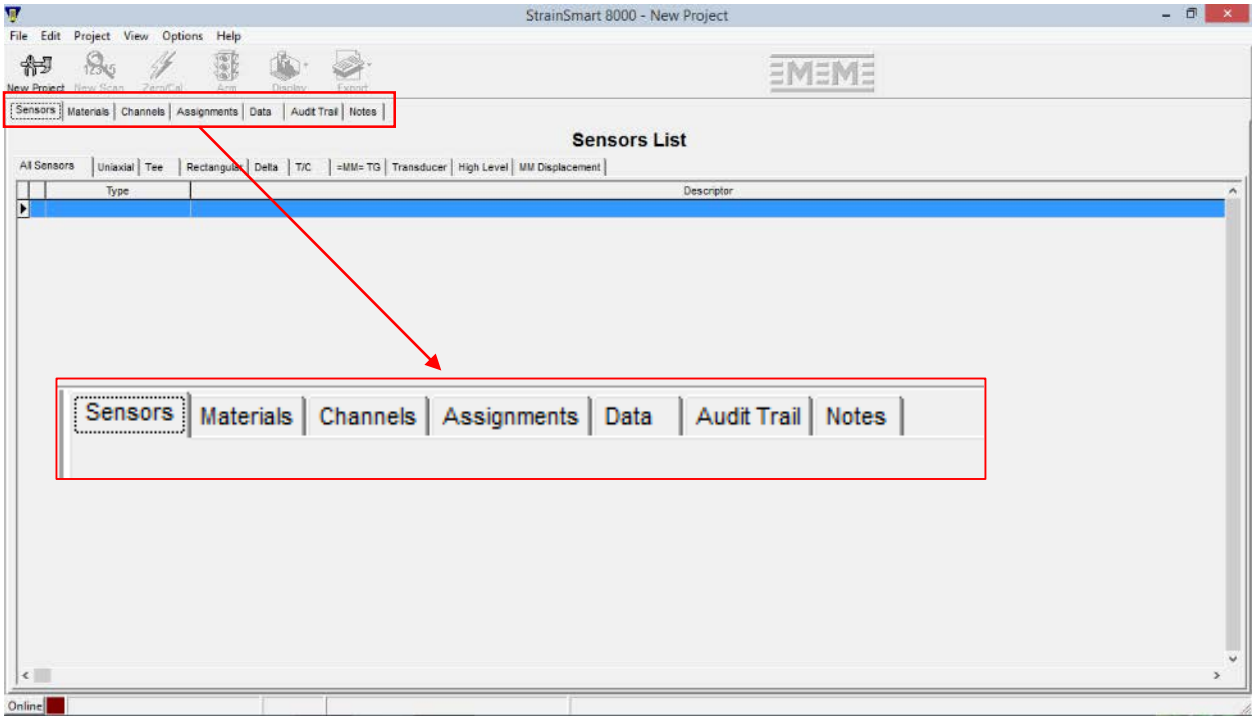

Figure 61: Main tabs on the StrainSmart scereen.

In the beginning of the setup of the test within the StrainSmart, it is important to know what type of sensors to plug to the DAQ system and know the calibration values for that sensor. Using the first tab (Sensors) will help identify all the sensors connected to the DAQ system though providing

the calibration values which are usually provided by the manufacturer. Figure 62 shows the different types of sensors the DAQ system is compatible with.

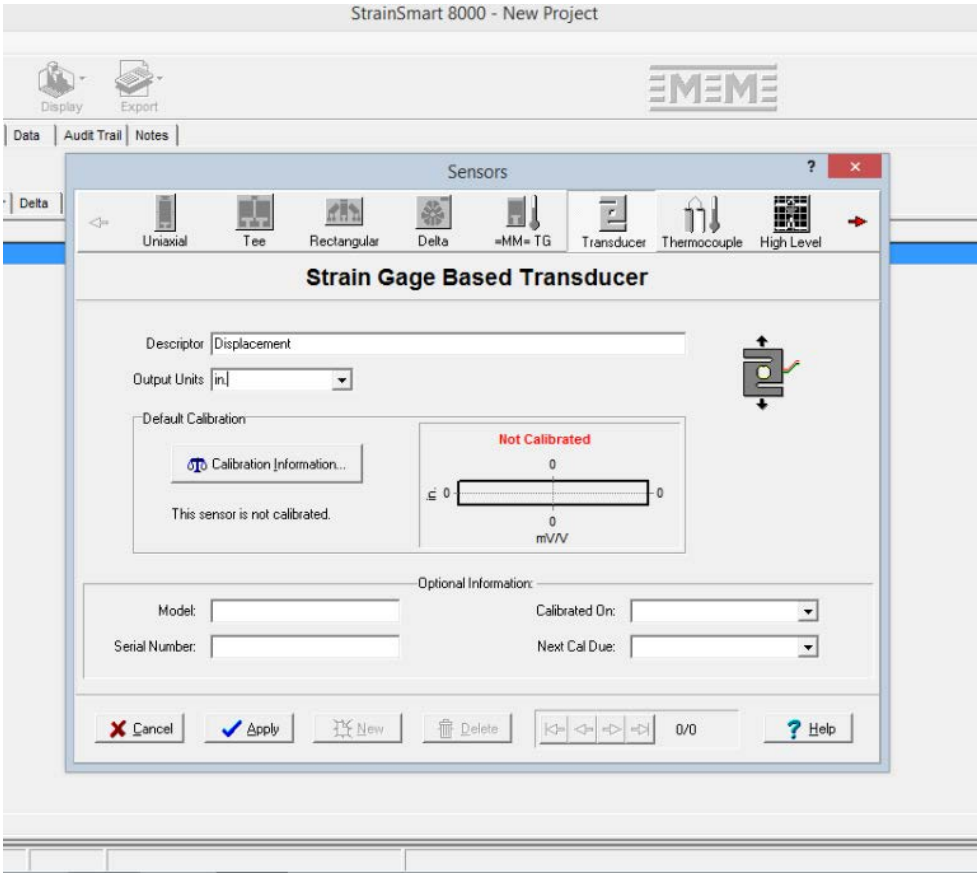

Figure 62: Types of sensors in the StrainSmart software.

In Figure 62, several types of sensors are shown. Most of the sensors used in our tests are Strain Gauge-Based Transducers. The sensor can be given a certain name in the (descriptor field) and the output units are selected. For the cable-extension displacement sensor, a name was given to it as "Displacement" and the measuring units are in inches. In the calibration sheet provided by the manufacturer, there must be some values relating the milli-volts per volts measured for 1 inch or displacement. By clicking on the (Calibration Information) button at the center of the above

picture, a new screen will appear to input the calibration data and assign it to that sensor as shown in Figure 63.

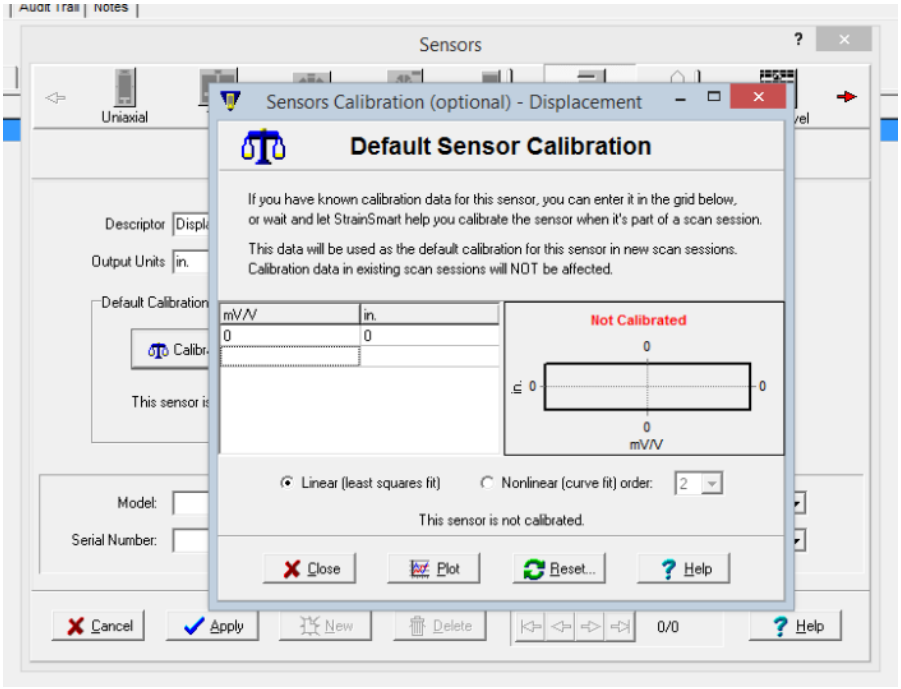

Figure 63: Calibration values input to the system.

After the calibration values are input in the above screen, the plot button is clicked to show the calibration curve and then the close button is clicked to save the calibration information to that specific sensor. Usually when the same type of sensors produced by the same manufacturer, they are expected to come with different calibration values. It is recommended to label the different sensors to know which sensor has those specific calibration data.

After the completion of the calibration data for one sensor, the calibration information for the second sensor can be added and so on until all the sensors calibration information are defined.

The back panel of the DAQ system has eight Ethernet ports to which eight different sensors can be connected. For the strain gauge-based transducers, the type (strain gauge) is selected. There are

two other types of sensors which are the thermocouple and the high-level sensors. Usually the thermocouple is used to read thermal readings which are not included in the current study. The high-level sensor was used in our tests when reading the load and displacement from the MTS machine in the tension test for the tension coupons. Therefore, for the channels tab in the StrainSmart software, each Ethernet is assigned based on the type of the sensor connected to it as shown in Figure 64. Channels are assigned by type, by highlighting the channel number and the type of the sensor associated with it.

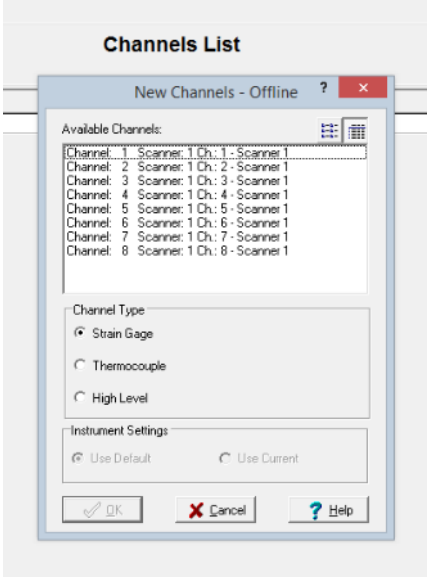

Figure 64: Assigning channels type based on the sensors.

After finishing this step, it is time to assign each sensor to a specific channel. For example, if we have four load cells, the label will help us to know which load cell (based on the calibration information) is connected to which channel after being assigned as a strain gauge, thermocouple or high-level channel.

Next, the data tab is clicked to name the test either automatically or manually. The screen below (Figure 65) shows that it is possible to select the scan rate, which is usually 10, 100, 1000 and 10000 scans per second. In all the tests performed in our research, a scan rate of 10 was used. It is also possible in this stage to select some of the sensors to take measurements as desired by the person performing the test.

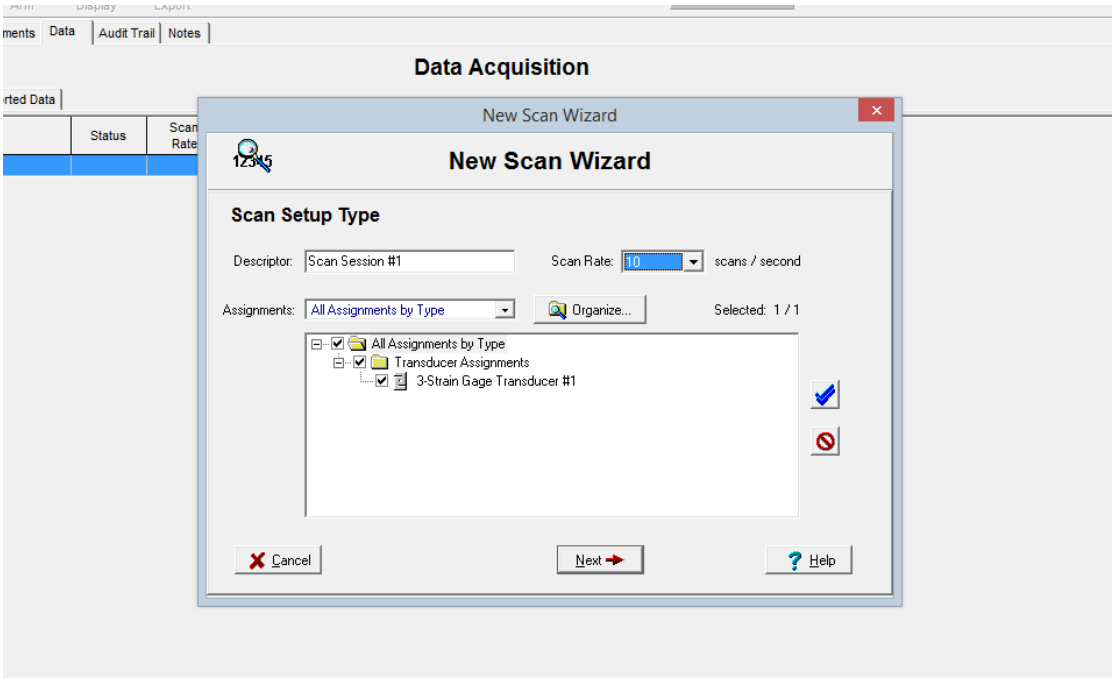

Figure 65: Data tab in StrainSmart.

Up to this point, even though the Ethernet cable is connected between the DAQ system and the computer, the actual connection is not achieved. This can be done by clicking the (online) button on the lower left corner of the software and the red color square turns into green. With all the sensors connected to the DAQ system and to the assigned points on the test specimens, the sensors must be zeroed at the stage of zero readings. This can be done by clicking the (Zero) icon above the 7 main tabs and the sensors' readings will be zeroed at this point.

The last part is to arm the test which means to start recording data from the sensors and this is done by clicking the Arm button (shaped as a traffic signal). A wizard will show, and the start button must be pressed to start recording data. At this point, it is possible to view the reading for each sensor, change the font and size, view data in charts, etc. Once the test is completed, the stop button will be pressed to stop recording and save the data to the DAQ system.

If several tests are performed in the same session, from the data tab, it is possible to define another data session and name it and do all the successive steps in the same way. Once a single test is saved, it can be exported to different type or file extension. Usually the files are exported to either text file or excel file in order to enable the user to plot graphs and read data in an easier way.

For the D-load test and as mentioned earlier, a load cell was used to record the readings of the applied load to the top of the pipe through the rigid wooden beam and the flat rubber strip. The load cell comes with the calibration values on a sticker placed on its side. Those values must be entered manually to the StrainSmart software as previously explained for the load cell configuration in order for the system to sense the change in voltage and convert it to force values.

The wiring of all the sensors is one of the most important issues to consider. The wiring diagram must be read carefully to know the polarity of each wire. The positive and negative power and signal wires must be connected to the proper pins of the Ethernet connector. For the case of the strain gauge-based sensors, the majority of the sensor come with the same wiring diagram as below:

1- Pin 1 of the connector is the positive power pin (P+)
2- Pin 2 of the connector is the negative power pin (P-)
3- Pin 3 of the connector is the negative signal pin (S-)

4- Pin 6 of the connector is the positive signal pin (S+)

Figure 66 (a) shows a close view of the back of the system 8000 where it indicates where each wire of a specific sensor goes to which pin of the connector which is shown in Figure 66 (b).

(a) (b)

Figure 66: (a) back of the system 8000 and (b) the connector used to connect different types of sensors to the back of system 8000.

For each sensor, the wires (usually come in different colors) are assigned so that the user has to be able to figure out which wire is connected to which pin.

CHAPTER 5. RESULTS

5.1 Overview

Here in this chapter, the results for the D-load, tension test, weight loss measurements, volume loss and diameter reduction will be presented for every month.

5.2 D-load Test Results

A sample of the results for the D-load tests for the pre-immersion phase is shown in Figure 67. All the pre-immersion test results are presented in Appendix A.

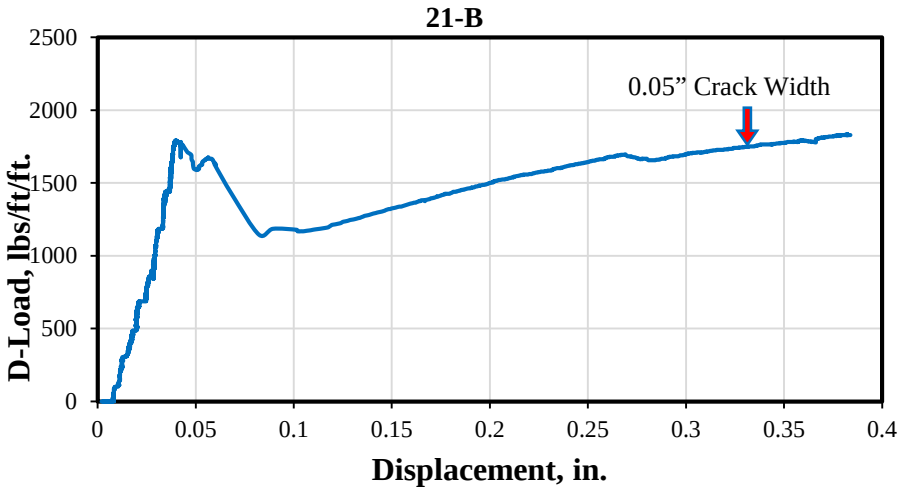

(a)

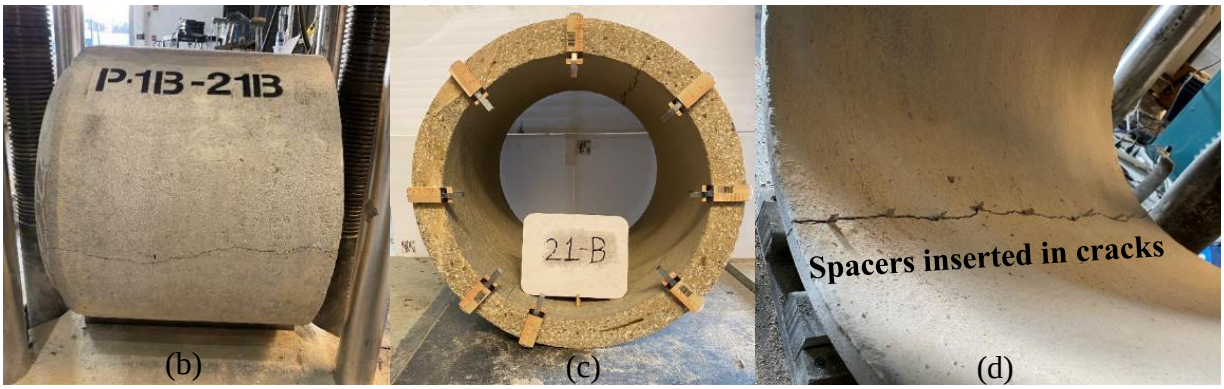

(b) (c) (d)

Figure 67: (a) D-load-displacement curve for pipe 21-B for the pre-immersion phase, (b) pipe 21-B under the test machine, (c) wall thickness measurements and (d) spacers inside the crack.

The first tests done were the D-load tests on the control specimen. Three pipes from the top sections for the 1st day of production, three pipes from the top sections for the 2nd day of production, three pipes from the bottom sections for the 1st day of production and three pipes from the top sections for the 2nd day of production were tested as control specimen. It should be noted that the loading of the control specimens must match the pre-immersion and post-immersion loading protocols in order for them to provide valid results. Therefore, the control specimens were loaded first until a crack of 0.063 inch was observed and the spacers were inserted inside the cracks. Then they were unloaded. Up to this point, this is a replica of the pre-immersion phase. The pipes were re-loaded to ultimate load and failure, which mimics the post-immersion phase of the test.

Figures 68 through 71 show the D-load test results for the top sections – 1st day, top sections – 2nd day, bottom sections – 1st day and bottom sections – 2nd day, respectively. The red and blue horizontal lines in Figures 68 through 71 represent the service and ultimate load requirements for class III - wall-B pipes as per ASTM C76 (2019), respectively.

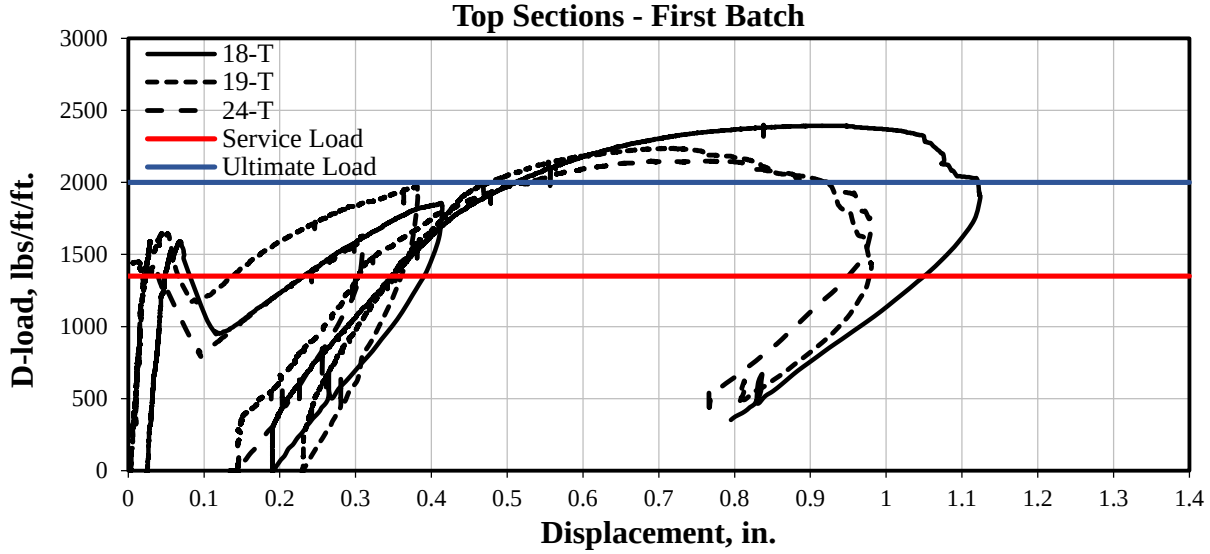

Figure 68: D-load test for the Top Sections – 1st Day of production.

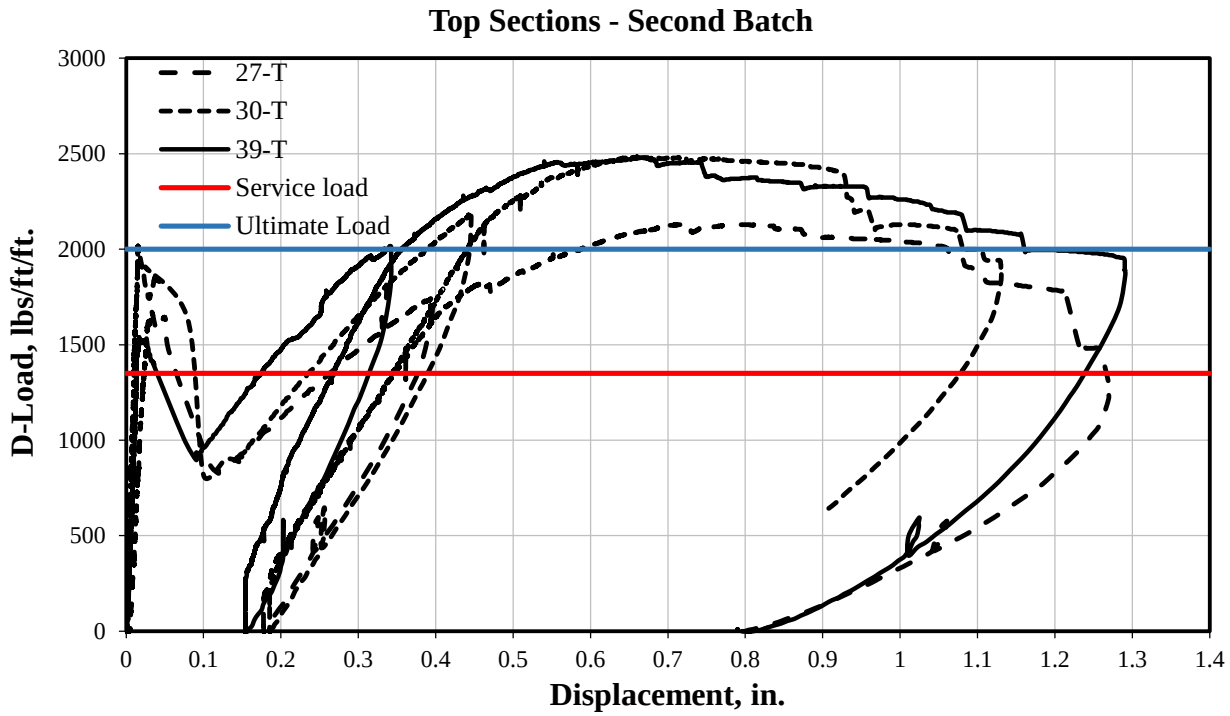

Figure 69: D-load test for the Top Sections – 2nd Day of production.

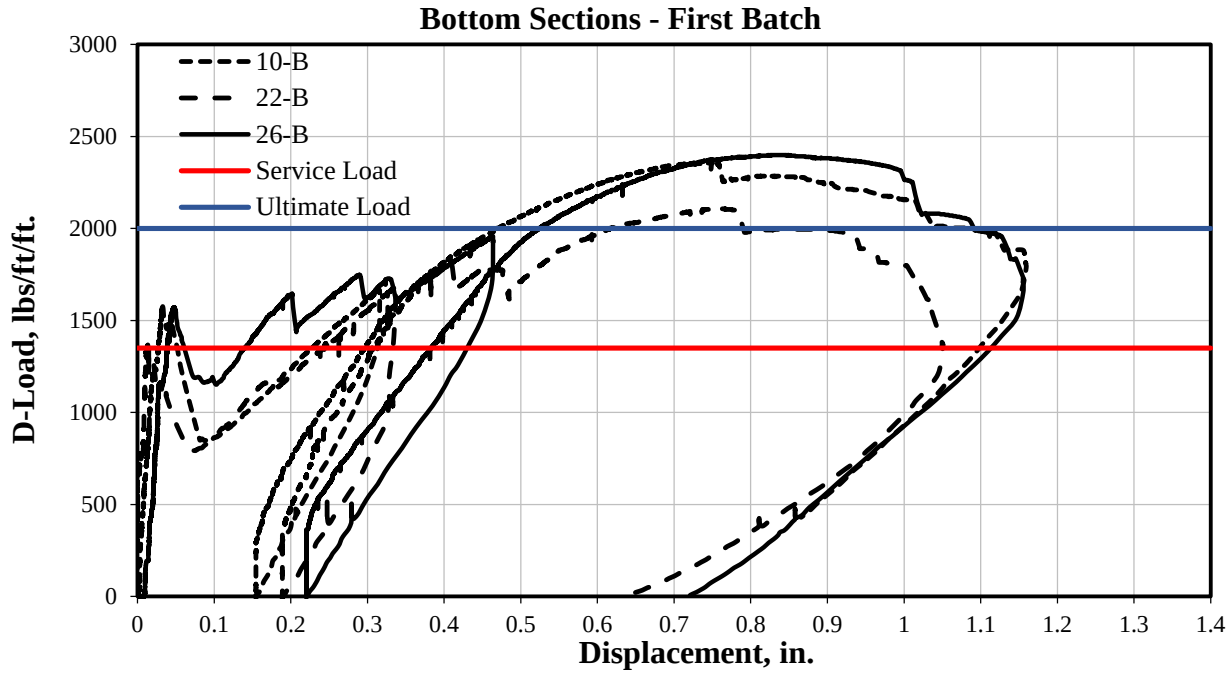

Figure 70: D-load test for the Bottom Sections – 1st Day of production.

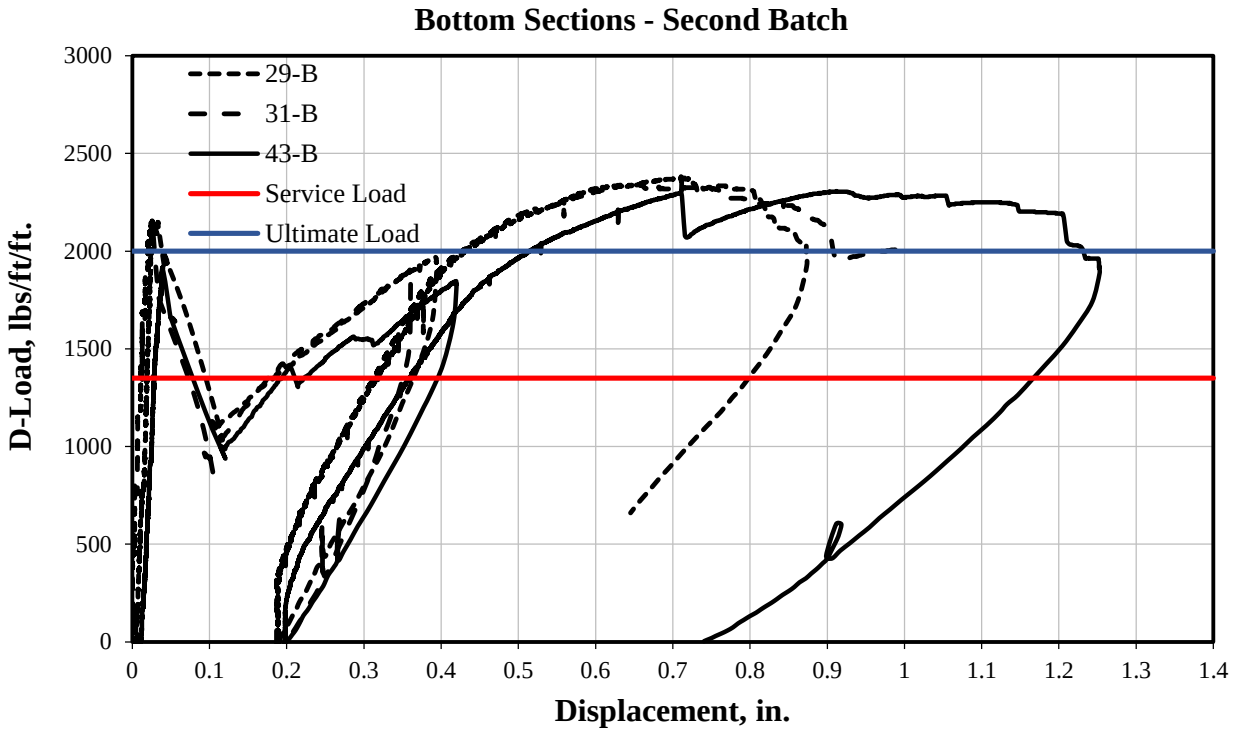

Figure 71: D-load test for the Bottom Sections – 2nd Day of production.

From Figures 68-71, the maximum load obtained from each test is ultimate load which will be the control value to which the monthly and bi-monthly test results will be compared. Using Excel, the ultimate load from each test was extracted. The ultimate loads are shown in Figures 72 and 73 for the top and bottom sections, respectively.

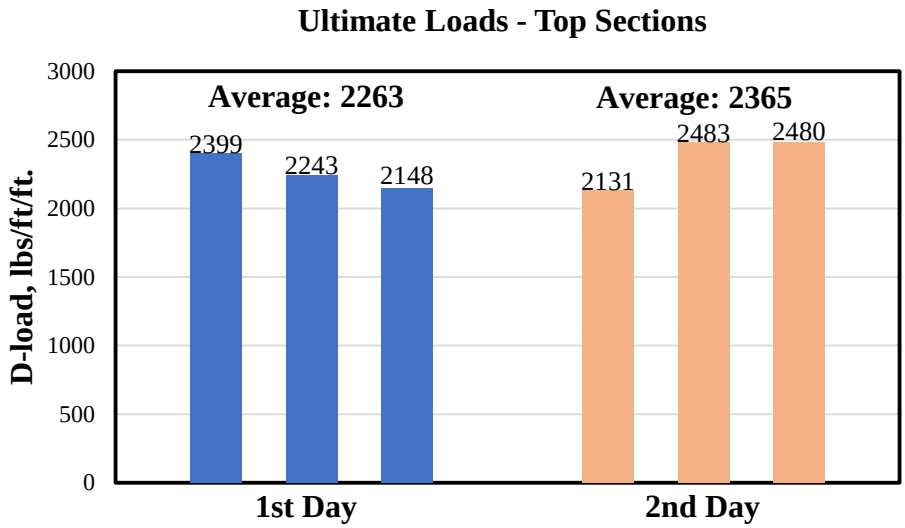

Figure 72: Ultimate loads for the top sections of the control specimens.

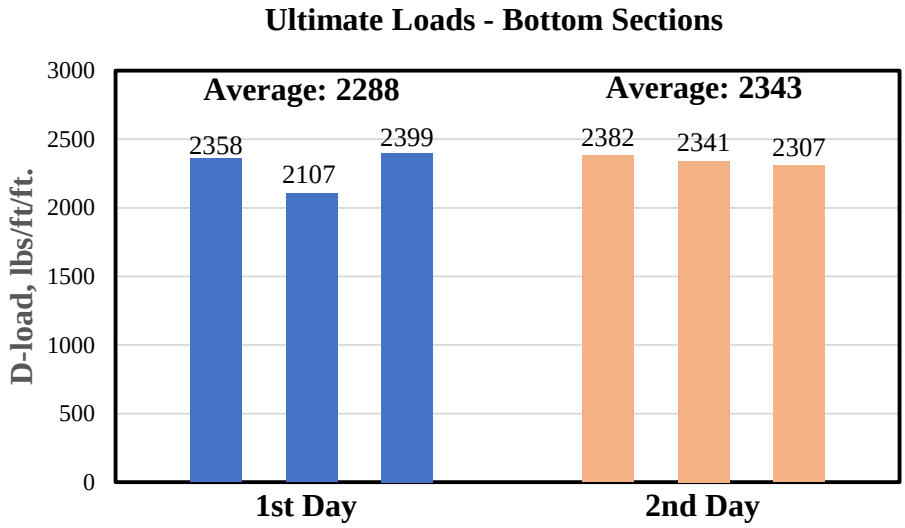

Figure 73: Ultimate loads for the top sections of the control specimens.

Figures 74 through 85 represent the post-immersion Ultimate D-load results for pipes subjected to saline environments of 200, 2000 and 30000 PPM on a monthly basis for the 30000 PPM and bi-monthly basis for the 200 and 2000 PPM.

First month test results:

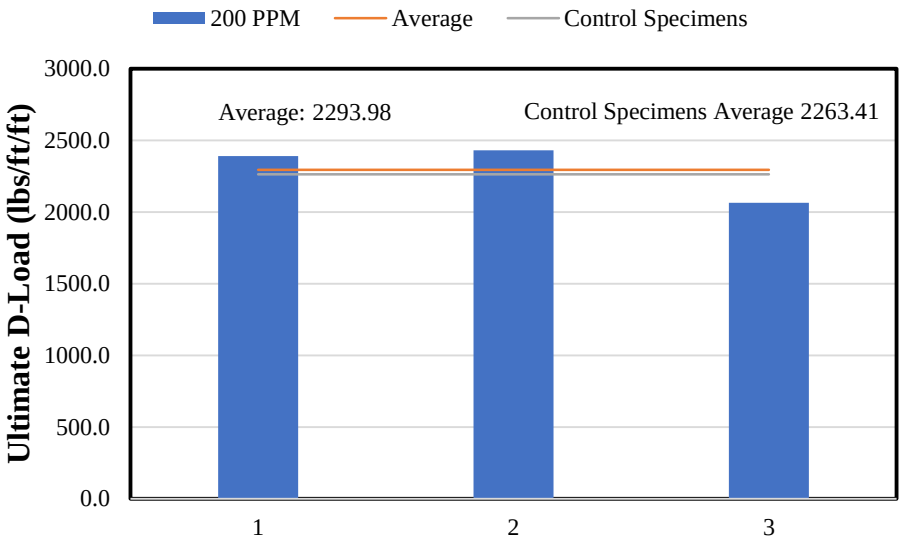

Figure 74: Post-immersion D-load test results for Month-01 for pipes 02-T, 16-T and 20-T subjected to 200 PPM Sodium Chloride Solution

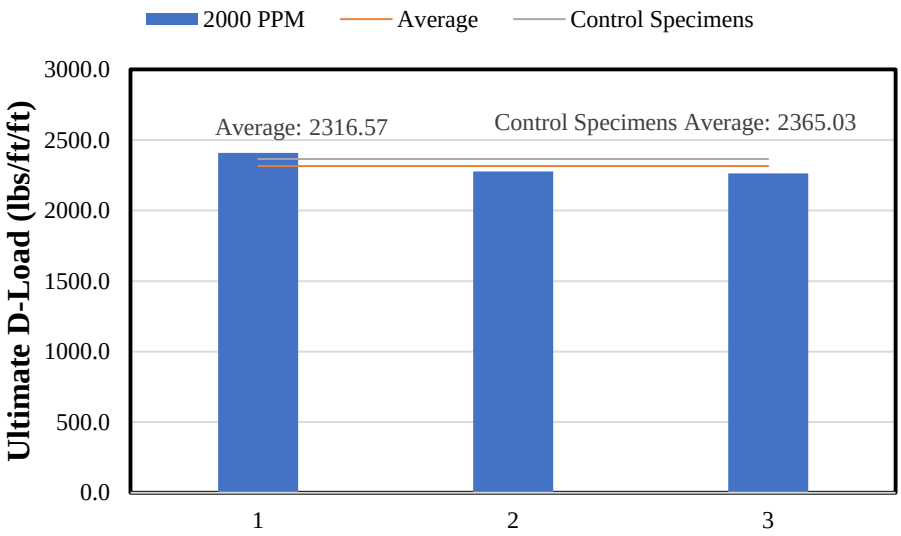

Figure 75: Post-immersion D-load test results for Month-01 for pipes 44-T, 48-T and 50-T subjected to 2,000 PPM Sodium Chloride Solution

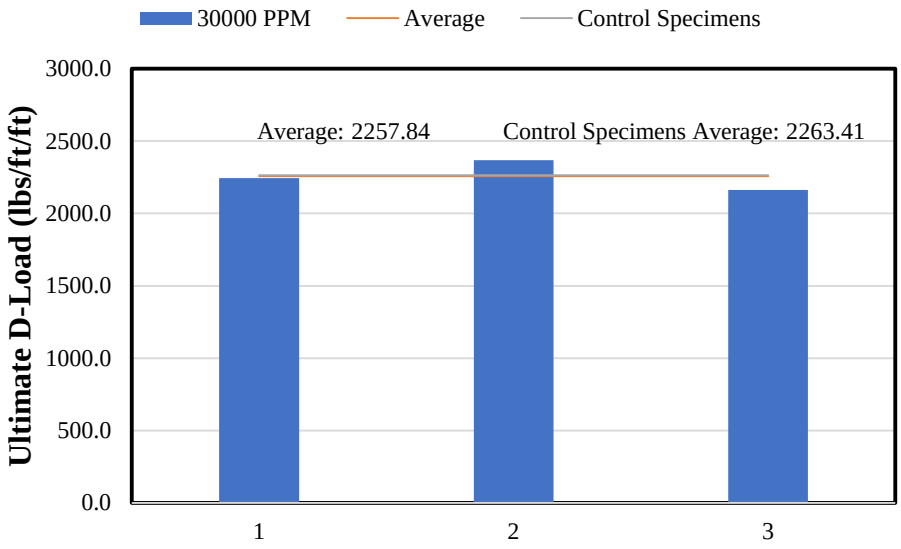

Figure 76: Post-immersion D-load test results for Month-01 for pipe 04-T, 10-T and 15-T subjected to 30,000 PPM Sodium Chloride Solution

Second month test results:

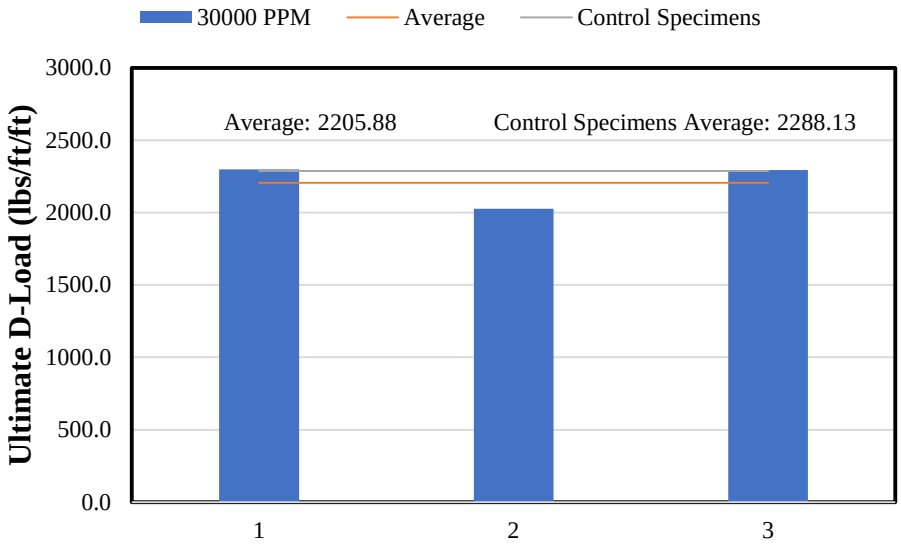

Figure 77: Post-immersion D-load test results for Month-02 for pipe 15-B, 19-B and 25-B subjected to 30,000 PPM Sodium Chloride Solution

Third month test results:

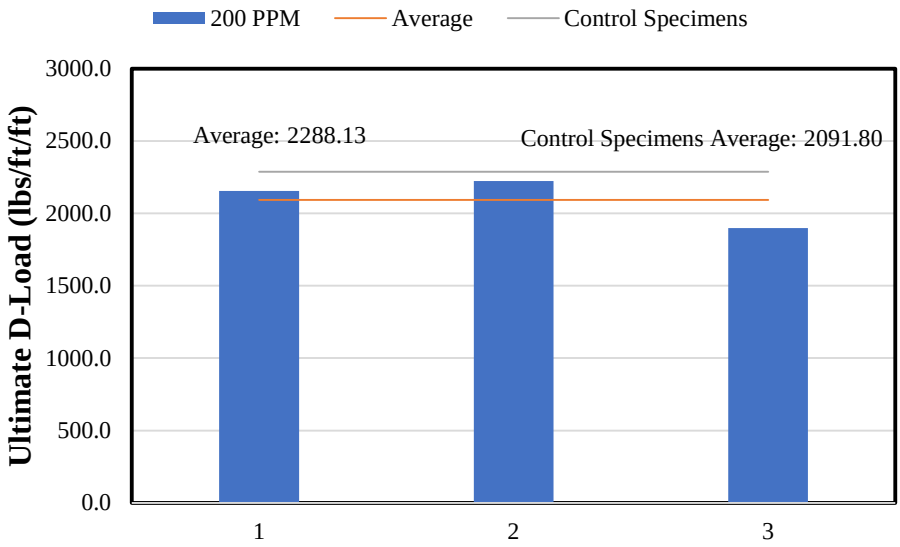

Figure 78: Post-immersion D-load test results for Month-03 for pipe 01-B, 04-B and 05-B subjected to 200 PPM Sodium Chloride Solution

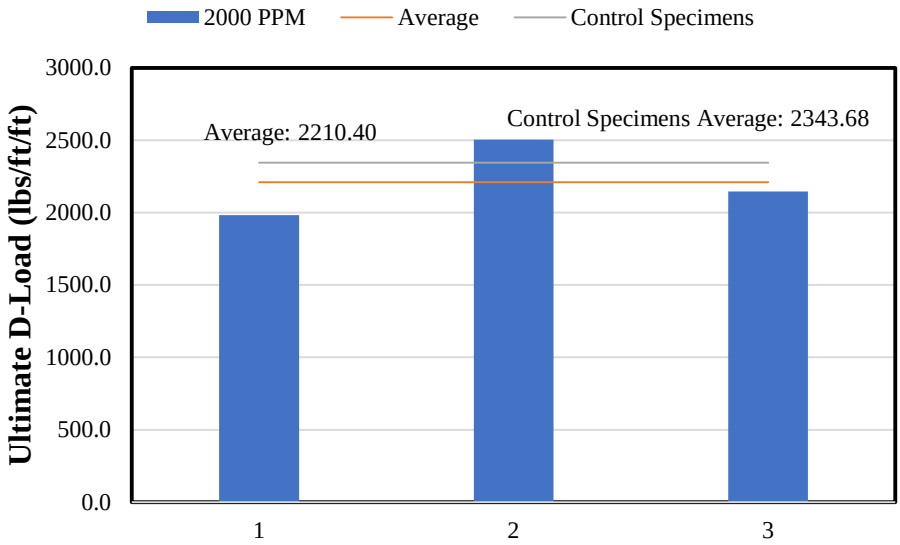

Figure 79: Post-immersion D-load test results for Month-03 for pipe 39-B, 41-B and 42-B subjected to 2,000 PPM Sodium Chloride Solution

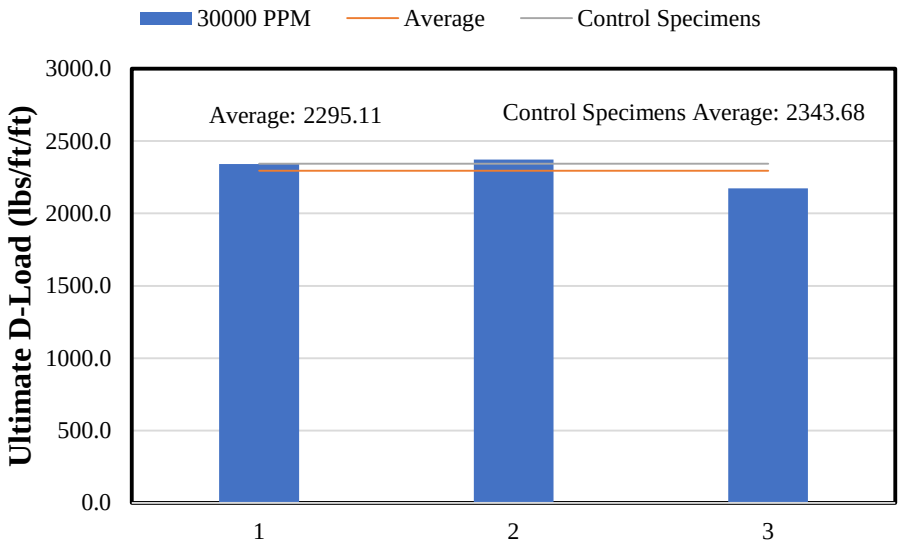

Figure 80: Post-immersion D-load test results for Month-03 for pipe 27-B, 30-B and 38-B subjected to 30,000 PPM Sodium Chloride Solution

Fourth month test results:

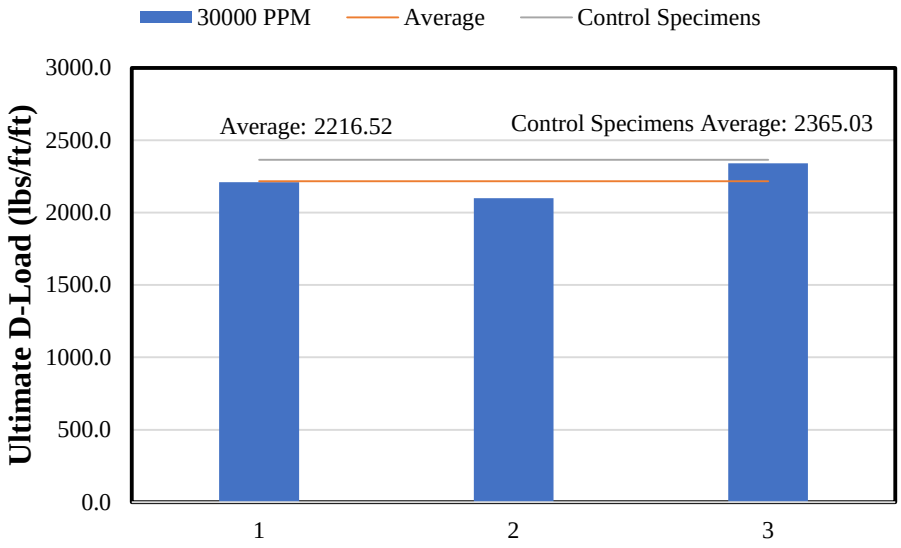

Figure 81: Post-immersion D-load test results for Month-04 for pipe 35-T, 40-T and 43-T subjected to 30,000 PPM Sodium Chloride Solution

Fifth month test results:

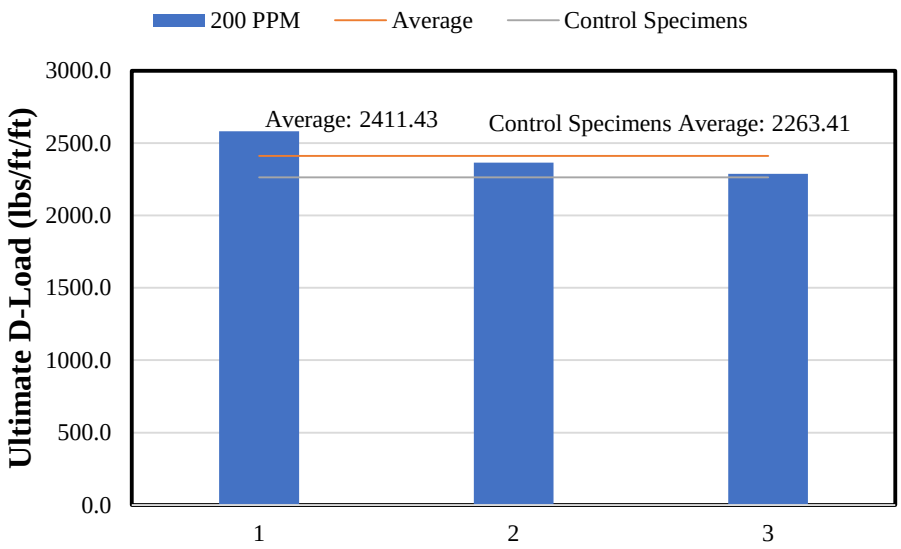

Figure 82: Post-immersion D-load test results for Month-05 for pipe 03-T, 06-T and 07-T subjected to 200 PPM Sodium Chloride Solution

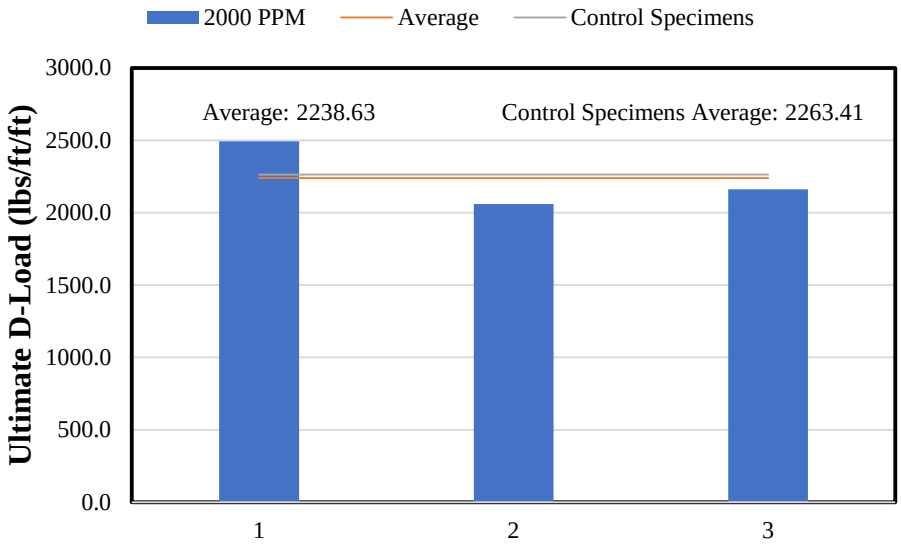

Figure 83: Post-immersion D-load test results for Month-05 for pipe 01-T, 05-T and 14-T subjected to 2,000 PPM Sodium Chloride Solution

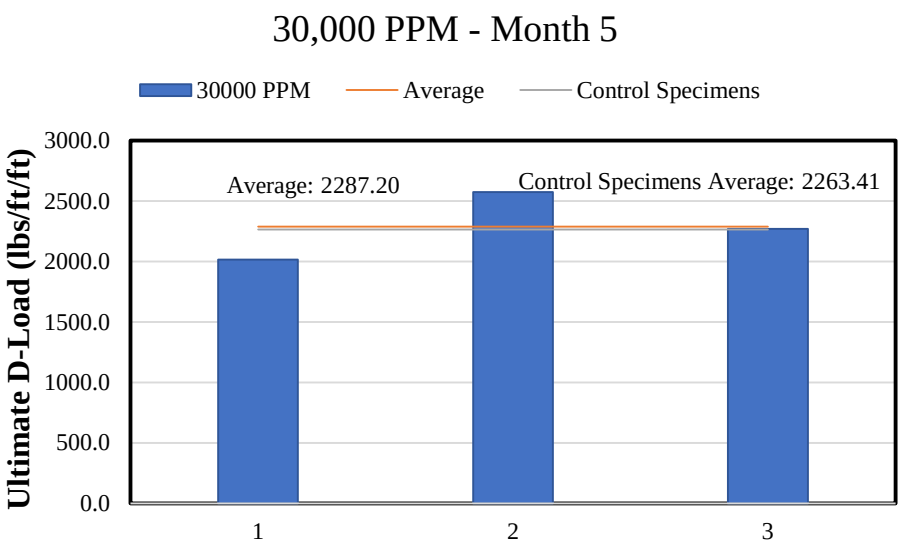

Figure 84: Post-immersion D-load test results for Month-05 for pipe 08-T, 09-T and 12-T subjected to 30,000 PPM Sodium Chloride Solution

Sixth month test results:

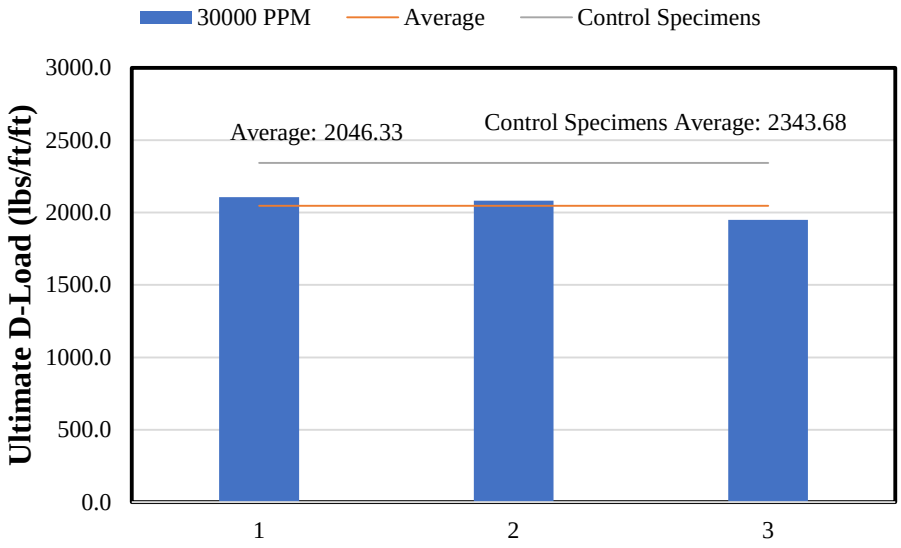

Figure 85: Post-immersion D-load test results for Month-06 for pipe 32-B, 37-B and 40-B subjected to 30,000 PPM Sodium Chloride Solution

The individual D-load – displacement curves for the post-immersion phase of this research are shown in Appendix B.

An important information can be obtained from the above charts when the averages are compared to their corresponding control specimens' averages. For example, the second month results for 30,000 PPM show ultimate loads of 2297.37, 2026.29 and 2293.98 lbs/ft/ft. The average for those three ultimate loads is 2205.88 lbs/ft/ft. Since the pipes tested in the second month are bottom sections and 1st day production, this average must be compared to the bottom section – 1st day production which is 2288 as shown in Figure 73.Therefore, the change in the ultimate load in this case will be (2205.88-2288)/2288= -3.58%. Figure 86 shows the percentage of ultimate load change for the reinforced concrete pipes subjected to 200, 2000 and 30000 PPM sodium chloride solutions.

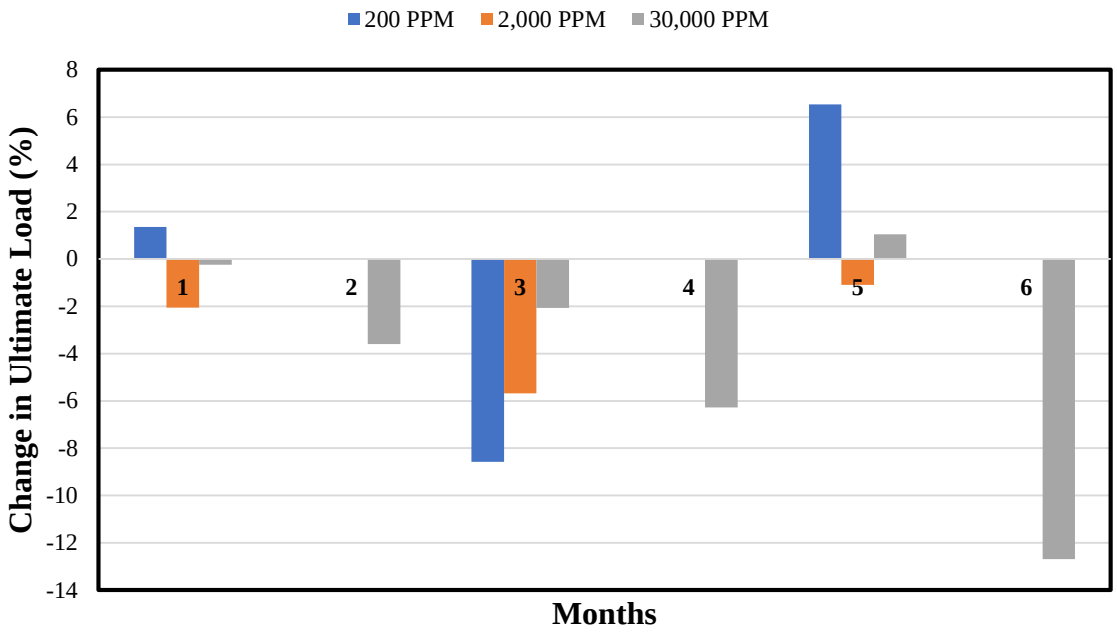

Figure 86: Ultimate load change over time for reinforced concrete pipes subjected to 200, 2000 and 30000 PPM sodium chloride solutions.

5.3 Statistical Analysis of D-load test data

According to Bonta (2015), outliers test was performed to determine whether any of the individual test data is an outlier. The outlier test was performed for both the control specimens and the actual monthly data. For the control specimens, the outlier test showed an upper and lower boundary of 2775 and 1771 lbs/ft/ft, respectively. Since all the data of the control specimens are within the upper and lower limits, there is no need to omit any data from the control specimens.

For the actual monthly test data, the outliers test showed an upper boundary of 2771 and a lower boundary of 1698 lbs/ft/ft. Since all the test data are within this range, there is also no need to omit any of the test data.

According to McLeod (2019), a t-test was run to inspect the D-load test data if they were random data or significant. The null hypothesis states that there is no relationship between the two variables we are studying. In other words, the null hypothesis is stating that data from the D-load test and the control specimens are not related to each other and the results were only obtained in a random way. The alternative hypothesis states that both set of data are significant and related to each other.

The t-test helps us to decide whether to reject the null hypothesis or fail to reject it. This decision is based on the *p*-value which is the outcome of the t-test. If the *p*-value is less than 0.05, we reject the null hypothesis and accept the alternative hypothesis. If the *p*-value is greater than 0.05, the null hypothesis is not rejected. The t-test for the D-load test data gave a *p*-value of 0.123 which means that we cannot reject the null hypothesis and that there is 12.3% chance that the results occurred by chance. Table 14 shows the t-test and the p-value obtained using Excel 2013.

Table 11: t-test and *p*-value for the D-load test data.

Month	Solution	Pipe #	D-load				
1st Month	200 PPM	2-T	2388.86			2399.02	Top Control Sections
		16-T	2429.52			2243.20	
		20-T	2063.57			2148.00	
	2000 PPM	44-T	2409.19			2480.35	
		48-T	2277.04			2131.00	
		50-T	2263.49			2483.74	
	30000 PPM	4-T	2243.16			2107.00	Bottom Control Sections
		10-T	2368.53			2358.36	
		15-T	2161.83			2399.02	
2nd Month	30000 PPM	15-B	2297.37			2341.43	
		19-B	2026.29			2382.08	
		25-B	2293.98			2307.54	
3rd Month	200 PPM	1-B	2155.06				
		4-B	2222.82				
		5-B	1897.53				
	2000 PPM	39-B	1982.24			*p* -value=	0.123258
		41-B	2504.07				
		42-B	2144.89				
	30000 PPM	27-B	2341.42				
		30-B	2371.92				
		38-B	2172.00				
4th Month	30000 PPM	35-T	2209.27				
		40-T	2100.30				
		43-T	2339.99				
5th Month	200 PPM	3-T	2582.00				
		6-T	2365.10				
		7-T	2287.20				
	2000 PPM	1-T	2493.90				
		5-T	2060.20				
		14-T	2161.80				
	30000 PPM	8-T	2016.10				
		9-T	2575.22				
		12-T	2270.26				
6th Month	30001 PPM	32-B	2107.00				
		37-B	2083.00				
		40-B	1949.00				

Of course, this is an acceptable number regarding the errors accompanying the production and testing of the reinforced concrete pipes. Among those errors:

1- Human errors

2- Test setup can lead to misalignment even though there is a lot of efforts to align everything as precisely as possible.

3- Cover measurements showed a lot of variation in the results which indicates in some cases the cover at the critical sections may be higher than it should be and the steel bars don't contribute that much to the ultimate strength of the pipe at that section.
4- Some of the pipes were showing uneven surface at the bearing area (lower side of the pipe) which may lead to additional misalignment.

The results show that there is not an actual reduction of ultimate strength over time for the pipes immersed in the 200 and the 2000 PPM sodium chloride solutions. It is more of a flocculation than it is a reduction. However, for the pipes immersed in the 30,000 PPM sodium chloride solution, there is a tendency for the ultimate load to decrease over the six months testing period.

5.4 Tensile Test

Tension or coupon tests were performed for the tension coupons using 4 specimens for each period for each sodium chloride solution. The load application (displacement control) was controlled by the Station manager software that is controlling the operation of the MTS machine. Reading of the extensometer led to get the strain readings within the 10 mm gauge length of the extensometer. Figure 87 shows the stress-strain chart for the tension coupons of the control specimens. Four control specimens were tested but during testing one of them a technical issue happened which resulted in losing all the extensometer readings while the load data were saved for that specimen.

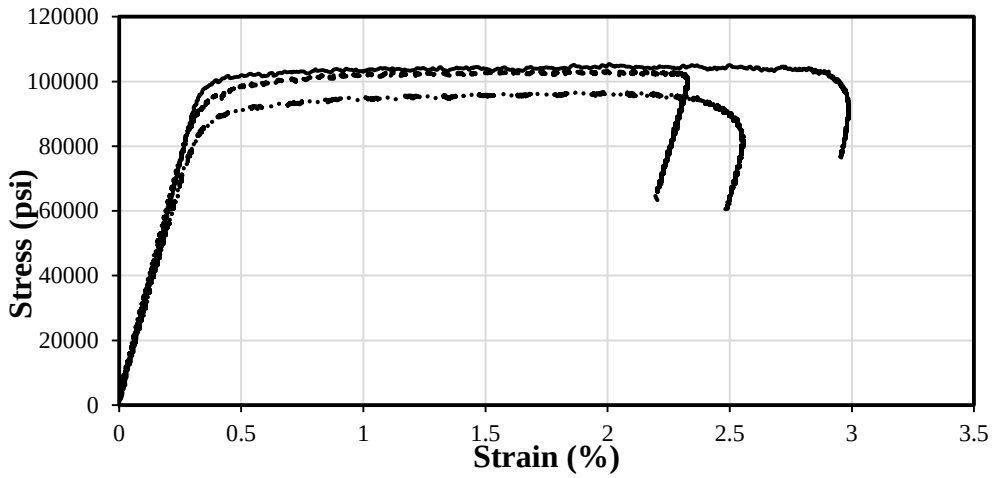

Figure 87: Stress-Strain curve for the tension coupons – control specimens.

Since all the tension coupons had a reduced section diameter of 3.00 mm as per ASTM A370 (2019) and ASTM E8/8M, (2013) comparing the stress-strain curves will not show a significant change over time because it is basically one of the material properties. Figure 88 shows the ultimate tensile loads for four control tension coupons.

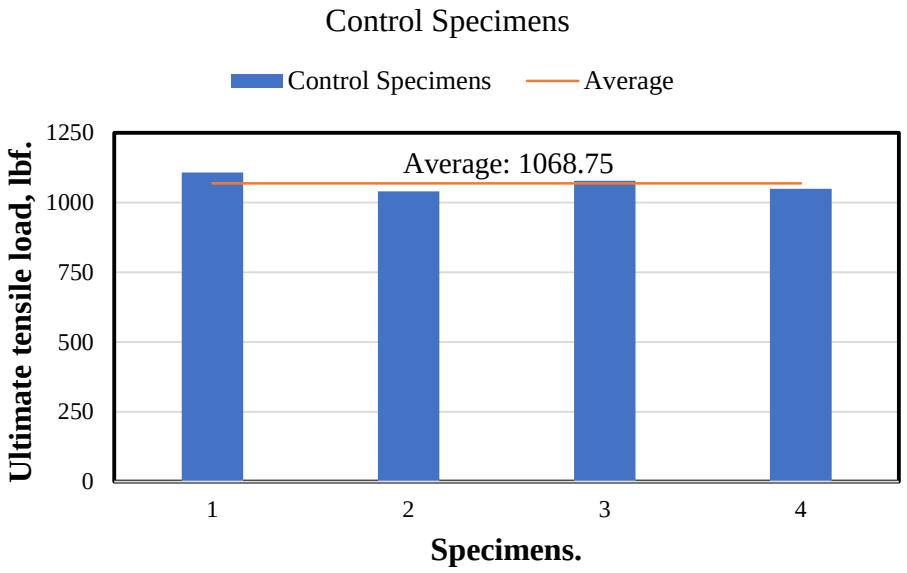

Figure 88: Ultimate tensile loads for the control tension coupons.

For the first month, the results of the tensile test are shown in Figure 89 for 200, 2000 and 30000 PPM solutions.

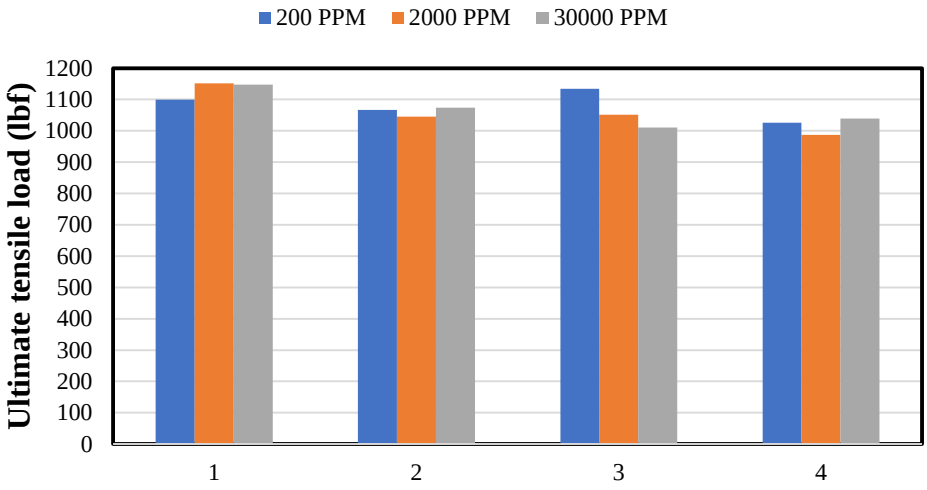

Figure 89: First month tensile test results for 200, 2000 and 30000 PPM solutions.

For the second month, only the specimens immersed in the 30000 PPM solution were tested and their results are shown in Figure 90.

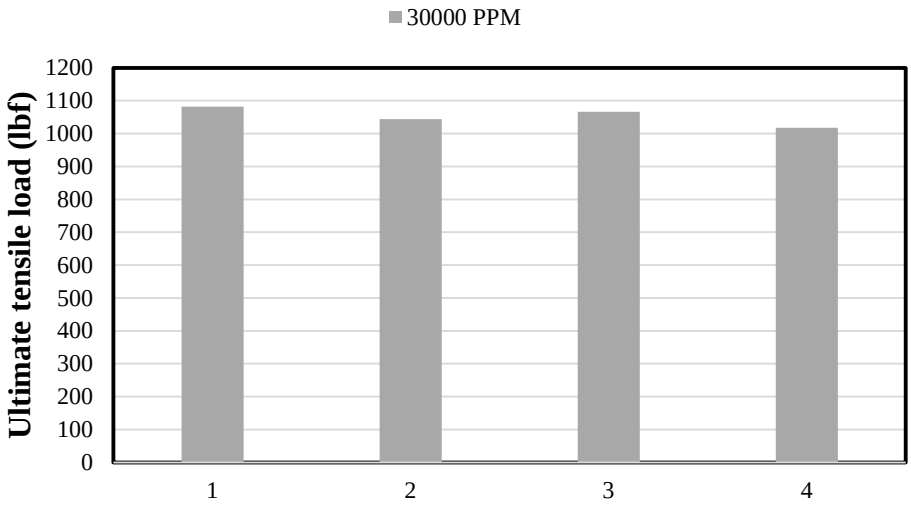

Figure 90: Second month tensile test results for 30000 PPM solution.

Figure 91 shows the tensile test results for 200, 2000 and 30000 PPM solutions for the third month.

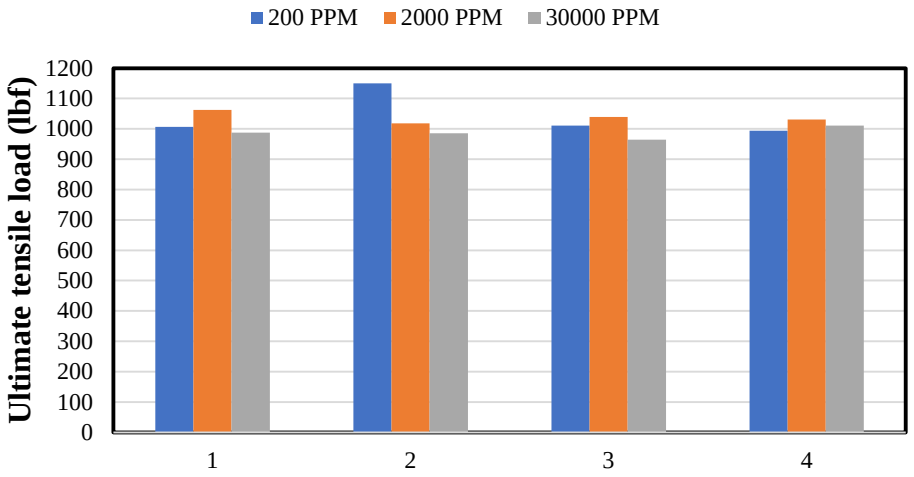

Figure 91: Third month tensile test results for 200, 2000 and 30000 PPM solutions.

The fourth month test results are shown in Figure 92 for the tension coupons immersed in the 30000 PPM solution only.

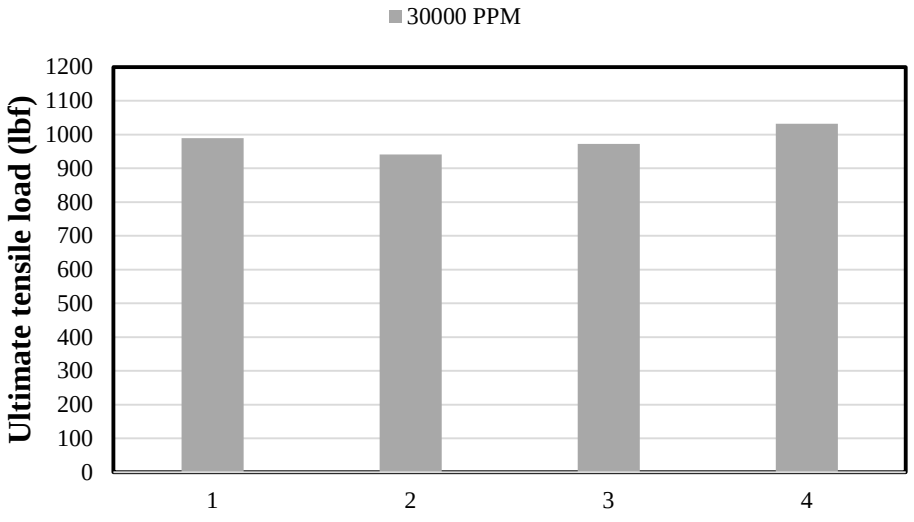

Figure 92: Fourth month tensile test results for 30000 PPM solution.

The fifth month test was performed for the tension coupons immersed in 200, 2000 and 30000 PPM solutions and their results are shown in Figure 93.

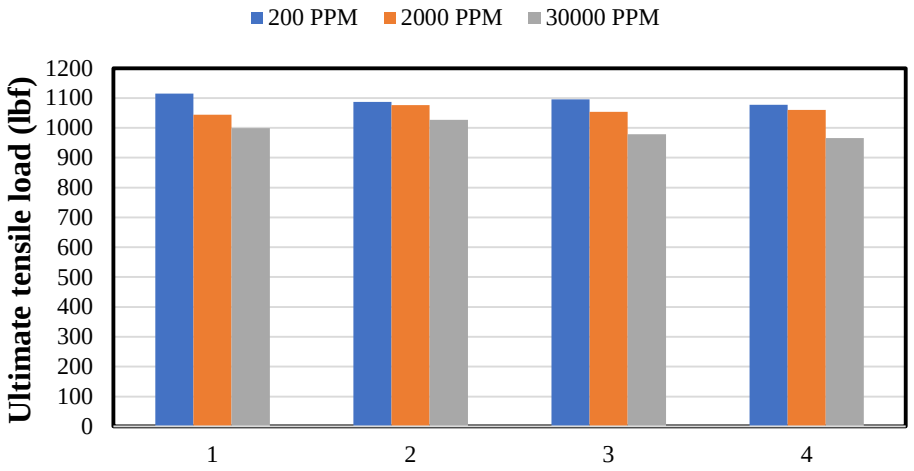

Figure 93: Fifth month tensile test results for 200, 2000 and 30000 PPM solutions.

Finally, the sixth month test results are shown in Figure 94 for tension coupons immersed in 30000 PPM solutions.

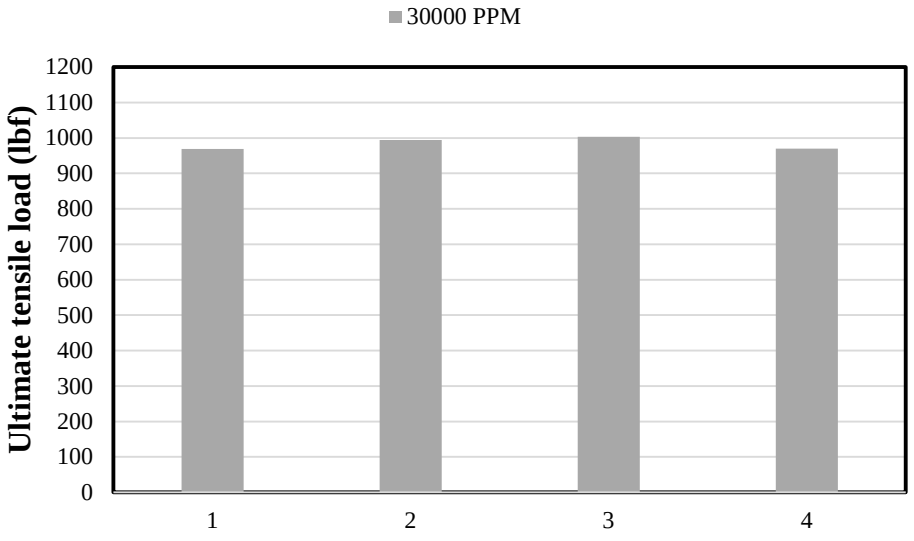

Figure 94: Sixth month tensile test results for 30000 PPM solution.

A better indication of strength loss will be obtained by comparing the average of the ultimate tensile loads each month and for each sodium chloride solution to the average of the ultimate tensile load of the control specimens. For example, for 2000 PPM, on the third month, the ultimate tensile loads for the 4 tension coupons were 1062, 1018, 1039 and 1031 lbf. The average is 1037.5 lbf. The average of the control specimens was 1069 lbf. Therefore, the percentage of change in the ultimate tensile load is (1037.5-1069)/1069= -2.94% which means 2.94% reduction in tensile load. Figure 95 shows the average ultimate tensile loads for the tension coupons subjected to 200, 2000 and 30000 PPM sodium chloride solutions for the period of six months. Figure 96 shows the percentage of change in ultimate tensile loads along a period of six months for the three sodium chloride concentrations.

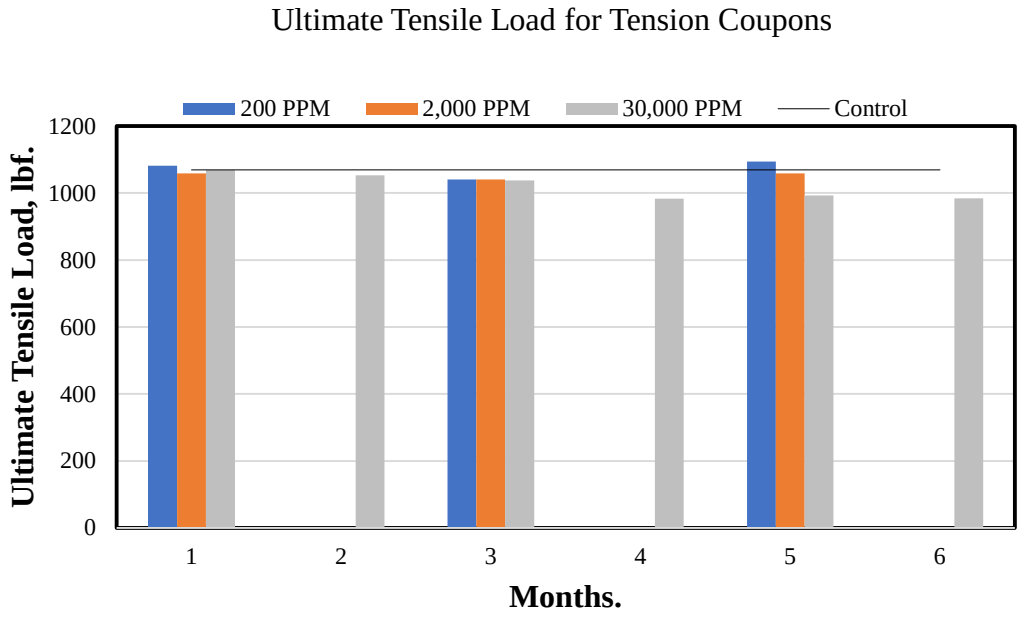

Figure 95: Ultimate tensile loads over time.

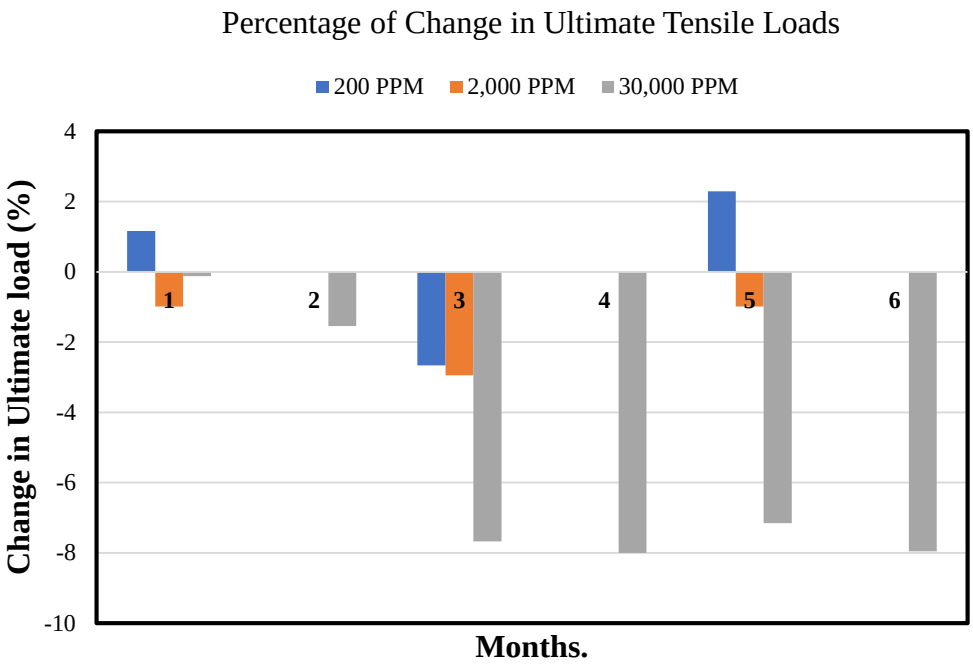

Figure 96: Change in ultimate tensile load over time.

5.5 Statistical Analysis of Tensile Test Data

Outliers test was performed to determine whether any of the individual test data is an outlier. The outlier test was performed for both the control specimens and the actual monthly test data. For the control specimens, the outlier test showed an upper and lower boundary of 1144 and 1008 lbf, respectively. Maximum and minimum control tensile loads are 1086 and 1040 lbf, respectively. Therefore, there is no need to eliminate any data from the control specimens.

For the actual monthly test data, the outliers test showed an upper boundary of 1181 and a lower boundary of 881 lbf. The maximum and minimum tensile loads are 1151and 941. Therefore, all the data is fine and no need to omit any of the test data from the actual monthly test data.

Again, t-test analysis was performed to the steel tension test data and a p-value of 0.119 was obtained using the existing formula in Excel 2013. Since we have only 4 data points for the control

specimens, the p-value was relatively high because the steel does not have that much variability and errors compared to concrete.

Similar trend to that of the D-load test data, the specimens immersed in 200 and 2,000 PPM sodium chloride solutions did not show a significant change in their ultimate tensile load while the specimens immersed in the 30,000 PPM sodium chloride solution shows an obvious decrease in strength over time until it reached around 8% in the last three months because of the highly corrosive environment in which those specimens were immersed compared to the 200 and 2,000 PPM solutions.

5.6 Weight loss measurements

3 steel half cages and 3 helical bars were cleaned (every month for the specimens immersed in the 30,000 PPM solutions and every two months for the specimens immersed in 200 and 2,000 PPM solutions) to remove the rust from them to measure how much weight of steel was lost over the months of immersion. The original weight of each specimen was already recorded and labeled on each specimen. Therefore, the change in weight which must usually show a reduction in weight due to corrosion will be equal to (weight after immersion – original weight)/original weight. It should be emphasized that all the weights are in a rust-free state. Figures 97 and 98 show the percentage of weight loss over time in helical bars and steel half cages, respectively.

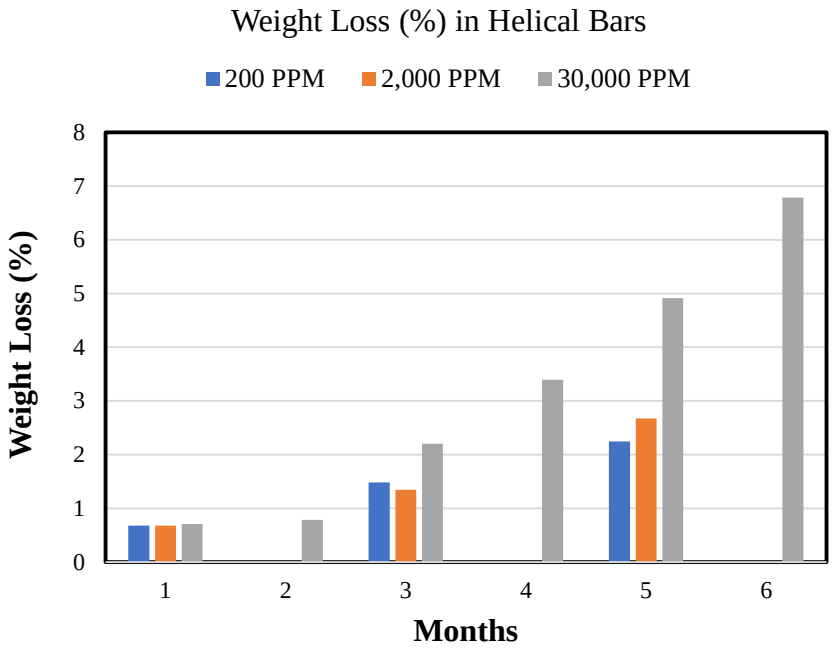

Figure 97: Percentage of weight loss in helical bars.

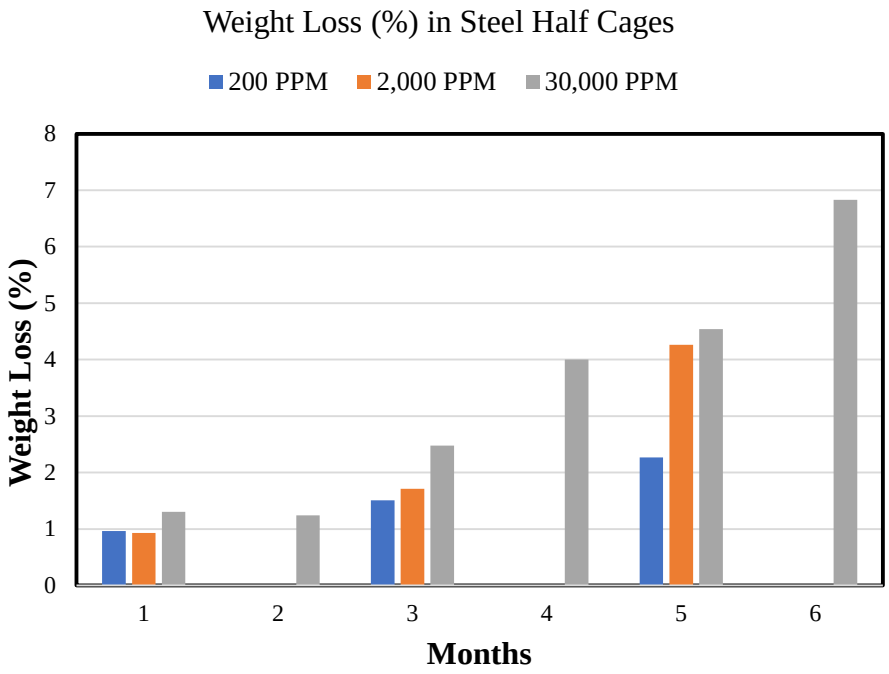

Figure 98: Percentage of weight loss in steel half cages.

A loss trend is so clear in the above charts for both the half cages and the helical bars. As mentioned earlier, because the rust is getting harder as time passes, the cleaning process shows an increased weight loss especially in the 5^{th} and 6^{th} months.

Table 12 below shows the data recorded for the fifth month for steel half cages and helical bars immersed in 30,000 sodium chloride solution as a sample of calculations of the weight loss data.

It is worth mentioning that as the immersion time increases, more corrosion is noticed, and the rust becomes harder to clean even with the use of power brush. This might also lead to extra weight loss on the latest two months because there is more effort to clean the specimens from rust and the areas surrounding the rust might be eroded more than needed which results in more weight loss than the actual conditions.

A sample picture of the steel half cages and helical bars for their conditions before and after cleaning is shown in Figure 99 The corrosion noticed in these specimens is much more than the one noticed in the specimens of the SEM taken from the broken pipes after testing them. It is clear that the concrete provides a certain level of protection to the steel bars against corrosion since it delays the infusion of the sodium chloride and the oxygen to the steel bars. The autogenous healing is also another factor that significantly reduces the ingress of oxygen to the steel bars in the cracked areas. The crack width at the outer layer is visibly open but dramatically reduced due to the autogenous healing phenomena and there is a high chance that at the steel bars level the crack is sealed, which is good in terms of corrosion protection or delay.

Figure 99: (a) helical bar before cleaning, (b) helical bar after cleaning, (c) half steel cage before cleaning and (d) half steel cage after cleaning.

Table 12: weight loss sample calculations for steel half cages and helical bars for specimens immersed in 30,000 PPM sodium chloride solution for five months.

30,000 PPM					
Helical Bars					
Sample #		Weight (g)	Weight loss (g)	% weight loss	Average % Loss
36	Original Weight	27.625	1.246	4.510407	4.914289
	After immersion + rust	27.736			
	After immersion - rust	26.379			
81	Original Weight	27.359	1.234	4.510399	
	After immersion + rust	27.124			
	After immersion - rust	26.125			
44	Original Weight	26.092	1.493	5.72206	
	After immersion + rust	26.123			
	After immersion - rust	24.599			
Steel Cages					
Sample #		Weight (g)	Weight loss (g)	% weight loss	Average % Loss
11	Original Weight	216.683	9.428	4.351057	4.537557
	After immersion + rust	216.718			
	After immersion - rust	207.255			
63	Original Weight	218.597	10.165	4.65011	
	After immersion + rust	219.07			
	After immersion - rust	208.432			
27	Original Weight	214.16	9.876	4.611505	
	After immersion + rust	213.498			
	After immersion - rust	204.284			

5.7 Volume and Diameter Reduction

Volume reduction is related to the diameter change in the reduced section of the tension coupons. The diameter reduction is converted to volume loss with the assumption of uniform loss because

all the tension coupons are exposed to the same solution and are under the same conditions of wet/dry cycles. Since the loss is considered on the surface area and the losses on the cross-sectional area is not considered, it will be easier to consider a unit length of the reduced section and consider the volume loss. Therefore, the new volume is subtracted from the original volume and then divided by the original volume. Similarly, the diameter loss is the new diameter subtracted from the original diameter and the result is divided by the original diameter. Figures 100 and 101 show the volume and diameter loss over time.

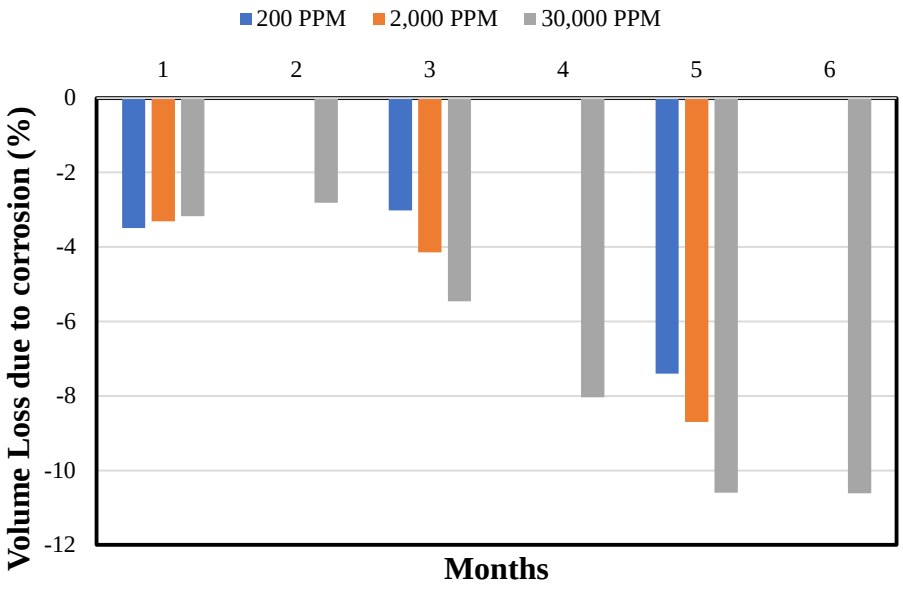

Figure 100: Volume loss in steel over time.

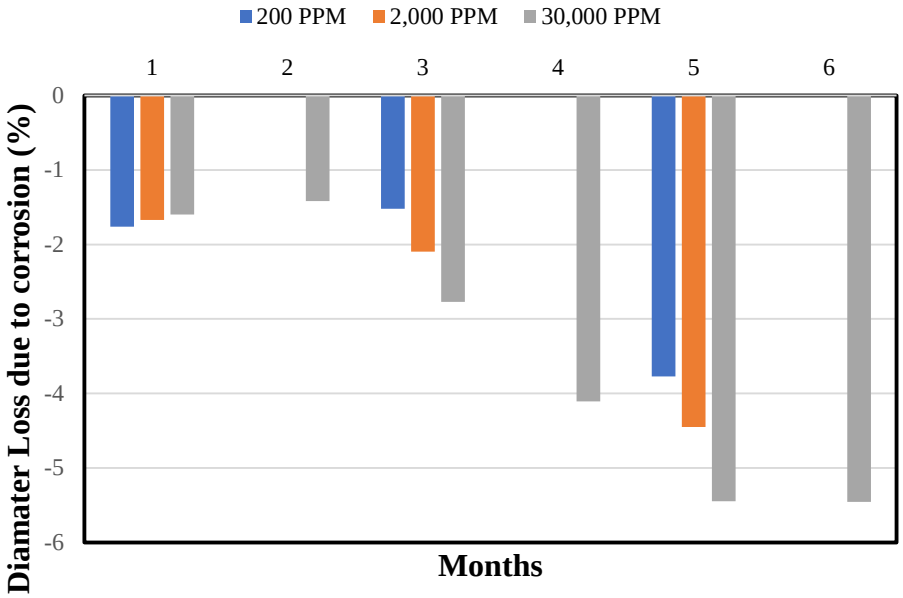

Figure 101: Diameter loss in steel over time.

From the specimens used for SEM analysis, another chart for diameter loss is shown in Figure 102. Results are totally different because of the protection provided to the steel specimens by concrete and the autogenous healing phenomena.

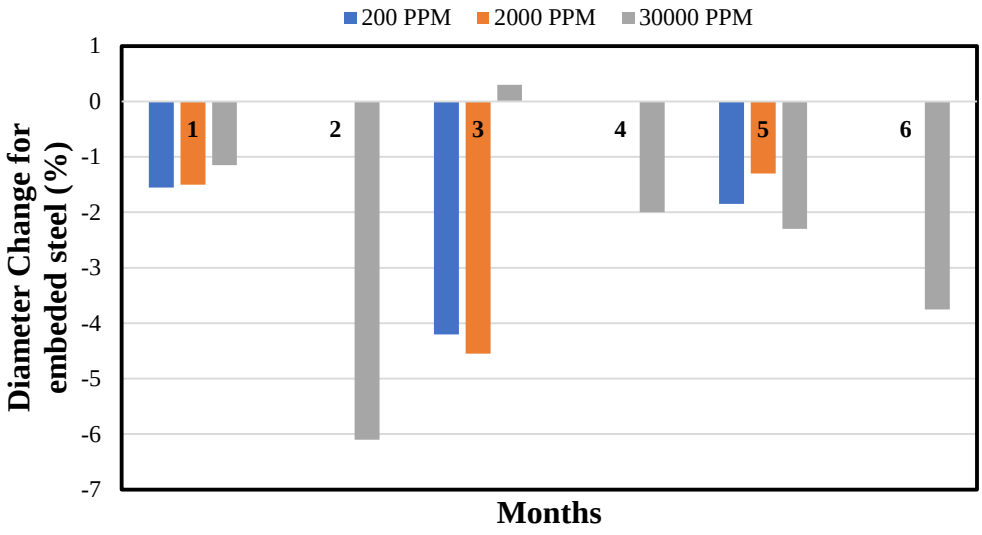

Figure 102: Diameter reduction in embedded steel specimens using SEM.

A significant decrease in volume is noticed in the last two months. The reason is because of the tougher rust in the last two months that required more cleaning and accordingly resulted in more material loss. Also, it is logical to expect that the corrosion effects will increase as immersion time increases with the help of the wet/dry cycles action.

5.8 SEM/EDX results

Figure 103 show the surface condition of helical steel bars (as control specimens) at different magnification levels. One of the results the user can get from the SEM machine is the dimension as the software controlling the machine has the ability to show two straight lines and measure the distance between them to a very high precision because of the powerful magnification. Figure 104 show the diameter measurements for two helical steel specimens.

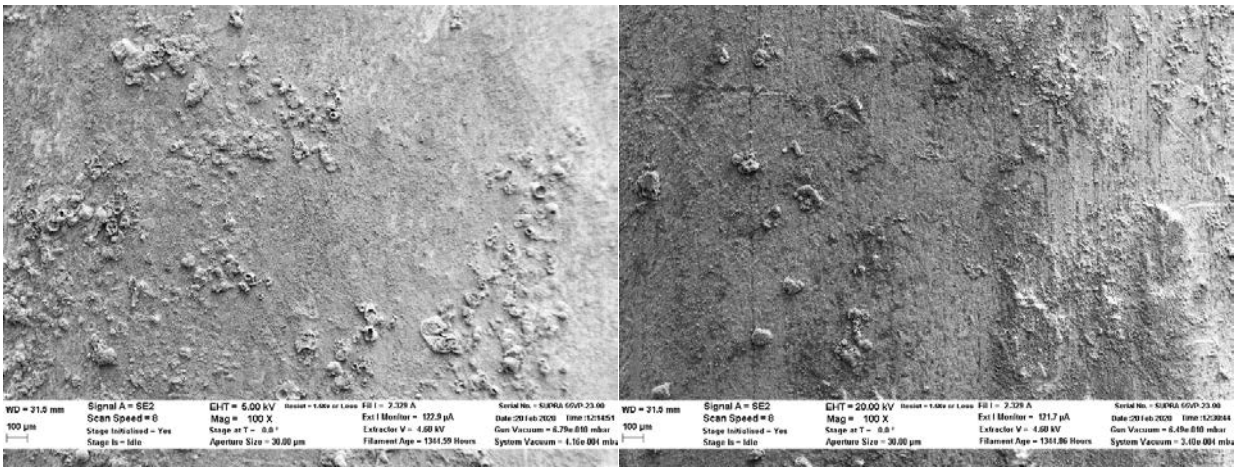

(a) (b)

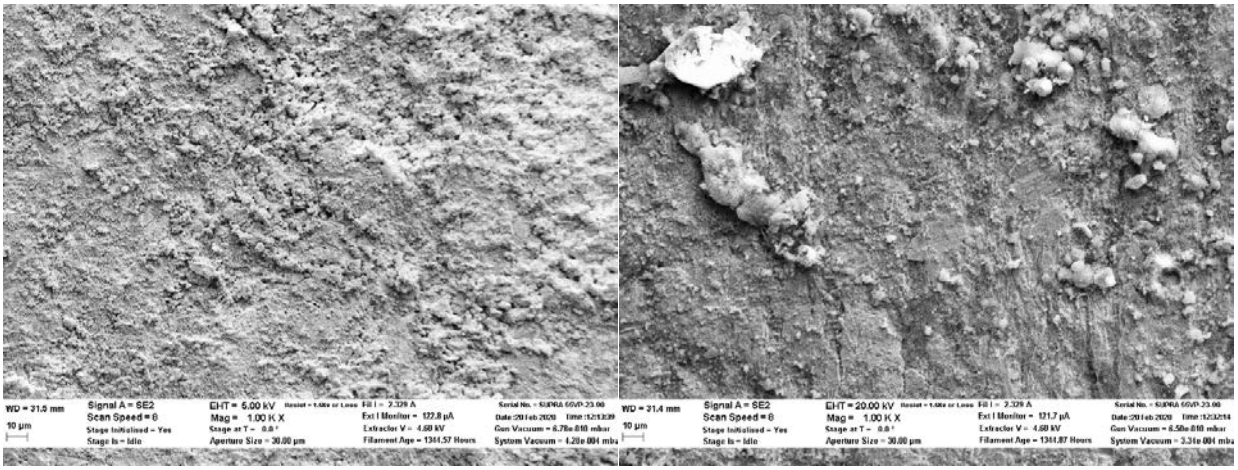

(c) (d)

Figure 103: Control Specimens (a) specimen 1 under 100x (b) specimen 2 under 100x (c) specimen 1 under 1000x and (d) specimen 2 under 1000x magnification power.

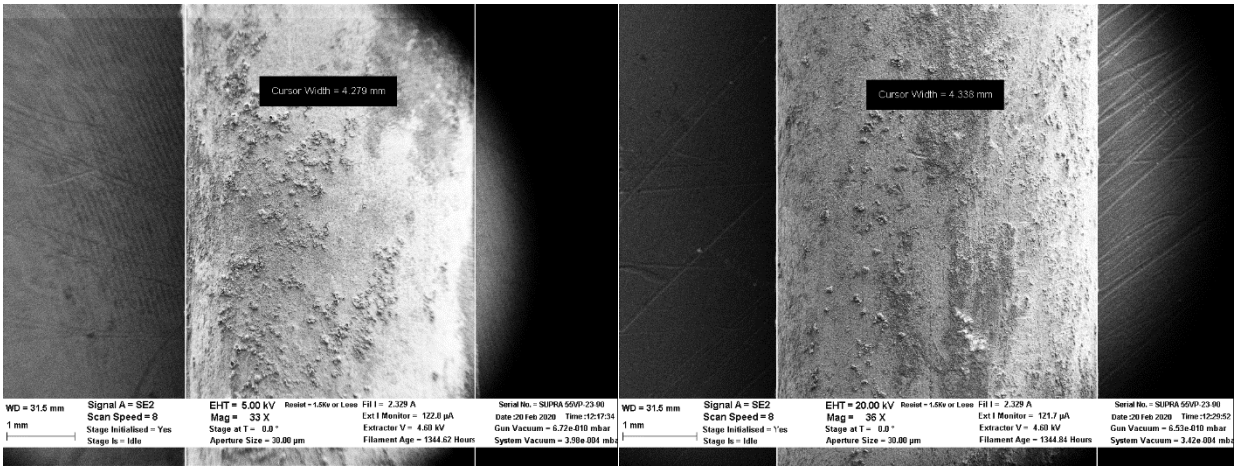

Figure 104: Average diameter of two control steel specimens is 4.308 mm.

Table 13 shows the normalized mass and the elemental analysis of the steel bars surface using SEM technique.

Table 13: Normalized mass of the elements scanned on the steel bars.

Element	Mass	Mass Norm. (%)	Atom. Mass (%)
Iron	42.35	41.26	16.99
Oxygen	30.43	29.64	42.61
Carbon	17.75	17.3	33.12
Calcium	10.08	9.82	5.64
Silicon	1.5	1.46	1.19
Aluminum	0.53	0.52	0.44
	102.65	100	100

The reason for showing the oxygen data in a different color is because this is the element that plays the most important role in the corrosion process. All the monthly scans will measure the oxygen level and compare it to the above value.

The magnified pictures and results of scanning the concrete control specimens are shown in Figures 105 and Table 14, respectively.

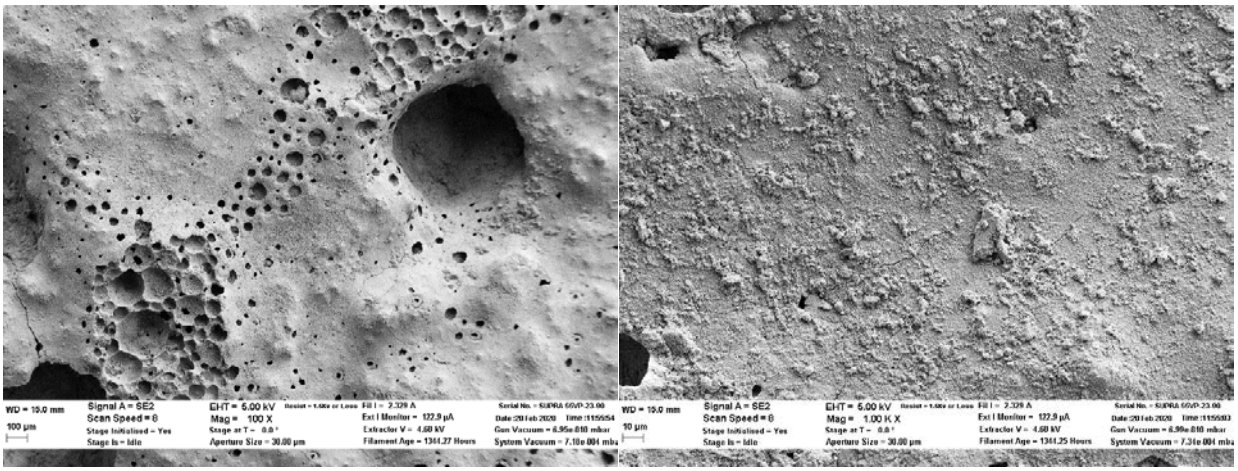

(a) (b)

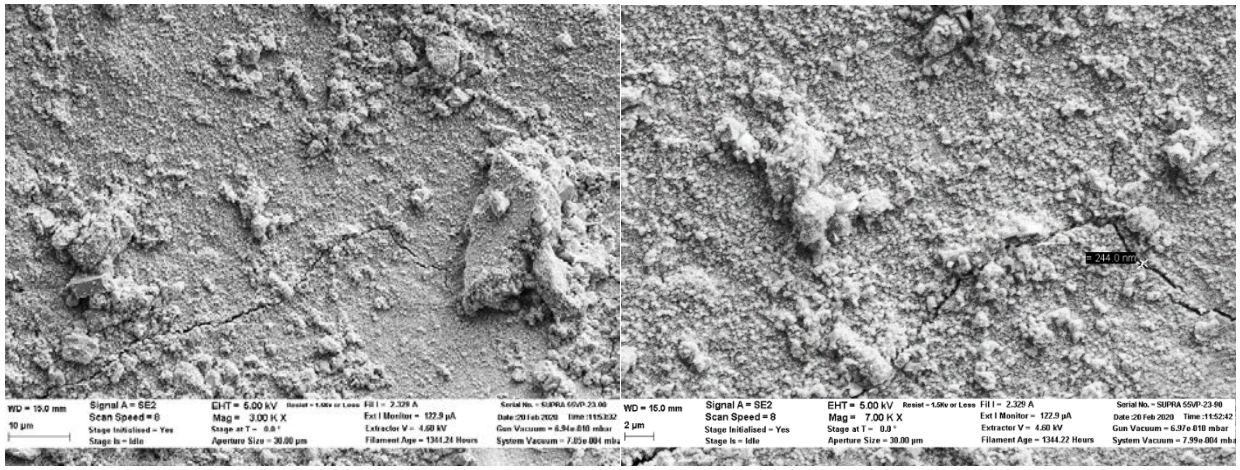

(c) (d)

Figure 105: Concrete surface with (a) 100x (b) 1000x (c) 3000x and (d) 7000x.

Table 14: Elemental Analysis of concrete control specimens.

Element	Mass	Mass Norm. (%)	Atom. Mass (%)
Oxygen	55.57	50.36	61.74
Calcium	38.59	34.97	17.11
Carbon	12.83	11.62	18.98
Silicon	3.11	2.82	1.97
Sodium	0.26	0.23	0.2
	110.35	100	100

For one-month data, diameter changes of -1.56%, -1.53% and 1.149% was noticed for specimens immersed in 200, 2000 and 30000 PPM, respectively as shown in Figures 106, 107 and 108.

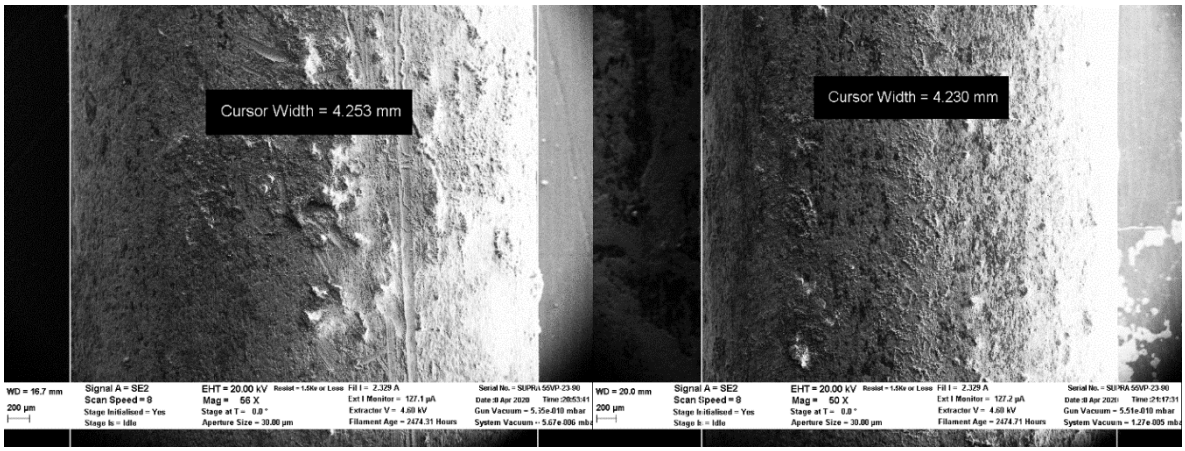

Figure 106: Diameter change for 200 PPM specimens for the first month

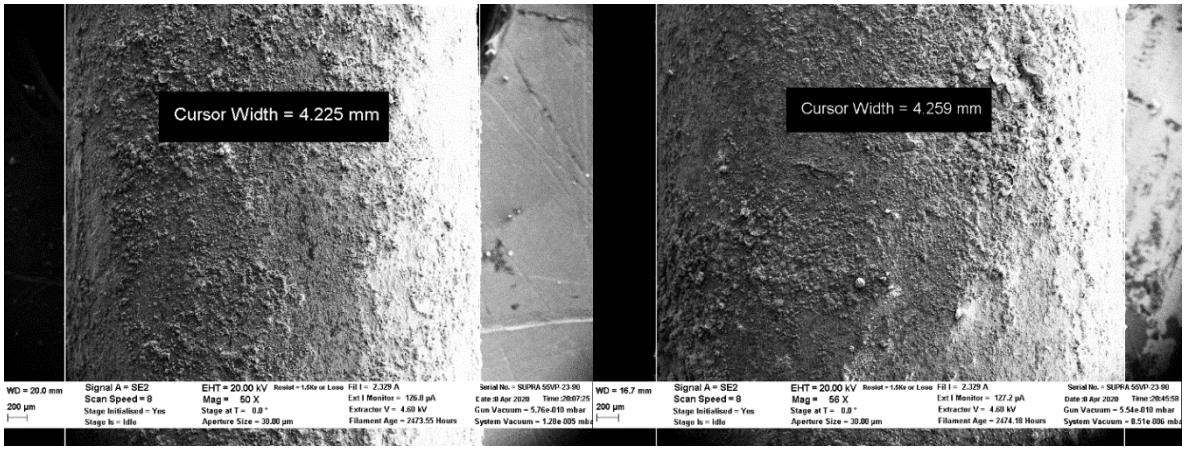

Figure 107: Diameter change for 2,000 PPM specimens for the first month

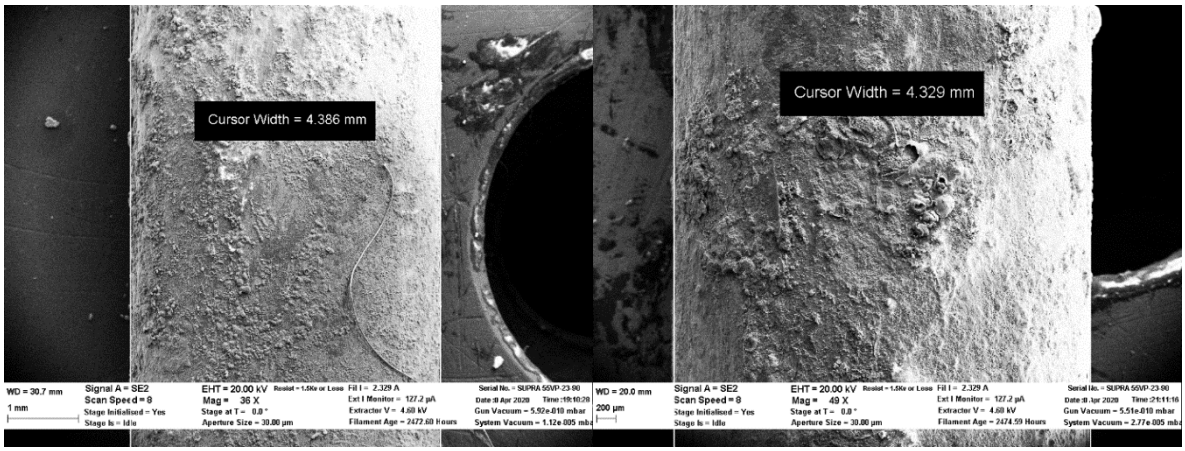

Figure 108: Diameter change for 30,000 PPM specimens for the first month

The pictures for the diameter measurements using the SEM technique are shown in Appendix C.

Figure 109 shows the normalized mass of oxygen along the six months testing period as an indication of corrosion intensity on the surface of the scanned steel specimens immersed in the three different solutions.

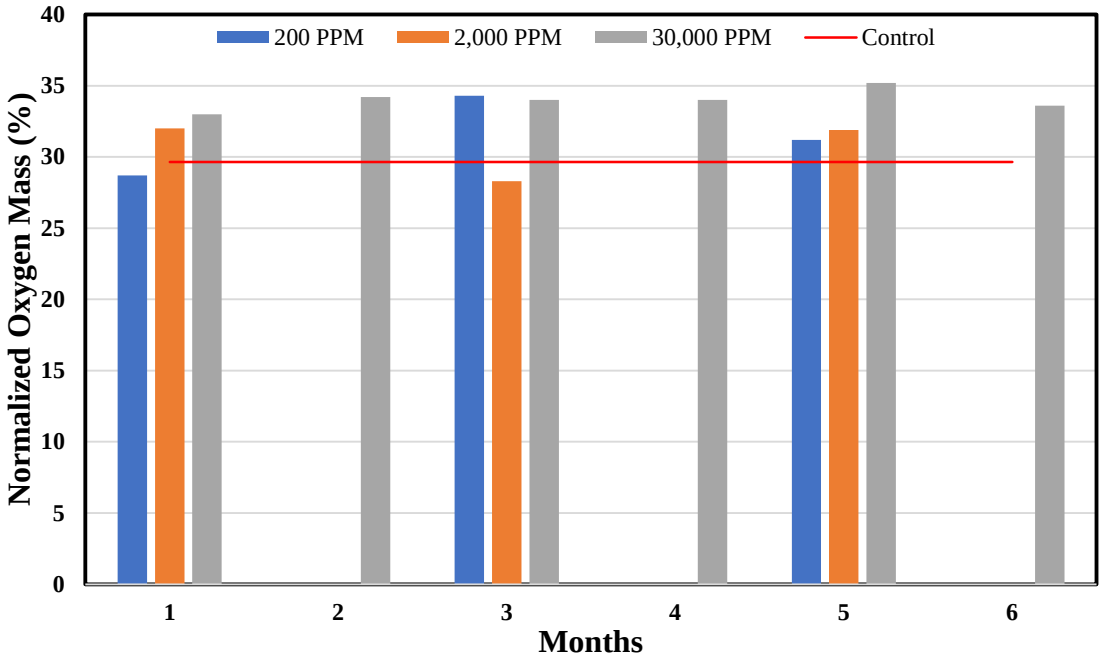

Figure 109: Normalized oxygen mass for six months testing period extracted from steel specimens immersed in 200, 2000 and 30000 PPM solutions.

As shown in Figure 109, the level of oxygen is not showing a major change as these samples are extracted from the concrete pipes. So, this confirms that the concrete provides a certain level of protection against corrosion even when it was cracked at certain locations.

In Figures 110 and 111, the shape of iron oxide crystals on the scanned steel specimens using a magnification power of 3000 and 5000, respectively.

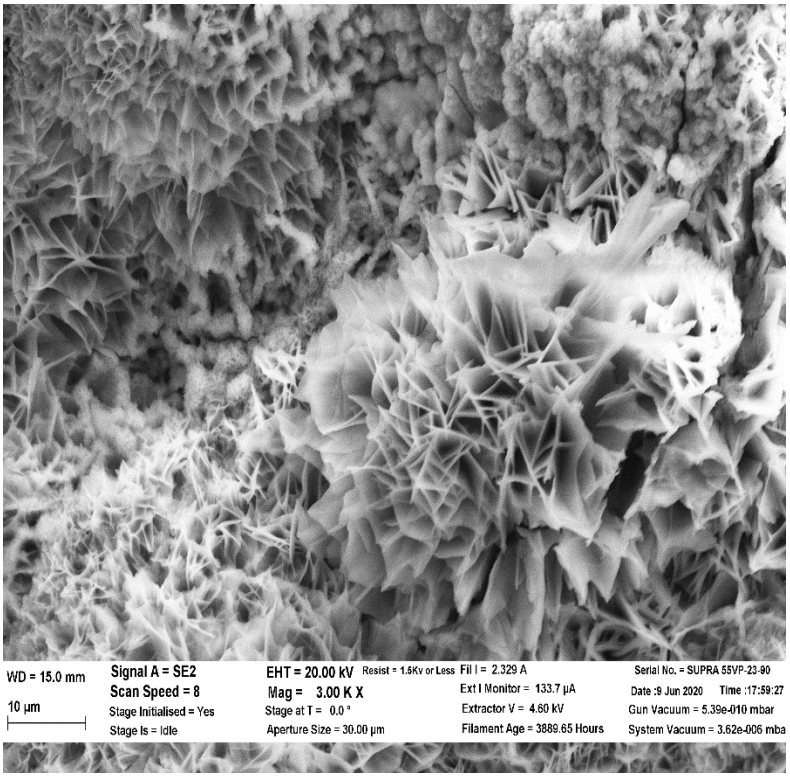

Figure 110: Crystalline form of iron oxide on steel specimen at the age of 3 months immersed in 30,000 PPM sodium chloride solution.

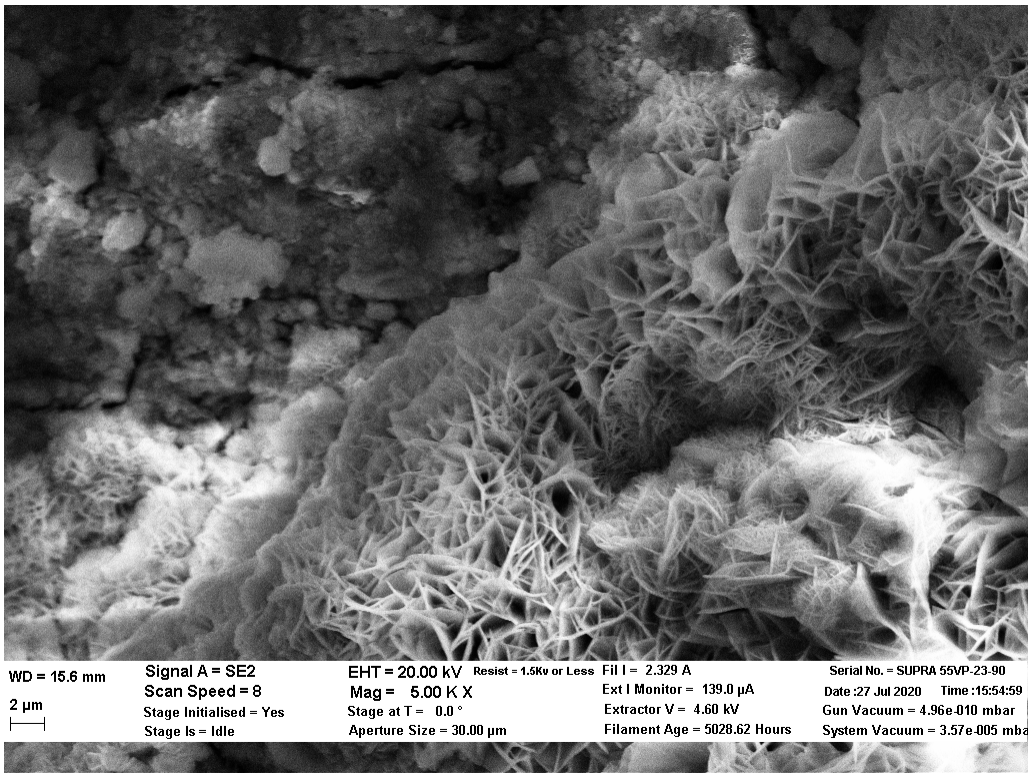

Figure 111: Crystalline form of iron oxide on steel specimen at the age of 4 months immersed in 30,000 PPM sodium chloride solution.

5.9 Autogenous Healing

The autogenous healing was first noticed at the age of 4 months for the cracked reinforced concrete pipes immersed in 30,000 PPM sodium chloride solutions. A significant crack sealing was noticed for several pipes in the 30,000 PPM solutions. Figure 112 shows some of the first noticed pipes that exhibited autogenous healing. The totes contain both the steel half cages and the helical bars along with the concrete pipes. Therefore, the corrosion products, dust, sodium chloride higher concentration, etc. all participated in the process of the autogenous healing of the cracks and the cracks were partially but significantly sealed as seen inside the cracks from the fourth month on for the 30,000 PPM solution and month 5 and 6 for the 200, and 2,000 PPM solutions. The agitation

of the above-mentioned suspended materials will increase the probability of them to seal the cracks mechanically.

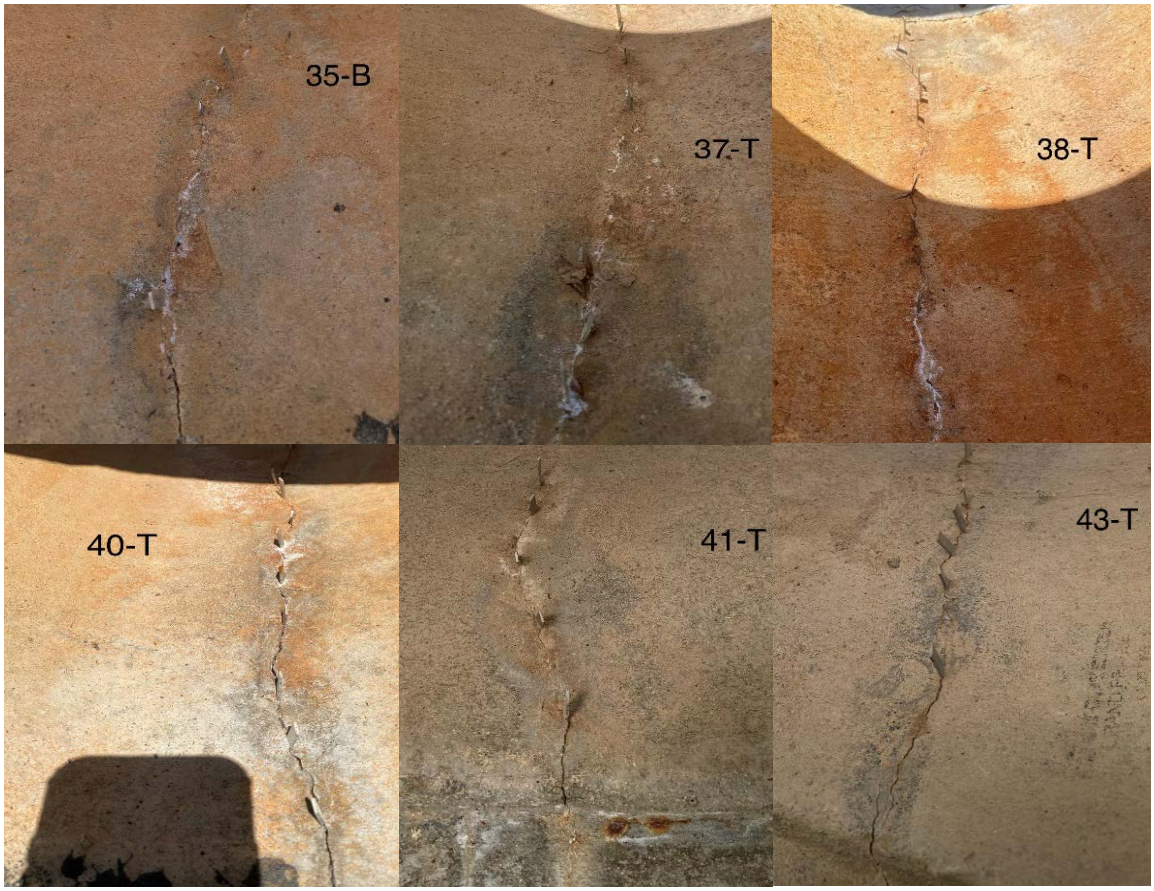

Figure 112: Autogenous healing and cracks sealing in the 30,000 PPM solutions.

CHAPTER 6. SUMMARY, CONCLUSION AND RECOMMENDATIONS FOR FUTURE WORK

6.1 Summary

This research studies the performance of cracked reinforced concrete pipe sections of 2 ft long under environmental conditions. To this end, the RCPs were subjected to 200, 2000 and 30,000 PPM sodium chloride solution. D-load tests were performed on the cracked RCPs to determine any potential strength reduction. Steel specimens were used as well to determine their strength and weight loss due to exposure to corrosive environments. The following section presents the conclusions obtained from the immersion of full-size RCPs in sodium chloride solution and how it has affected their performance in terms of strength loss in the RCPs, as well as weight and strength loss in steel specimen.

6.2 Conclusions

From the D-load test results, the following conclusions can be drawn:

1- The outliers test for the D-load test data showed that all the data were within the limits and there is no need to omit any of them.
2- The t-test showed that there is 12.3% chance that the data were random which is an acceptable value for concrete results since concrete is not a homogenous material and the production and testing of the reinforced concrete pipes involves a lot of errors such as human errors, misplacement of cages, misalignment in the D-load test, defect and deformations in the concrete pipes, etc.
3- For 200 and 2,000 PPM sodium chloride solutions, the ultimate D-load did not show a significant reduction and only fluctuation of results was noticed.

4- For the 30,000 PPM solution, the pipe showed a decrease in ultimate D-load compared to the corresponding control specimens, but the decrease was not following a certain trend.

5- Since the test data did not show any type of relationship between time and strength degradation and more tests are still pending as per the test plan of this study, it is anticipated to obtain a correlation between time and strength degradation for each solution.

6- Because of the smaller sampling size, a new statistical analysis method should be adopted to test the data obtained where the sampling size is enlarged, and a statistically more reliable data analysis is obtained.

7- One of the limitations of this study is that the test data obtained for up to six months is not enough to predict the behavior of the cracked reinforced concrete pipes. More test data (by increasing the number of the specimens and/or the testing period) will increase the probabilities of showing correlations between strength degradation and time for the three different solutions of this study.

For the tension coupon test, 4 tension coupons were tested each month for the 30,000 PPM solution and every two months for the 200 and 2,000 PPM solutions. From the results, the following conclusions can be drawn:

1- The outliers test for the tensile load test data showed that all the data were good and there was no need to omit any of them.

2- The t-test showed that there is around 11.9% chance that the data were random which is not an acceptable value in the steel specimens since steel is a homogenous material and not much chances of errors compared to those in concrete specimens.

3- For the specimens immersed in 200 and 2,000 PPM solutions, there was not significant reduction in the ultimate tensile load over the testing period of six months. The maximum reduction was 2.94% for the specimens immersed in 2,000 PPM solution for the third month.
4- For the specimens immersed in 30,000 PPM solutions, a significant strength loss can be noticed or around 8% for the last 4 months.

From the weight loss measurements, one can conclude the following:

1- Bare specimens showed greater loss in weight compared to embedded specimens.
2- An increase in weight loss for both steel half cages, and helical bars is obvious from the weight loss charts. The data is following a specific trend in weight loss.
3- More weight loss is seen in the last two months because the rust becomes harder to remove. To clean the steel half cages and the helical bars, the cleaning will take more steel around the tough rust resulting in more than the actual weight loss.

From the SEM/DEX scanning results, the following conclusions can be drawn:

1- The oxygen content on the surfaces of the scanned steel bars specimens did not change in a significant manner indicating that no significant corrosion occurred in the steel bars embedded inside the concrete pipes for 200, 2,000 and 30,000 PPM sodium chloride solutions.
2- The reduction in diameter measurements for the embedded steel bars shows almost 50% less reduction when compared to the measurements of the tension coupons. This can be justified by the protection provided by concrete and the autogenous healing of the cracks in the concrete pipes.

Autogenous healing process was noticed at the 4th month for the 30,000 PPM solutions and at the 5th month for the 200 and 2,000 PPM solutions. The suspended materials inside the totes in addition to the sodium chloride concentration helped to mechanically seal the cracks when the suspended materials are agitated for any reason.

6.3 Recommendation for Future Work

As per the experience gained while working on this research project, the following is recommended for future work:

1- Statistically speaking, more pipe sections for each testing period will decrease the p-value resulting in a much more significant data.
2- Repeat the same test protocol for different corrosive environments which are likely to occur for concrete pipes
3- Using different sizes of pipes and different wall thicknesses to determine whether those parameters will affect the results (size effects) obtained in this study.
4- Adopt an alternative cleaning method for the steel specimens that can assure the tougher layers of rust are totally removed, and in the meantime satisfy one of the standard practices.
5- A regression analysis for the weight loss vs. time to be done for the results obtained from this study for the results obtained through the 1-year testing period.

REFERENCES

American Concrete Pipe Association, (2011). Concrete Pipe Design Manual. *www.concrete-pipe.org*.

Angst, U., Larsen, C. K., Vennesland, O., & Elsener, B. (2010, July). Influence of casting direction on chloride-induced rebar corrosion. In *Concrete under Severe Conditions: Environment and Loading-Proceedings of the 6th International Conference on Concrete under Severe Conditions, CONSEC'10*.

Ann, K. Y., & Song, H. W. (2007). Chloride threshold level for corrosion of steel in concrete. *Corrosion Science*, 49(11), 4113–4133. https://doi.org/10.1016/j.corsci.2007.05.007

ASTM A370. (2019). Standard Test Methods and Definitions for Mechanical Testing of Steel Products. *American Standards for Testing and Materials*. http://doi.org/10.1520/A0370-14.2

ASTM C14. (2020). Standard Specification for Nonreinforced Concrete Sewer, Storm Drain, and Culvert Pipe. *American Standards for Testing and Materials*. https://doi.org/10.1520/C0014M-11.2

ASTM C1818-19. (2020). Standard Specification for Synthetic Fiber Reinforced Concrete Culvert, Storm Drain, and Sewer Pipe. *American Standards for Testing and Materials*. https://doi.org/10.1520/C0076-19B.2

ASTM C497-19a (2020). Standard Test Methods for Concrete Pipe, Manhole Sections, or Tile [Metric] 1. *American Standards for Testing and Materials*. https://doi.org/10.1520/C0497M-05.2.

ASTM C506. (2019). Standard Specification for Nonreinforced Concrete Sewer, Storm Drain, and Culvert Pipe. *American Standards for Testing and Materials*. https://doi.org/10.1520/C0014M-11.2

ASTM C507. (2019). Standard Specification for Nonreinforced Concrete Sewer, Storm Drain, and Culvert Pipe. *American Standards of Testing and Materials*. https://doi.org/10.1520/C0014M-11.2

ASTM C655. (2019). Standard Specification for Reinforced Concrete D-Load Culvert, Storm Drain, and Sewer Pipe. *American Standards for Testing and Materials*. https://doi.org/10.1520/C0655-19A.2

ASTM C76-19b. (2019). Standard Specification for Reinforced Concrete D-Load Culvert, Storm Drain, and Sewer Pipe. *American Standards for Testing and Materials*. https://doi.org/10.1520/C0076-19B.2

ASTM C985. (2019). Standard Specification for Nonreinforced Concrete Specified Strength Culvert, Storm Drain, and Sewer Pipe. *American Standards for Testing Ad Materials*. https://doi.org/10.1520/C0014M-11.2

ASTM E8/E8M. (2013). Standard test methods for tension testing of metallic materials. *American Standards for Testing and Materials*. https://doi.org/10.1520/E0008

ASTM G1-09 (2011). Standard Practice for Preparing, Cleaning, and Evaluating Corrosion Test. Significance, 90(Reapproved 2011). *American Standards for Testing and Materials*. https://doi.org/10.1520/G0001-03R11.2

Baweja, D., Roper, H., & Sirivivatnanon, V. (1998). Chloride-induced steel corrosion in concrete: Part 1 - Corrosion rates, corrosion activity, and attack areas. *ACI Materials Journal*, 95(3), 207–217. https://doi.org/10.14359/364

Baweja, D., Roper, H., & Sirivivatnanon, V. (1999). Chloride-induced steel corrosion in concrete: Part 2 - Gravimetric and electrochemical comparisons. *ACI Materials Journal*, 96(3), 306–313. https://doi.org/10.14359/627

Bonta, Chris (2015). Outlier Test, this is an example of how to use the outlier test when determining if a given data set contains outliers. https://www.youtube.com/watch?v=Pfk9tlWy500

Brandt, M. J., Johnson, K. M., Elphinston, A. J., & Ratnayaka, D. D. (2017). Chemistry, Microbiology and Biology of Water. *Twort's Water Supply* (Vol. 0). https://doi.org/10.1016/b978-0-08-100025-0.00007-7

Busba, E., & Sagüés, A. A. (2013). Localized corrosion of embedded steel in cracked reinforced concrete pipes. *Corrosion Engineering Section*, 69(4), 403–416. https://doi.org/10.5006/0871E

Darabnoush Tehrani, A. (2016). Finite Element Analysis for ASTM C-76 Reinforced Concrete Pipes with Reduced Steel Cage. (Master thesis).

Darabnoush Tehrani, A., Kohankar Kouchesfehani, Z., Chimauriya, H. R., Raut, S., Najafi, M., & Yu, X. (2020). Structural evaluation of invert-cut circular and arch shape corrugated steel pipes through laboratory testing. *Canadian Journal of Civil Engineering*, (999), 1-15.

Deziel, C. (April 26, 2018). How to Write the Balanced Chemical Reaction for the Rusting of Iron The First Step : Oxidation of Solid Iron The Second Step : *Formation of Hydrated Iron Oxide (Rust)*. "https://sciencing.com/write-chemical-reaction-rusting-iron-8558862.html". Accessed 6/20/2020.

Florida Department of Transportation. (2020). State of Florida Department of Transportation Drainage Manual. *Office of Design, Drainage Section*.

Hearn, N. (1998). Self-sealing, autogenous healing and continued hydration: What is the difference, *Materials and Structures/Materiaux et Constructions*, 31(8), 563–567. https://doi.org/10.1007/bf02481539

Kouchesfehani, Z. K., Tehrani, A. D., Najafi, M., Syar, J. E., & Kampbell, E. (2019). Adding Additional Reinforcement to Improve the Structural Performance of Spray Applied Pipe Lining Rehabilitation Technology: A Review. In Pipelines 2019: Multidisciplinary Topics, Utility Engineering, and Surveying (pp. 10-23). Reston, VA: *American Society of Civil Engineers*.

Lee, H., Cody, R. D., Cody, a M., & Spry, P. G. (2000). Effects of Various Deicing Chemicals on Pavement Concrete Deterioration. *Proceedings of Mid-Continent Transportation Symposium*, 151–155.

Maes, M., Snoeck, D., & De Belie, N. (2016). Chloride penetration in cracked mortar and the influence of autogenous crack healing. *Construction and Building Materials*, 115, 114–124. https://doi.org/10.1016/j.conbuildmat.2016.03.180

Mahdavi, M. (2019). Development of protocol for 100-Year Service Life of Synthetic Fiber-Reinforced Concrete Pipes. (Ph.D. Dissertation).

Marston, A. (1930). The theory of external loads on closed conduits in the light of the latest experiments. *Highway Research Board*, 9, 138–170.

McLeod, S. (2019). Statistics/p-value. What a p-value tells you about statistical significance, https://www.simplypsychology.org/p-value.html

Mohammed, T. U., Hamada, H., & Yokota, H. (2013). Autogenous Healing; Ingress of Chloride and Sulfate through Cracks in Concrete under Marine Environment. *Journal of Chemical Information and Modeling*, 53(9), 135–154. https://doi.org/10.1017/CBO9781107415324.004

Mussato, B. T., Gepraegs, O. K., & Farnden, G. (2004). Relative effects of sodium chloride and magnesium chloride on reinforced concrete: State of the art. *Transportation Research Record*, 1866, 59–66.

Olander, H. C. (1950). Stress Analysis of Concrete Pipe. United States Department of the Interior, *Bureau of Reclamation.* Denver, Colorado.

Otieno, M., Beushausen, H., & Alexander, M. (2016). Chloride-induced corrosion of steel in cracked concrete - Part II: Corrosion rate prediction models. *Cement and Concrete Research*, 79, 386–394.

Palin, D., Wiktor, V., & Jonkers, H. M. (2015). Autogenous healing of marine exposed concrete: Characterization and quantification through visual crack closure. *Cement and Concrete Research*, 73, 17–24. https://doi.org/10.1016/j.cemconres.2015.02.021

Peck, R., Olsen, C., & Devore, J. (2008). Introduction to Statistics and Data Analysis (3rd ed.). *Thomson Brooks/Cole*.

Ragab, A. M., Elgammal, M. A., Hodhod, O. A. G., & Ahmed, T. E. S. (2016). Evaluation of field concrete deterioration under real conditions of seawater attack. *Construction and Building Materials*, 119, 130–144.

Robert D. Cody, Anita D. Cody, P. G. S. and G.-L. G. (1996). Experimental Deterioration of Highway Concrete by Chloride Deicing Salts. *Environmental and Engineering Geoscience*, Volume 2, (No. 4), 575–588.

Rossi, E., Polder, R., Copuroglu, O., Nijland, T., & Šavija, B. (2020). The influence of defects at the steel/concrete interface for chloride-induced pitting corrosion of naturally deteriorated 20-years-old specimens studied through X-ray Computed Tomography. *Construction and Building Materials*, 235, 117474. https://doi.org/10.1016/j.conbuildmat.2019.117474

Sewer History (2004). Tracking down the Roots of Our Sanitary Sewers, https://www.sewerhistory.org/chronos/early_roots.htm

Shao, W., & Li, J. (2014). Service life prediction of cracked RC pipe piles exposed to marine environments. *Construction and Building Materials*, 64, 301–307. https://doi.org/10.1016/j.conbuildmat.2014.04.094

Stutzman, P. E., & Clifton, J. R. (1999). Specimen Preparation for scanning electron microscopy. *National Institute of Standards and Technology*, 24(12), 10–22.

The British Museum (2020). Drain-Pipe, Pottery drain-pipe; wheel-thrown hollow cylinder; stamped cuneiform inscription on body. https://www.britishmuseum.org/collection/object/W_1927-0527-257

Vavpetic, P. (2008). Corrosion in concrete steel. *University of Ljubljana*.

Watkins, R. K., and Anderson L. R., (2000). Structural Mechanics of Buried Pipes. 1st ed., *CRC Press.*

Watkins, R. K., and Spangler, M. G. (1958). Some Characteristics of The Modulus of Passive Resistance of Soil: A Study in Similitude. *Proceedings of the Thirty-Seventh Annual Meeting of the Highway Research Board*, 37, 576–583.

Wilson, A. (2012). Performance Evaluation and Finite Element Analysis of Fiber Reinforced Precast Concrete Underground Structures. (Master thesis).

Wilson, A., & Abolmaali, A. (2014). Performance of synthetic fiber-reinforced concrete pipes. *Journal of Pipeline Systems Engineering and Practice*, 5(3), 1–7. https://doi.org/10.1061/(ASCE)PS.1949-1204.0000166

Wilson, A., Abolmaali, A., Park, Y., & Attiogbe, E. (2017). Research and Concepts Behind the ASTM C1818 Specification for Synthetic Fiber Concrete Pipes. *Concrete Pipe and Box Culverts,* 42–49. https://doi.org/10.1520/stp160120160125

APPENDIX – A

Pre-immersion D-Load – Displacement Curves:

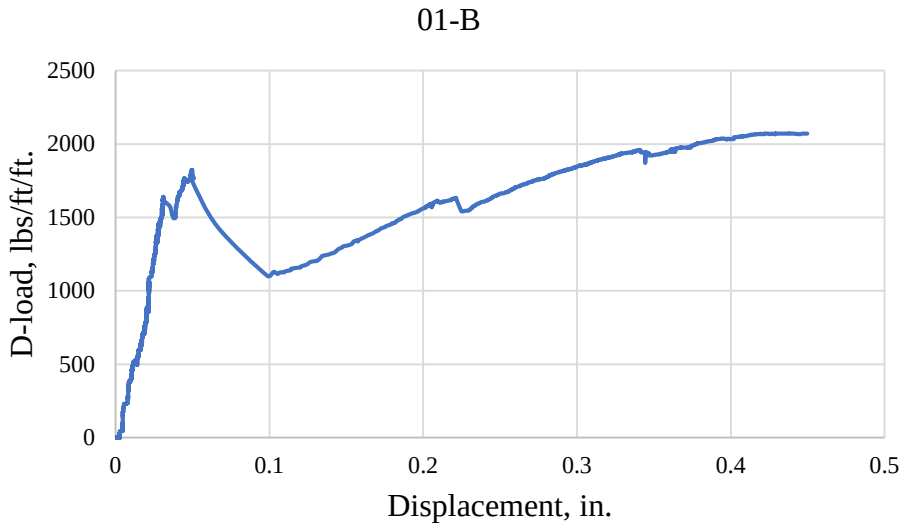

Figure A- 1: Pre-immersion D-load – Displacement Curve for pipe 01-B

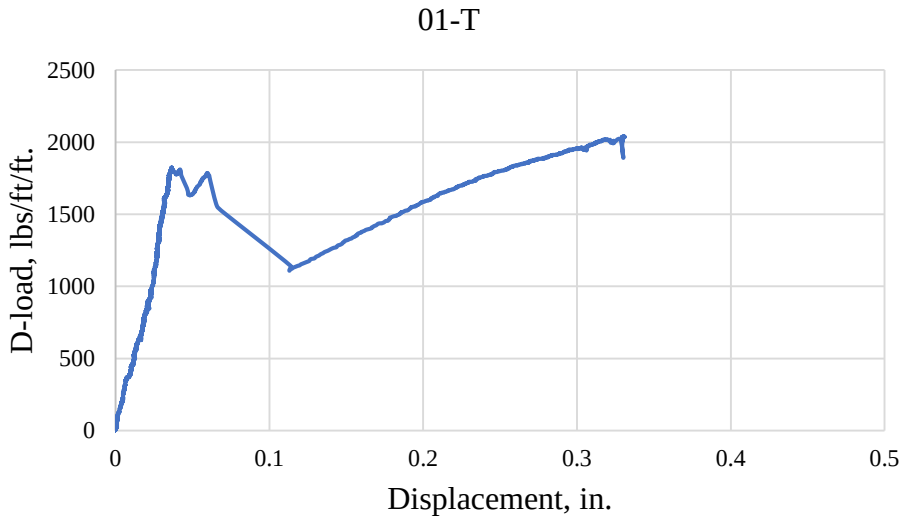

Figure A- 2: Pre-immersion D-load – Displacement Curve for pipe 01-T

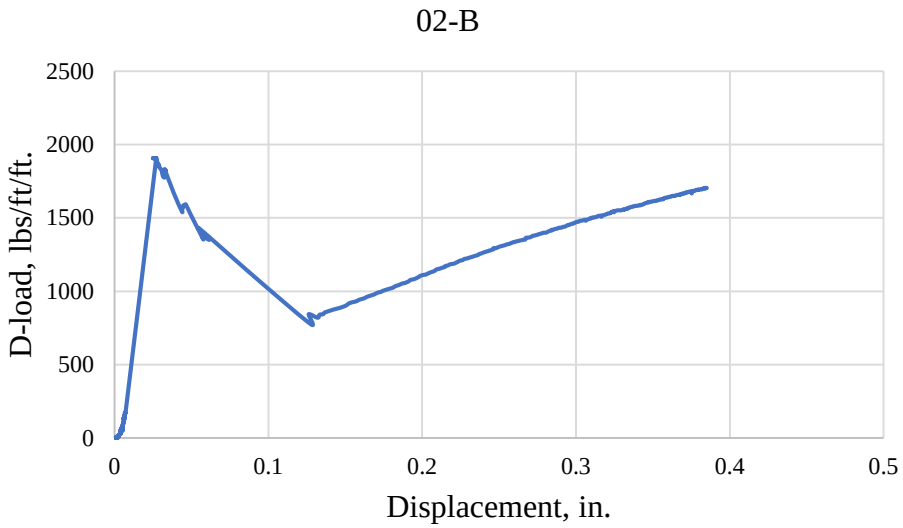

Figure A- 3: Pre-immersion D-load – Displacement Curve for pipe 02-B

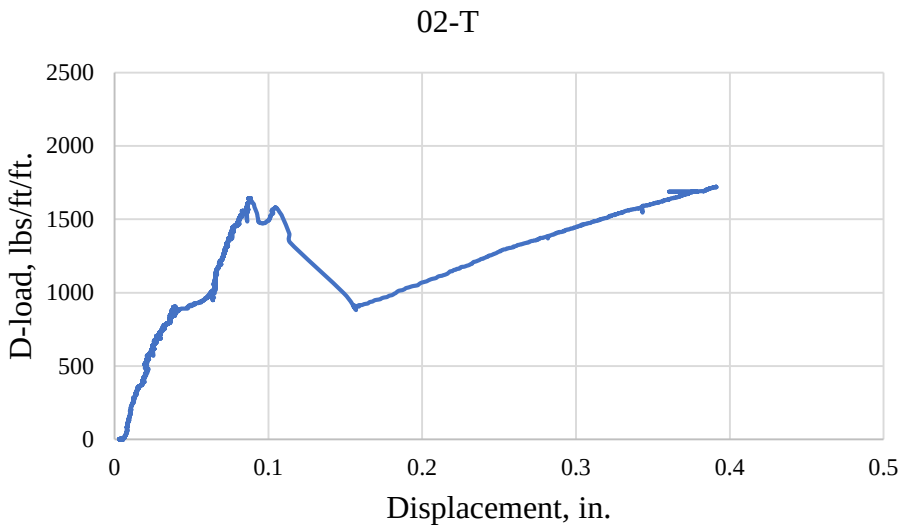

Figure A- 4: Pre-immersion D-load – Displacement Curve for pipe 02-T

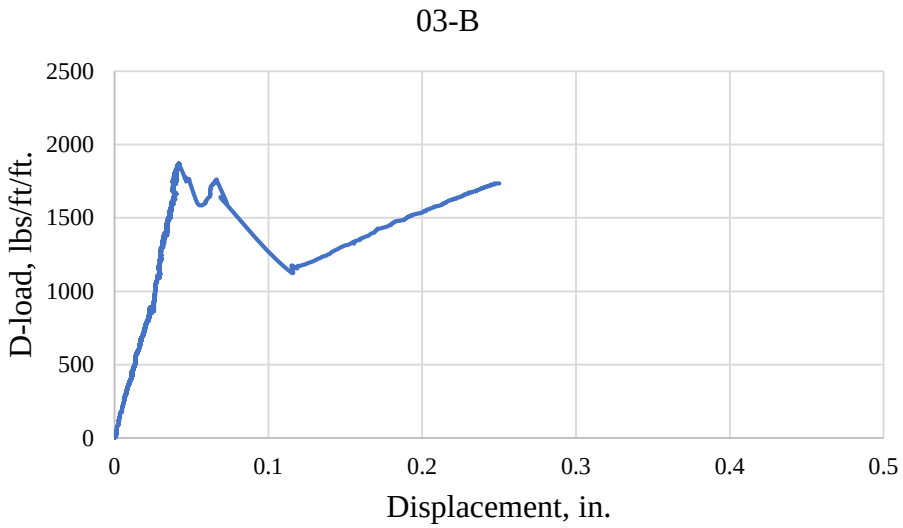

Figure A- 5: Pre-immersion D-load – Displacement Curve for pipe 03-B

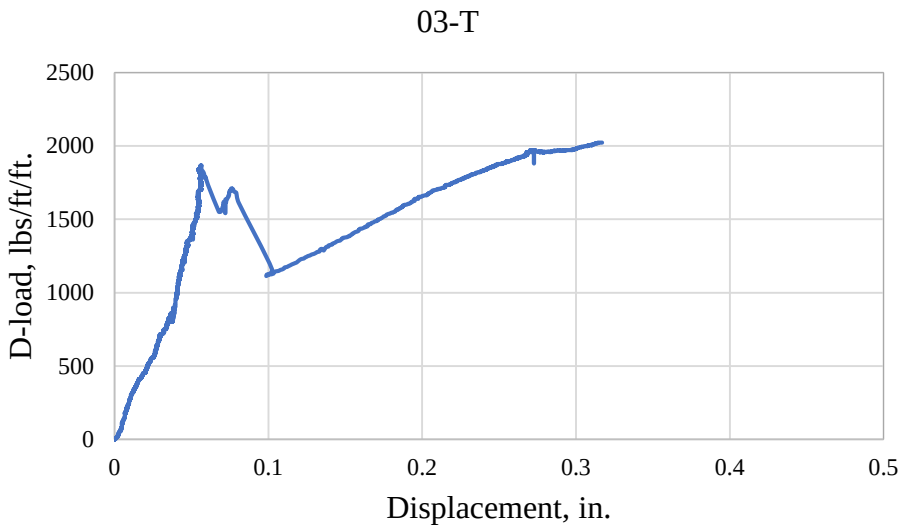

Figure A- 6: Pre-immersion D-load – Displacement Curve for pipe 03-T

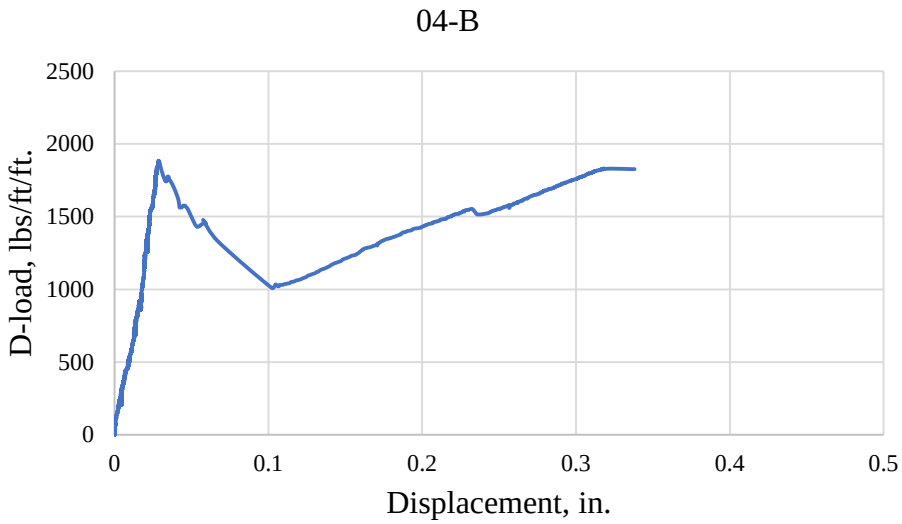

Figure A- 7: Pre-immersion D-load – Displacement Curve for pipe 04-B

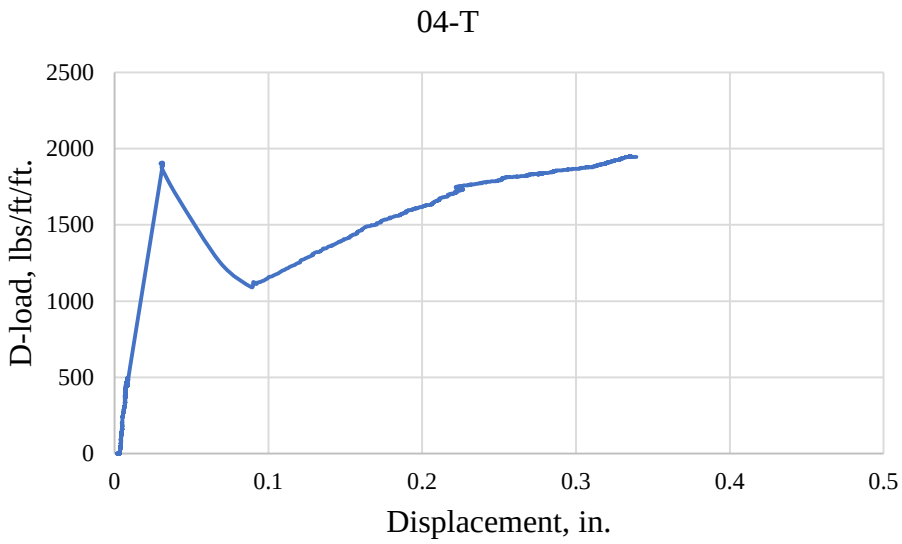

Figure A- 8: Pre-immersion D-load – Displacement Curve for pipe 04-T

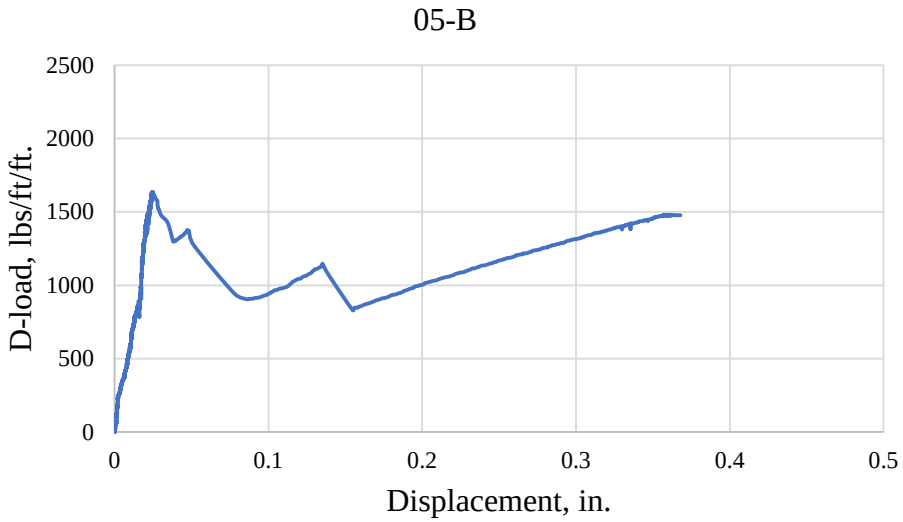

Figure A- 9: Pre-immersion D-load – Displacement Curve for pipe 05-B

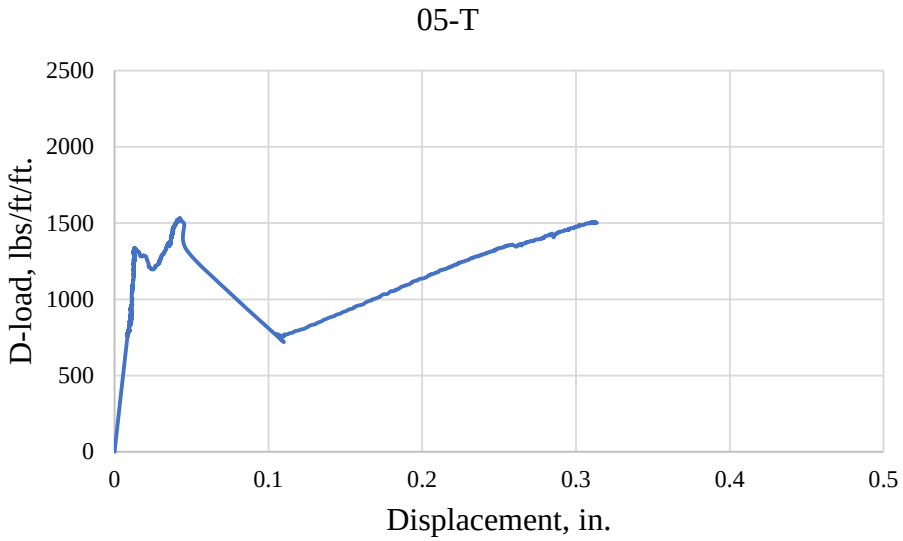

Figure A- 10: Pre-immersion D-load – Displacement Curve for pipe 05-T

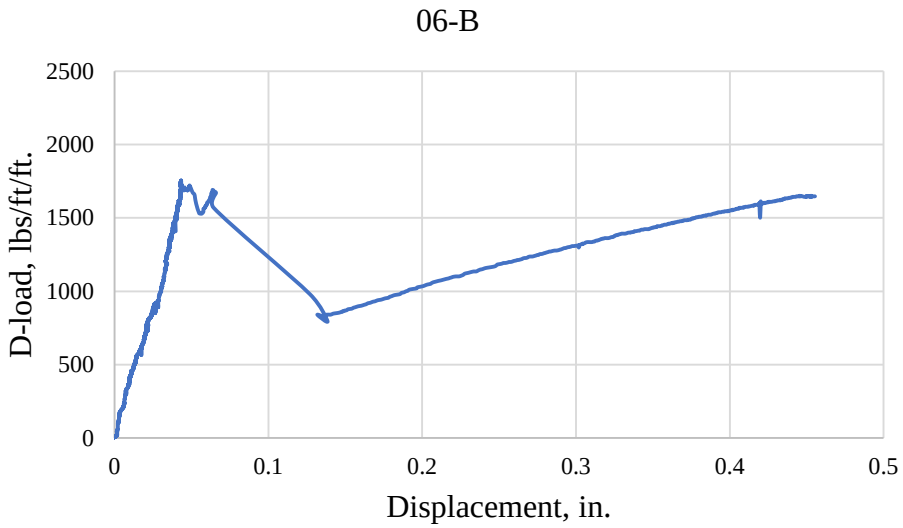

Figure A- 11: Pre-immersion D-load – Displacement Curve for pipe 06-B

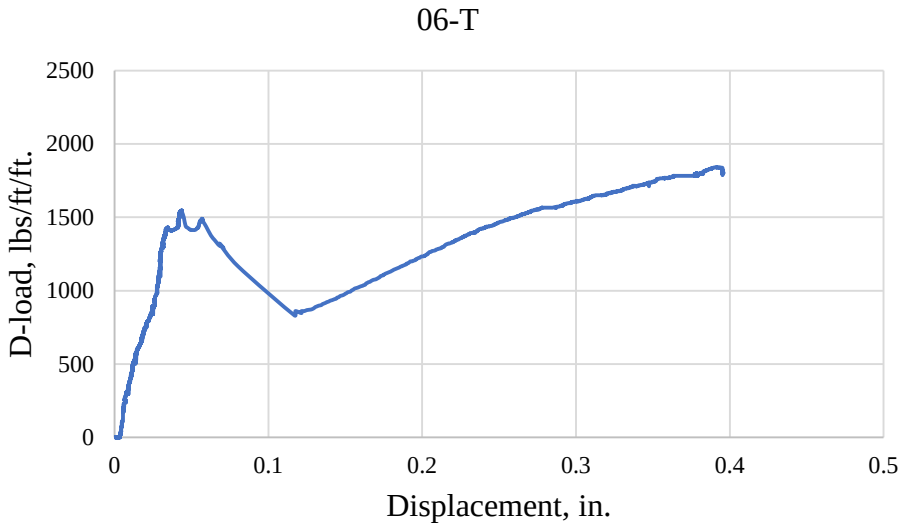

Figure A- 12: Pre-immersion D-load – Displacement Curve for pipe 06-T

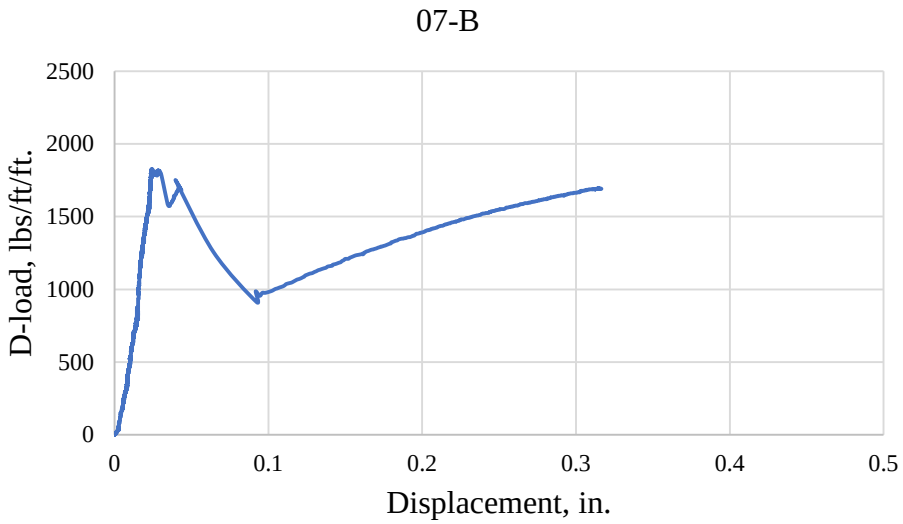

Figure A- 13: Pre-immersion D-load – Displacement Curve for pipe 07-B

Figure A- 14: Pre-immersion D-load – Displacement Curve for pipe 07-T

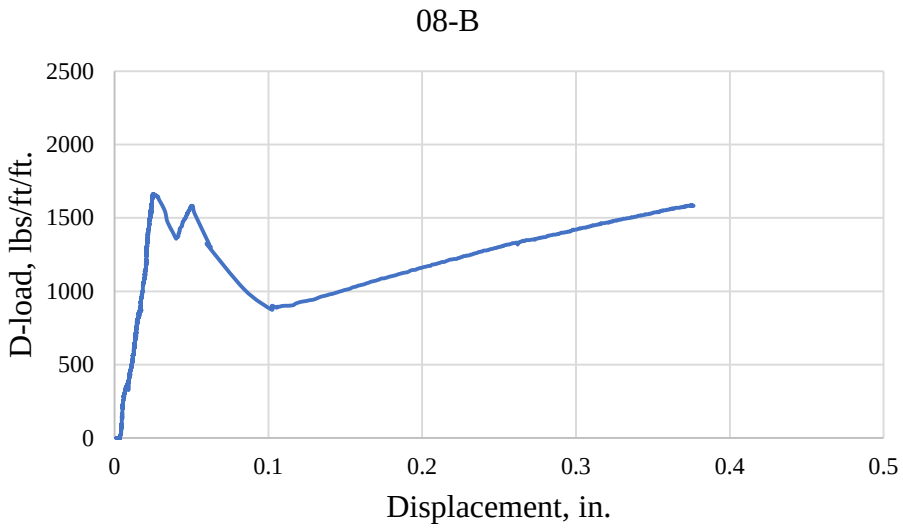

Figure A- 15: Pre-immersion D-load – Displacement Curve for pipe 08-B

Figure A- 16: Pre-immersion D-load – Displacement Curve for pipe 08-T

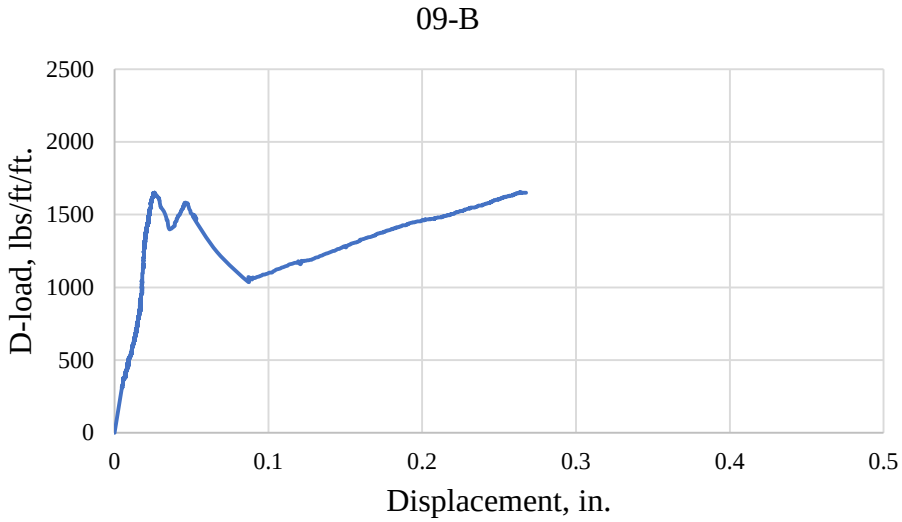

Figure A- 17: Pre-immersion D-load – Displacement Curve for pipe 09-B

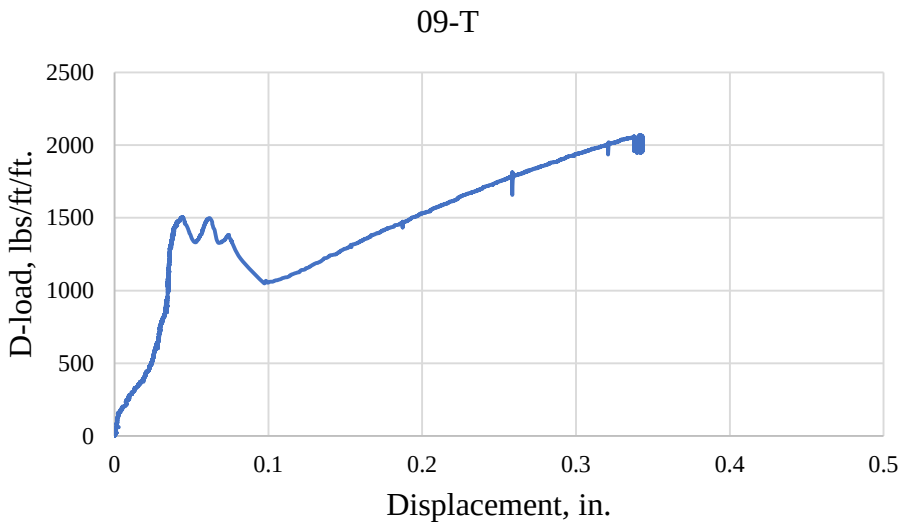

Figure A- 18: Pre-immersion D-load – Displacement Curve for pipe 09-T

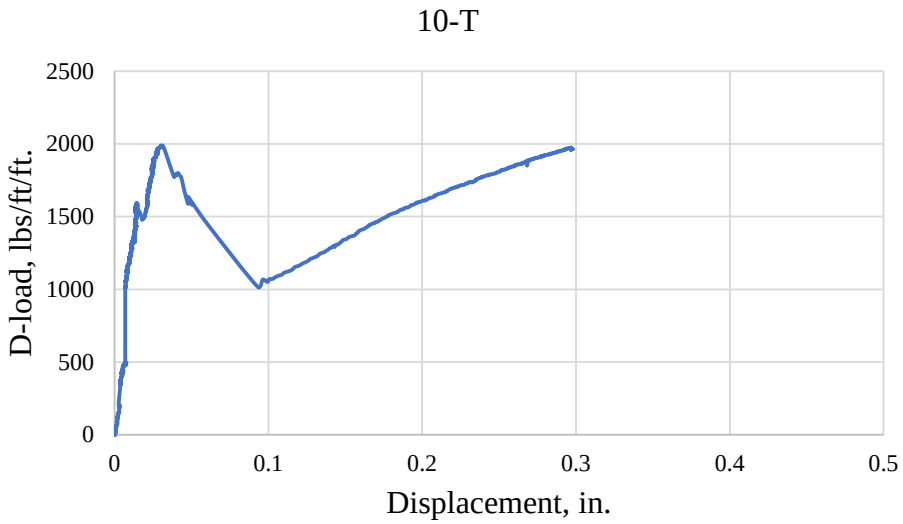

Figure A- 19: Pre-immersion D-load – Displacement Curve for pipe 10-T

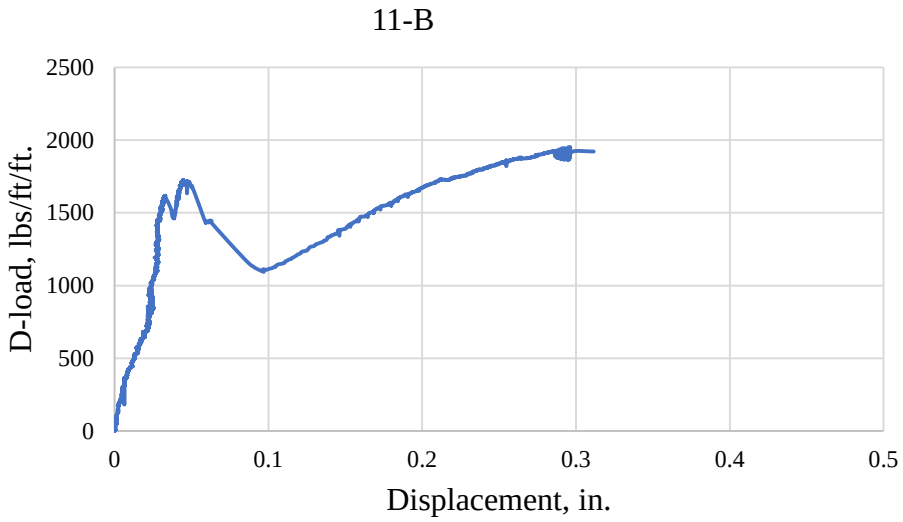

Figure A- 20: Pre-immersion D-load – Displacement Curve for pipe 11-B

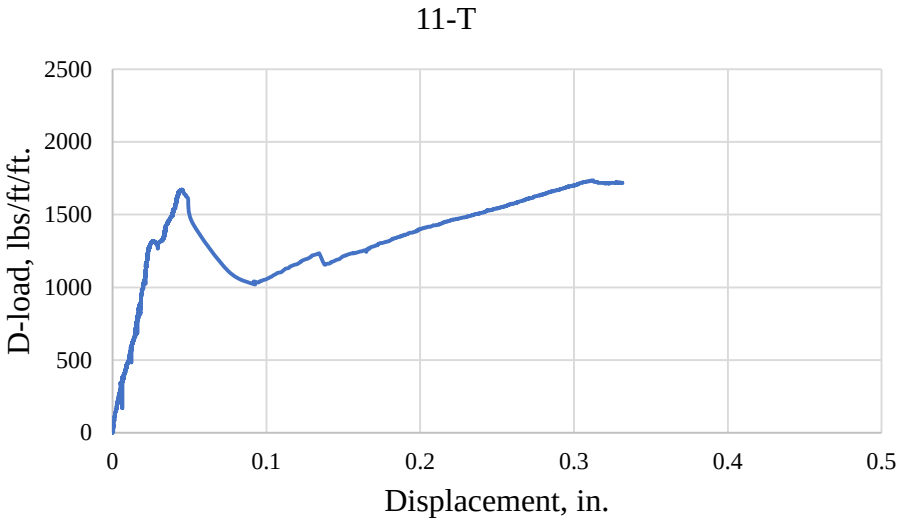

Figure A- 21: Pre-immersion D-load – Displacement Curve for pipe 11-T

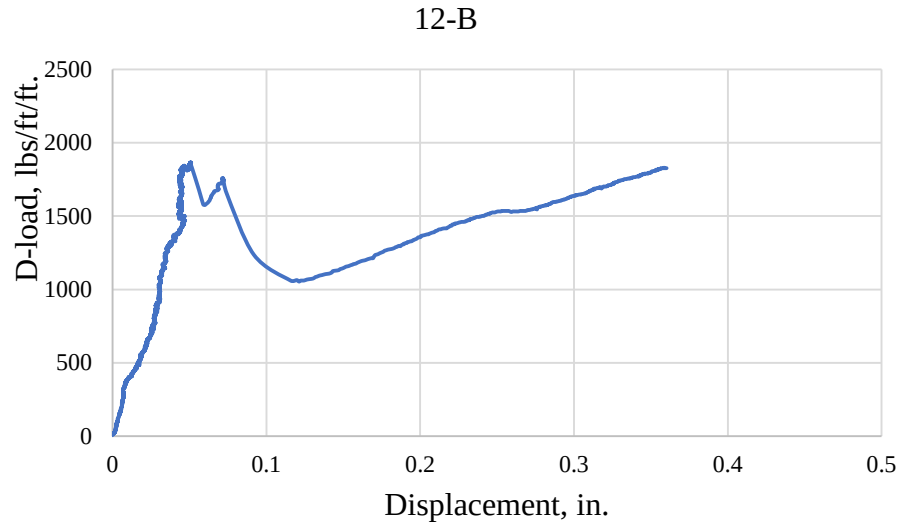

Figure A- 22: Pre-immersion D-load – Displacement Curve for pipe 12-B

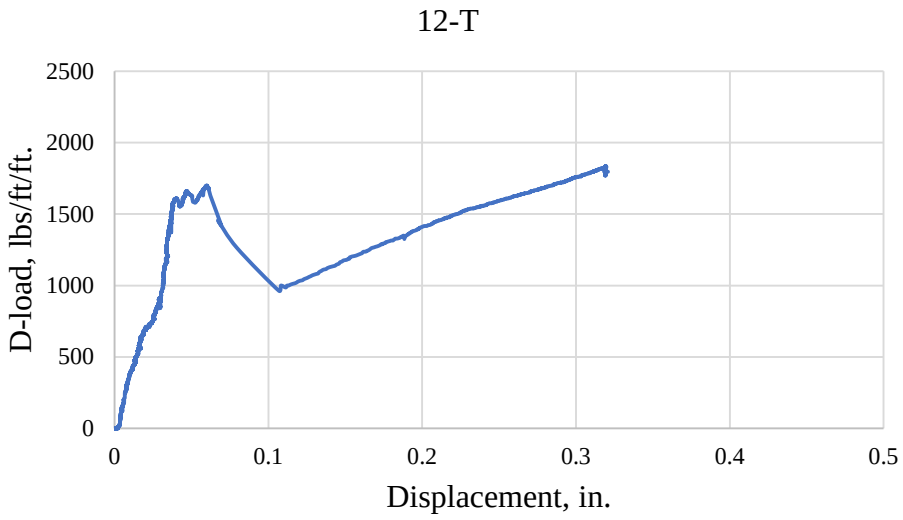

Figure A- 23: Pre-immersion D-load – Displacement Curve for pipe 12-T

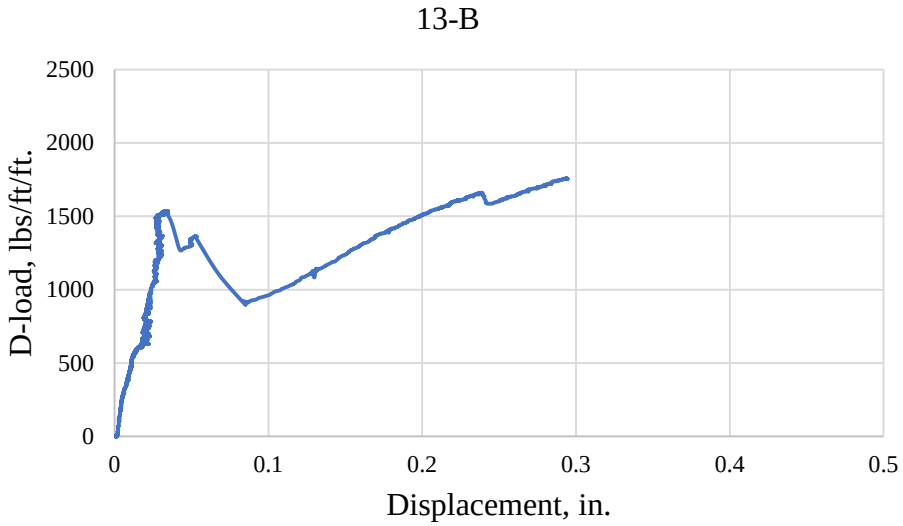

Figure A- 24: Pre-immersion D-load – Displacement Curve for pipe 13-B

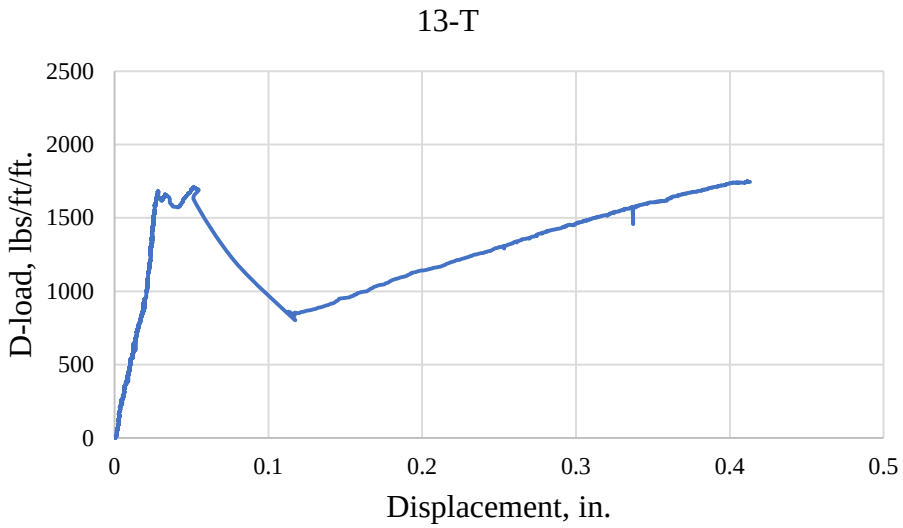

Figure A- 25: Pre-immersion D-load – Displacement Curve for pipe 13-T

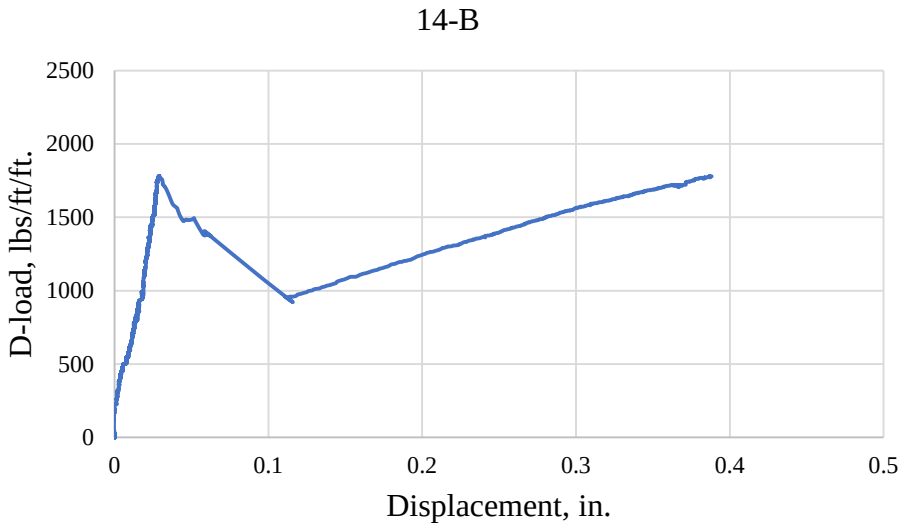

Figure A- 26: Pre-immersion D-load – Displacement Curve for pipe 14-B

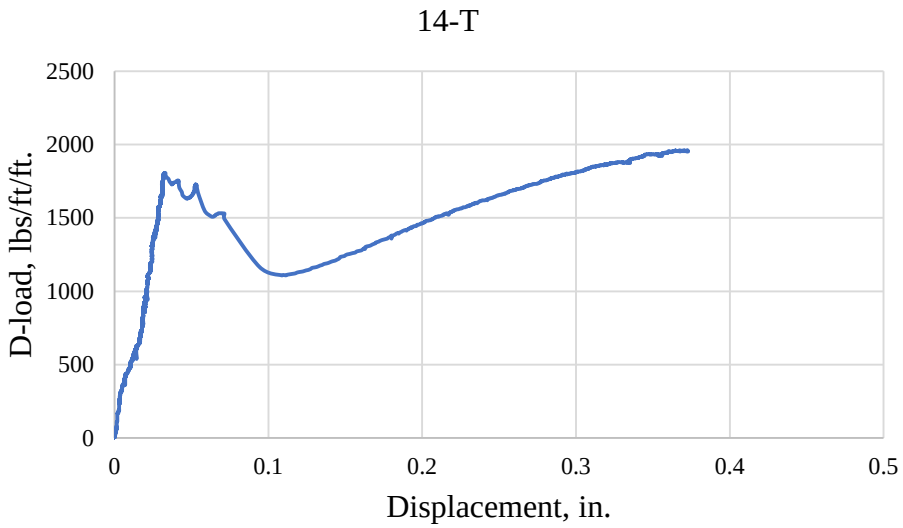

Figure A- 27: Pre-immersion D-load – Displacement Curve for pipe 14-T

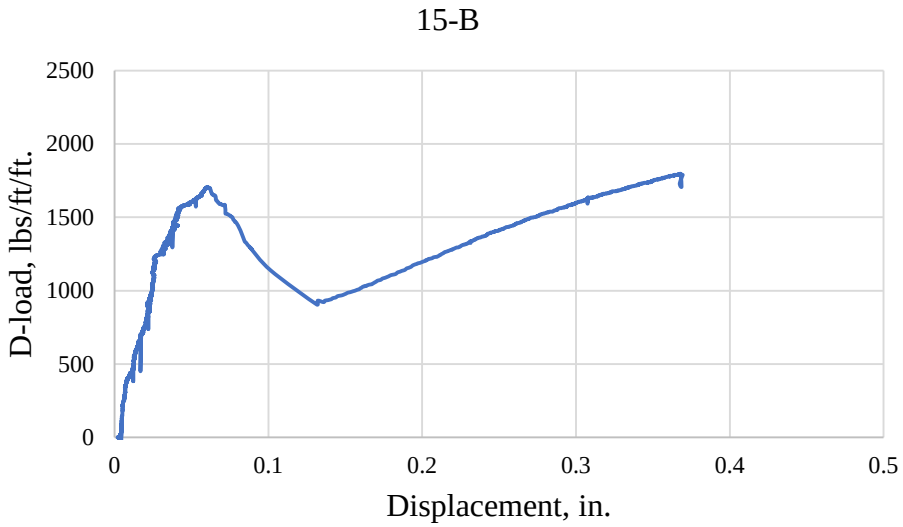

Figure A- 28: Pre-immersion D-load – Displacement Curve for pipe 15-B

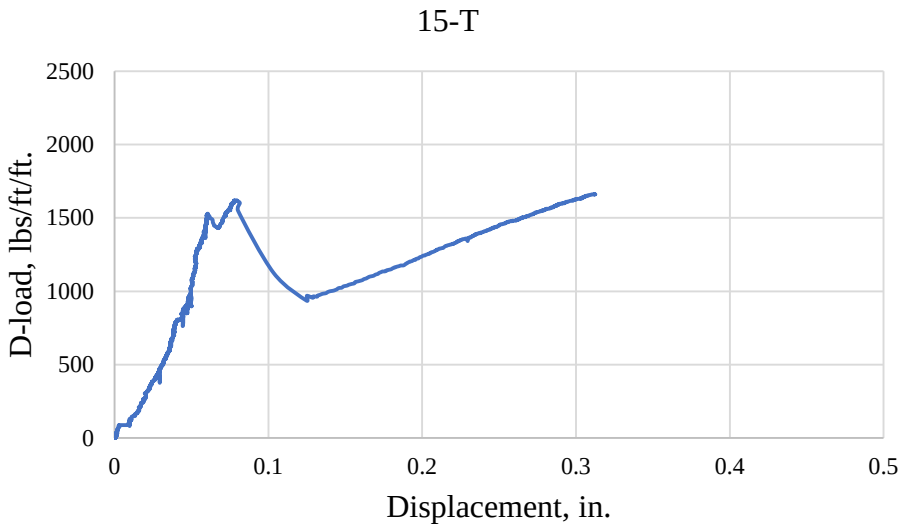

Figure A- 29: Pre-immersion D-load – Displacement Curve for pipe 15-T

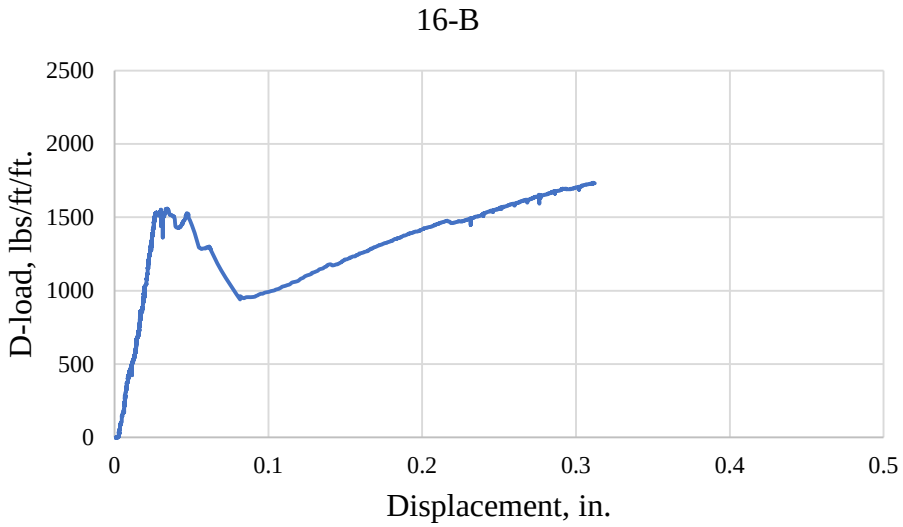

Figure A- 30: Pre-immersion D-load – Displacement Curve for pipe 16-B

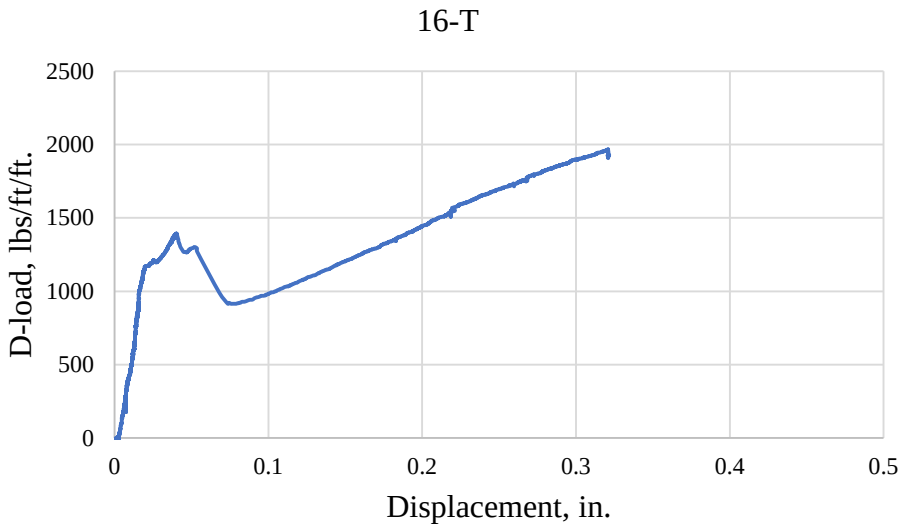

Figure A- 31: Pre-immersion D-load – Displacement Curve for pipe 16-T

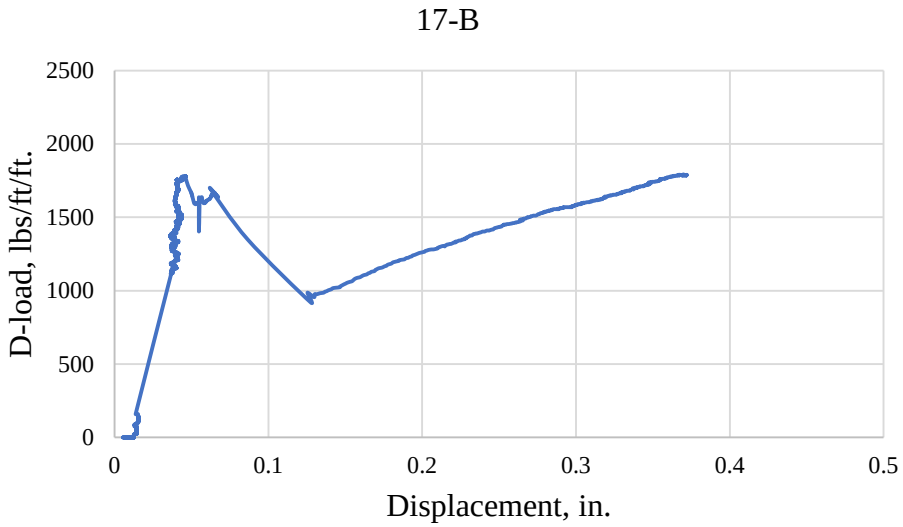

Figure A- 32: Pre-immersion D-load – Displacement Curve for pipe 17-B

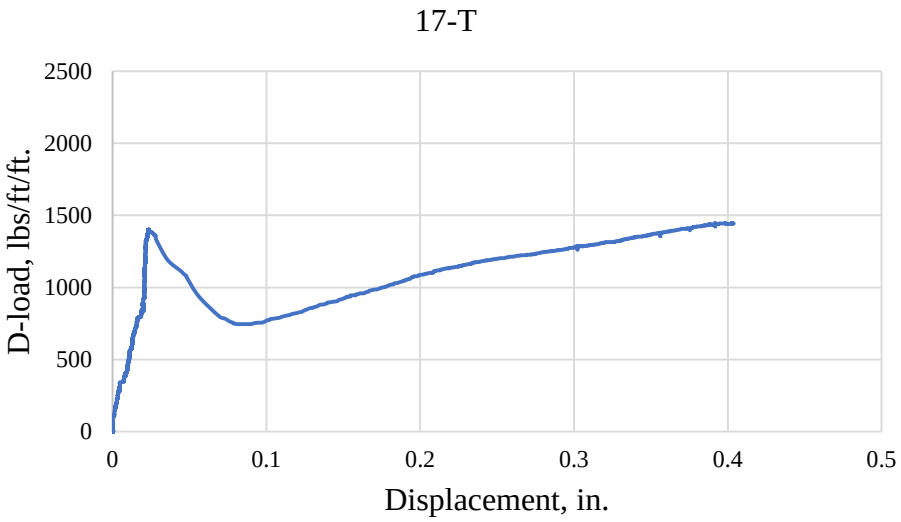

Figure A- 33: Pre-immersion D-load – Displacement Curve for pipe 17-T

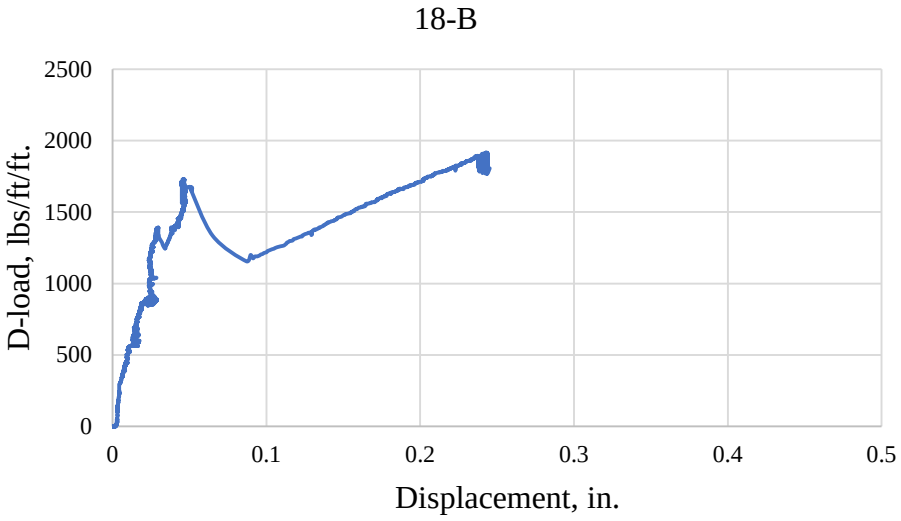

Figure A- 34: Pre-immersion D-load – Displacement Curve for pipe 18-B

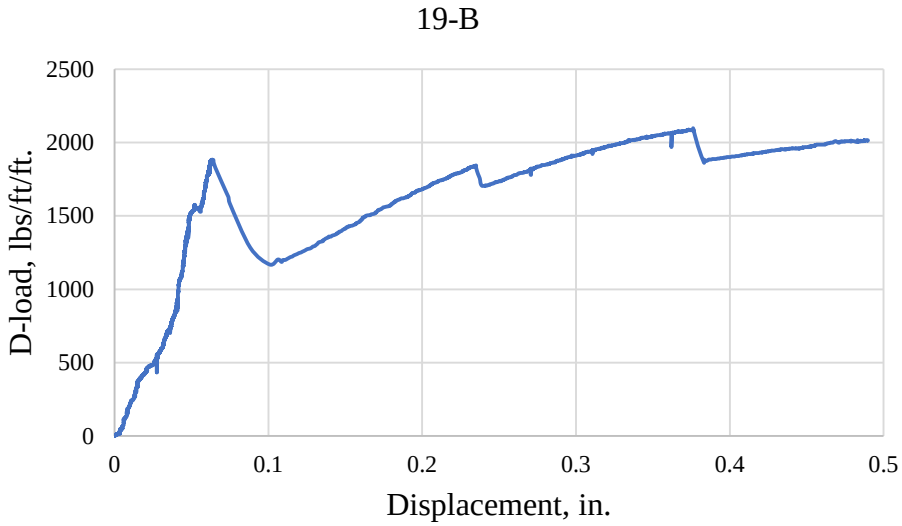

Figure A- 35: Pre-immersion D-load – Displacement Curve for pipe 19-B

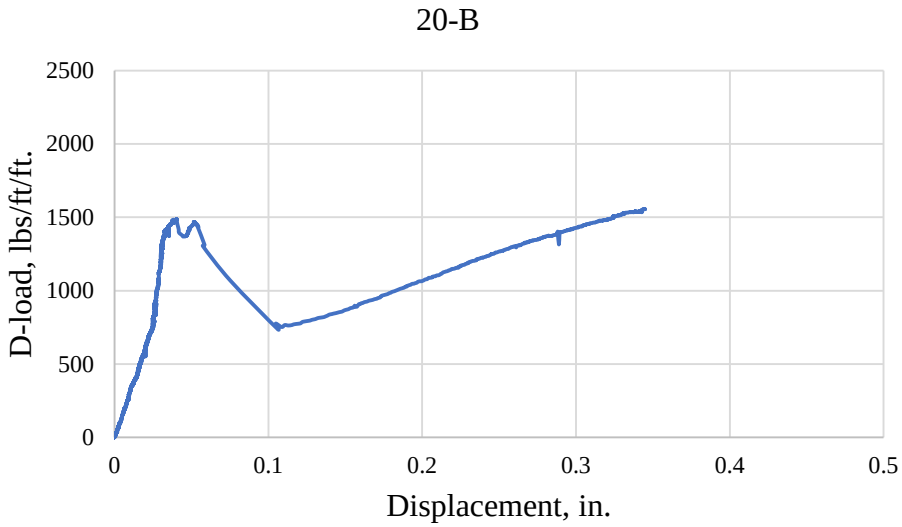

Figure A- 36: Pre-immersion D-load – Displacement Curve for pipe 20-B

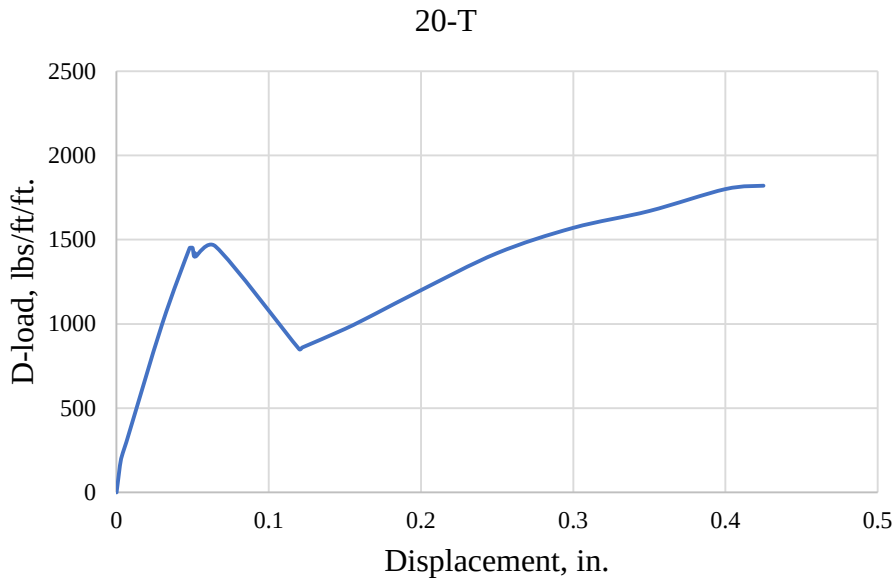

Figure A- 37: Pre-immersion D-load – Displacement Curve for pipe 20-T

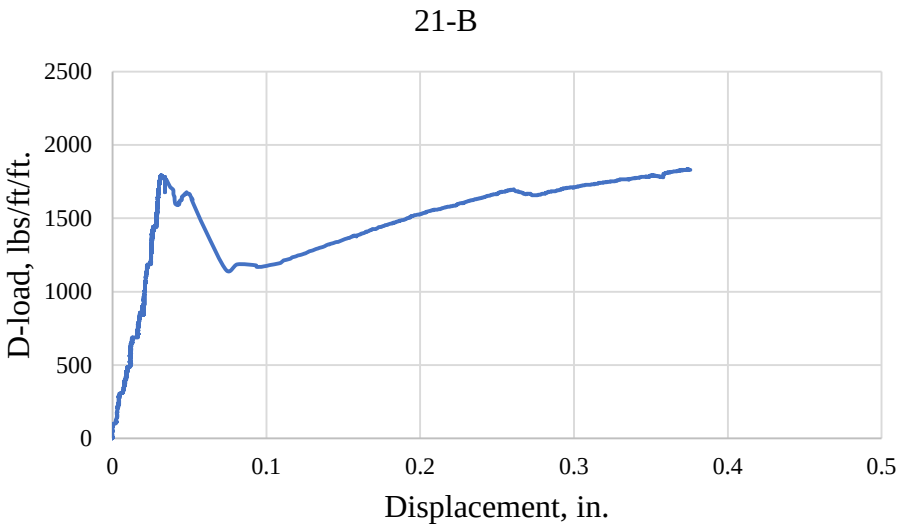

Figure A- 38: Pre-immersion D-load – Displacement Curve for pipe 21-B

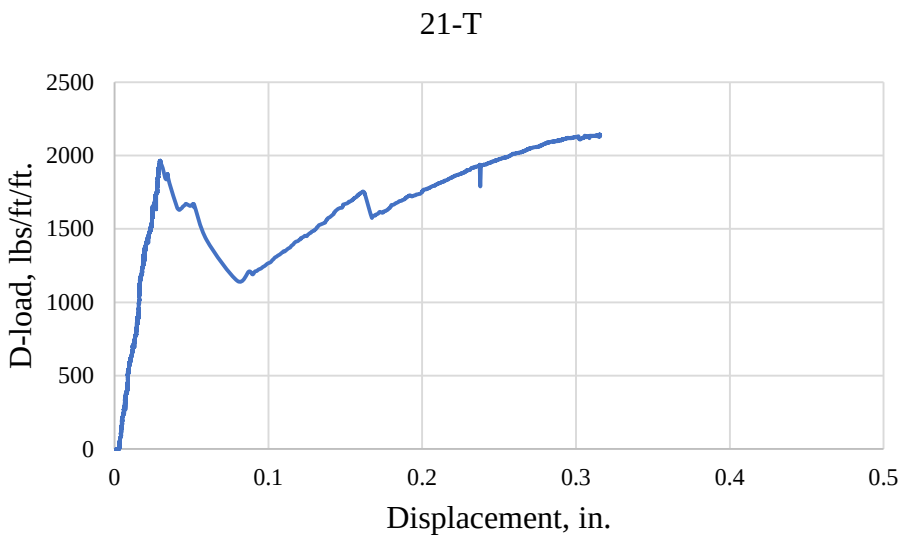

Figure A- 39: Pre-immersion D-load – Displacement Curve for pipe 21-T

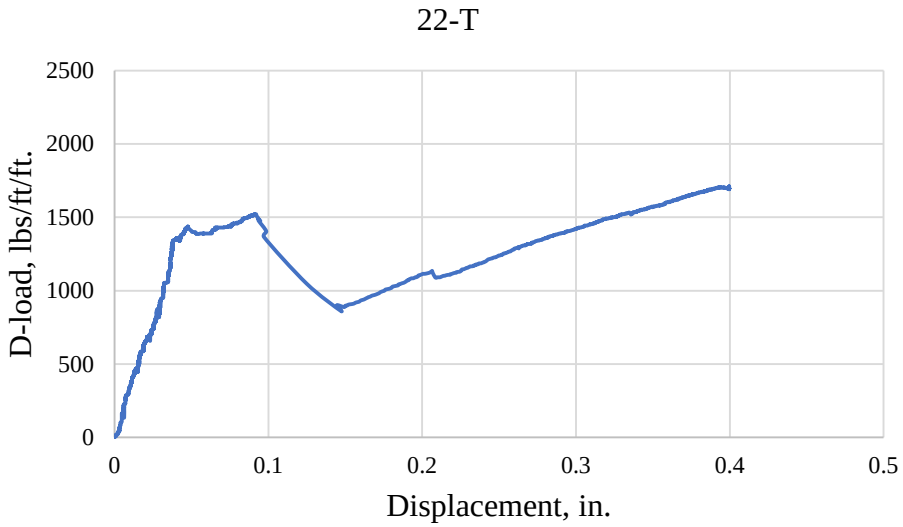

Figure A- 40: Pre-immersion D-load – Displacement Curve for pipe 22-T

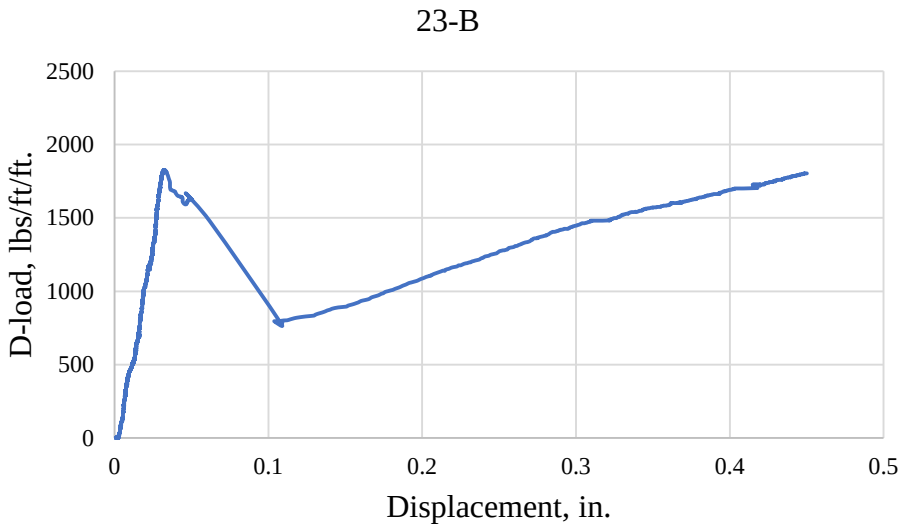

Figure A- 41: Pre-immersion D-load – Displacement Curve for pipe 23-B

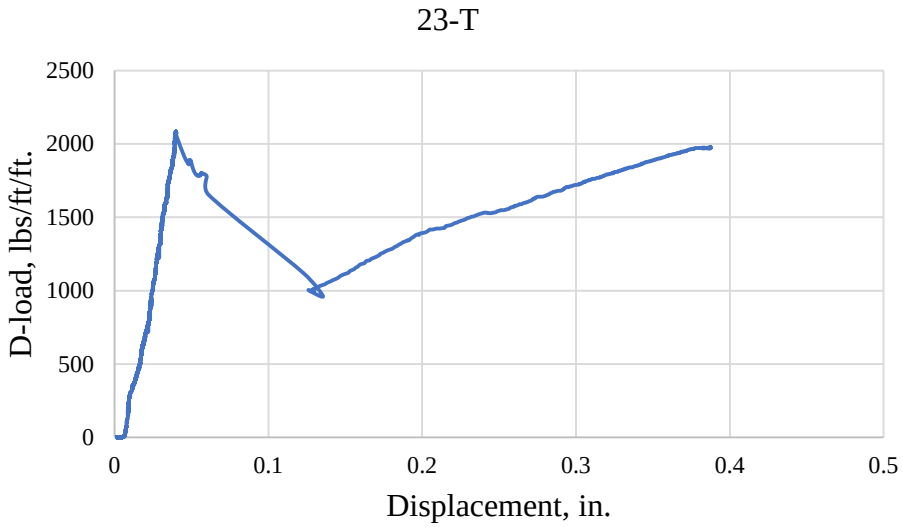

Figure A- 42: Pre-immersion D-load – Displacement Curve for pipe 23-T

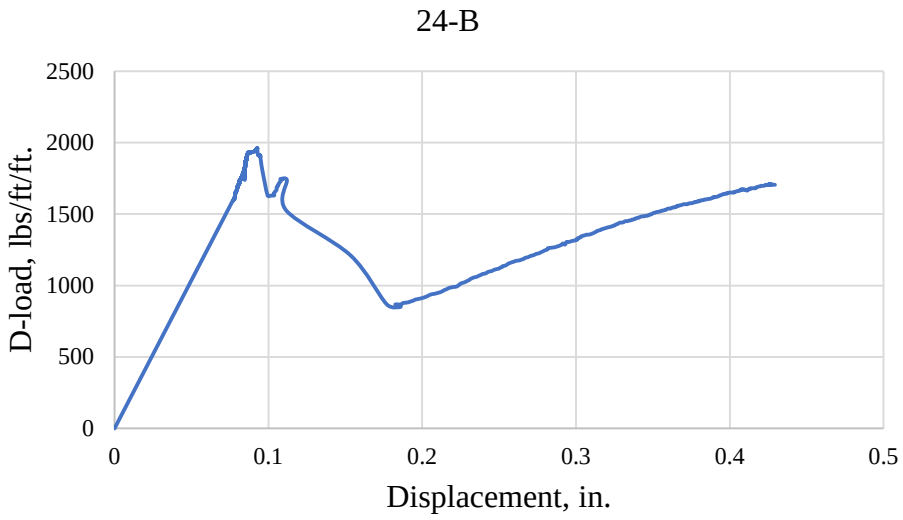

Figure A- 43: Pre-immersion D-load – Displacement Curve for pipe 24-B

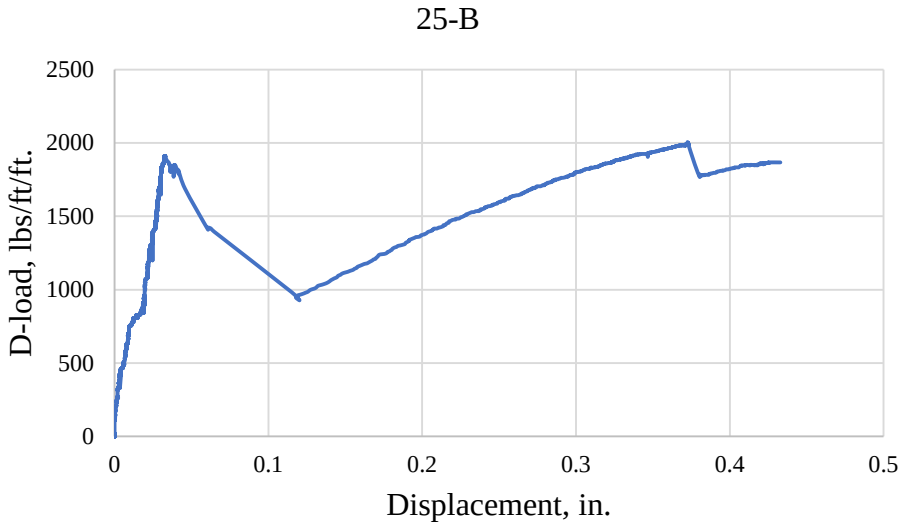

Figure A- 44: Pre-immersion D-load – Displacement Curve for pipe 25-B

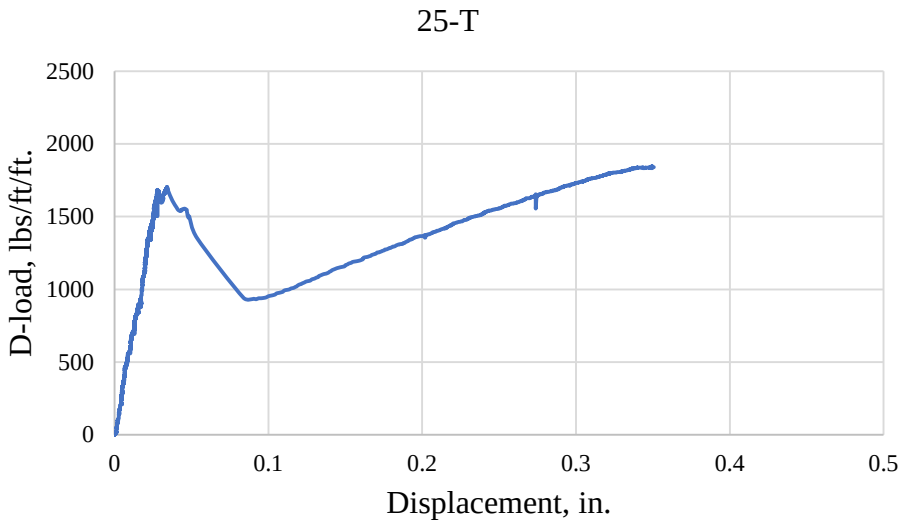

Figure A- 45: Pre-immersion D-load – Displacement Curve for pipe 25-T

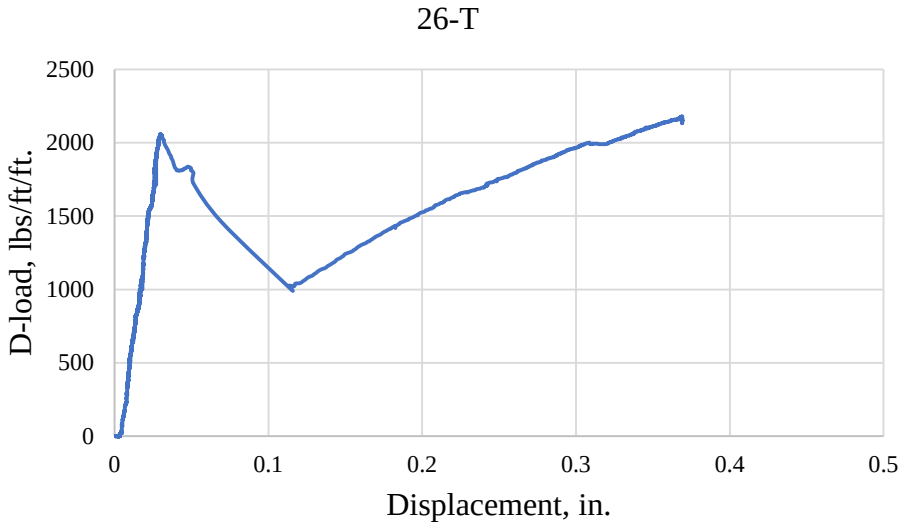

Figure A- 46: Pre-immersion D-load – Displacement Curve for pipe 26-T

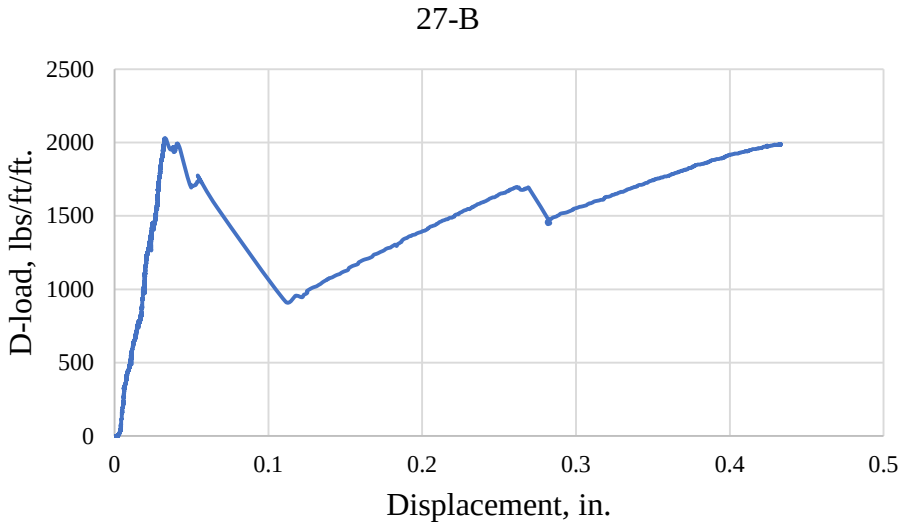

Figure A- 47: Pre-immersion D-load – Displacement Curve for pipe 27-B

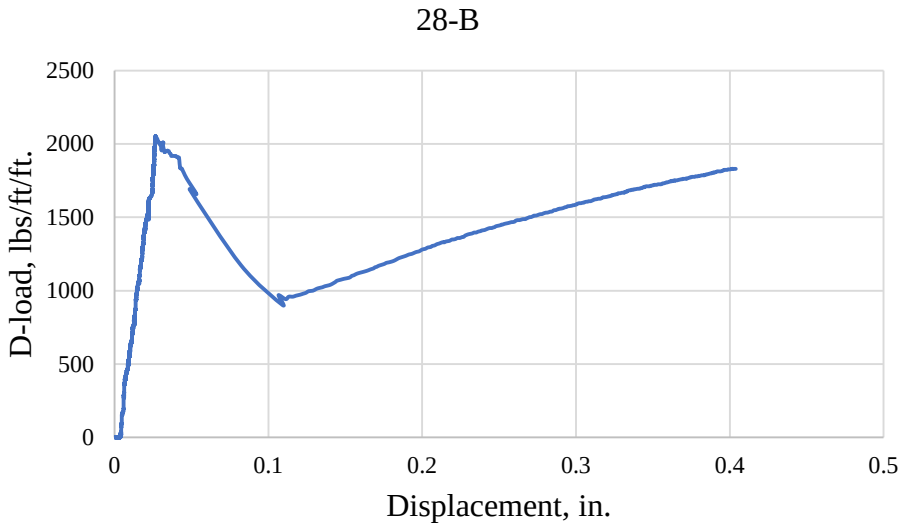

Figure A- 48: Pre-immersion D-load – Displacement Curve for pipe 28-B

Figure A- 49: Pre-immersion D-load – Displacement Curve for pipe 28-T

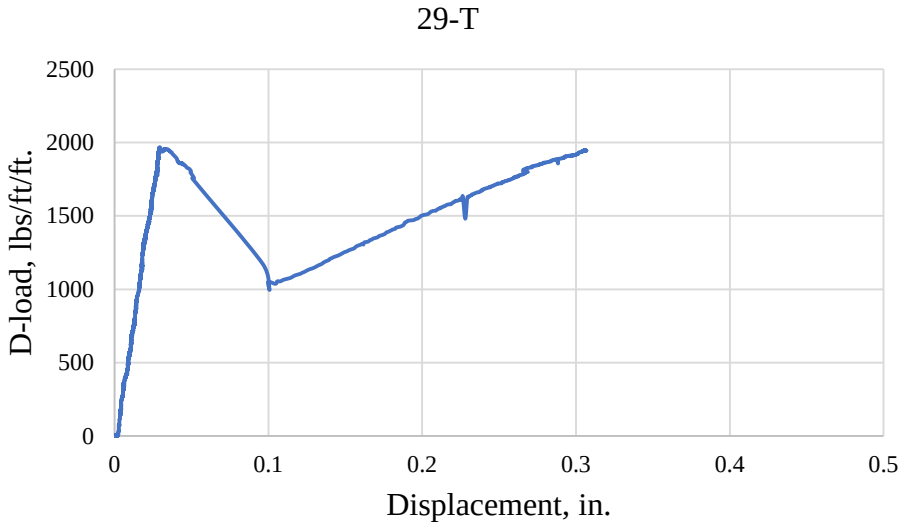

Figure A- 50: Pre-immersion D-load – Displacement Curve for pipe 29-T

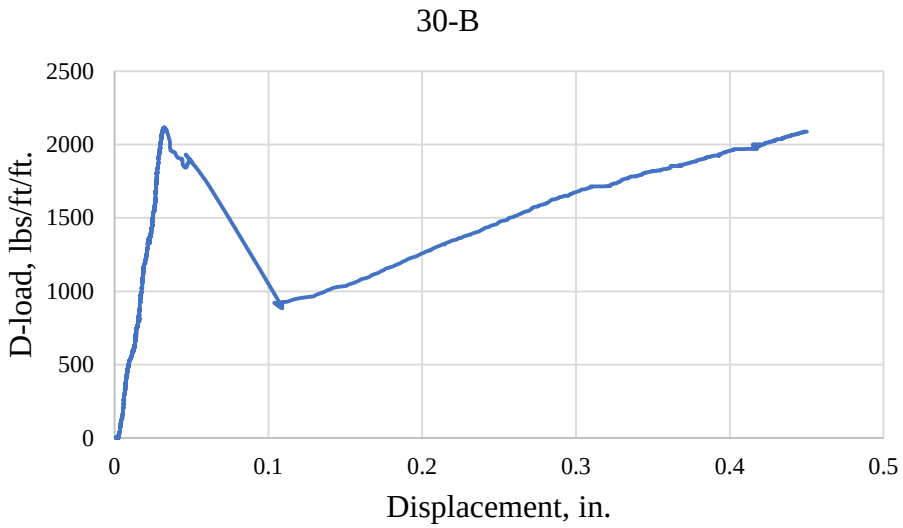

Figure A- 51: Pre-immersion D-load – Displacement Curve for pipe 30-B

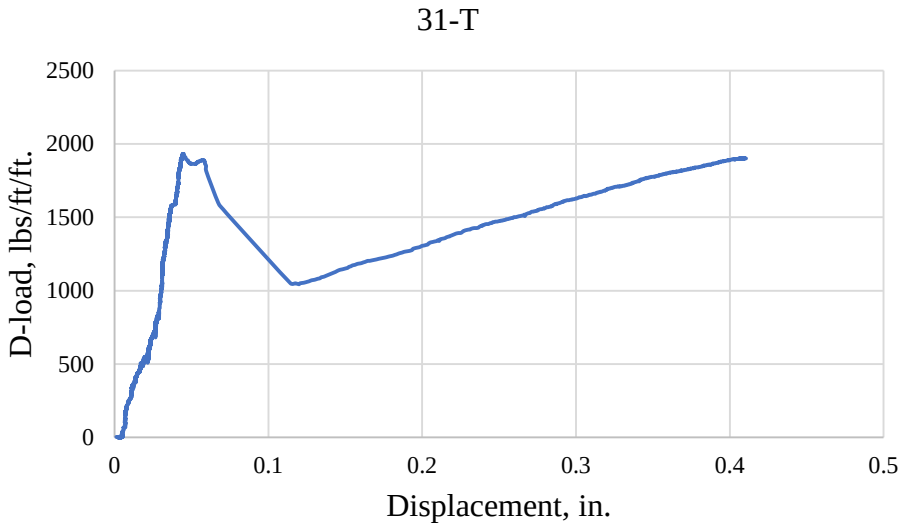

Figure A- 52: Pre-immersion D-load – Displacement Curve for pipe 31-T

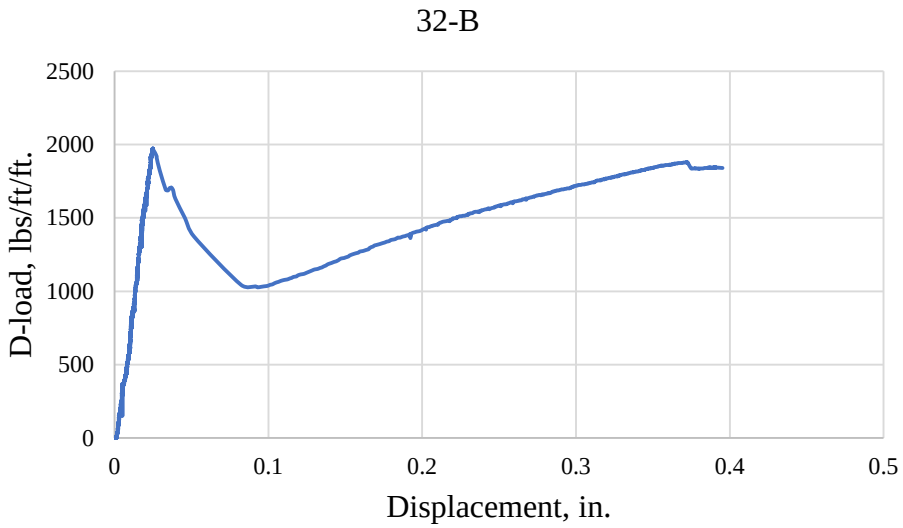

Figure A- 53: Pre-immersion D-load – Displacement Curve for pipe 32-B

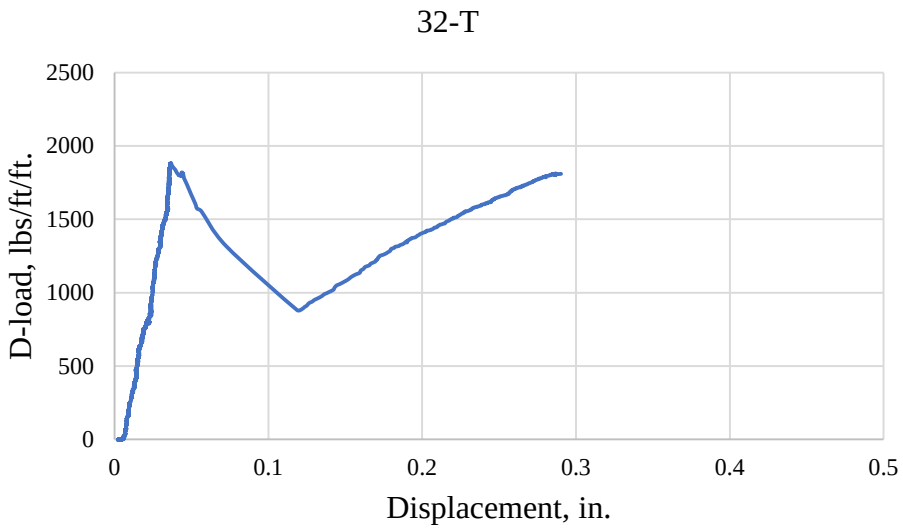

Figure A- 54: Pre-immersion D-load – Displacement Curve for pipe 32-T

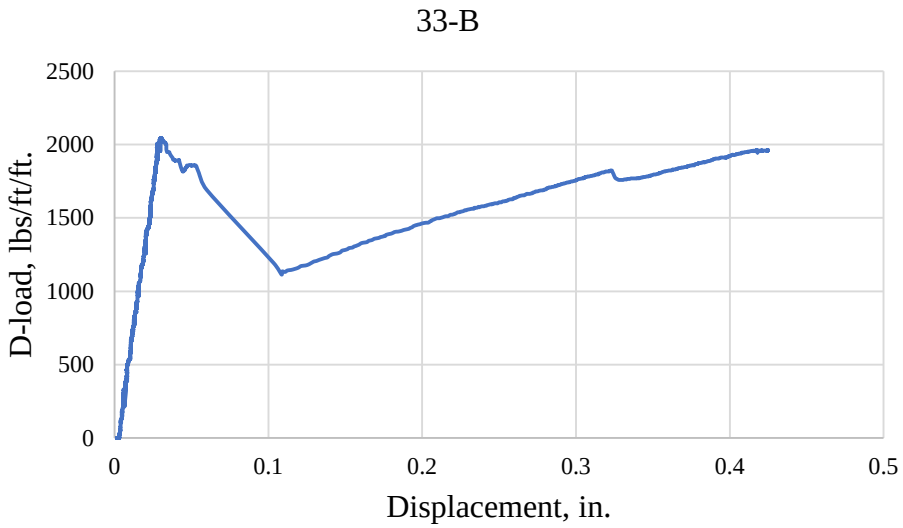

Figure A- 55: Pre-immersion D-load – Displacement Curve for pipe 33-B

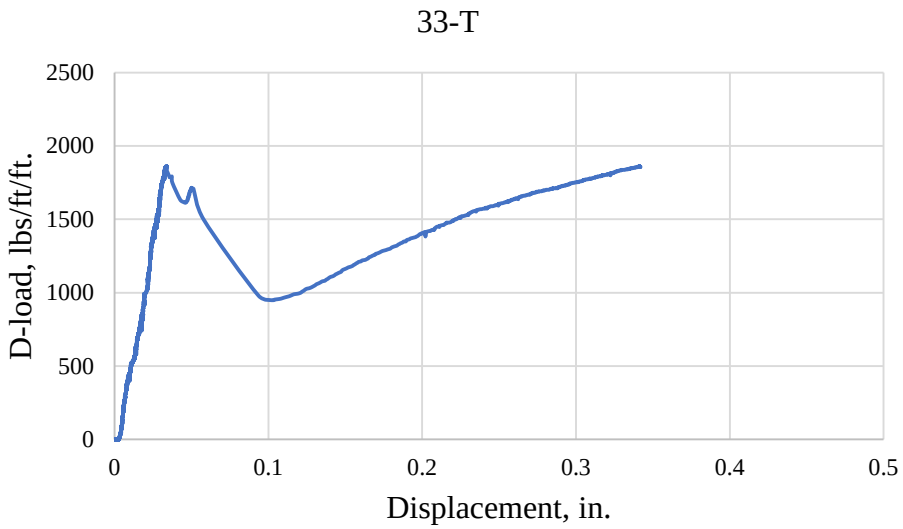

Figure A- 56: Pre-immersion D-load – Displacement Curve for pipe 33-T

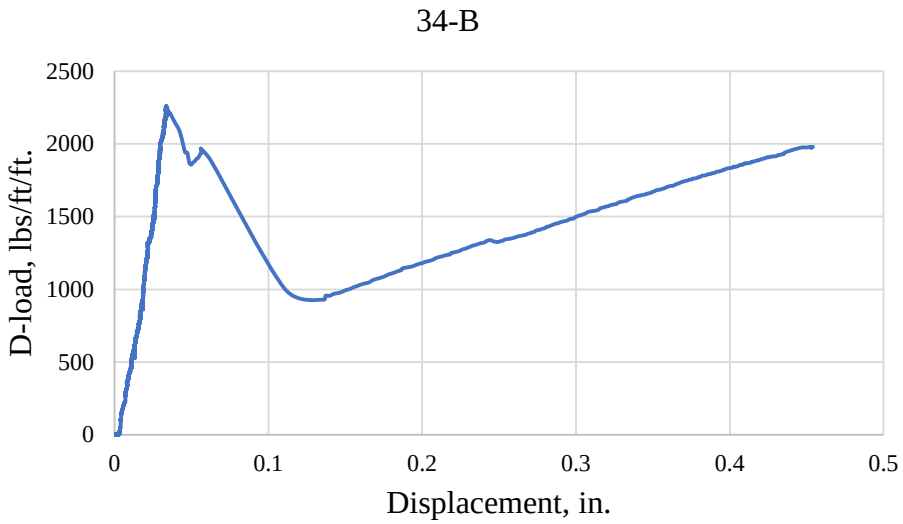

Figure A- 57: Pre-immersion D-load – Displacement Curve for pipe 34-B

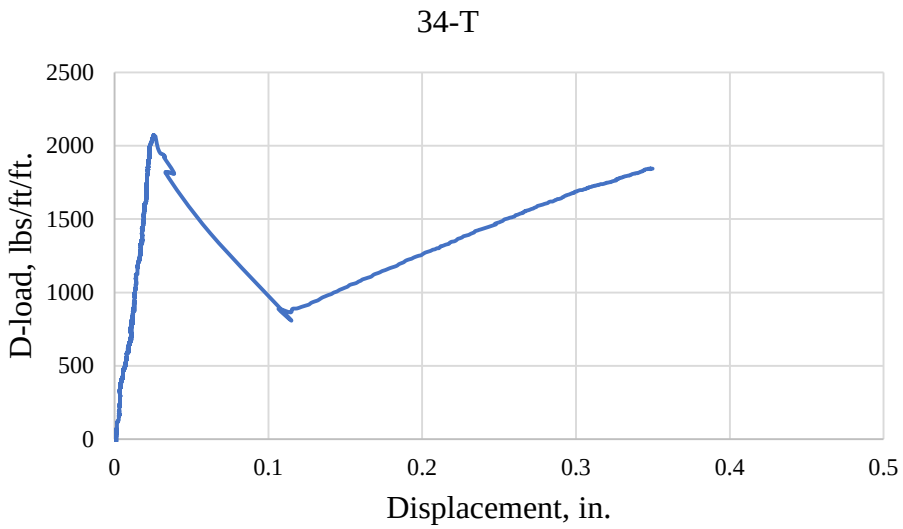

Figure A- 58: Pre-immersion D-load – Displacement Curve for pipe 34-T

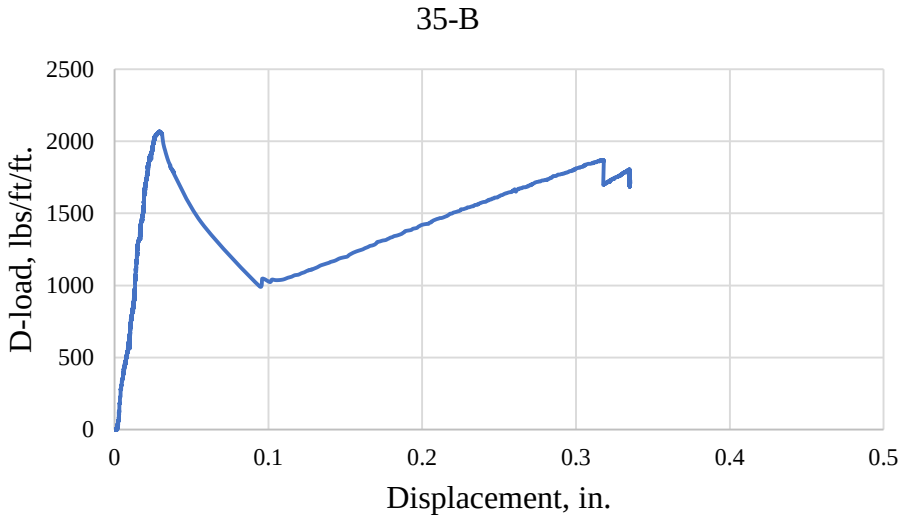

Figure A- 59: Pre-immersion D-load – Displacement Curve for pipe 35-B

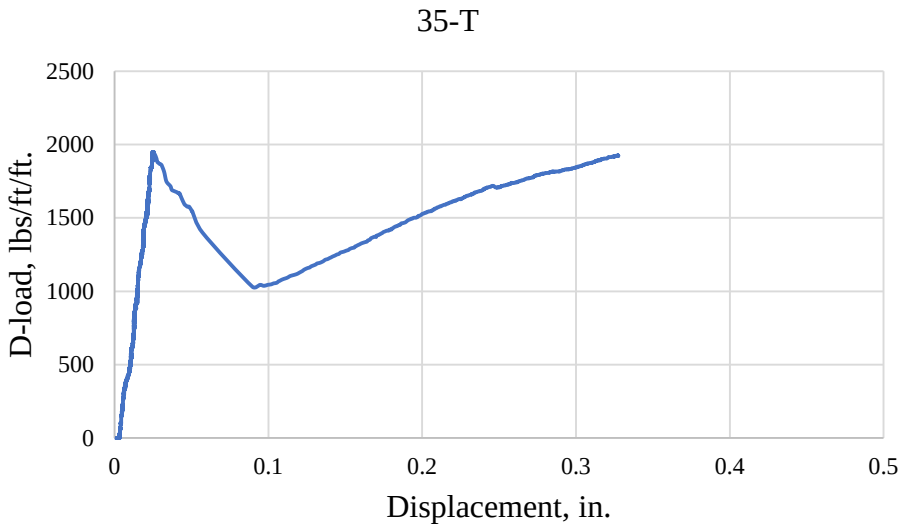

Figure A- 60: Pre-immersion D-load – Displacement Curve for pipe 35-T

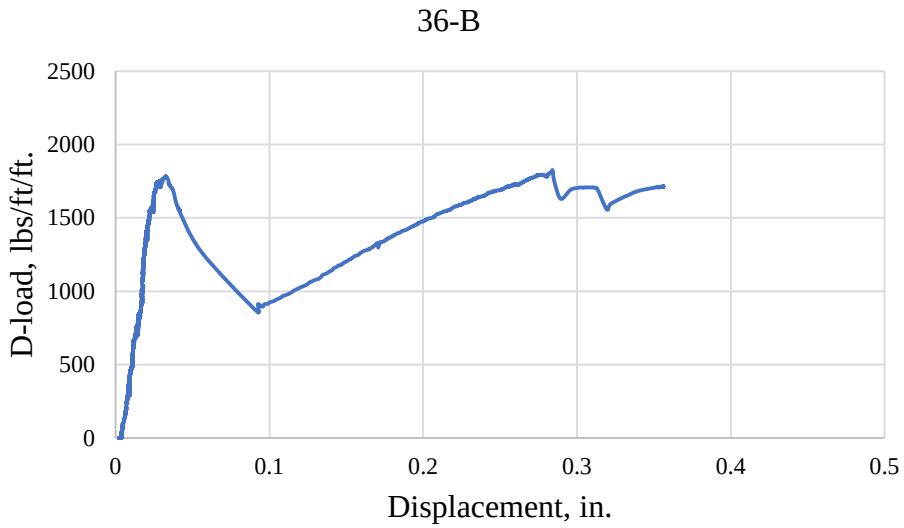

Figure A- 61: Pre-immersion D-load – Displacement Curve for pipe 36-B

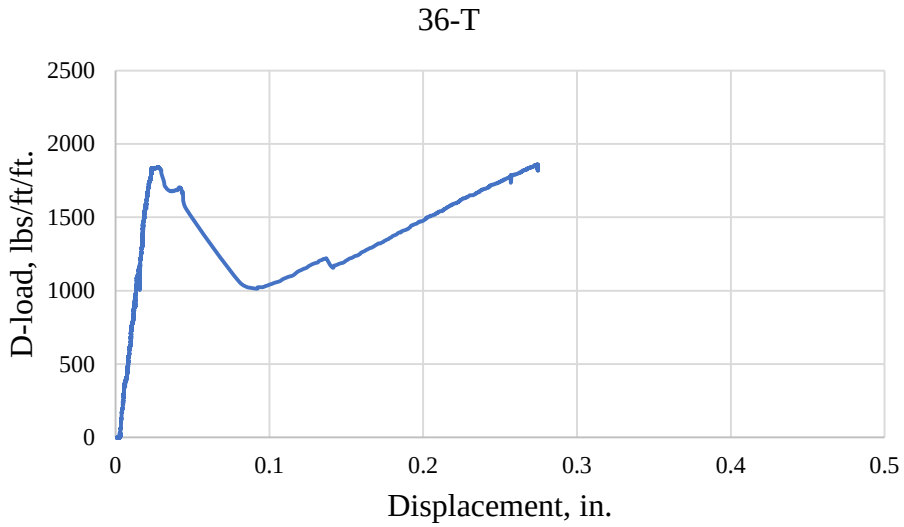

Figure A- 62: Pre-immersion D-load – Displacement Curve for pipe 36-T

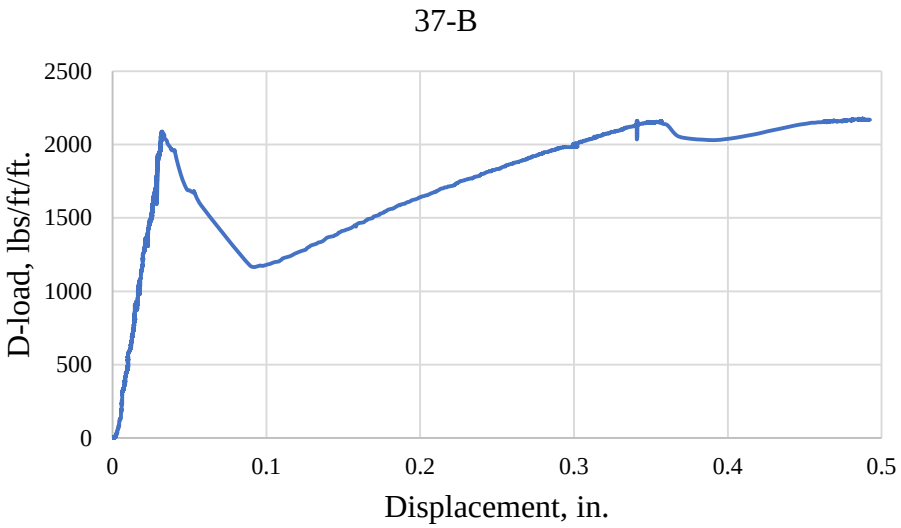

Figure A- 63: Pre-immersion D-load – Displacement Curve for pipe 37-B

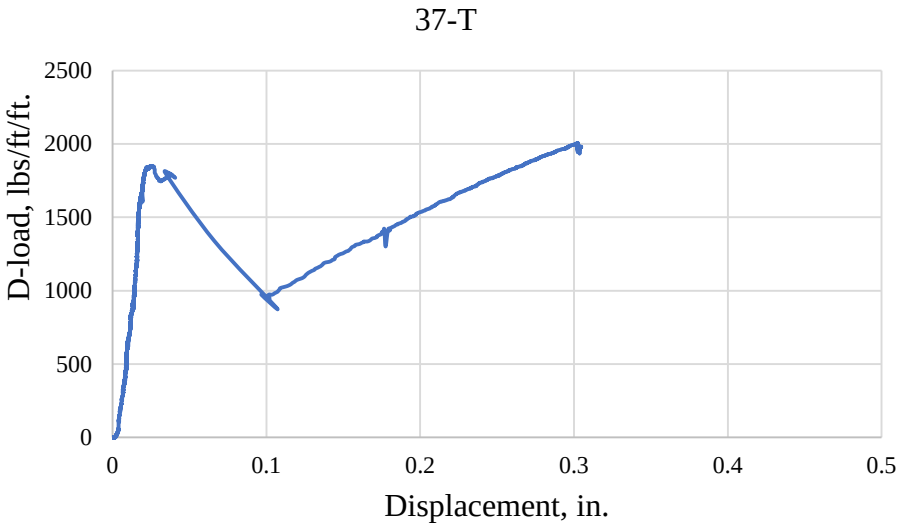

Figure A- 64: Pre-immersion D-load – Displacement Curve for pipe 37-T

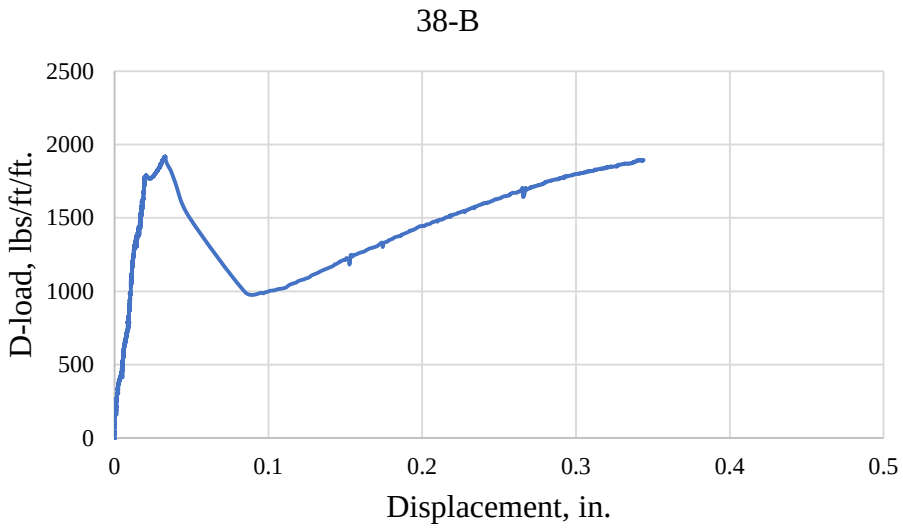

Figure A- 65: Pre-immersion D-load – Displacement Curve for pipe 38-B

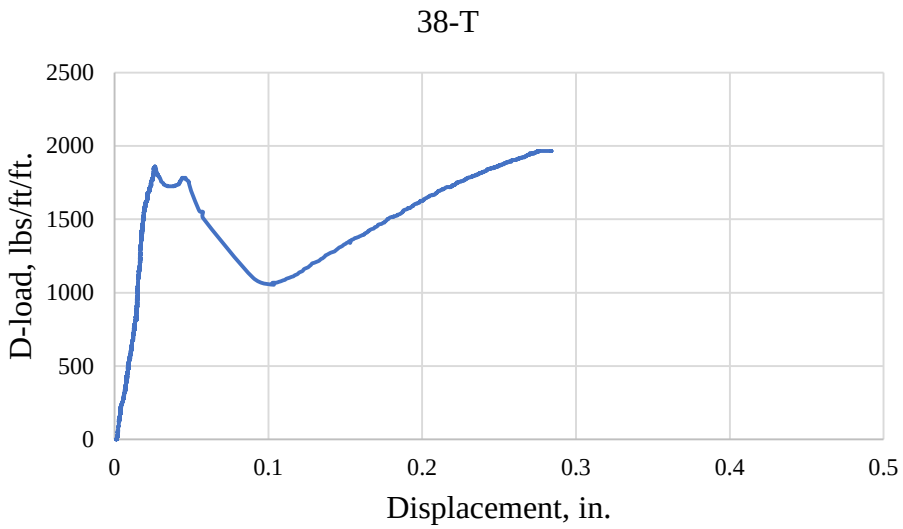

Figure A- 66: Pre-immersion D-load – Displacement Curve for pipe 38-T

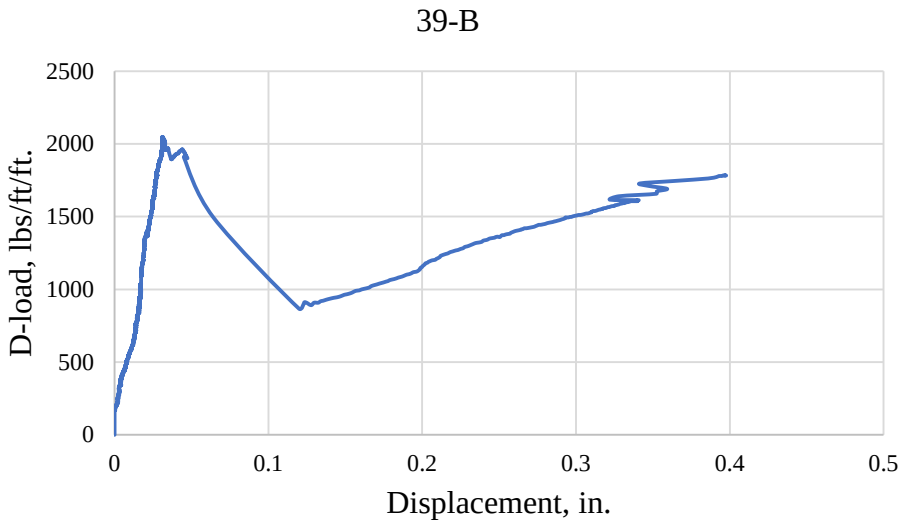

Figure A- 67: Pre-immersion D-load – Displacement Curve for pipe 39-B

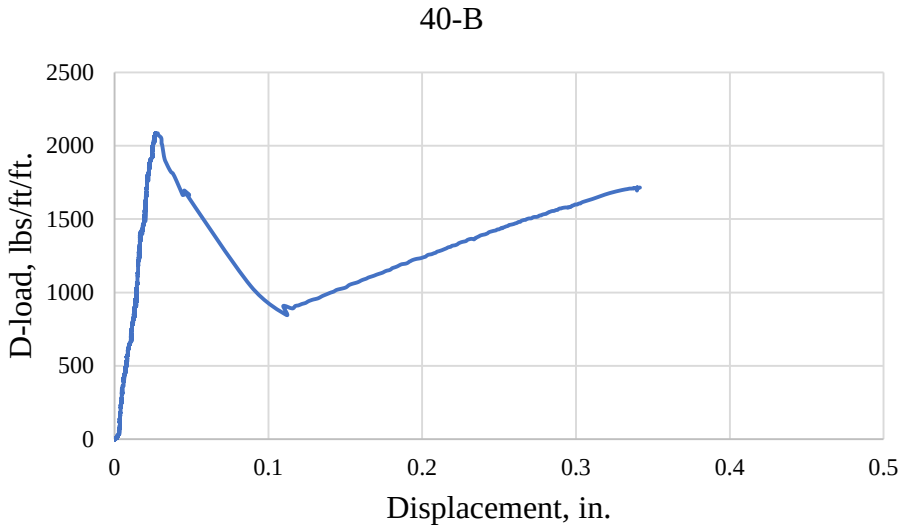

Figure A- 68: Pre-immersion D-load – Displacement Curve for pipe 40-B

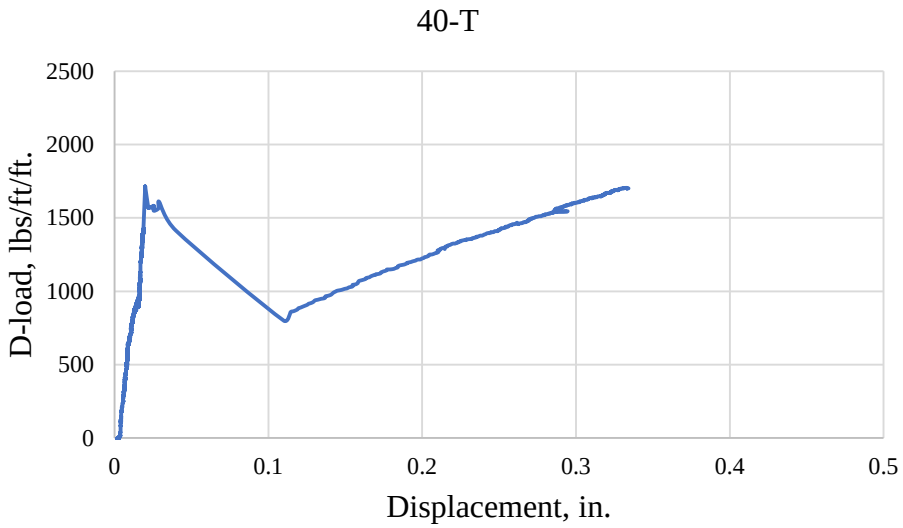

Figure A- 69: Pre-immersion D-load – Displacement Curve for pipe 40-T

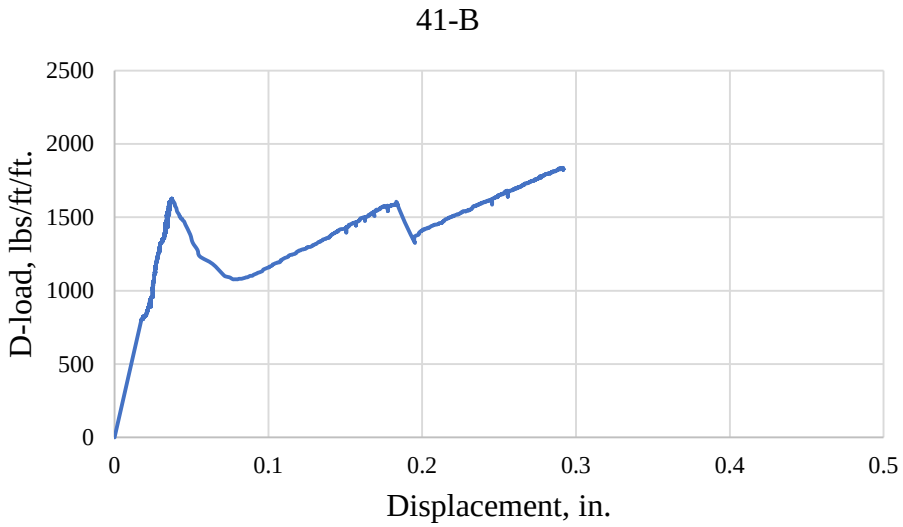

Figure A- 70: Pre-immersion D-load – Displacement Curve for pipe 41-B

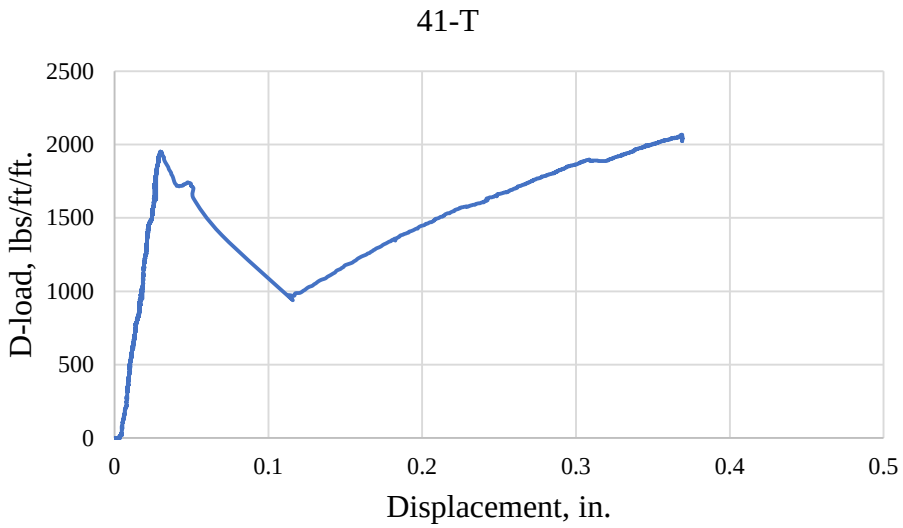

Figure A- 71: Pre-immersion D-load – Displacement Curve for pipe 41-T

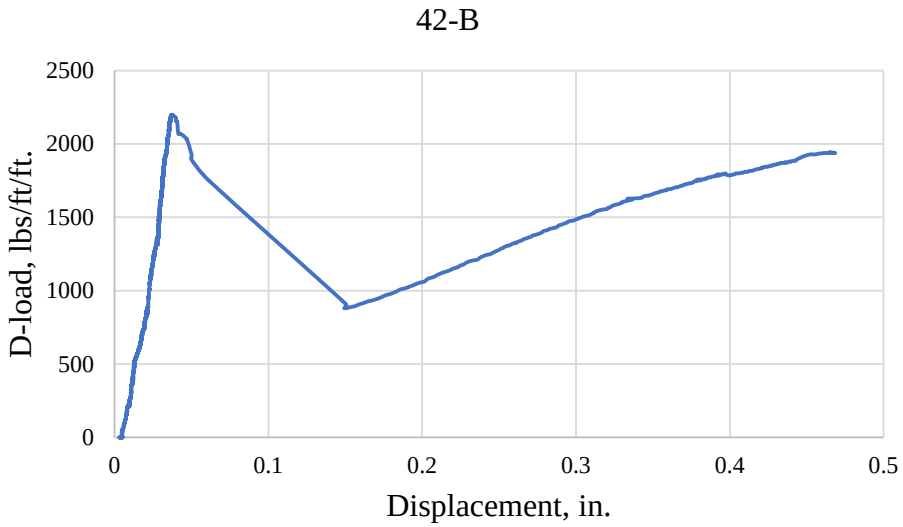

Figure A- 72: Pre-immersion D-load – Displacement Curve for pipe 42-B

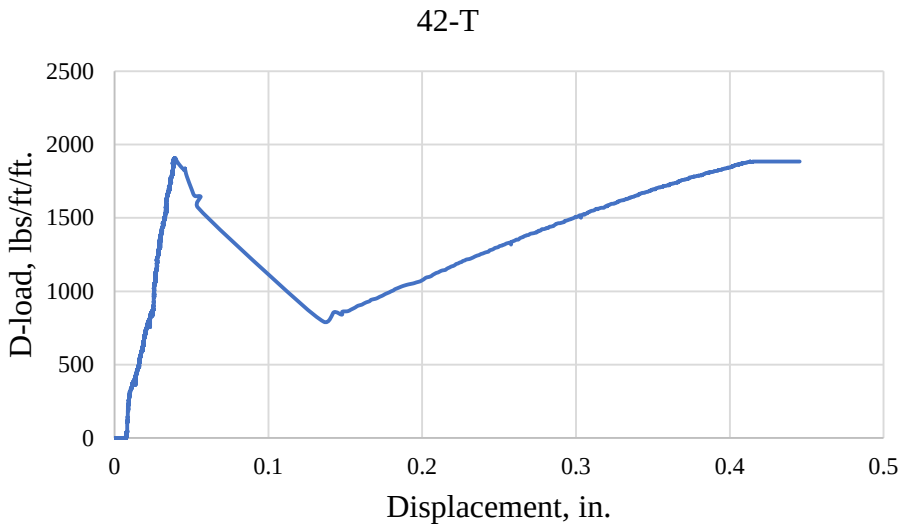

Figure A- 73: Pre-immersion D-load – Displacement Curve for pipe 42-T

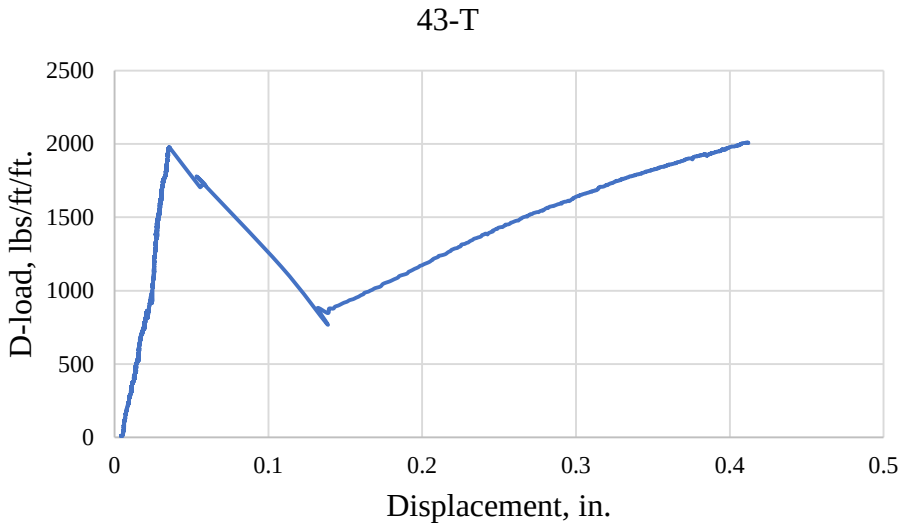

Figure A- 74: Pre-immersion D-load – Displacement Curve for pipe 43-T

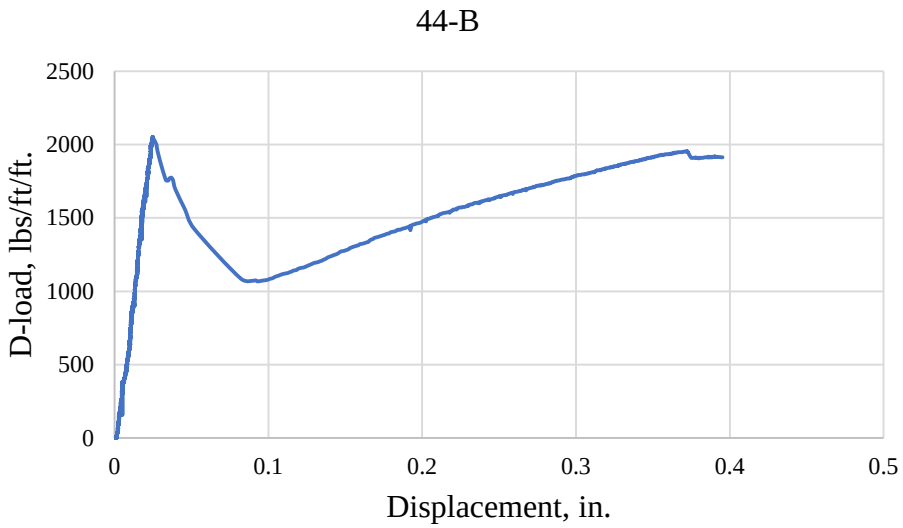

Figure A- 75: Pre-immersion D-load – Displacement Curve for pipe 44-B

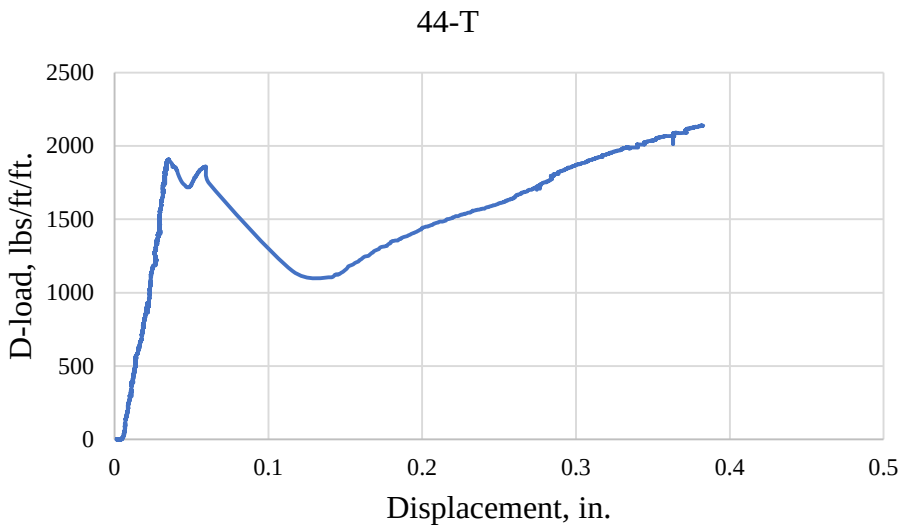

Figure A- 76: Pre-immersion D-load – Displacement Curve for pipe 44-T

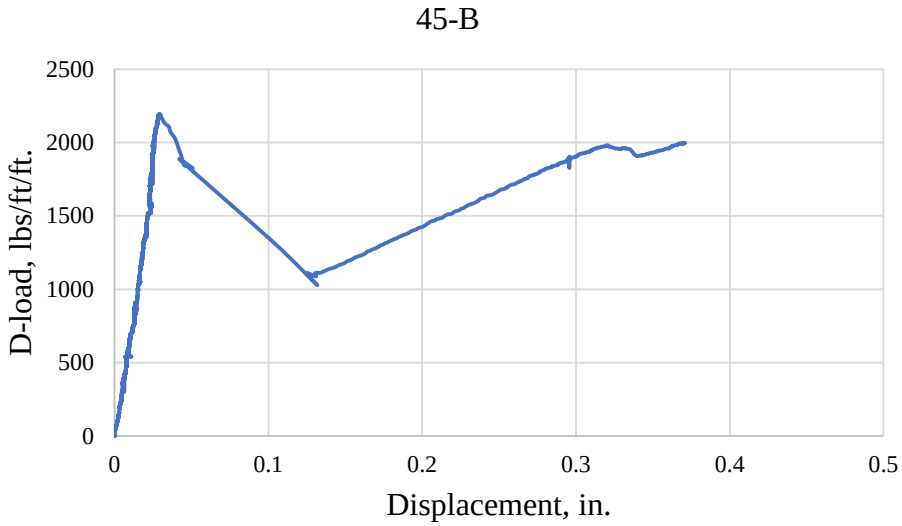

Figure A- 77: Pre-immersion D-load – Displacement Curve for pipe 45-B

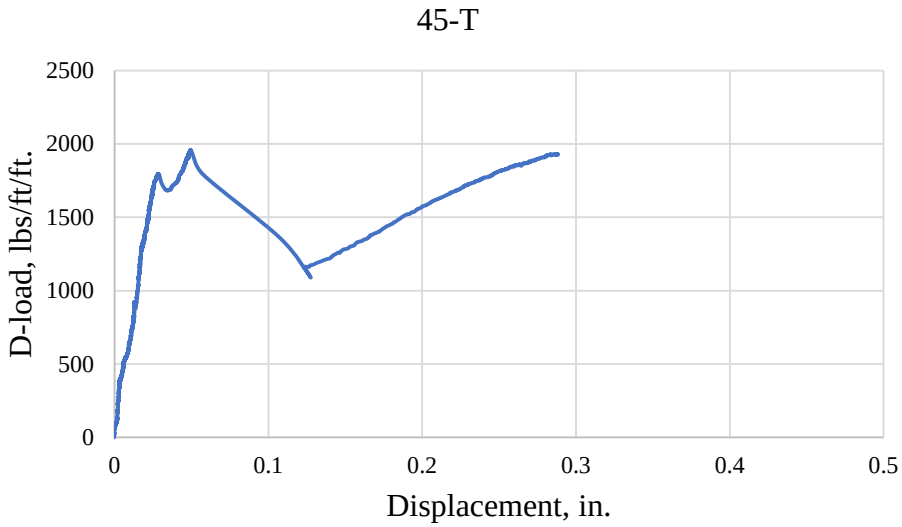

Figure A- 78: Pre-immersion D-load – Displacement Curve for pipe 45-T

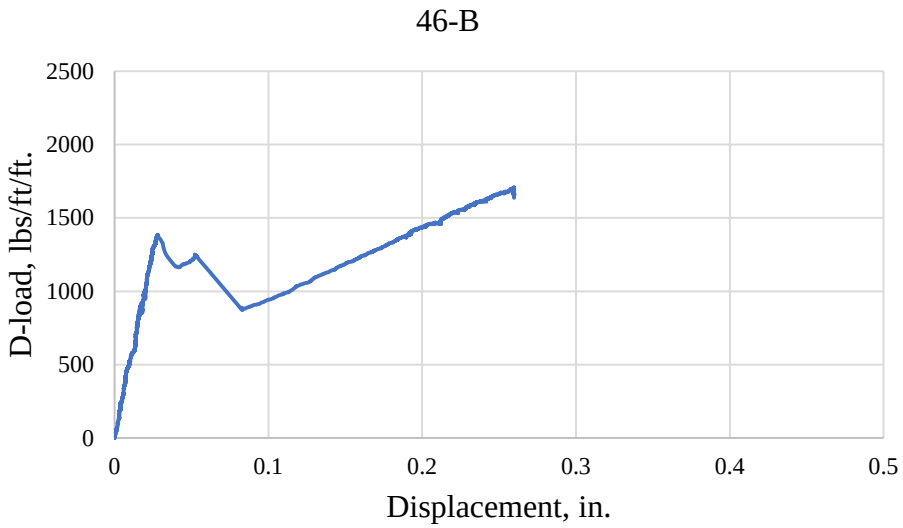

Figure A- 79: Pre-immersion D-load – Displacement Curve for pipe 46-B

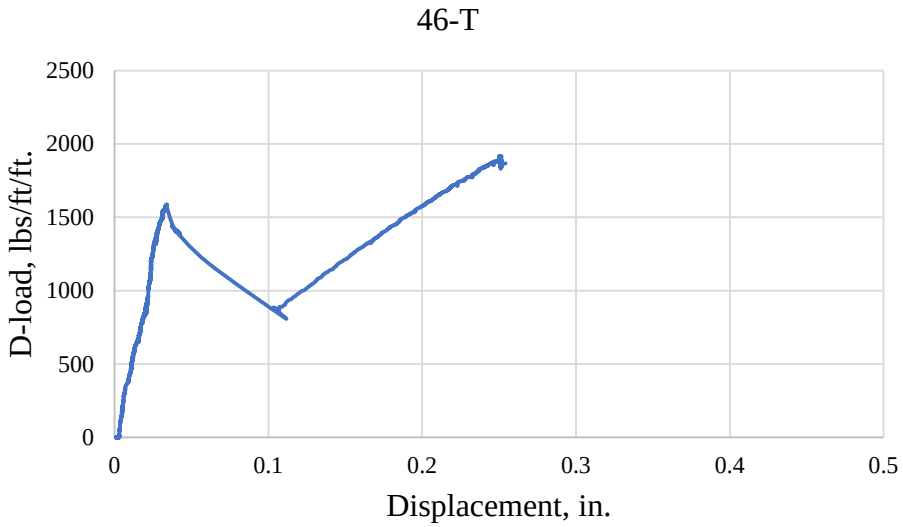

Figure A- 80: Pre-immersion D-load – Displacement Curve for pipe 46-T

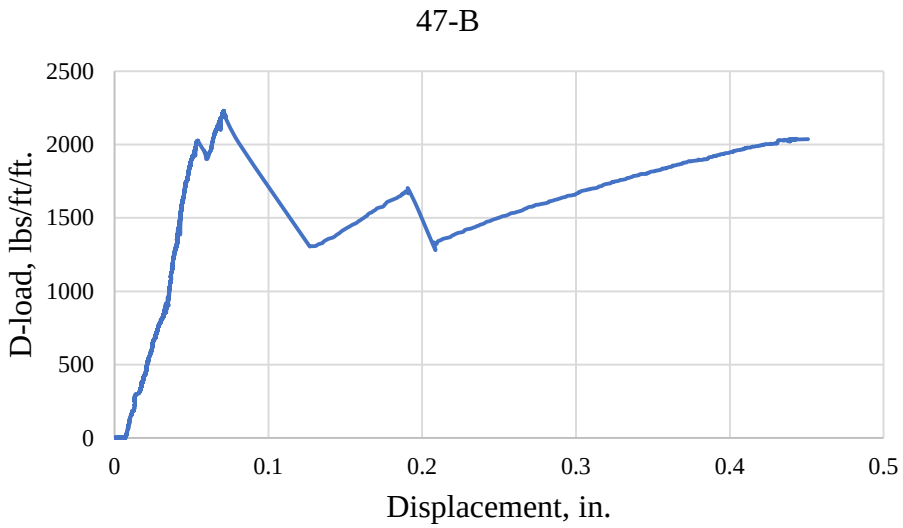

Figure A- 81: Pre-immersion D-load – Displacement Curve for pipe 47-B

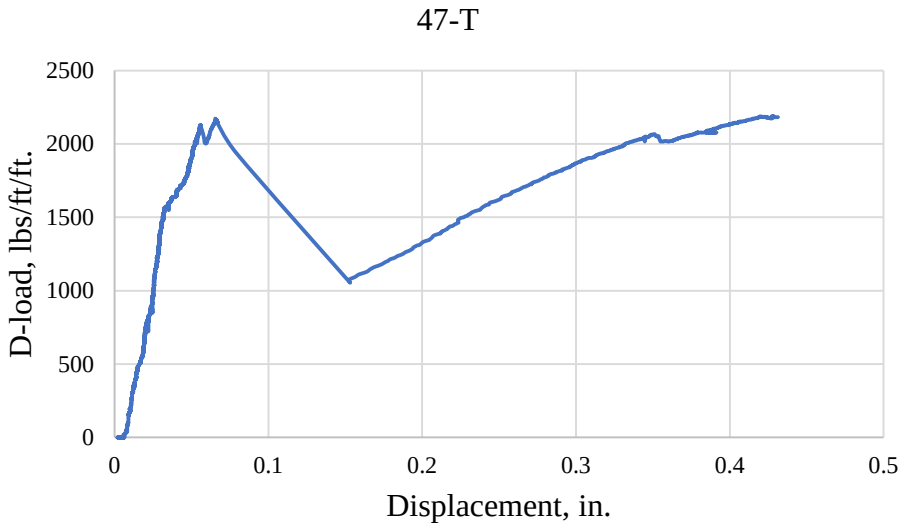

Figure A- 82: Pre-immersion D-load – Displacement Curve for pipe 47-T

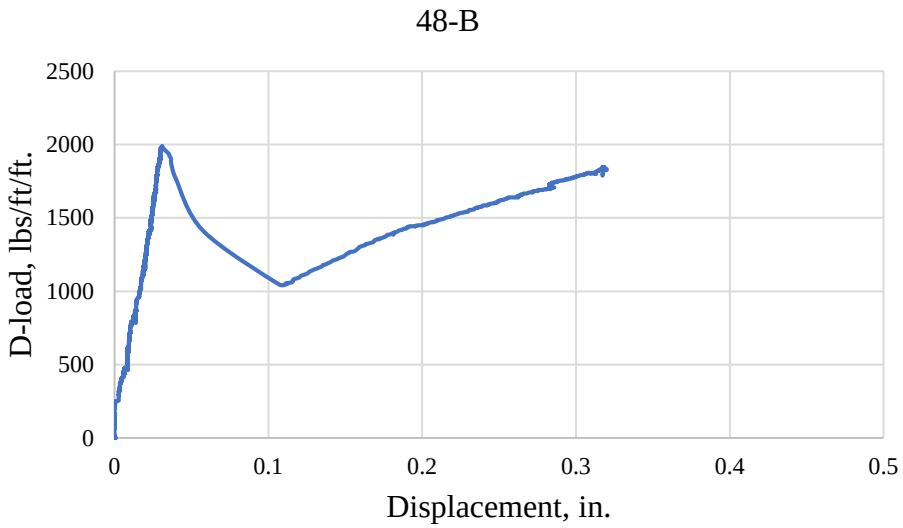

Figure A- 83: Pre-immersion D-load – Displacement Curve for pipe 48-B

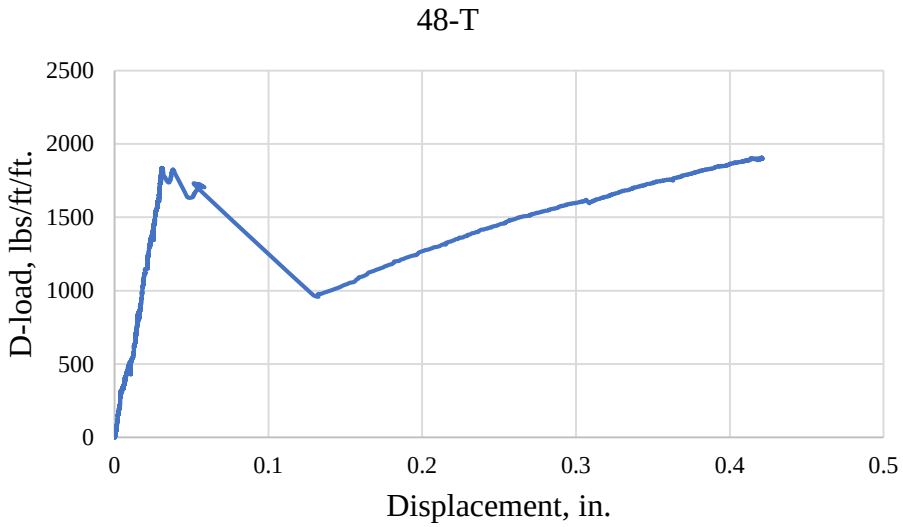

Figure A- 84: Pre-immersion D-load – Displacement Curve for pipe 48-T

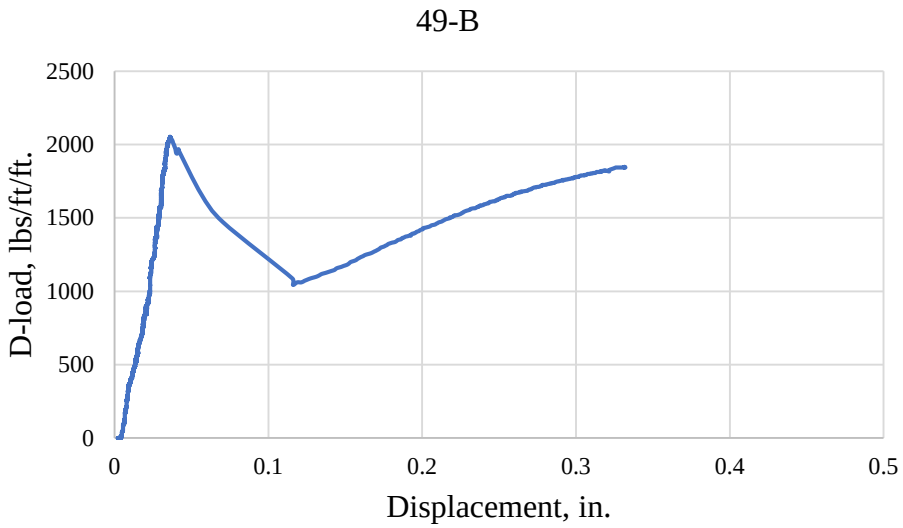

Figure A- 85: Pre-immersion D-load – Displacement Curve for pipe 49-B

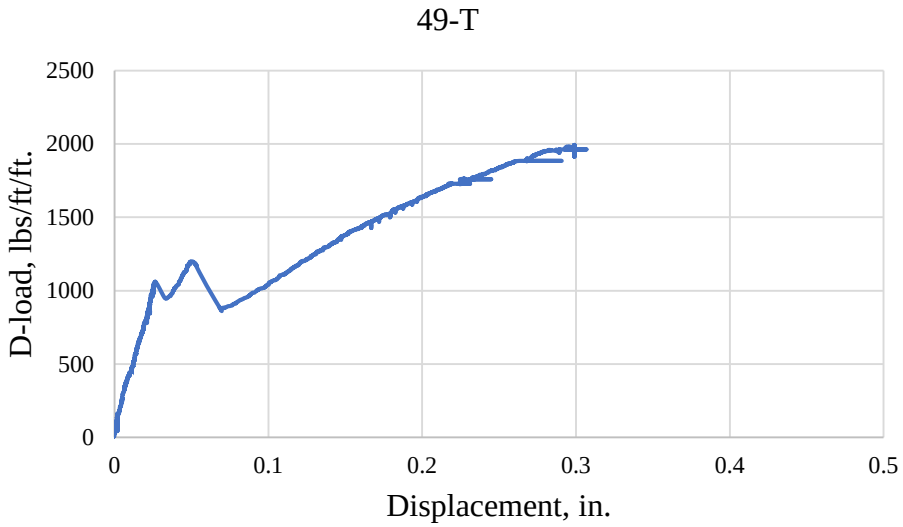

Figure A- 86: Pre-immersion D-load – Displacement Curve for pipe 49-T

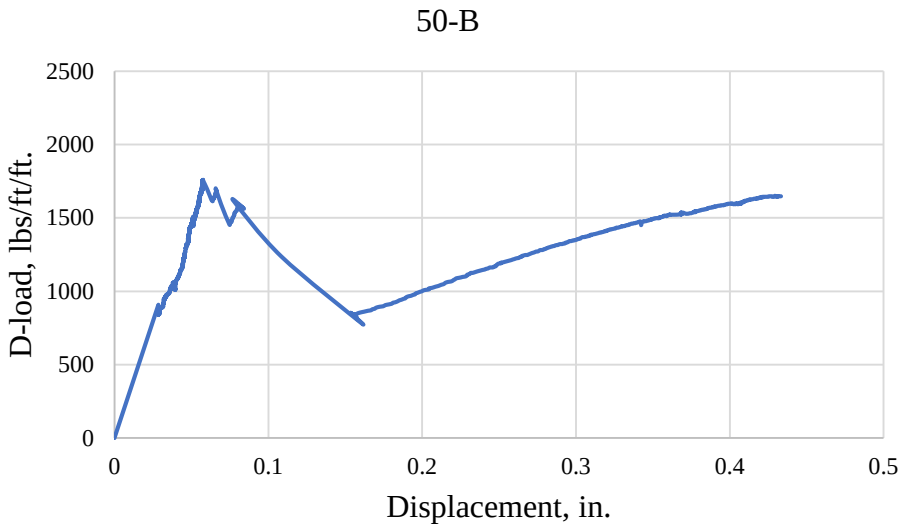

Figure A- 87: Pre-immersion D-load – Displacement Curve for pipe 50-B

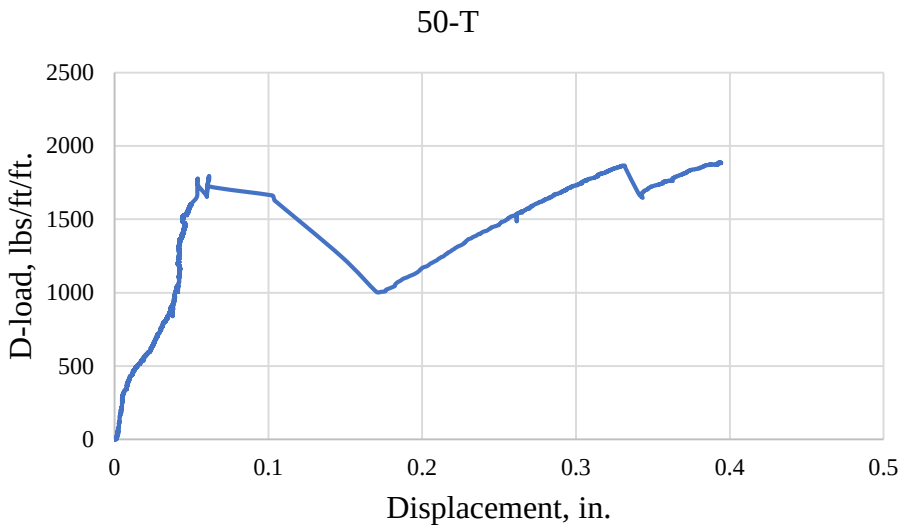

Figure A- 88: Pre-immersion D-load – Displacement Curve for pipe 50-T

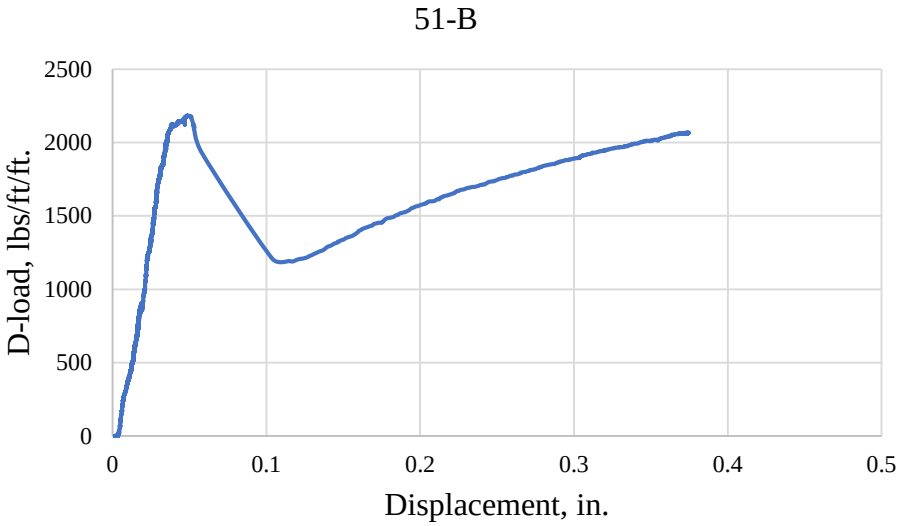

Figure A- 89: Pre-immersion D-load – Displacement Curve for pipe 51-B

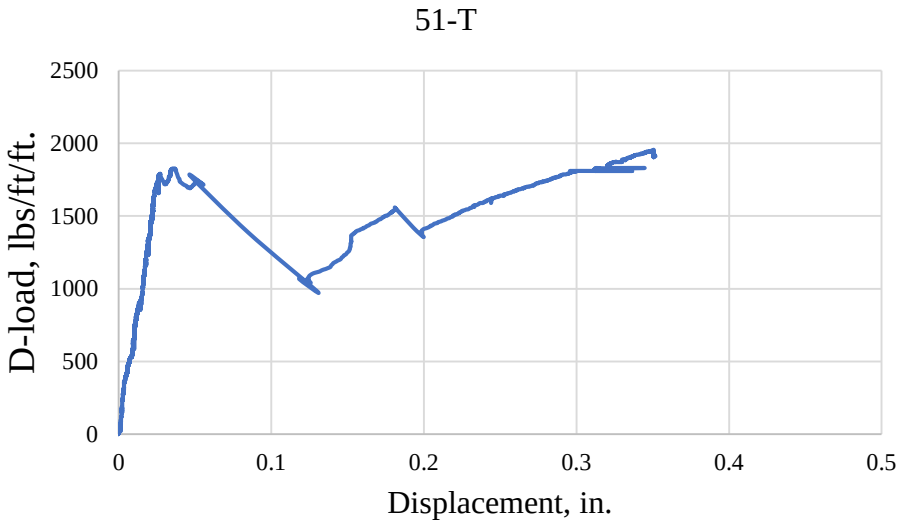

Figure A- 90: Pre-immersion D-load – Displacement Curve for pipe 51-T

APPENDIX – B

Post-immersion D-Load – Displacement Curves:

First month test results:

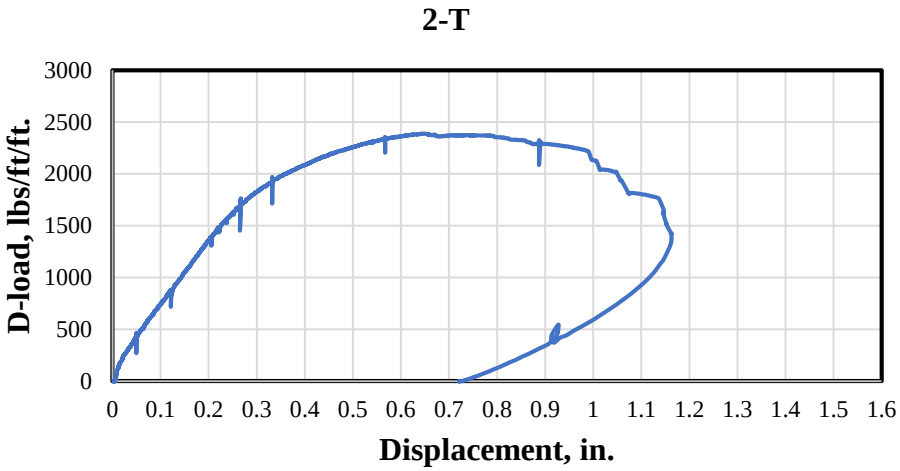

Figure B- 1: Post-immersion D-load test results for Month-01 for pipe 02-T subjected to 200 PPM Sodium Chloride Solution

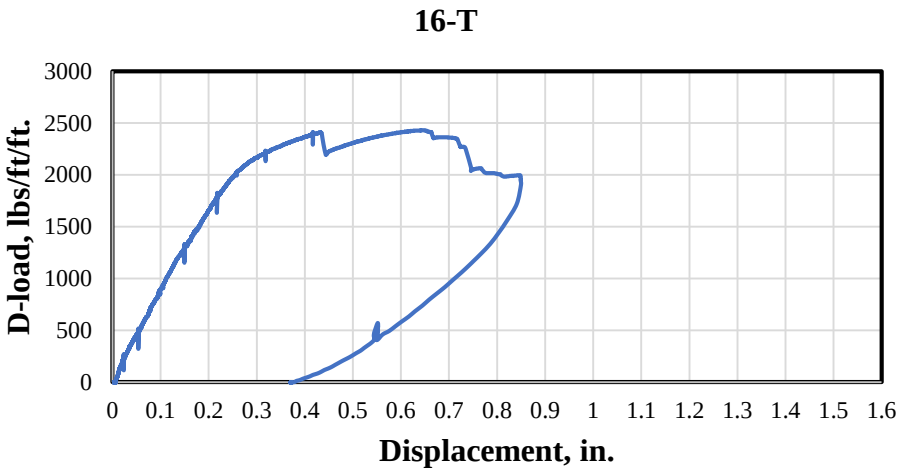

Figure B- 2: Post-immersion D-load test results for Month-01 for pipe 16-T subjected to 200 PPM Sodium Chloride Solution

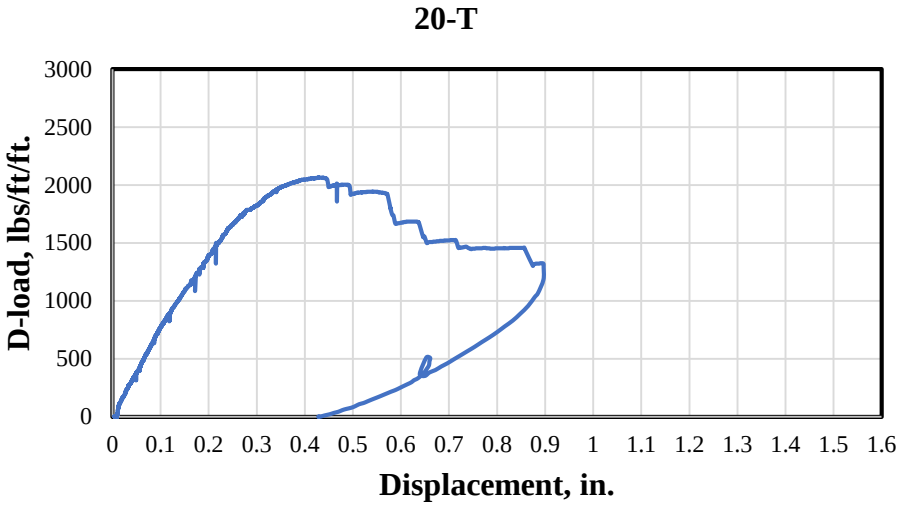

Figure B- 3: Post-immersion D-load test results for Month-01 for pipe 20-T subjected to 200 PPM Sodium Chloride Solution

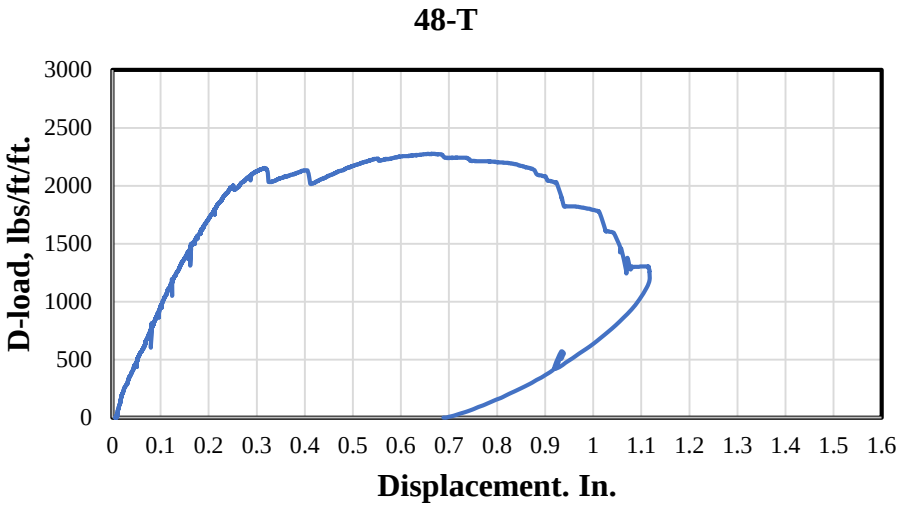

Figure B- 4: Post-immersion D-load test results for Month-01 for pipe 48-T subjected to 2,000 PPM Sodium Chloride Solution

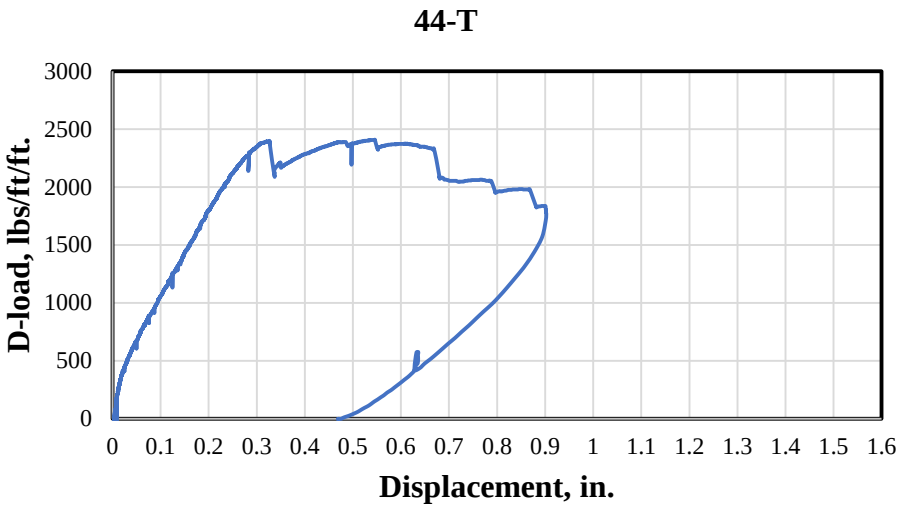

Figure B-5: Post-immersion D-load test results for Month-01 for pipe 44-T subjected to 2,000 PPM Sodium Chloride Solution

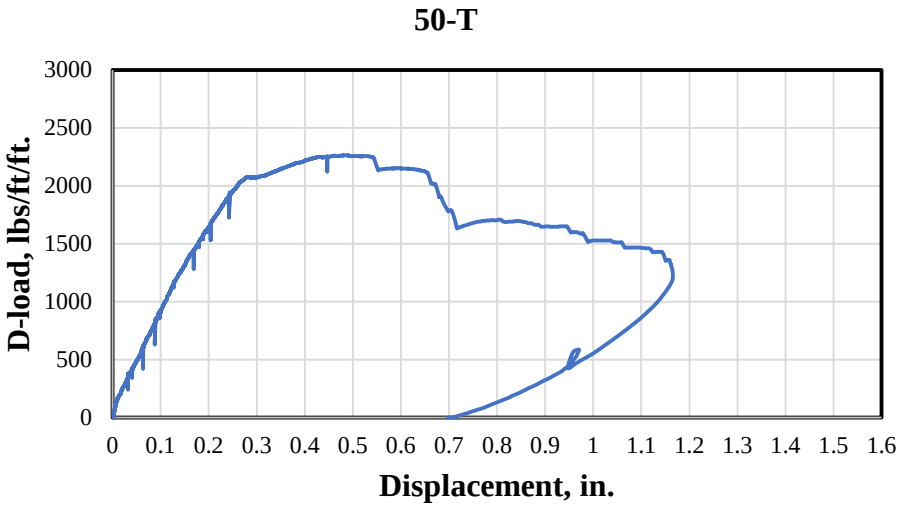

Figure B-6: Post-immersion D-load test results for Month-01 for pipe 50-T subjected to 2,000 PPM Sodium Chloride Solution

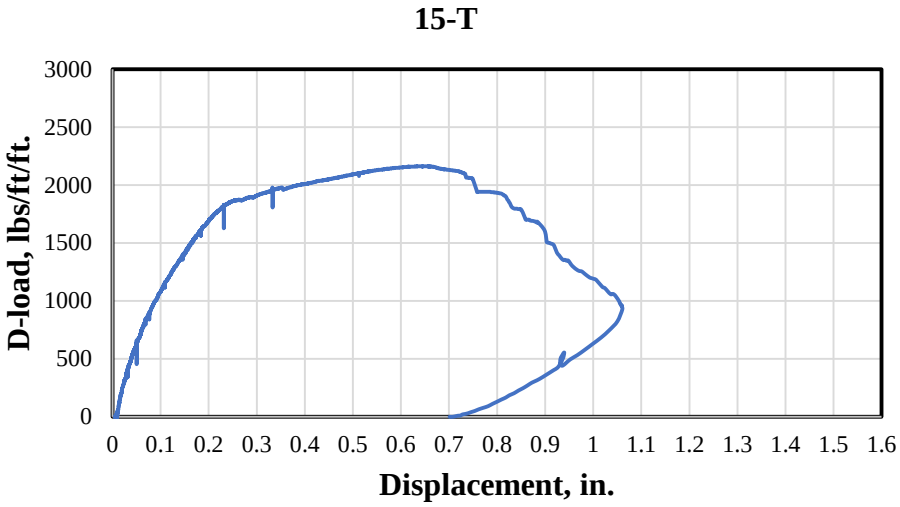

Figure B-7: Post-immersion D-load test results for Month-01 for pipe 15-T subjected to 30,000 PPM Sodium Chloride Solution

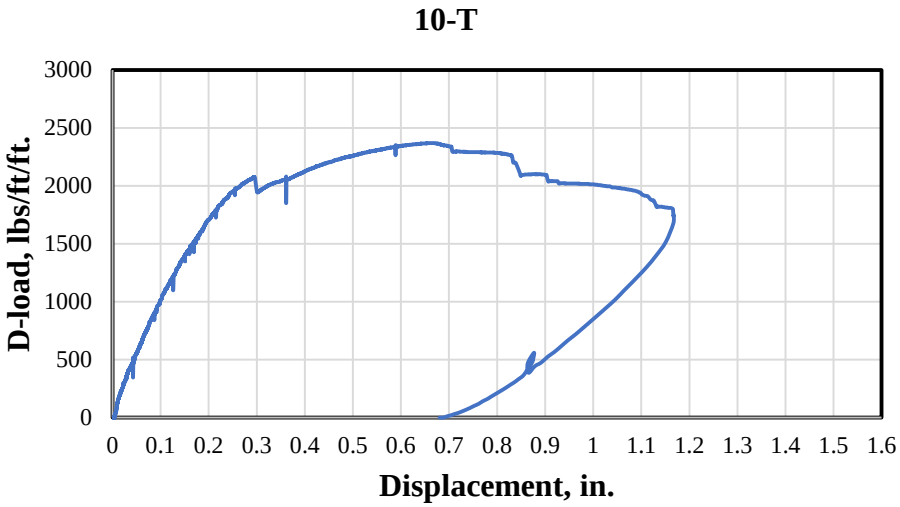

Figure B-8: Post-immersion D-load test results for Month-01 for pipe 10-T subjected to 30,000 PPM Sodium Chloride Solution

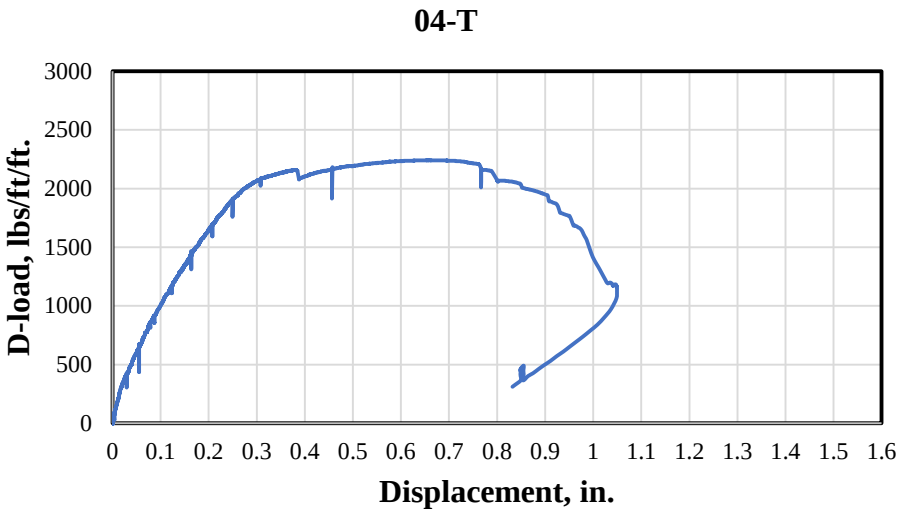

Figure B-9: Post-immersion D-load test results for Month-01 for pipe 04-T subjected to 30,000 PPM Sodium Chloride Solution

Second month test results:

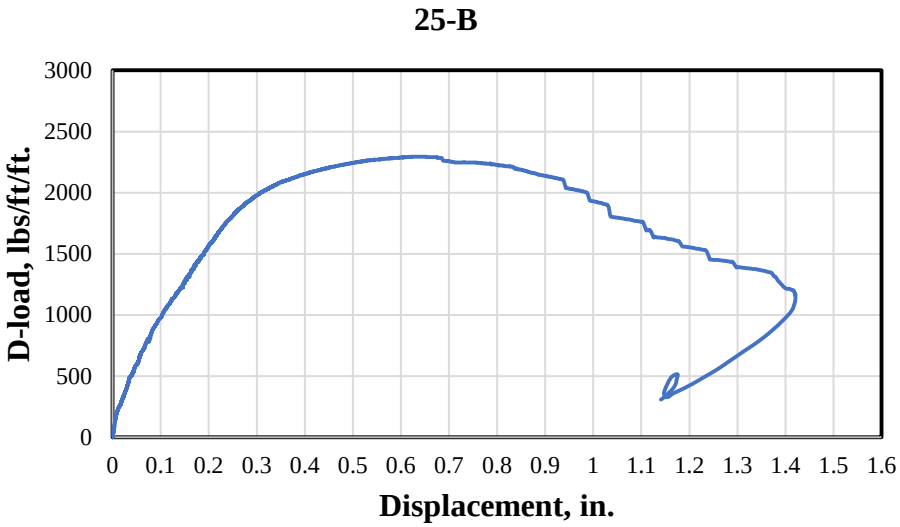

Figure B-10: Post-immersion D-load test results for Month-02 for pipe 25-B subjected to 30,000 PPM Sodium Chloride Solution

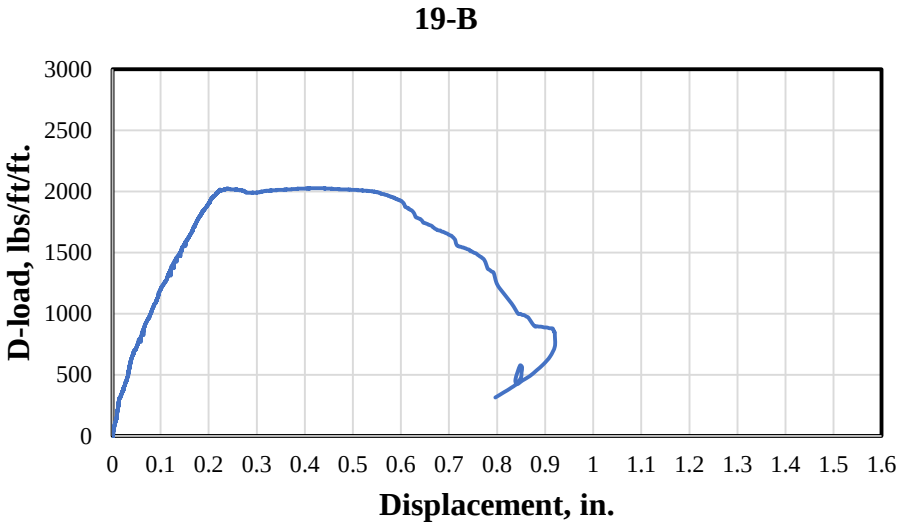

Figure B-11: Post-immersion D-load test results for Month-02 for pipe 19-B subjected to 30,000 PPM Sodium Chloride Solution

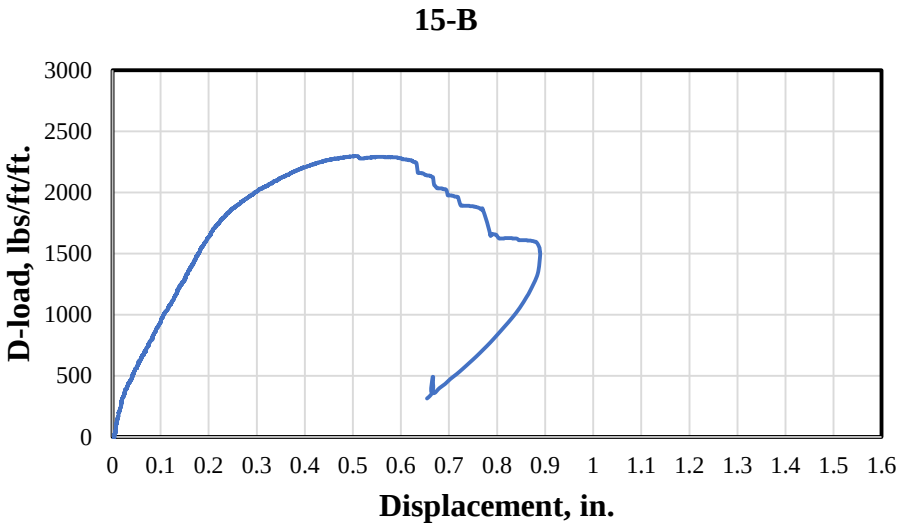

Figure B-12: Post-immersion D-load test results for Month-02 for pipe 15-B subjected to 30,000 PPM Sodium Chloride Solution

Third month test results:

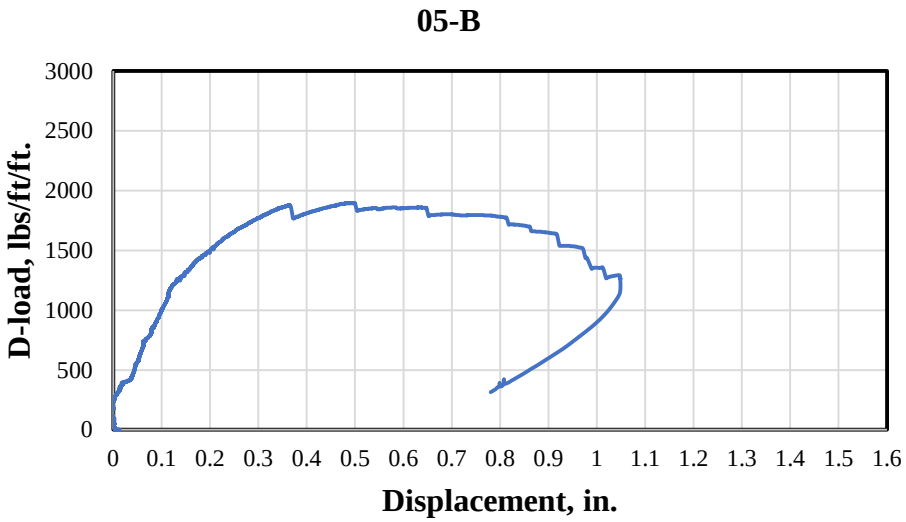

Figure B-13: Post-immersion D-load test results for Month-03 for pipe 05-B subjected to 200 PPM Sodium Chloride Solution

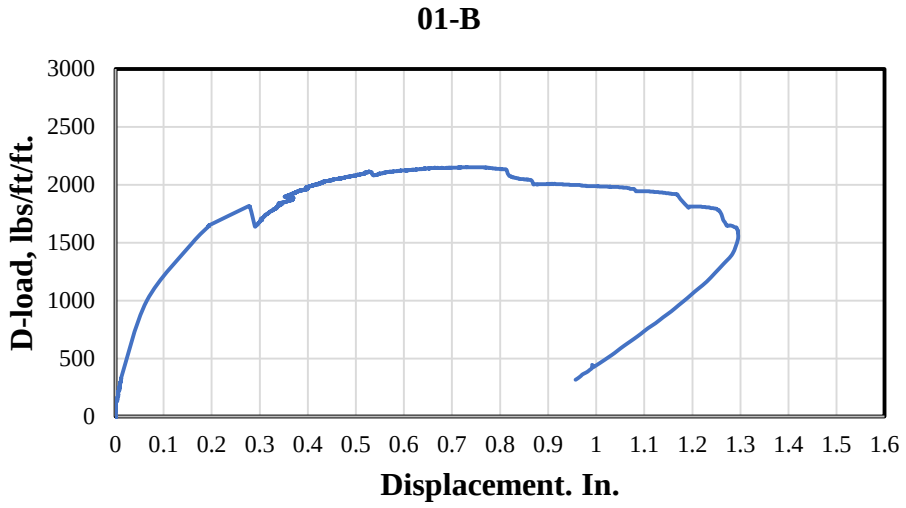

Figure B-14: Post-immersion D-load test results for Month-03 for pipe 01-B subjected to 200 PPM Sodium Chloride Solution

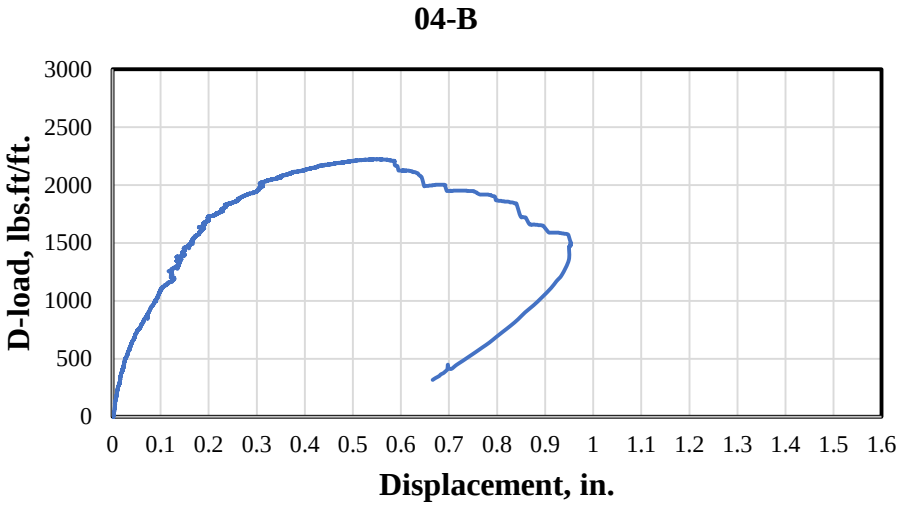

Figure B-15: Post-immersion D-load test results for Month-03 for pipe 04-B subjected to 200 PPM Sodium Chloride Solution

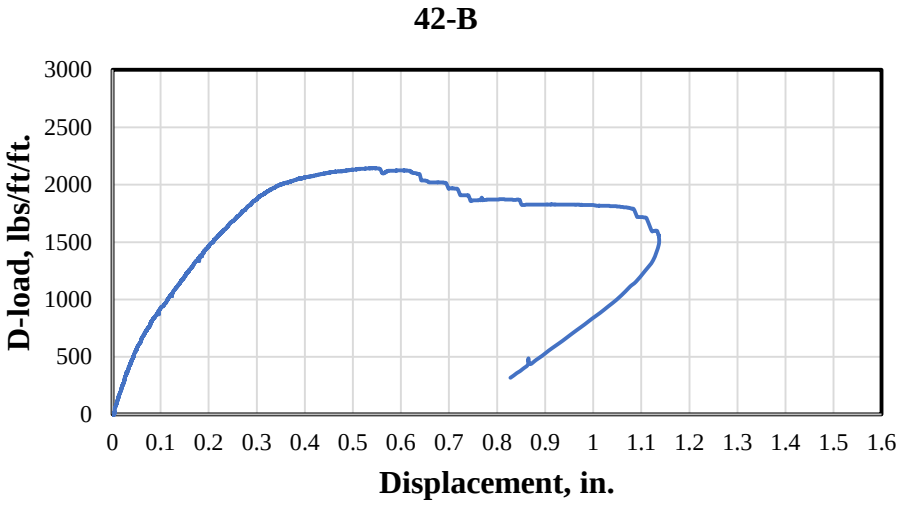

Figure B-16: Post-immersion D-load test results for Month-03 for pipe 42-B subjected to 2,000 PPM Sodium Chloride Solution

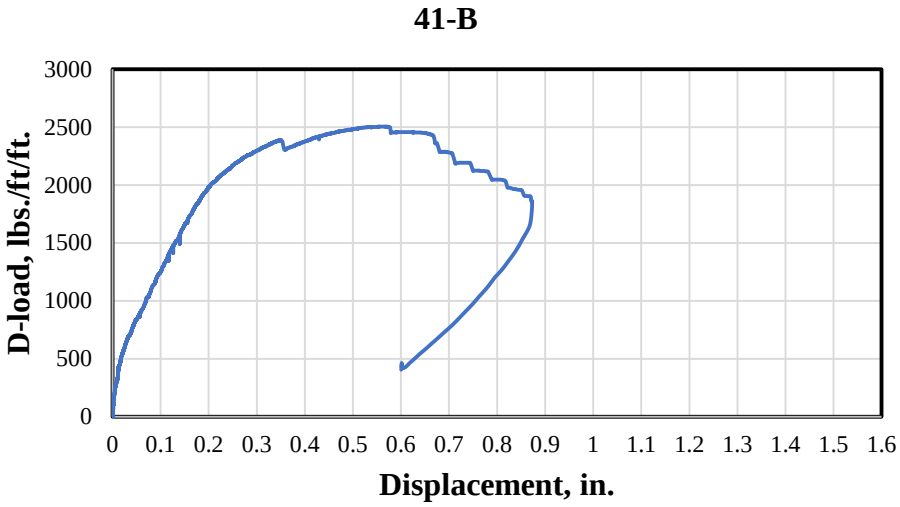

Figure B-17: Post-immersion D-load test results for Month-03 for pipe 41-B subjected to 2,000 PPM Sodium Chloride Solution

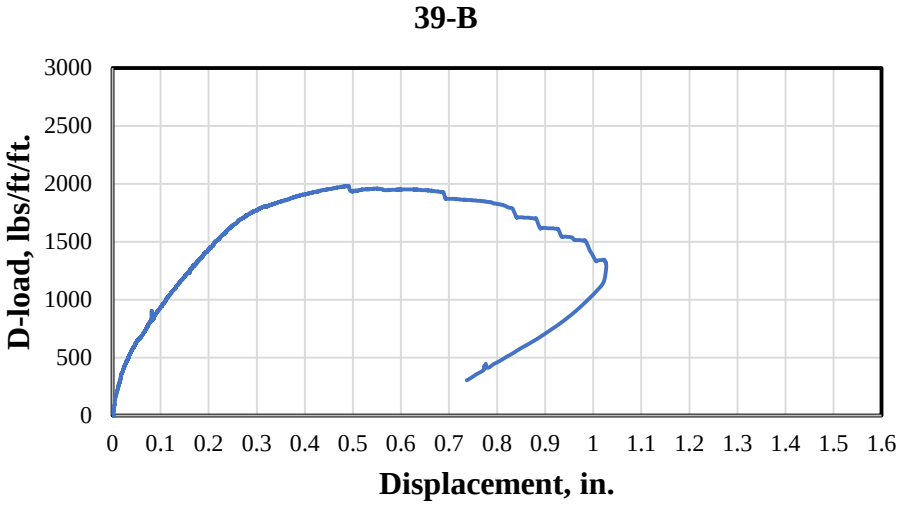

Figure B-18: Post-immersion D-load test results for Month-03 for pipe 39-B subjected to 2,000 PPM Sodium Chloride Solution

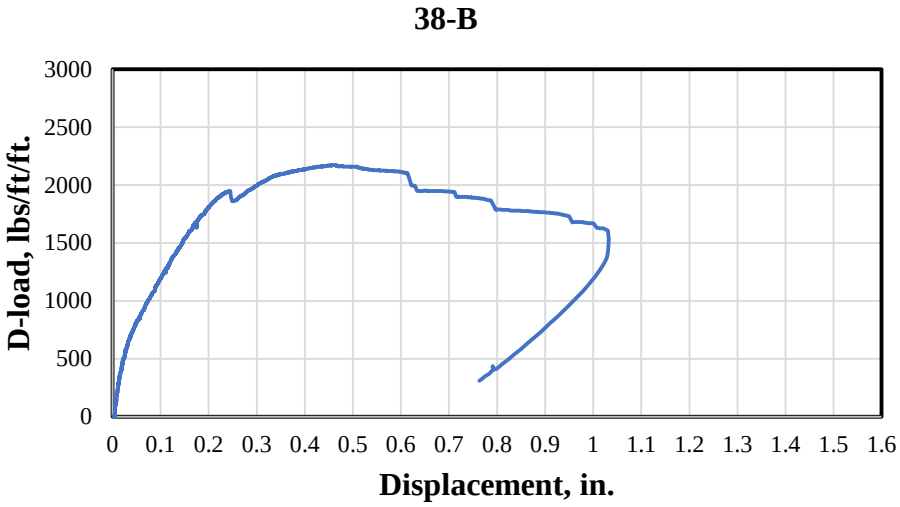

Figure B-19: Post-immersion D-load test results for Month-03 for pipe 38-B subjected to 30,000 PPM Sodium Chloride Solution

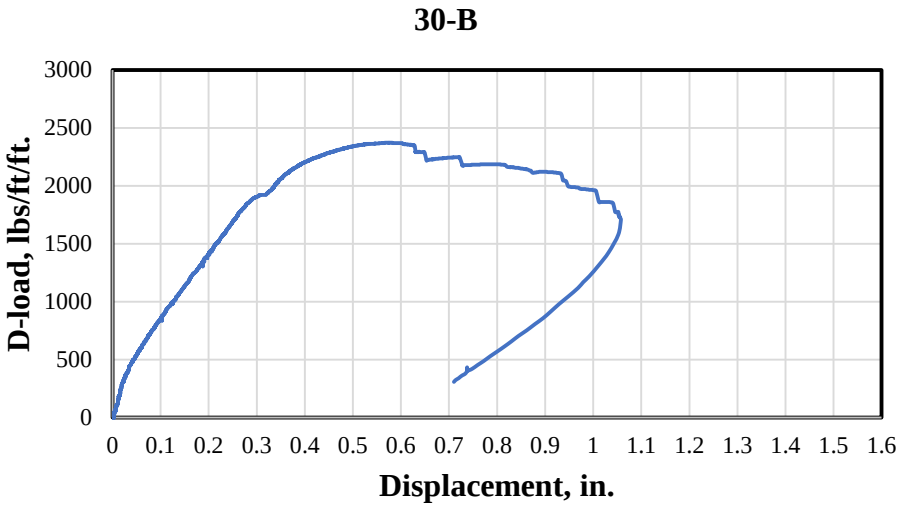

Figure B-20: Post-immersion D-load test results for Month-03 for pipe 30-B subjected to 30,000 PPM Sodium Chloride Solution

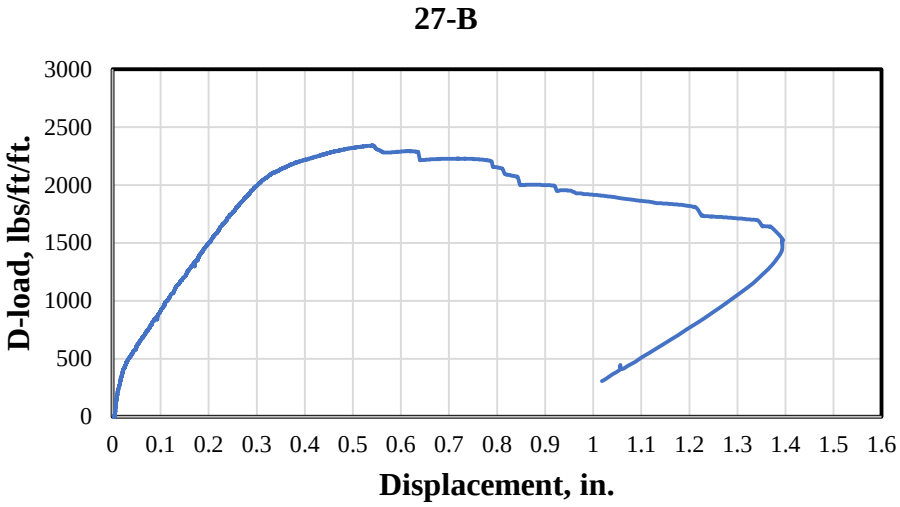

Figure B-21: Post-immersion D-load test results for Month-03 for pipe 27-B subjected to 30,000 PPM Sodium Chloride Solution

Fourth month test results:

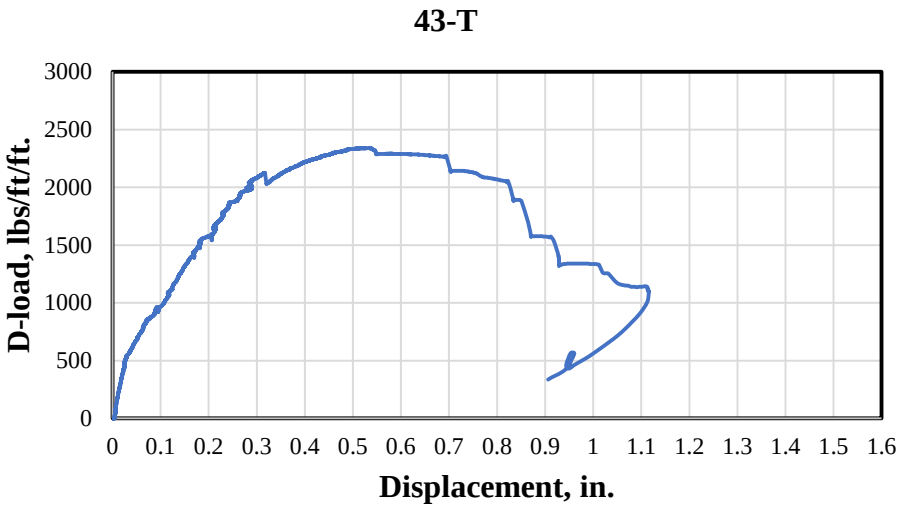

Figure B-22: Post-immersion D-load test results for Month-04 for pipe 43-T subjected to 30,000 PPM Sodium Chloride Solution

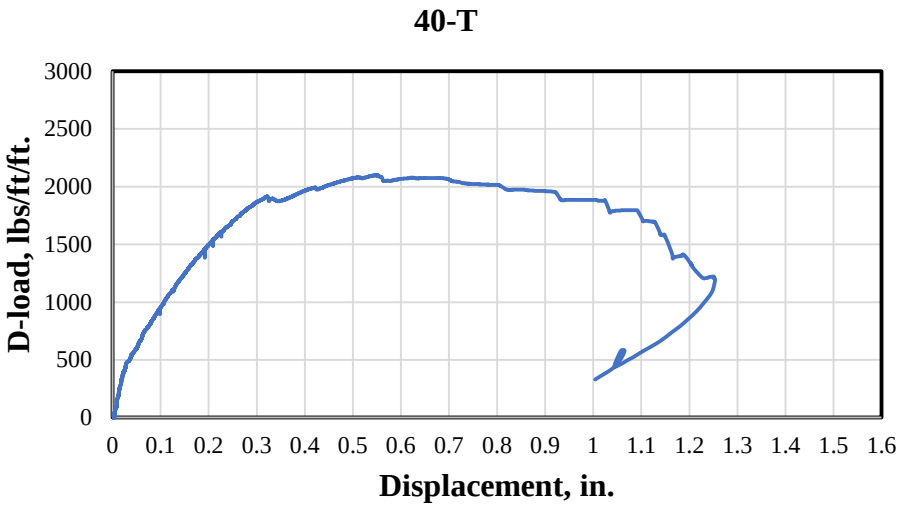

Figure B-23: Post-immersion D-load test results for Month-04 for pipe 40-T subjected to 30,000 PPM Sodium Chloride Solution

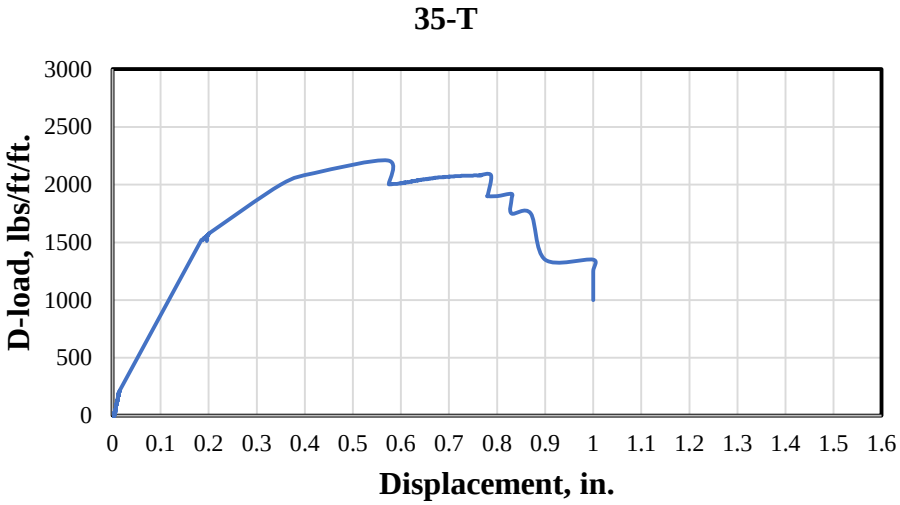

Figure B-24: Post-immersion D-load test results for Month-04 for pipe 35-T subjected to 30,000 PPM Sodium Chloride Solution

Fifth Month test results:

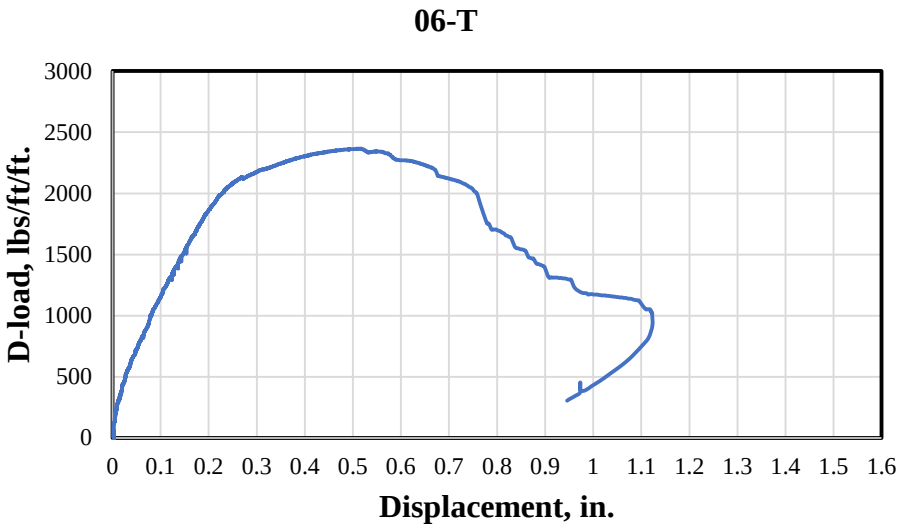

Figure B-25: Post-immersion D-load test results for Month-05 for pipe 06-T subjected to 200 PPM Sodium Chloride Solution

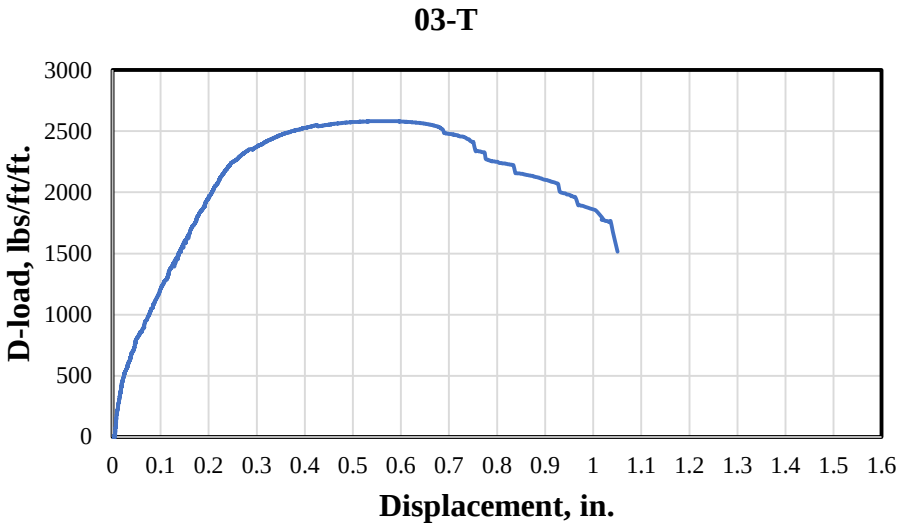

Figure B-26: Post-immersion D-load test results for Month-05 for pipe 03-T subjected to 200 PPM Sodium Chloride Solution

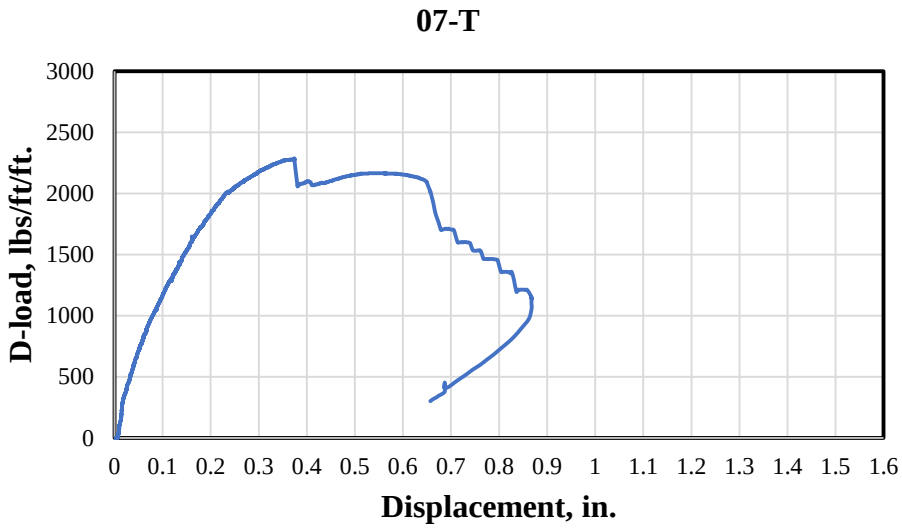

Figure B-27: Post-immersion D-load test results for Month-05 for pipe 07-T subjected to 200 PPM Sodium Chloride Solution

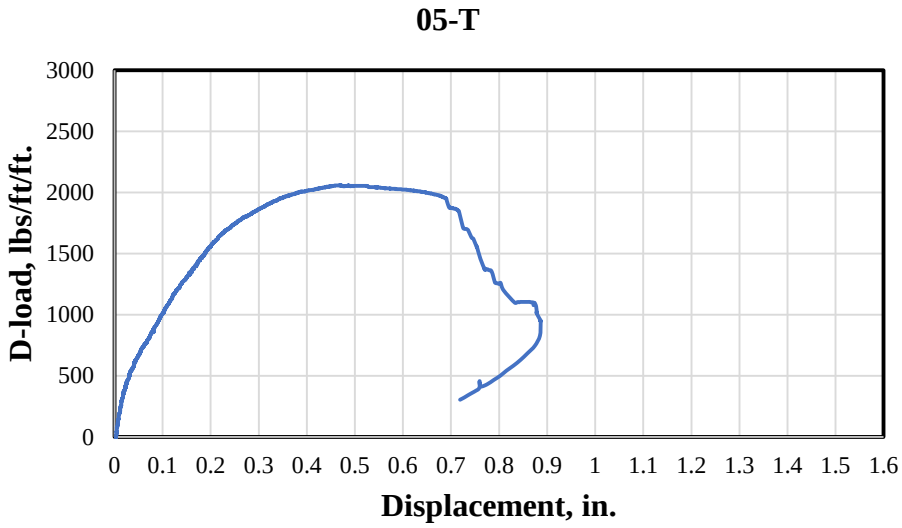

Figure B-28: Post-immersion D-load test results for Month-05 for pipe 05-T subjected to 2,000 PPM Sodium Chloride Solution

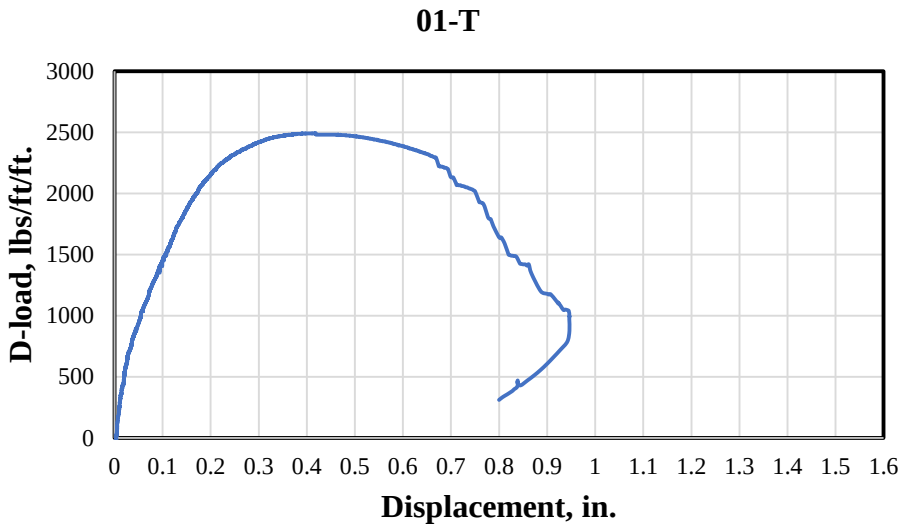

Figure B-29: Post-immersion D-load test results for Month-05 for pipe 01-T subjected to 2,000 PPM Sodium Chloride Solution

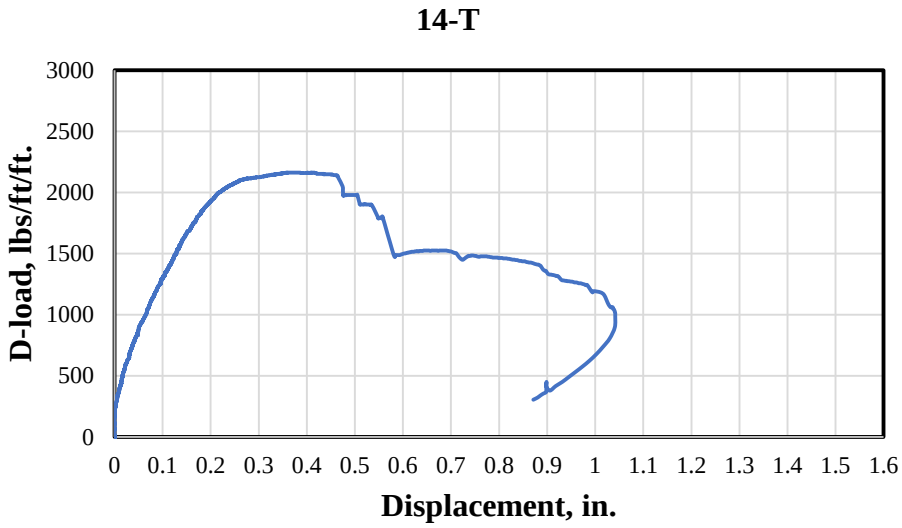

Figure B-30: Post-immersion D-load test results for Month-05 for pipe 14-T subjected to 2,000 PPM Sodium Chloride Solution

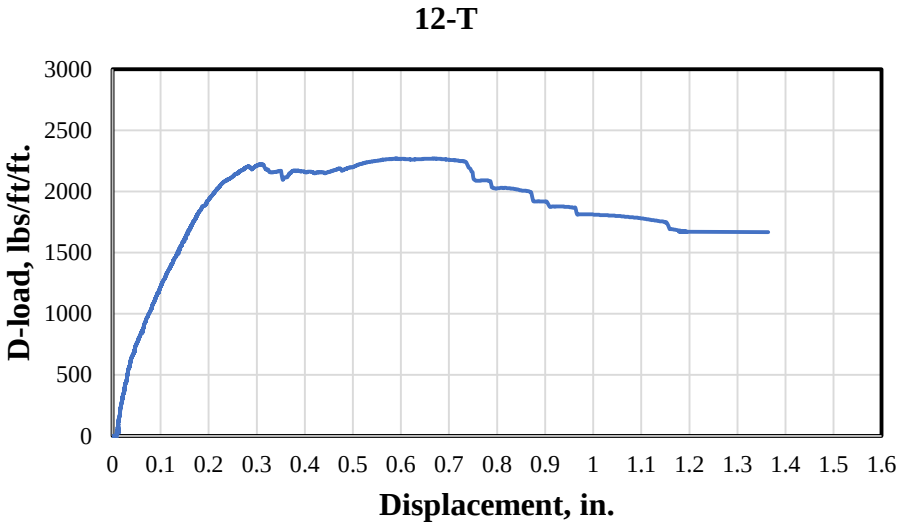

Figure B-31: Post-immersion D-load test results for Month-05 for pipe 12-T subjected to 30,000 PPM Sodium Chloride Solution

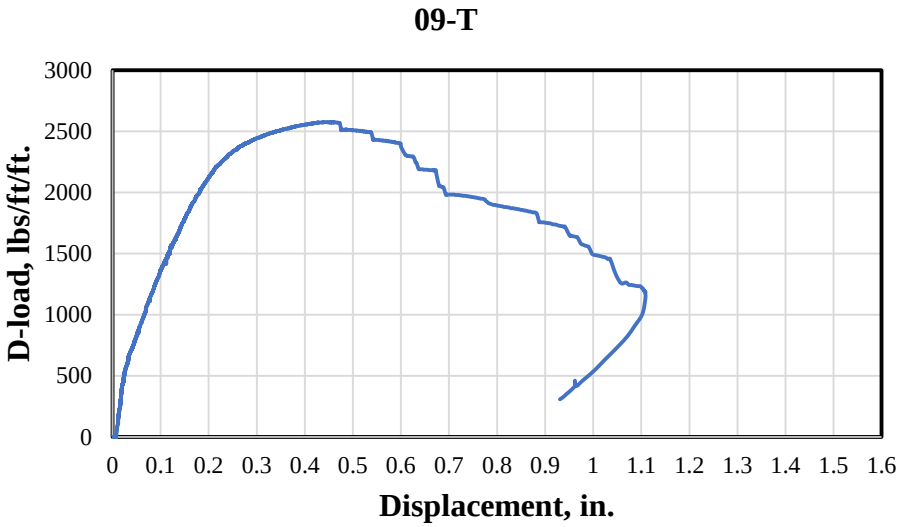

Figure B-32: Post-immersion D-load test results for Month-05 for pipe 09-T subjected to 30,000 PPM Sodium Chloride Solution

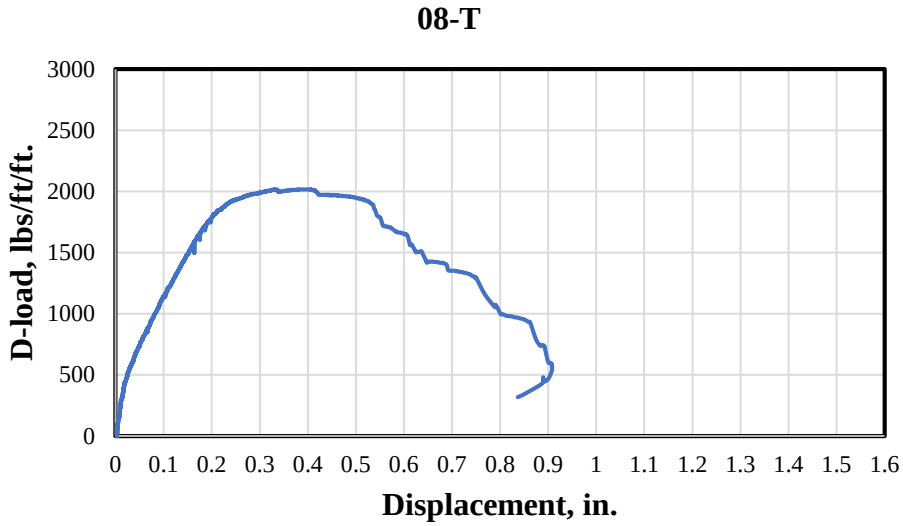

Figure B-33: Post-immersion D-load test results for Month-05 for pipe 08-T subjected to 30,000 PPM Sodium Chloride Solution

Sixth months test results:

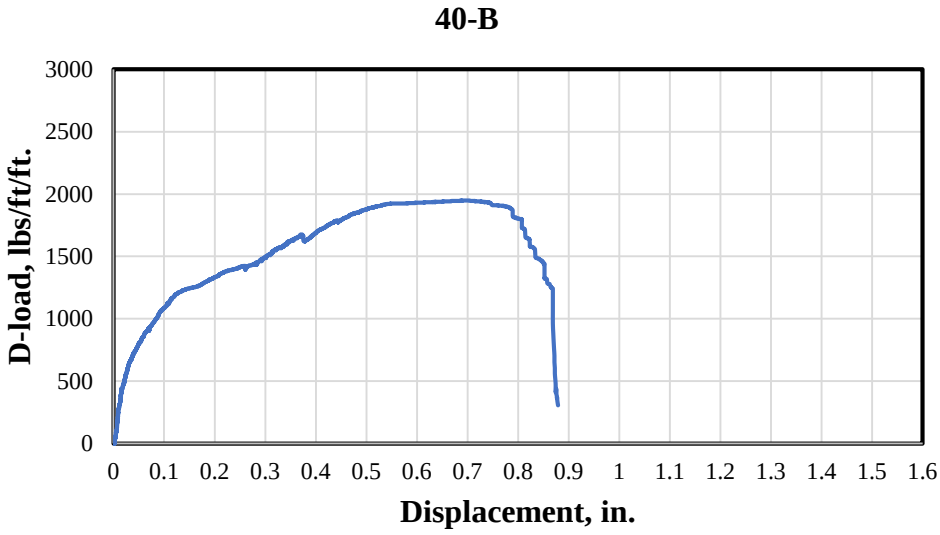

Figure B-34: Post-immersion D-load test results for Month-06 for pipe 40-B subjected to 30,000 PPM Sodium Chloride Solution

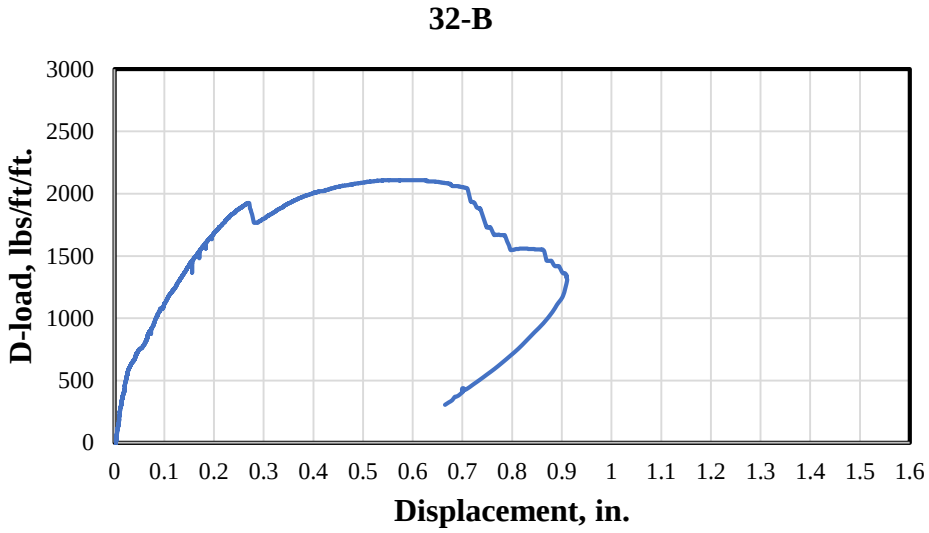

Figure B-35: Post-immersion D-load test results for Month-06 for pipe 32-B subjected to 30,000 PPM Sodium Chloride Solution

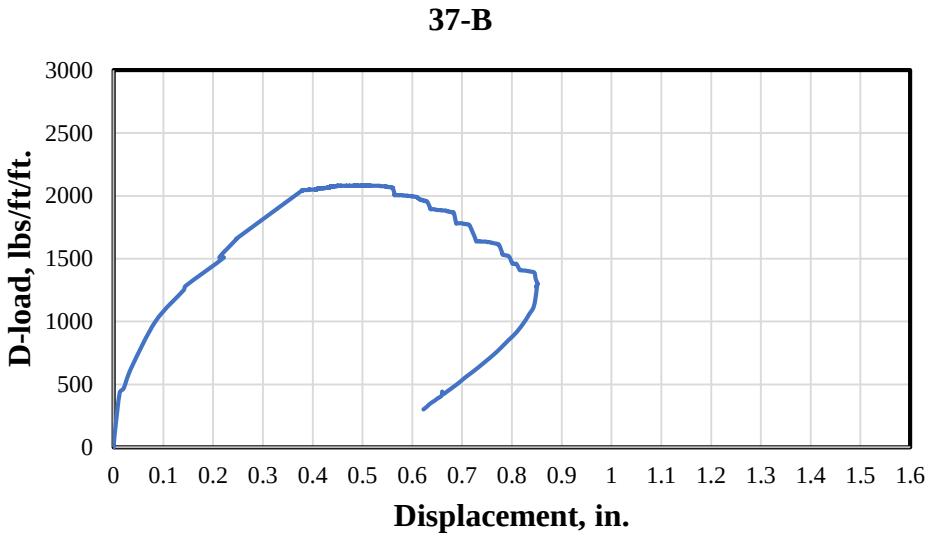

Figure B-36: Post-immersion D-load test results for Month-06 for pipe 37-B subjected to 30,000 PPM Sodium Chloride Solution

APPENDIX – C

SEM Pictures:

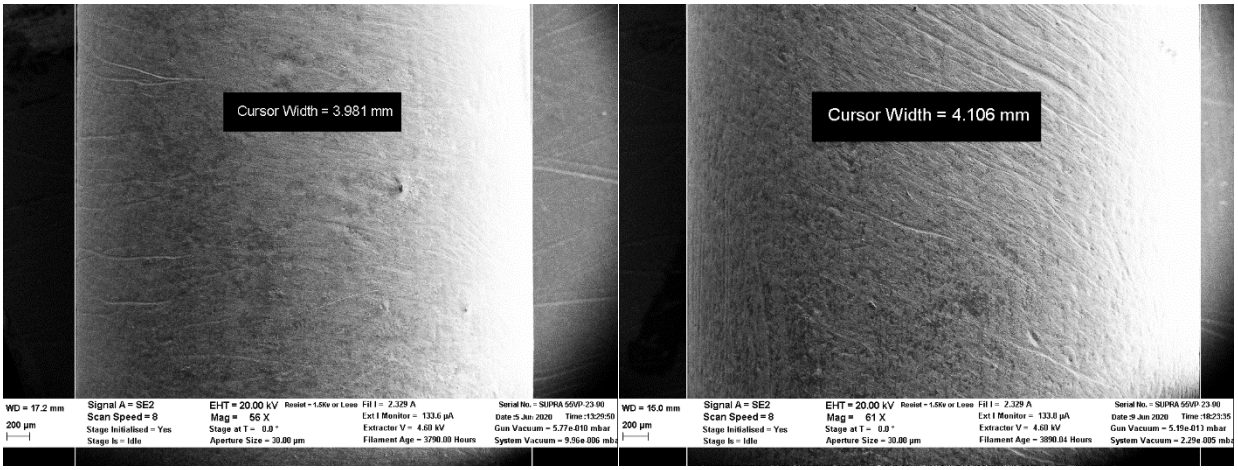

Figure C- 1: Diameter change for 30,000 PPM specimens for the second month

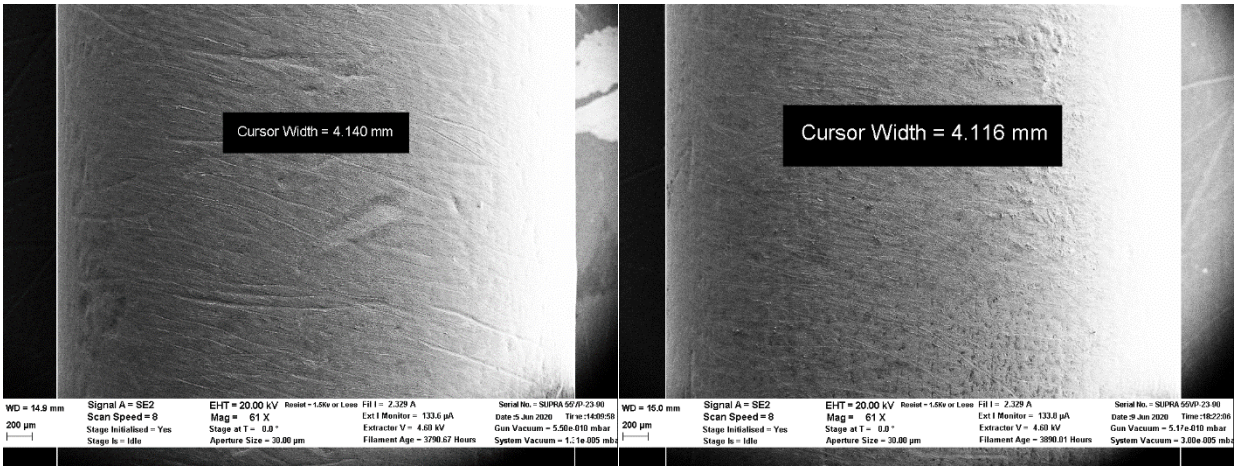

Figure C- 2: Diameter change for 200 PPM specimens for the third month

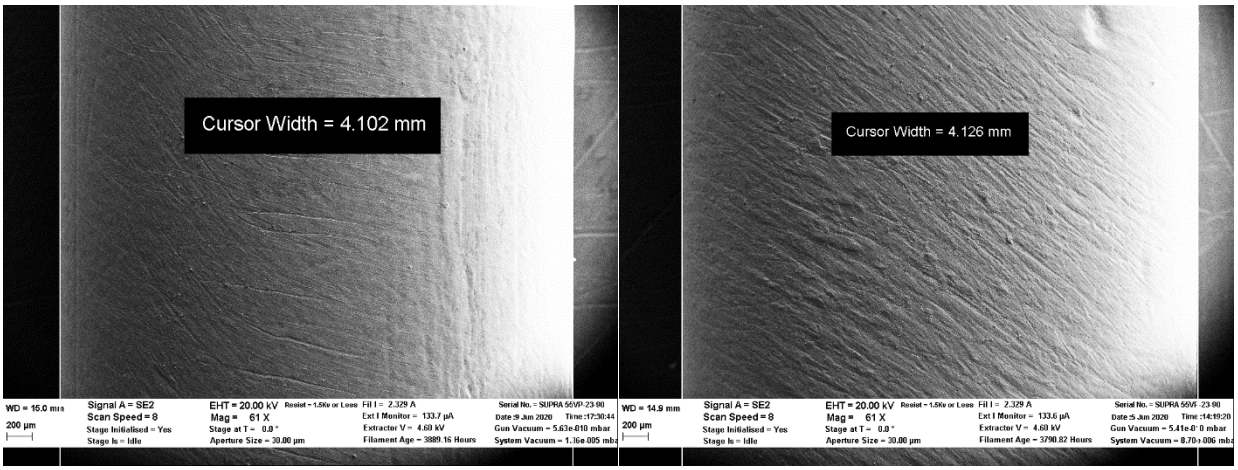

Figure C- 3: Diameter change for 2,000 PPM specimens for the third month

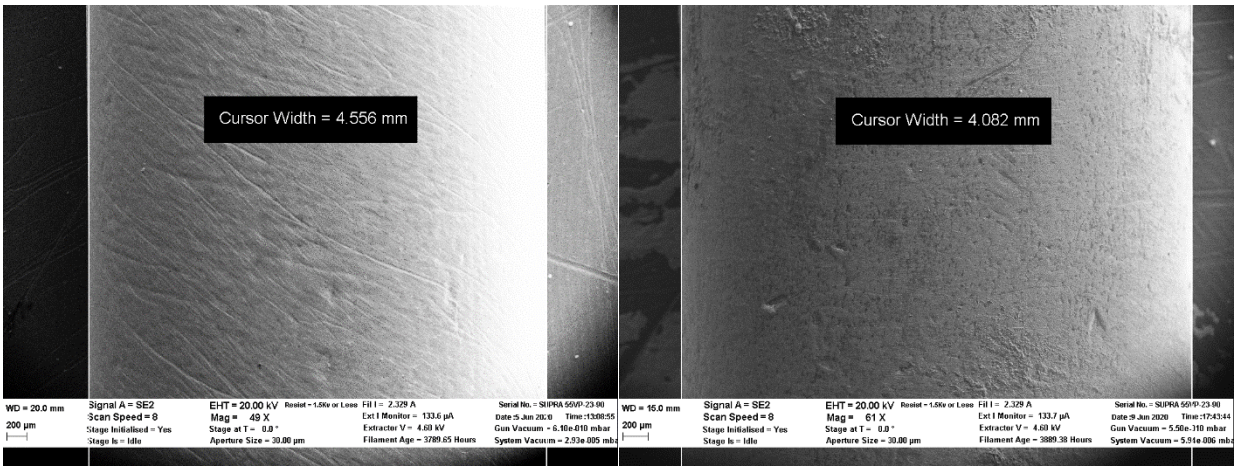

Figure C- 4: Diameter change for 30,000 PPM specimens for the third month

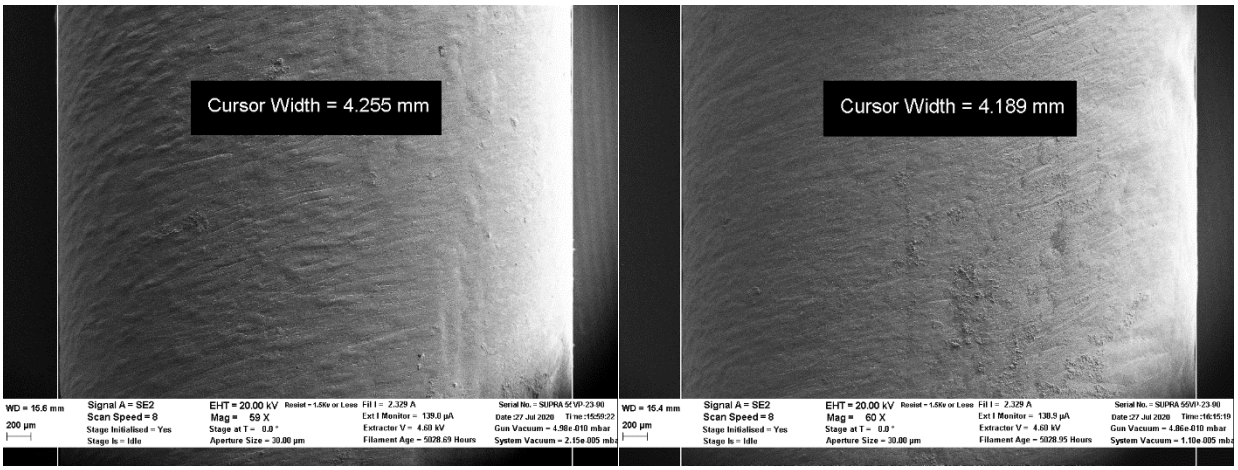

Figure C- 5: Diameter change for 30,000 PPM specimens for the fourth month.

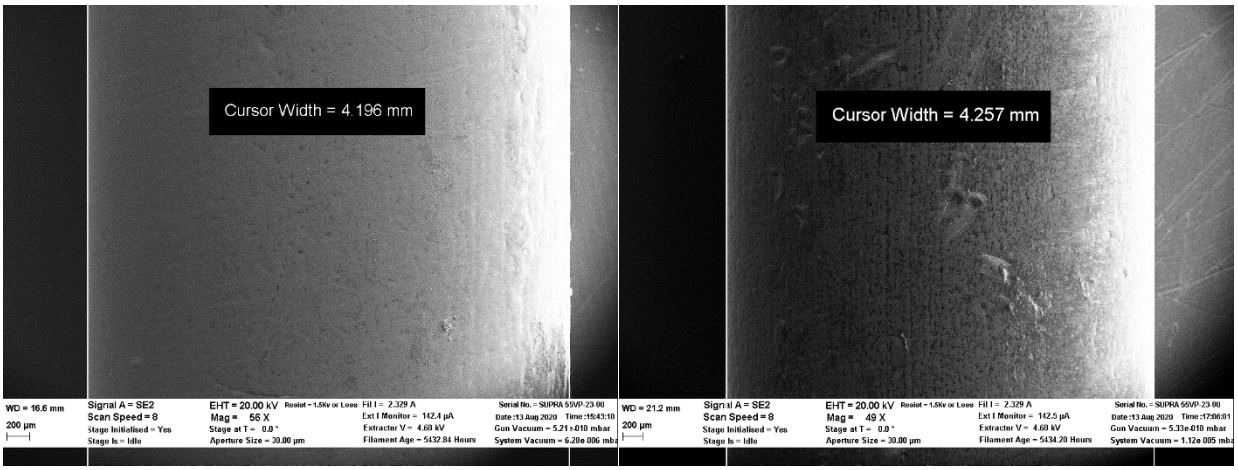

Figure C- 6: Diameter change for 200 PPM specimens for the fifth month.

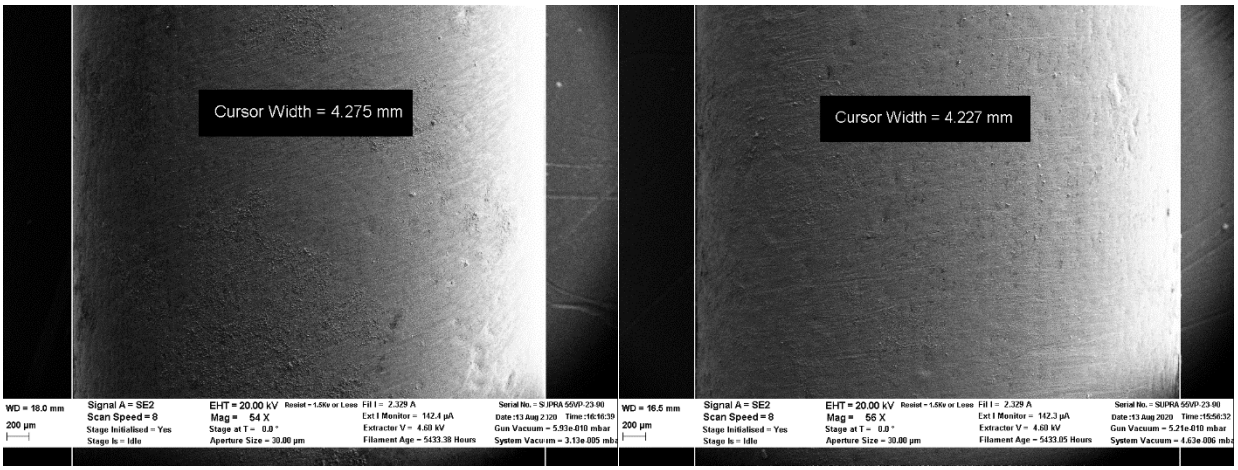

Figure C- 7: Diameter change for 2,000 PPM specimens for the fifth month.

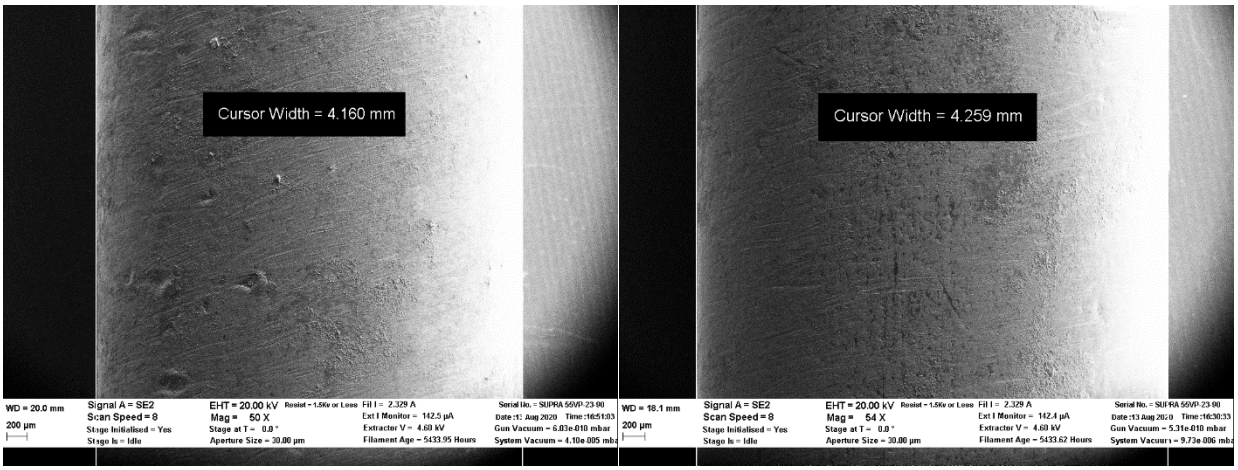

Figure C- 8: Diameter change for 30,000 PPM specimens for the fifth month.

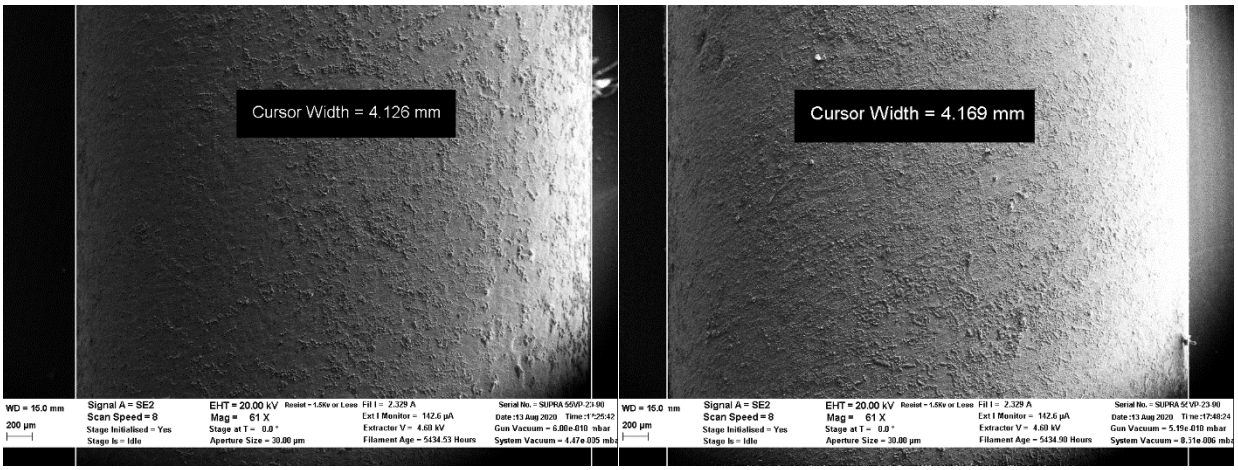

Figure C- 9: Diameter change for 30,000 PPM specimens for the sixth month.